Title
Nano-Optical Plasmonic Tweezers based on Engineered Hyperbolic and Nonreciprocal Metasurfaces

Author
Paul, Nayan Kumar

Publication Date
2022

Peer reviewed|Thesis/dissertation

Nano-Optical Plasmonic Tweezers based on
Engineered Hyperbolic and Nonreciprocal Metasurfaces

By

NAYAN KUMAR PAUL

DISSERTATION

Submitted in partial satisfaction of the requirements for the degree of

DOCTOR OF PHILOSOPHY

in

Electrical and Computer Engineering

in the

OFFICE OF GRADUATE STUDIES

of the

UNIVERSITY OF CALIFORNIA

DAVIS

Approved:

Juan Sebastián Gómez Díaz, Chair

Andre Knoesen

William Putnam

Committee in Charge
2022

To my parents, my brother,

and Aishorjo.

Dedicated to the memory of my cousin and best friend

Sujan Kumar Paul

Acknowledgements

I would like to express my deep gratitude and give warmest thanks to my thesis supervisor, Professor Juan Sebastian Gomez-Diaz, for the continuous support of my doctoral studies and research. It was a great privilege and honor for me to have the opportunity of working under his guidance. His dynamism, sincerity, passionate teaching, and immense knowledge deeply inspired me to learn about science and engineering as well as enhance my dedication and professionalism which is far beyond the scope of this thesis. In a word, the kind and considerate behavior of Sebastian make him a role model and one of the best possible mentors a student could imagine.

I would also like to thank Prof. Alejandro Alvarez Melcon, professor of Telecommunication Engineering at the Technical University of Cartagena, Spain. During his one-year visit at UC Davis, I had the opportunity to work next to his desk, and discuss on numerous topics in the field of electromagnetics. He provided many fruitful comments on my research projects that really helped to enhance the quality of this work.

I am extremely indebted to my master's supervisor Professor Brandon Kemp, department of Electrical Engineering at the Arkansas State University, USA. My research career began under his supervision as a graduate research assistant, and I will be deeply grateful to him in the rest of my life for giving me the opportunity to work with him. Dr. Kemp is the person who taught me the fundamental of electrodynamics with a great level of clarity that helped me during the next phase of my career.

Last but not the least, I am extremely thankful to my parents, Manindra Nath Paul and Nila Rani Paul, for their continuous support and motivation throughout my entire life. Their unconditional love and guidance cannot be described in words. I would not be at this stage and this journey would never be possible without them. I am also grateful to my brothers for always being on my side and encourage me. To my wife, Aishorjo, for her unlimited support, sacrifice and love during this long journey and for being the best partner.

I would also like to acknowledge National Science Foundation for supporting this work with Grant No. ECCS-1808400 and a CAREER Grant No. ECCS-1749177.

Abstract

Artificially engineered structures, namely metamaterials and their two-dimensional (2D) counterpart – metasurfaces, have been proven as promising platforms to realize unusual light-matter interactions. Such structures have enabled the efficient manipulation of electromagnetic waves in unprecedented ways that cannot be obtained using conventional materials and thus have triggered exciting applications such as hyperlensing, canalization of light, negative refraction, hyperbolic dispersion, cloaking, or the enhancement of the spontaneous emission rate of dipole emitters, amongst many others. Moreover, the discovery of graphene and other 2D materials, and their electrical tunability, have enabled the use of surface plasmon polaritons at terahertz and infrared frequencies in numerous nanophotonic applications.

In this thesis, I propose novel nano-optical plasmonic tweezers based on hyperbolic and nonreciprocal metasurfaces to efficiently trap and manipulate nanoparticles in the near field with superior performance compared to the state of the art. To this purpose, I develop a rigorous theoretical framework able to compute optical forces on dipolar Rayleigh nanoparticles located near the metasurfaces. The theoretical model is based on Lorentz force within the dipole approximation combined with the scattered dyadic Green's function of the system. Analytical expressions show that the force strength is directly proportional to the fourth power of wavenumber of the supported surface plasmons. This tells that the strength can be dramatically enhanced by the proper choice of metasurfaces that support ultra-confined surface plasmons with larger wavenumber. One potential candidate to achieve such response is the use of hyperbolic metasurface that supports surface plasmons with wavenumbers up to ~ 200 times larger than the ones supported in free space. My theoretical and numerical results using full wave simulations show that the use of hyperbolic metasurfaces enables unusual enhancement of the force strength (up to 3 orders of magnitude) in comparison to the one obtained above conventional isotropic media. Importantly, such response enables stable lateral trapping and efficient manipulation of nanoparticles using low-power laser beam thus reducing the photodamage threat. However, these general optical tweezers are static in the sense that their response cannot be dynamically controlled.

In this context, drift-biased nonreciprocal graphene has emerged as a promising platform to electrically tune and manipulate the dispersion characteristic of the supported modes. I propose the use of this platform as a planar plasmonic hyperlens that provides ultra-subwavelength imaging with remarkable resolution over a broadband frequency range that cannot be obtained by other artificially engineered structure. In addition, drift-biased graphene can also readily be applied in the context of optical tweezers to provide novel responses: (i) particles can be manipulated unidirectionally independent to the direction of the incoming light, overcoming beam alignment challenges occurring in conventional optical tweezers; and (ii) the location of optical traps can efficiently be manipulated over a few microns range thanks to the electrically tunable response. In summary, I envisage that the proposed nano-optical hyperbolic and nonreciprocal plasmonic tweezers may open unprecedented venues for routing, trapping, and assembling nanoparticles and can effectively address some of the shortcomings of current techniques.

Table of Contents

Chapter 1: Introduction

1.1 METAMATERIALS AND METASURFACES

Metamaterials are artificially designed electromagnetic materials designed on subwavelength scale to achieve extreme light-matter interactions that cannot be obtained using naturally available conventional media. They are constructed by a repeating pattern of metals or dielectrics at scales much smaller than the operating wavelength. The macroscopic constitutive parameters of the metamaterials are not directly determined by the electrical properties of the base materials (metal or dielectrics), rather they depend on the orientation, shape, density, and composition of the newly designed structures. Within the electromagnetics and nanophotonic research community, metamaterials have gathered significant attention over the past few decades, and the unusual light-matter interactions provided by them have triggered numerous applications, including negative refraction of light [1-4], focusing and superlensing [5-8], ultra-subwavelength imaging [9,10], optical cloaking [11-14], hyperbolic dispersion characteristics [15-17], micro-electromechanical systems [18-20], optical tweezers [21-24], surface enhanced Raman scattering [25,26], Cherenkov radiation [27,28], amongst many others. Figure 1.1 shows examples of two important electromagnetic effects using metamaterials: (a) hyperlensing with sub-diffractive resolution using split ring resonators [29], and (b) Cherenkov radiation using periodically organized metal-dielectric layers

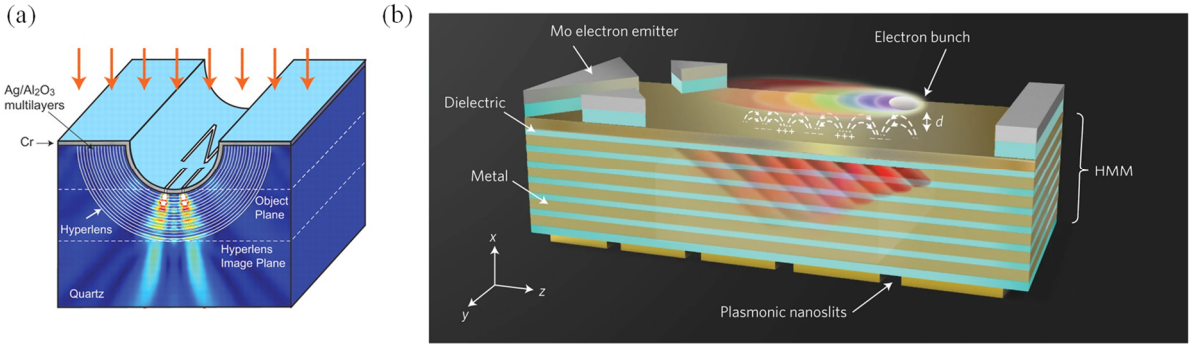

Figure 1.1: Nanophotonic applications of hyperbolic metamaterials. (a) Hyperlens with sub-diffractive resolutions [29], and (b) Cherenkov radiation in the presence of electron beam flowing nearby [27].

overcoming the velocity threshold of moving charges [27]. Despite offering promising electromagnetic features, the three-dimension size, bulk volumetric loss, fabrication challenges and difficulties to access energy always restrict the uses of metamaterials in modern nanophotonic devices.

In a parallel development, recent years have witnessed the emergence of metasurfaces [30-32] –a two-dimensional equivalent of bulk metamaterials– that enable planar photonics technologies [33,34]. Specifically, metasurfaces are constructed in a similar fashion as metamaterials, but in a single or few layers along planar dimension the with subwavelength thickness. The ultrathin thickness in the wave propagation confirms significantly reduced ohmic loss of the devices and provides an easy access to the stored energy. Moreover, the reduced dimensionality enables an easy integration with on-chip nanophotonic devices. Over the years, metasurfaces have provided a plethora of nanophotonic applications with outstanding performance, including canalization of electromagnetic waves [35,36], planar hyperlensing [37,38], planar nanoantennas and transceivers [39], ultra-sensitive sensors [40], invisibility cloaks [41,42] amongst many others.

One of the unique features of metasurfaces is their ability to couple evanescent waves in the form of surface plasmon polaritons – an electromagnetic surface wave that propagates through a dielectric-metal interface with evanescent wavefront in the vertical direction. The use of metasurfaces permits to obtain extremely confined surface plasmons with large wavenumber, up to hundreds of times with respect to the one available in free space [43-47]. The feature of such surface waves can be tuned by modifying the size, arrangement and periodicity of the unit cells that compose the metasurface. Importantly, exotic light-matter interactions can be obtained with a properly designed structure that provides highly anisotropic response, including in-plane hyperbolic-like dispersion [48,49] in analogy to bulk hyperbolic mode in metamaterials [17,50]. Hyperbolic metasurfaces exhibit fascinating electromagnetic properties, such as extreme confinement of surface wave with very large wavenumber and local density of states over a broad frequency band [38,51,52]. The origin of the in-plane hyperbolic dispersion can be realized as follows: when a metasurface exhibits metallic (i.e., inductive, L) and dielectric (i.e., capacitive, C) responses along the

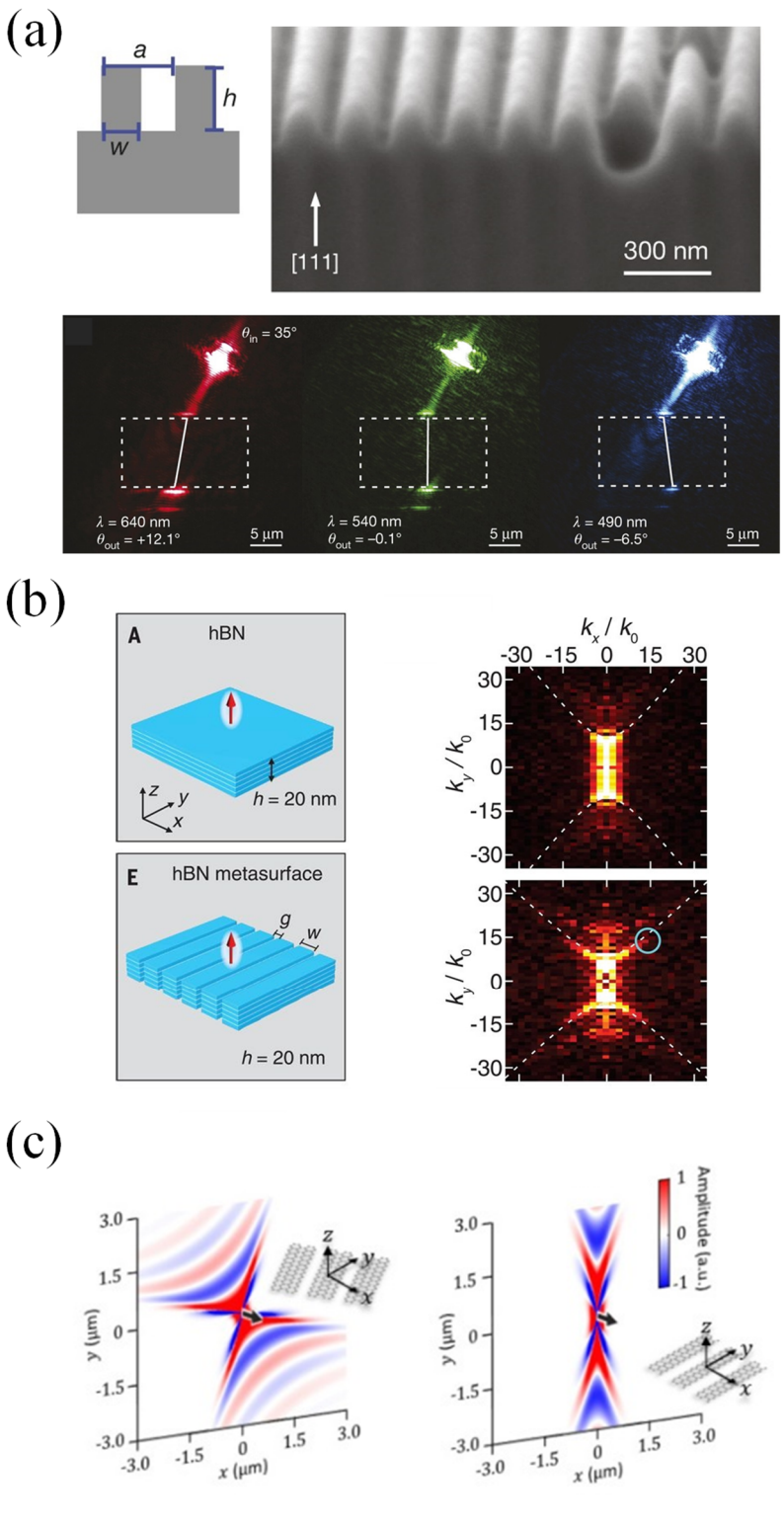

Figure 1.2: Realistic hyperbolic metasurfaces. (a) Visible frequency hyperbolic metasurface constructed by nanostructured silver allows negative refraction of light [48]. (b) Infrared and (c) terahertz hyperbolic metasurface constructed by hexagonal boron-nitride [49] and graphene strips [52], respectively, and their supported modes.

optical axes as a function of electric field polarization, the LC resonance introduces a hyperbolic dispersion in the momentum space. Hyperbolic metasurfaces can easily be constructed in practice with subwavelength periodically organized structures made of gold [53], silver [48], hexagonal boron nitride [49], graphene [51,52,54], and other two-dimensional materials [35,36]. Figure 1.2 shows few examples of realistic hyperbolic metasurfaces constructed by periodically organized (a) single crystalline silver, (b) hexagonal boron nitride and (c) graphene strips. The frequency range within which such structures support hyperbolic surface plasmons is primarily determined by the electrical properties of the composing cells. For instance, the use of gold and silver permits to design broadband hyperbolic metasurfaces ranging from visible to near-infrared frequencies [48], whereas hexagonal boron nitride [49] and graphene [51,52] covers infrared, and far-infrared to terahertz, respectively.

Given these unusual electromagnetic properties and reduced dimensionality, it is not a surprise that hyperbolic metasurfaces is one of the most discussed and emerging topics in the field of plasmonics and nanophotonics. The ability of this platform to strongly interact with light simultaneously allowing dynamic processing of extremely confined surface waves, and easy integration with on-chip devices enables the design of optical tweezers using low power laser beam with superior performance, as will be investigated in this thesis.

1.2 NONRECIPROCAL PLASMONICS

The electromagnetic responses of conventional photonic devices are constrained by Lorentz reciprocity law that is based on the invariance of Maxwell's equation under time-reversal symmetry [55]. It entails that signal transmission between two points in space must remain identical for both propagation directions when the source and receiver positions are interchanged [56]. This mechanism forbids one-way propagation of electromagnetic waves in linear plasmonic and photonic platforms.

The last decade has witnessed enormous interests in breaking reciprocity to meet the ever-growing demands of all-photonic highly integrated systems [57-64]. One of the standard approaches to obtain

nonreciprocal responses relies on magneto-optical effects. Unfortunately, bulky, lossy, and expensive magnets required to achieve such responses are not compatible with integrated circuits, that lessen their interest in practice. Alternative solutions based on nonlinear effects [65,66], optomechanical interactions [67,68] and spatiotemporal modulations [69-71] have opened interesting opportunities. Among these approaches, nonlinear effects can be employed to break nonreciprocity for certain power levels of the incoming signals that is applied to a single port at the time. Nonreciprocal responses provided by the opto-mechanical resonators are somehow complex to implement, narrowband, and relatively weak [72,73]. The other approach, spatiotemporal modulation, requires hundreds of gating pads to impart very high modulation frequencies able to impart linear or angular momentum to the devices, thus demanding very complicated fabrication process and feeding networks. All these challenges make the above approaches challenging to implement in practice.

Recently, a novel mechanism has been put forward to realize nonreciprocal plasmonic structures by applying a drift-bias to efficiently shape the characteristics of the surface plasmon polaritons (SPPs) supported by them [61-64,74-76]. Such drift-biased materials host drifting electrons that causes the SPPs to feel different media towards and in the opposite of drifting direction. This mechanism strongly influences and interacts with the travelling plasmons, forcing them to exhibit a non-symmetrical propagation through the structure.

Large part of the ability of the drift-bias approach in breaking reciprocity depends on the velocity of drifting electrons that interacts with the supported plasmons. For instance, strong nonreciprocal responses are extremely difficult to obtain in semiconductors and metals due to their weak-electron mobility [62]. In this context, graphene has recently opened new opportunities. This 2D material possesses ultrahigh electron mobility and the drifting electrons can acquire large velocities up to $v_d \approx 0.95v_F$, very close to the Fermi velocity ($v_F = 10^6 m/s$) of electrons there [77,78]. Remarkably, these values are several orders of magnitude lager than those obtained in typical metals [62], and many times larger than in semi-conductors with high electron mobility [79]. Combining graphene plasmonics with drift-bias schemes has recently

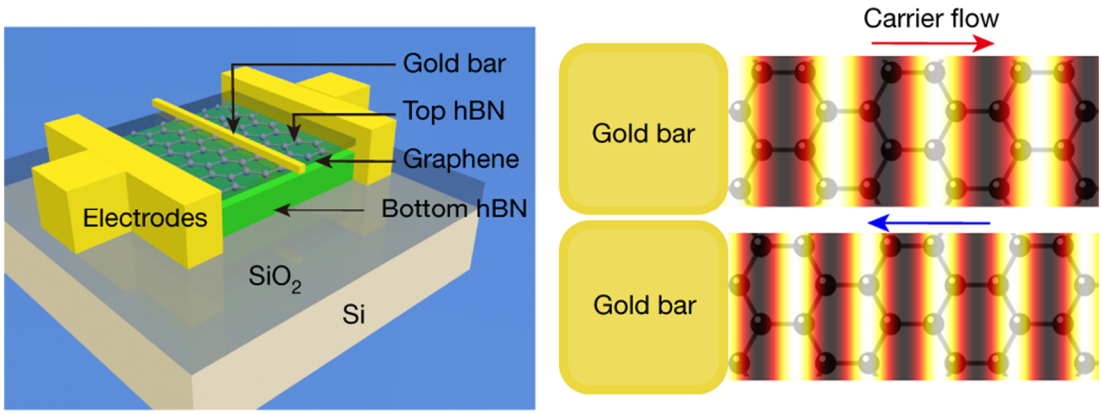

Figure 1.3: Drift-biased nonreciprocal graphene. (a) Schematic of the configuration, and (b) properties of the surface plasmons flowing along and against the drift [81].

opened simple yet extremely efficient ways to collimate, steer and shape SPPs over a broad frequency band [61,63,64]. I stress that the nonreciprocal properties of the surface plasmons supported by drift-biased graphene have been verified experimentally in the recent years [80,81]. Figure 1.3 shows the feature of the supported surface modes: plasmons flowing against the drifting electrons possess larger wavenumber than the one following along the drift. This mechanism will be further discussed in Chapter 3 of this thesis with a proposed application of drift-biased graphene acting as a planar plasmonic hyperlens.

1.3 NANO-OPTICAL TWEEZERS

The manipulation and trapping of particles was first reported in the seminal work of Prof. Ashkin in 1970 [82]. This pioneering effort confirmed that light can exert actual forces on matter thanks to a momentum exchange during scattering processes. In the micrometer-sized range, conventional optical tweezers formed at the diffraction-limited focus of a laser beam have been proven as a powerful tool to manipulate a wide variety of objects [83], including cells and other biological components. Such tweezers have also been combined with confocal Raman spectroscopy [84-88] for label-free chemical analysis of single particles [89,90] and even single living cells [91,92]. At the sub nanometer scale, light-matter mechanical coupling has led to the cooling of atoms, ions, and molecules [93-95], giving rise to modern ultracold atom technology [96]. However, optical forces acting at the nanoscale, i.e. on particles between

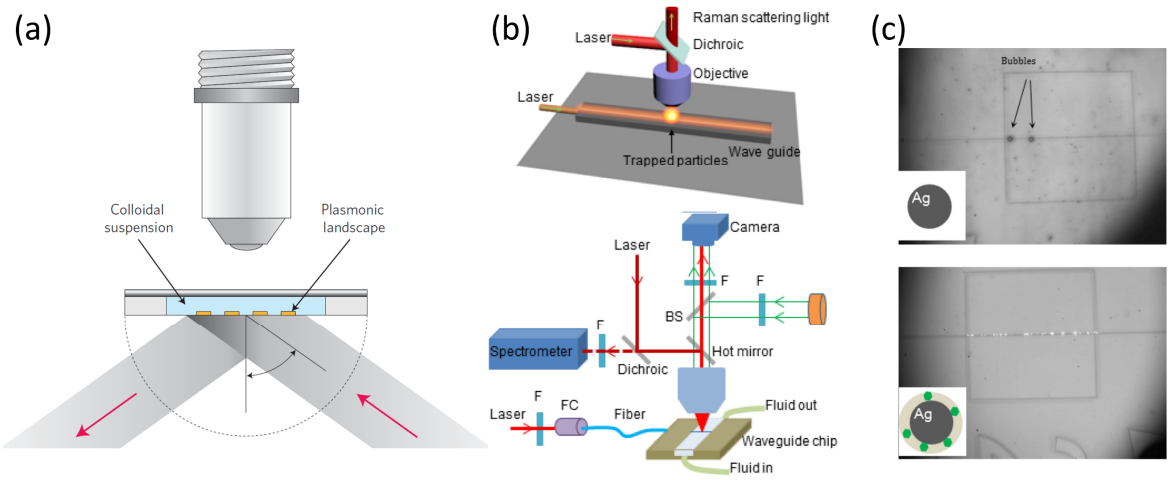

Figure 1.4: Examples of trapping and manipulation of particles using plasmonic nanostructures. (a) Schematic of an experimental microparticle trapping set-up [98]: a pattern of micrometer-sized gold disks is illuminated under the Kretschmann configuration through a glass prism. (b) Schematic of an experimental nano-tweezer system combined with surface enhanced Raman spectroscopy developed at Center for Biophotonics Science & Technology at the University of California Davis [108] and (c) images of the system trapping biomolecules.

~1 and 100 nm, have been elusive in practical configurations due to the challenges present at this range [97,98]: scaling-down the techniques for manipulating microparticles, based on electric dipole interaction energy [99,100], leads to thermal fluctuations large enough to allow the particles to escape from the trap whereas scaling-up the efficient laser cooling of atoms requires scattering processes with very narrow spectral lines and without significant radiative losses, features that common nanostructures do not possess [96]. The development of optical tweezers operating at the nanoscale would open extraordinary opportunities in many fields of bioengineering and nanotechnology, including the accurate positioning of individual objects (such as quantum dots, nanowires, nanotubes, and two-dimensional materials) and exciting applications in bioengineering, biochemistry, and biophysics.

In this context, recent years have witnessed the emergence of nano-optical plasmonic tweezers aiming to trap and manipulate nanometer-sized particles and objects [97,98]. These devices enhance optical forces thanks to the excitation of SPPs with evanescent fields that can be concentrated beyond the diffraction limit. A wide variety of nano-optical tweezers have been put forward, including metallic structures with micrometer-size patterning [101,102], optical antennas that exploit the field enhancement between their

arms [103-105], and nanostructured substrates [106], just to name a few. Figure 1.4 illustrates two configurations relevant to this application. Specifically, Figure 1.4(a) shows the first experiment of SPP-based trapping [98,102,107]: a patterned metallic surface was illuminated using the Kretschmann configuration by a transverse magnetic (TM or p)-polarized beam, thus exciting evanescent optical waves able to manipulate and trap dielectric and metallic particles located in the near-field. Figure 1.4(b) highlights the integration of an optical tweezer with a confocal Raman spectroscopy setup, a system recently developed in Center for Biophotonics Science & Technology at the University of California Davis [108]. This integrated tweezer uses a 785 nm laser coupled to a silicon nitride waveguide to generate near-field evanescent waves capable of (i) trapping nanoparticles on the surface of the structure; and (ii) exciting surface-enhanced Raman spectroscopy signals to characterize such particles. Despite recent and significant progress in this field, the exponential growth of nanotechnology and bioengineering is continuously imposing challenging demands to modern nano-optical tweezers in terms of much larger optical forces and trapping potentials, lower laser intensities, deeply subwavelength resolution, and enhancement of the associated surface-enhanced Raman spectroscopy processes employed to characterize biological nanoparticles.

1.4 SCOPE OF THIS THESIS

The overarching objective of this thesis is to investigate the light-matter interactions provided by hyperbolic and nonreciprocal metasurfaces, and exploit their unusual near-field functionalities to design novel nanophotonic devices, with emphasis on nano-optical tweezers. Each Chapter investigates different physical scenarios within this common subject, and connect them with the previous analysis and results.

In Chapter 2, I overview the dispersion relation of anisotropic metasurfaces, the feature of surface plasmons supported by them and the scattered dyadic Green's function of the system. Then, I summarize the electromagnetic modelling and characterization of practical reciprocal anisotropic and hyperbolic metasurfaces constructed by periodically organized subwavelength metal or graphene strips covering visible, infrared and terahertz frequencies. In Chapter 3, I transition from reciprocal structures to design

and model nonreciprocal metasurfaces based on drift-biased graphene. I investigate the properties of surface plasmons supported by these structures and propose planar plasmonic hyperlenses capable of ultra-subwavelength imaging. In Chapter 4, I develop a rigorous theoretical framework to calculate optical forces on a dipolar nanoparticle located near reciprocal anisotropic metasurfaces under illumination with a laser beam. I then extended my theory to the case when the metasurface reciprocity is broken in the presence of an external in-plane momentum bias, such as drift-biased graphene. These models are based on the scattered dyadic Green's function of the system that I solve analytically by combining the complex integration techniques and residue theorem. This allows to develop analytical expressions of the optical forces that unveil the physical meaning and origin of such forces. In the following Chapters, I employ my theoretical model to compute the force response in several structures. Specifically, Chapter 5 and 6 investigate the response of giant lateral optical forces and stable optical trapping of nanoparticles located near reciprocal hyperbolic metasurfaces when illuminated by a plane wave and focused Gaussian beam, respectively. In Chapter 7, I investigate the force response near drift-biased nonreciprocal graphene in the presence of plane wave. Chapter 8 shows that when a nanoparticle located near a nonreciprocal surface is illuminated by a Gaussian beam, the trap position can be precisely manipulated in nanoscale by tuning the applied bias. This is the first nonreciprocal optical tweezer that does not rely on the magneto-optic effect. Finally, Chapter 9 briefly overviews and details preliminary experimental efforts to experimentally measure such optical forces near reciprocal anisotropic media. In summary, this thesis investigates the exotic light-matter interactions and the near field-effects provided by hyperbolic and nonreciprocal metasurfaces, and their capability to trap and manipulate nanoparticles.

1.5 CHAPTER REFERENCES

[1] García-Vidal, F.J. and Pendry, J.B., 1996. Collective theory for surface enhanced Raman scattering. *Physical Review Letters*, *77*(6), p.1163.

[2] Pendry, J.B., 2008. Time reversal and negative refraction. *Science*, *322*(5898), pp.71-73.

[3] Fan, X., Wang, G.P., Lee, J.C.W. and Chan, C.T., 2006. All-angle broadband negative refraction of metal waveguide arrays in the visible range: theoretical analysis and numerical demonstration. *Physical Review Letters*, *97*(7), p.073901.

[4] Eleftheriades, G.V., 2009. EM transmission-line metamaterials. *Materials Today*, *12*(3), pp.30-41.

[5] Fang, N., Lee, H., Sun, C. and Zhang, X., 2005. Sub-diffraction-limited optical imaging with a silver superlens. *Science*, *308*(5721), pp.534-537.

[6] Pendry, J.B., 2000. Negative refraction makes a perfect lens. *Physical Review Letters*, *85*(18), p.3966.

[7] Urbas, A.M., Jacob, Z., Dal Negro, L., Engheta, N., Boardman, A.D., Egan, P., Khanikaev, A.B., Menon, V., Ferrera, M., Kinsey, N. and DeVault, C., 2016. Roadmap on optical metamaterials. *Journal of Optics*, *18*(9), p.093005.

[8] Belov, P.A., Simovski, C.R. and Ikonen, P., 2005. Canalization of subwavelength images by electromagnetic crystals. *Physical Review B*, *71*(19), p.193105.

[9] Bronnikov, K., Arriaga, J., Krokhin, A. and Drachev, V.P., 2021. Sub-Diffraction-Limit Imaging System with two Interfacing Hyperbolic Metamaterials. *Physical Review Applied*, *16*(4), p.044054.

[10] Wood, B., Pendry, J.B. and Tsai, D.P., 2006. Directed subwavelength imaging using a layered metal-dielectric system. *Physical Review B*, *74*(11), p.115116.

[11] Sounas, D.L., Fleury, R. and Alù, A., 2015. Unidirectional cloaking based on metasurfaces with balanced loss and gain. *Physical Review Applied*, *4*(1), p.014005.

[12] Fleury, R. and Alù, A., 2013. Quantum cloaking based on scattering cancellation. *Physical Review B*, *87*(4), p.045423.

[13] Leonhardt, U. and Tyc, T., 2009. Broadband invisibility by non-Euclidean cloaking. *Science*, *323*(5910), pp.110-112.

[14] Gabrielli, L.H., Cardenas, J., Poitras, C.B. and Lipson, M., 2009. Silicon nanostructure cloak operating at optical frequencies. *Nature Photonics*, *3*(8), pp.461-463.

[15] Biehs, S.A., Tschikin, M. and Ben-Abdallah, P., 2012. Hyperbolic metamaterials as an analog of a blackbody in the near field. *Physical Review Letters*, *109*(10), p.104301.

[16] Iorsh, I.V., Mukhin, I.S., Shadrivov, I.V., Belov, P.A. and Kivshar, Y.S., 2013. Hyperbolic metamaterials based on multilayer graphene structures. *Physical Review B*, *87*(7), p.075416.

[17] Poddubny, A., Iorsh, I., Belov, P. and Kivshar, Y., 2013. Hyperbolic metamaterials. *Nature Photonics*, *7*(12), pp.948-957.

[18] Ren, Z., Chang, Y., Ma, Y., Shih, K., Dong, B. and Lee, C., 2020. Leveraging of MEMS technologies for optical metamaterials applications. *Advanced Optical Materials*, *8*(3), p.1900653.

[19] Liu, X. and Padilla, W.J., 2013. Dynamic manipulation of infrared radiation with MEMS metamaterials. *Advanced Optical Materials*, *1*(8), pp.559-562.

[20] Tao, H., Strikwerda, A.C., Fan, K., Padilla, W.J., Zhang, X. and Averitt, R.D., 2011. MEMS based structurally tunable metamaterials at terahertz frequencies. *Journal of Infrared, Millimeter, and Terahertz Waves*, *32*(5), pp.580-595.

[21] Ginis, V., Tassin, P., Soukoulis, C.M. and Veretennicoff, I., 2013. Enhancing optical gradient forces with metamaterials. *Physical Review Letters*, *110*(5), p.057401.

[22] Zhao, R., Tassin, P., Koschny, T. and Soukoulis, C.M., 2010. Optical forces in nanowire pairs and metamaterials. *Optics Express*, *18*(25), pp.25665-25676.

[23] Jin, R., Xu, Y., Dong, Z.G. and Liu, Y., 2021. Optical Pulling Forces Enabled by Hyperbolic Metamaterials. *Nano Letters*, *21*(24), pp.10431-10437.

[24] Bogdanov, A.A., Shalin, A.S. and Ginzburg, P., 2015. Optical forces in nanorod metamaterial. *Scientific Reports*, *5*(1), pp.1-9.

[25] Zhang, X., Zheng, Y., Liu, X., Lu, W., Dai, J., Lei, D.Y. and MacFarlane, D.R., 2015. Hierarchical porous plasmonic metamaterials for reproducible ultrasensitive surface-enhanced Raman spectroscopy. *Advanced Materials*, *27*(6), pp.1090-1096.

[26] Wen, X., Li, G., Zhang, J., Zhang, Q., Peng, B., Wong, L.M., Wang, S. and Xiong, Q., 2014. Transparent free-standing metamaterials and their applications in surface-enhanced Raman scattering. *Nanoscale*, *6*(1), pp.132-139.

[27] Liu, F., Xiao, L., Ye, Y., Wang, M., Cui, K., Feng, X., Zhang, W. and Huang, Y., 2017. Integrated Cherenkov radiation emitter eliminating the electron velocity threshold. *Nature Photonics*, *11*(5), pp.289-292.

[28] Fernandes, D.E., Maslovski, S.I. and Silveirinha, M.G., 2012. Cherenkov emission in a nanowire material. *Physical Review B*, *85*(15), p.155107.

[29] Liu, Z., Lee, H., Xiong, Y., Sun, C. and Zhang, X., 2007. Far-field optical hyperlens magnifying sub-diffraction-limited objects. *Science*, *315*(5819), pp.1686-1686.

[30] Chen, H.T., Taylor, A.J. and Yu, N., 2016. A review of metasurfaces: physics and applications. *Reports on Progress in Physics*, *79*(7), p.076401.

[31] Hsiao, H.H., Chu, C.H. and Tsai, D.P., 2017. Fundamentals and applications of metasurfaces. *Small Methods*, *1*(4), p.1600064.

[32] Li, A., Singh, S. and Sievenpiper, D., 2018. Metasurfaces and their applications. *Nanophotonics*, *7*(6), pp.989-1011.

[33] Yu, N. and Capasso, F., 2014. Flat optics with designer metasurfaces. *Nature Materials*, *13*(2), pp.139-150.

[34] Kildishev, A.V., Boltasseva, A. and Shalaev, V.M., 2013. Planar photonics with metasurfaces. *Science*, *339*(6125), p.1232009.

[35] Correas-Serrano, D., Gomez-Diaz, J.S., Melcon, A.A. and Alù, A., 2016. Black phosphorus plasmonics: anisotropic elliptical propagation and nonlocality-induced canalization. *Journal of Optics*, *18*(10), p.104006.

[36] Correas-Serrano, D., Alù, A. and Gomez-Diaz, J.S., 2017. Plasmon canalization and tunneling over anisotropic metasurfaces. *Physical Review B*, *96*(7), p.075436.

[37] Forati, E., Hanson, G.W., Yakovlev, A.B. and Alu, A., 2014. Planar hyperlens based on a modulated graphene monolayer. *Physical Review B*, *89*(8), p.081410.

[38] Gomez-Diaz, J.S. and Alu, A., 2016. Flatland optics with hyperbolic metasurfaces. *ACS Photonics*, *3*(12), pp.2211-2224.

[39] Esquius-Morote, M., Gómez-Dı, J.S. and Perruisseau-Carrier, J., 2014. Sinusoidally modulated graphene leaky-wave antenna for electronic beamscanning at THz. *IEEE Transactions on Terahertz Science and Technology*, *4*(1), pp.116-122.

[40] Rodrigo, D., Limaj, O., Janner, D., Etezadi, D., García de Abajo, F.J., Pruneri, V. and Altug, H., 2015. Mid-infrared plasmonic biosensing with graphene. *Science*, *349*(6244), pp.165-168.

[41] Chen, P.Y., Soric, J., Padooru, Y.R., Bernety, H.M., Yakovlev, A.B. and Alù, A., 2013. Nanostructured graphene metasurface for tunable terahertz cloaking. *New Journal of Physics*, *15*(12), p.123029.

[42] Yang, Y., Wang, H., Yu, F., Xu, Z. and Chen, H., 2016. A metasurface carpet cloak for electromagnetic, acoustic and water waves. *Scientific reports*, *6*(1), pp.1-6.

[43] Kawata, S., Inouye, Y. and Verma, P., 2009. Plasmonics for near-field nano-imaging and superlensing. *Nature Photonics*, *3*(7), pp.388-394.

[44] Zia, R., Schuller, J.A., Chandran, A. and Brongersma, M.L., 2006. Plasmonics: the next chip-scale technology. *Materials Today*, *9*(7-8), pp.20-27.

[45] Pelton, M., Aizpurua, J. and Bryant, G., 2008. Metal-nanoparticle plasmonics. *Laser & Photonics Reviews*, *2*(3), pp.136-159.

[46] Brongersma, M.L. and Shalaev, V.M., 2010. The case for plasmonics. *Science*, *328*(5977), pp.440-441.

[47] Kauranen, M. and Zayats, A.V., 2012. Nonlinear plasmonics. *Nature Photonics*, *6*(11), pp.737-748.

[48] High, A.A., Devlin, R.C., Dibos, A., Polking, M., Wild, D.S., Perczel, J., De Leon, N.P., Lukin, M.D. and Park, H., 2015. Visible-frequency hyperbolic metasurface. *Nature*, *522*(7555), pp.192-196.

[49] Li, P., Dolado, I., Alfaro-Mozaz, F.J., Casanova, F., Hueso, L.E., Liu, S., Edgar, J.H., Nikitin, A.Y., Vélez, S. and Hillenbrand, R., 2018. Infrared hyperbolic metasurface based on nanostructured van der Waals materials. *Science*, *359*(6378), pp.892-896.

[50] Ferrari, L., Wu, C., Lepage, D., Zhang, X. and Liu, Z., 2015. Hyperbolic metamaterials and their applications. *Progress in Quantum Electronics*, *40*, pp.1-40.

[51] Gomez-Diaz, J.S., Tymchenko, M. and Alu, A., 2015. Hyperbolic plasmons and topological transitions over uniaxial metasurfaces. *Physical Review Letters*, *114*(23), p.233901.

[52] Gomez-Diaz, J.S., Tymchenko, M. and Alù, A., 2015. Hyperbolic metasurfaces: surface plasmons, light-matter interactions, and physical implementation using graphene strips. *Optical Materials Express*, *5*(10), pp.2313-2329.

[53] Yermakov, O.Y., Permyakov, D.V., Porubaev, F.V., Dmitriev, P.A., Samusev, A.K., Iorsh, I.V., Malureanu, R., Lavrinenko, A.V. and Bogdanov, A.A., 2018. Effective surface conductivity of optical hyperbolic metasurfaces: from far-field characterization to surface wave analysis. *Scientific Reports*, *8*(1), pp.1-10.

[54] Gusynin, V.P. and Sharapov, S.G., 2006. Transport of Dirac quasiparticles in graphene: Hall and optical conductivities. *Physical Review B*, *73*(24), p.245411.

[55] Casimir, H.B.G., 1945. On Onsager's principle of microscopic reversibility. *Reviews of Modern Physics*, *17*(2-3), p.343.

[56] Deák, L. and Fülöp, T., 2012. Reciprocity in quantum, electromagnetic and other wave scattering. *Annals of Physics*, *327*(4), pp.1050-1077.

[57] Yu, Z., Veronis, G., Wang, Z. and Fan, S., 2008. One-way electromagnetic waveguide formed at the interface between a plasmonic metal under a static magnetic field and a photonic crystal. *Physical Review Letters*, *100*(2), p.023902.

[58] Wang, Z., Chong, Y.D., Joannopoulos, J.D. and Soljačić, M., 2008. Reflection-free one-way edge modes in a gyromagnetic photonic crystal. *Physical Review Letters*, *100*(1), p.013905.

[59] Davoyan, A.R. and Engheta, N., 2013. Theory of wave propagation in magnetized near-zero-epsilon metamaterials: evidence for one-way photonic states and magnetically switched transparency and opacity. *Physical Review Letters*, *111*(25), p.257401.

[60] Lin, X., Xu, Y., Zhang, B., Hao, R., Chen, H. and Li, E., 2013. Unidirectional surface plasmons in nonreciprocal graphene. *New Journal of Physics*, *15*(11), p.113003.

[61] Morgado, T.A. and Silveirinha, M.G., 2018. Drift-induced unidirectional graphene plasmons. *ACS Photonics*, *5*(11), pp.4253-4258.

[62] Bliokh, K.Y., Rodríguez-Fortuño, F.J., Bekshaev, A.Y., Kivshar, Y.S. and Nori, F., 2018. Electric-current-induced unidirectional propagation of surface plasmon-polaritons. *Optics Letters*, *43*(5), pp.963-966.

[63] Correas-Serrano, D. and Gomez-Diaz, J.S., 2019. Nonreciprocal and collimated surface plasmons in drift-biased graphene metasurfaces. *Physical Review B*, *100*(8), p.081410.

[64] Paul, N.K. and Gomez-Diaz, J.S., 2021. Broadband and unidirectional plasmonic hyperlensing in drift-biased graphene. *Applied Physics Letters*, *118*(9), p.091107.

[65] Soljačić, M., Luo, C., Joannopoulos, J.D. and Fan, S., 2003. Nonlinear photonic crystal microdevices for optical integration. *Optics letters*, *28*(8), pp.637-639.

[66] Gallo, K., Assanto, G., Parameswaran, K.R. and Fejer, M.M., 2001. All-optical diode in a periodically poled lithium niobate waveguide. *Applied Physics Letters*, *79*(3), pp.314-316.

[67] Fleury, R., Sounas, D.L., Sieck, C.F., Haberman, M.R. and Alù, A., 2014. Sound isolation and giant linear nonreciprocity in a compact acoustic circulator. *Science*, *343*(6170), pp.516-519.

[68] Weis, S., Rivière, R., Deléglise, S., Gavartin, E., Arcizet, O., Schliesser, A. and Kippenberg, T.J., 2010. Optomechanically induced transparency. *Science*, *330*(6010), pp.1520-1523.

[69] Yu, Z. and Fan, S., 2009. Complete optical isolation created by indirect interband photonic transitions. *Nature photonics*, *3*(2), pp.91-94.

[70] Lira, H., Yu, Z., Fan, S. and Lipson, M., 2012. Electrically driven nonreciprocity induced by interband photonic transition on a silicon chip. *Physical Review Letters*, *109*(3), p.033901.

[71] Sounas, D.L., Caloz, C. and Alu, A., 2013. Giant non-reciprocity at the subwavelength scale using angular momentum-biased metamaterials. *Nature Communications*, *4*(1), pp.1-7.

[72] Fang, K., Luo, J., Metelmann, A., Matheny, M.H., Marquardt, F., Clerk, A.A. and Painter, O., 2017. Generalized non-reciprocity in an optomechanical circuit via synthetic magnetism and reservoir engineering. *Nature Physics*, *13*(5), pp.465-471.

[73] Aspelmeyer, M., Kippenberg, T.J. and Marquardt, F., 2014. Cavity optomechanics. *Reviews of Modern Physics*, *86*(4), p.1391.

[74] Sabbaghi, M., Lee, H.W., Stauber, T. and Kim, K.S., 2015. Drift-induced modifications to the dynamical polarization of graphene. *Physical Review B*, *92*(19), p.195429.

[75] Wenger, T., Viola, G., Kinaret, J., Fogelström, M. and Tassin, P., 2018. Current-controlled light scattering and asymmetric plasmon propagation in graphene. *Physical Review B*, *97*(8), p.085419.

[76] Morgado, T.A. and Silveirinha, M.G., 2017. Negative Landau damping in bilayer graphene. *Physical Review Letters*, *119*(13), p.133901.

[77] Ramamoorthy, H., Somphonsane, R., Radice, J., He, G., Kwan, C.P. and Bird, J.P., 2016. "Freeing" graphene from its substrate: Observing intrinsic velocity saturation with rapid electrical pulsing. *Nano Letters*, *16*(1), pp.399-403.

[78] Yamoah, M.A., Yang, W., Pop, E. and Goldhaber-Gordon, D., 2017. High-velocity saturation in graphene encapsulated by hexagonal boron nitride. *ACS Nano*, *11*(10), pp.9914-9919.

[79] Chen, J.H., Jang, C., Xiao, S., Ishigami, M. and Fuhrer, M.S., 2008. Intrinsic and extrinsic performance limits of graphene devices on SiO2. *Nature Nanotechnology*, *3*(4), pp.206-209.

[80] Dong, Y., Xiong, L., Phinney, I.Y., Sun, Z., Jing, R., McLeod, A.S., Zhang, S., Liu, S., Ruta, F.L., Gao, H. and Dong, Z., 2021. Fizeau drag in graphene plasmonics. *Nature*, *594*(7864), pp.513-516.

[81] Zhao, W., Zhao, S., Li, H., Wang, S., Wang, S., Utama, M., Kahn, S., Jiang, Y., Xiao, X., Yoo, S. and Watanabe, K., 2021. Efficient Fizeau drag from Dirac electrons in monolayer graphene. *Nature*, *594*(7864), pp.517-521.

[82] Ashkin, A., 1970. Acceleration and trapping of particles by radiation pressure. *Physical Review Letters*, *24*(4), p.156.

[83] Moffitt, J.R., Chemla, Y.R., Smith, S.B. and Bustamante, C., 2008. Recent advances in optical tweezers. *Annual Review of Biochemistry.*, *77*, pp.205-228.

[84] Kong, L., Lee, C., Earhart, C.M., Cordovez, B. and Chan, J.W., 2015. A nanotweezer system for evanescent wave excited surface enhanced Raman spectroscopy (SERS) of single nanoparticles. *Optics Express*, *23*(5), pp.6793-6802.

[85] Thurn, R. and Kiefer, W., 1984. Raman-microsampling technique applying optical levitation by radiation pressure. *Applied Spectroscopy*, *38*(1), pp.78-83.

[86] Esen, C., Kaiser, T. and Schweiger, G., 1996. Raman investigation of photopolymerization reactions of single optically levitated microparticles. *Applied Spectroscopy*, *50*(7), pp.823-828.

[87] Xie, C., Dinno, M.A. and Li, Y.Q., 2002. Near-infrared Raman spectroscopy of single optically trapped biological cells. *Optics Letters*, *27*(4), pp.249-251.

[88] Gessner, R., Winter, C., Rösch, P., Schmitt, M., Petry, R., Kiefer, W., Lankers, M. and Popp, J., 2004. Identification of biotic and abiotic particles by using a combination of optical tweezers and in situ Raman spectroscopy. *ChemPhysChem*, *5*(8), pp.1159-1170.

[89] Petrov, D.V., 2007. Raman spectroscopy of optically trapped particles. *Journal of Optics A: Pure and Applied Optics*, *9*(8), p.S139.

[90] Cherney, D.P. and Harris, J.M., 2010. Confocal Raman microscopy of optical-trapped particles in liquids. *Annual Review of Analytical Chemistry*, *3*, pp.277-297.

[91] Chan, J.W., 2013. Recent advances in laser tweezers Raman spectroscopy (LTRS) for label-free analysis of single cells. *Journal of Biophotonics*, *6*(1), pp.36-48.

[92] Kong, L., Zhang, P., Wang, G., Yu, J., Setlow, P. and Li, Y.Q., 2011. Characterization of bacterial spore germination using phase-contrast and fluorescence microscopy, Raman spectroscopy and optical tweezers. *Nature Protocols*, *6*(5), pp.625-639.

[93] Chu, S., 1998. Nobel Lecture: The manipulation of neutral particles. *Reviews of Modern Physics*, *70*(3), p.685.

[94] Cohen-Tannoudji, C.N., 1998. Nobel Lecture: Manipulating atoms with photons. *Reviews of Modern Physics*, *70*(3), p.707.

[95] Metcalf, H.J. and Van der Straten, P., 2007. Laser cooling and trapping of neutral atoms. *The Optics Encyclopedia: Basic Foundations and Practical Applications*.

[96] Foot, C.J., 2004. *Atomic physics* (Vol. 7). OUP Oxford.

[97] Maragò, O.M., Jones, P.H., Gucciardi, P.G., Volpe, G. and Ferrari, A.C., 2013. Optical trapping and manipulation of nanostructures. *Nature Nanotechnology*, *8*(11), pp.807-819.

[98] Juan, M.L., Righini, M. and Quidant, R., 2011. Plasmon nano-optical tweezers. *Nature Photonics*, *5*(6), pp.349-356.

[99] Gordon, J.P., 1973. Radiation forces and momenta in dielectric media. *Physical Review A*, *8*(1), p.14.

[100] Purcell, E.M. and Pennypacker, C.R., 1973. Scattering and absorption of light by nonspherical dielectric grains. *The Astrophysical Journal*, 186, pp.705-714.

[101] Volpe, G., Quidant, R., Badenes, G. and Petrov, D., 2006. Surface plasmon radiation forces. *Physical Review Letters*, 96(23), p.238101.

[102] Righini, M., Zelenina, A.S., Girard, C. and Quidant, R., 2007. Parallel and selective trapping in a patterned plasmonic landscape. *Nature Physics*, 3(7), pp.477-480.

[103] Muhlschlegel, P., Eisler, H.J., Martin, O.J., Hecht, B. and Pohl, D.W., 2005. Resonant optical antennas. *Science*, 308(5728), pp.1607-1609.

[104] Schuck, P.J., Fromm, D.P., Sundaramurthy, A., Kino, G.S. and Moerner, W.E., 2005. Improving the mismatch between light and nanoscale objects with gold bowtie nanoantennas. *Physical Review Letters*, 94(1), p.017402.

[105] Sainidou, R. and De Abajo, F.G., 2008. Optically tunable surfaces with trapped particles in microcavities. *Physical Review Letters*, *101*(13), p.136802.

[106] Grigorenko, A.N., Roberts, N.W., Dickinson, M.R. and Zhang, Y.J.N.P., 2008. Nanometric optical tweezers based on nanostructured substrates. *Nature Photonics*, *2*(6), pp.365-370.

[107] Righini, M., Volpe, G., Girard, C., Petrov, D. and Quidant, R., 2008. Surface plasmon optical tweezers: tunable optical manipulation in the femtonewton range. *Physical Review Letters*, *100*(18), p.186804.

[108] UC Davis Center for Biophotonics Science and Technology. http://www.cbst.ucdavis.edu/

Chapter 2: Surface plasmons in Anisotropic Metasurfaces

Surface plasmon polaritons are electromagnetic waves that propagate along a dielectric-metal interface with an evanescent wavefront in the vertical direction [1]. In the case of conventional or isotropic metallic structures, these electromagnetic waves propagate symmetrically with identical wavenumber in any radial directions within the plane [2,3]. The wavevector and Poynting power carried out by such waves are aligned in the same direction. However, one can go beyond this paradigm by the use of anisotropic metasurfaces that open possibilities to manipulate the response of surface plasmons and allow to study novel physical mechanisms as well as exotic electromagnetic phenomena. For instance, the use of anisotropic metasurfaces significantly enhances the available density of states [4,5], boosts the spontaneous emission rate of nearby sources [6,7], and increases the efficiency of light-matter interactions. It is important to mention that the power and wavevector of plasmons in anisotropic metasurfaces are not aligned as in the case of isotropic ones. Anisotropic metasurfaces can be implemented in practice by using nanostructured ultrathin silver [8], gold [9], graphene [10], hexagonal boron-nitride [11], and other two-dimensional materials [12,13].

In this Chapter, I detail the electromagnetic modeling and characterization of anisotropic metasurfaces and investigate the light-matter interactions provided by them. To this purpose, first I develop a rigorous formalism to compute the effective electrical parameters (i.e., surface conductivity) to model nanostructured anisotropic metasurfaces. Then, I derive the dispersion relation and scattered dyadic Green's function of the system to investigate the response of surface plasmons and the metasurface topologies. Finally, I provide a brief overview of the photonic spin Hall effect [14-16] that enables directional excitation of surface plasmons taking advantage of the spin-angular momentum of nearby point sources. This formalism will be used in the following Chapters to investigate novel mechanisms provided by anisotropic metasurfaces such as canalization of surface plasmons and hyperbolic dispersion, and to exploit near-field effects to enhance the lateral optical forces on nanoparticles thus paving the way to develop next generation nano-optical plasmonic tweezers.

2.1 ELECTROMAGNETIC MODELING AND CHARACTERIZATION

In this section, I describe the electromagnetic modeling and characterization of ultrathin and subwavelength realistic anisotropic metasurfaces constructed by periodically organized metallic layers. First, I detail an analytical formalism to convert the electrical permittivity of an ultrathin and uniform layer with negligible out-of-plane electric field polarization [17,18] into a surface conductivity tensor. Then, I employ the effective medium theory to compute the effective conductivity tensor of the structure when it is nanopatterned in a periodic fashion. I also perform full wave numerical simulation in COMSOL Multiphysics [19] to validate the theory. Note that this theory is general and can be readily employed to compute effective conductivity of any nanostructured surfaces with subwavelength periodicity and width, including gold, silver, graphene, and other materials.

2.1.1 HOMOGENIZATION OF METASURFACE

Let me consider a free-standing pristine metal layer of subwavelength thickness H. Assuming an $e^{-i\omega t}$ time dependence*, the complex relative permittivity of this layer can be expressed as [20]

$$\varepsilon_s = \varepsilon_{s,r} + i\varepsilon_{s,i} = \frac{1}{\varepsilon_0}\left(-\frac{\sigma_i}{\omega H} + i\frac{\sigma_r}{\omega H} + \varepsilon_0\right), \tag{2.1}$$

where 'i' is the complex imaginary unit; subscripts 'r' and 'i' denote the real and imaginary parts of a complex number, respectively; ε_0 is the permittivity of free space; $\sigma = \sigma_r + i\sigma_i$ is the complex conductivity; and $\omega = 2\pi f$ is the radial frequency with f being the operation frequency. Separating out the real and imaginary parts from both sides of Eq. (2.1), the in-plane conductivity of the layer yields

$$\sigma = \omega H\varepsilon_0\varepsilon_{s,i} + i\omega H\varepsilon_0\left(1 - \varepsilon_{s,r}\right). \tag{2.2}$$

*A time-harmonic phasor convention of $e^{-i\omega t}$ is used in this thesis.

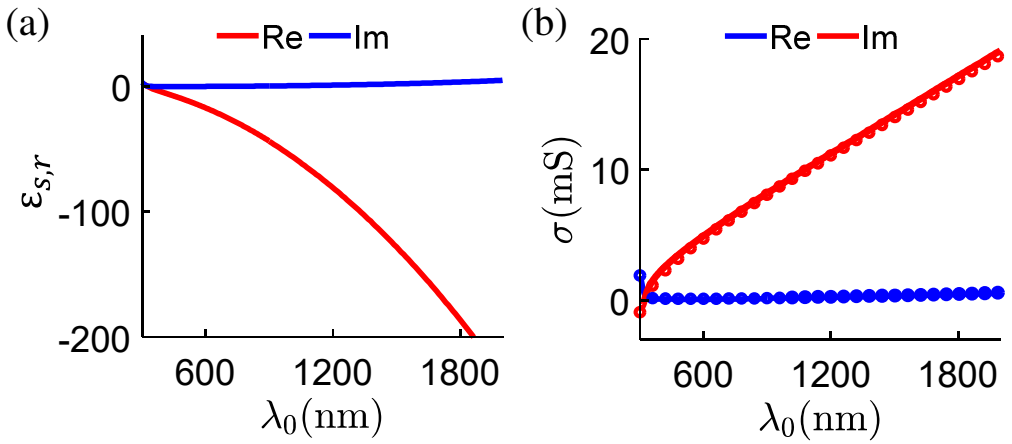

Figure 2.1: (a) Real and imaginary parts of silver relative permittivity as a function of wavelength λ_0. (b) Real and imaginary parts of the in-plane conductivity of a H=10 nm thin single crystalline pristine silver in free space versus λ_0. Solid lines and markers correspond to results computed using Eq. (2.2) and COMSOL Multiphysics, respectively.

As an example, Figure 2.1(a) shows the relative permittivity of silver [21] versus a wavelength range covering from the visible towards the infrared. Results show that at wavelengths larger than the plasmon resonance ~340 nm, the material possesses a permittivity with a negative real part that correspond to a plasmonic response [1]. Here, the imaginary part corresponds to the ohmic losses associated with silver.

Figure 2.1(b) shows the in-plane complex conductivity of a free-standing electrically thin layer of silver with $H = 10$ nm. In this case, the real part corresponds to the ohmic loss, and the imaginary part determines the metallic (i.e., $\mathrm{Im}\{\sigma\} > 0$) or dielectric (i.e., $\mathrm{Im}\{\sigma\} < 0$) response of the layer. I performed full wave simulation in COMSOL Multiphysics to compute the conductivity (will be detailed in Section 2.4) and results are in excellent agreement with the one computed using Eq. (2.2). It is important to mention that if the silver layer is extremely thin (i.e., $H \sim < 5$ nm), quantum effects may modify the electrical permittivity. Throughout this thesis, the silver layer thickness is always considered much larger than this limit to avoid such quantum effects thus confirming that the electrical permittivity remains same as in the case of bulk silver.

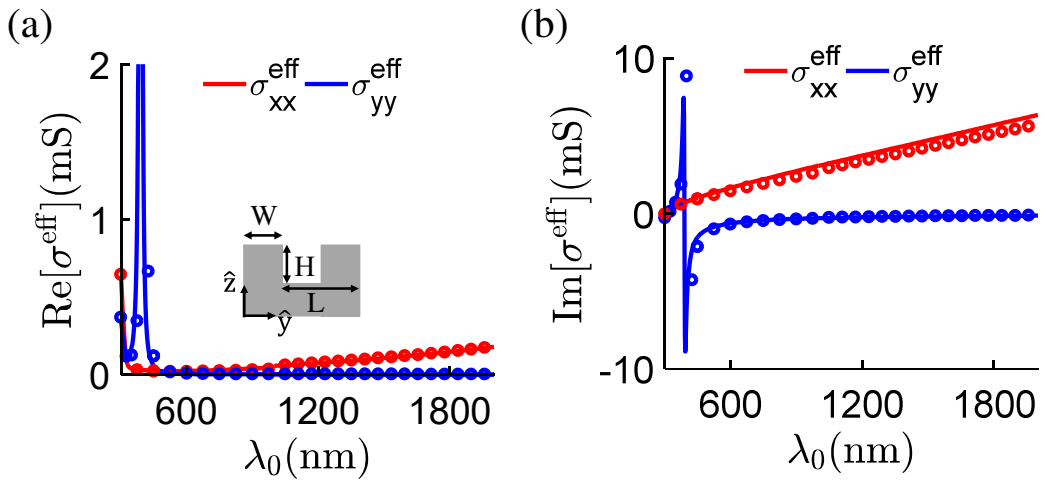

Figure 2.2: (a) Real and (b) imaginary parts of the diagonal components of the effective conductivity tensor of a silver-based anisotropic metasurface standing in free-space versus wavelength, λ_0. Solid lines and markers correspond to the results computed using effective medium theory in Eq. (2.3) and numerically in COMSOL Multiphysics, respectively. The geometrical parameters of the structure (see inset) are $W = 60$ nm, $L = 180$ nm and $H = 10$ nm.

2.1.2 EFFECTIVE MEDIUM THEORY

Let me consider a periodic set of metallic strips with thickness H, width W and periodicity L made of silver [see inset in Figure 2.2(a)]. The strips are oriented along the $\hat{y}$-axis of the coordinate system as shown in the figure. When the operation wavelength is much larger than the strip periodicity L, the entire structure can be homogenized using the effective medium theory as $\bar{\bar{\sigma}}^{eff} = (\sigma_{xx}^{eff}, 0; 0, \sigma_{yy}^{eff})$ with values [22,23]

$$\sigma_{xx}^{eff} = \frac{\sigma W}{L} \qquad \text{and} \qquad \sigma_{yy}^{eff} = \left(\frac{1}{\sigma} + \frac{i}{\omega C_{eff}}\right)^{-1} \tag{2.3}$$

where σ_{xx}^{eff} and σ_{yy}^{eff} denote the conductivity along and across the strips, respectively; $C_{eff} = (2\varepsilon_{eff}\varepsilon_0 L/\pi)\ln[\csc(\pi G/2L)]$ is a measure of the capacitive coupling among adjacent strips [13] with $G = L - W$; $\varepsilon_{eff} = (\varepsilon_1 + \varepsilon_2)/2$ with ε_1 and ε_2 being the relative permittivity of the media above and below the metasurface; 'csc' is the trigonometric cosecant function; and 'ln' is the logarithmic function with base *e*.

Figure 2.2 shows the diagonal components of $\overline{\overline{\sigma}}^{\text{eff}}$ versus the operation wavelength of an anisotropic metasurface constituted by periodically organized subwavelength silver strips along $\hat{y}$-axis of a reference coordinate system. The real and imaginary parts are shown in Figure 2.2(a) and Figure 2.2(b), respectively. Note that non-diagonal components are strictly zero in this example. Results show that within the frequency band from visible to infrared, the structure provides metallic (i.e., $\text{Im}\left[\sigma_{xx}^{\text{eff}}\right] > 0$), and dielectric (i.e., $\text{Im}\left[\sigma_{yy}^{\text{eff}}\right] < 0$) responses along $\hat{x}$ and $\hat{y}$ directions, respectively. Such response corresponds to a hyperbolic topology that will be discussed in Section 2.3 [23]. As the wavelength shifts toward the blue visible spectrum, a resonance condition (topological transition) with large dissipative loss appears. Further shift toward the near ultraviolet spectrum reaches the elliptic topology of the structure (i.e., $\text{Im}\left[\sigma_{xx}^{\text{eff}}\right] > 0$ & $\text{Im}\left[\sigma_{yy}^{\text{eff}}\right] > 0$). The transition between the hyperbolic and elliptic topologies implemented by this structure is determined by $W\sigma_c + (L - W)\sigma = 0$ which is a pole of σ_{yy}^{eff} [23]. Full wave numerical simulations are performed using COMSOL Multiphysics to compute the effective in-plane conductivity of the anisotropic metasurface (will be discussed in Section 2.4) and results are in good agreement with the ones computed using effective medium theory [see Figure 2.2].

2.2 ANISOTROPIC SURFACE PLASMONS IN METASURFACES

Anisotropic metasurfaces support surface waves that propagate with different characteristics along the surface. They exhibit exciting ways to manipulate electromagnetic waves with reduced resistive losses, and are relatively simple to fabricate. Surface plasmons on these structures can be excited using light sources located in the near field, such as aperture probe [24], irradiating dipolar particles [25], and fluorescent molecules [26], among many others [1]. The electromagnetic properties of such ultra-confined surface modes can be tailored by engineering the components of the metasurface conductivity tensor. In this section, I develop the dispersion relation of the metasurfaces and analyze different surface plasmon topologies supported by them. Next, I derive the dyadic Green's function formalism of an electric point dipole located

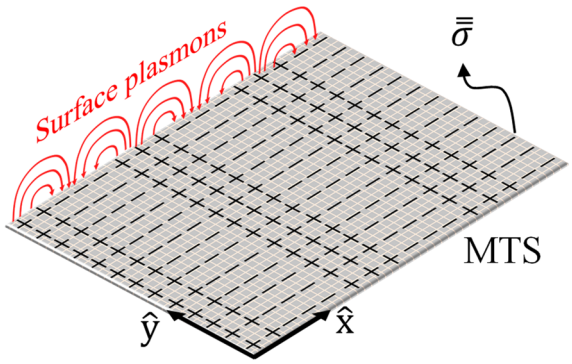

Figure 2.3: Surface plasmons polaritons above a free standing plasmonic metasurface (MTS) defined by an in-plane conductivity tensor $\bar{\bar{\sigma}}$ [1].

above anisotropic metasurfaces. This formalism will be applied to develop the theoretical framework to compute the optical forces induced on Rayleigh particles in Chapter 4.

2.2.1 DISPERSION RELATION

Let me consider an electrically thin, homogeneous, linear, and anisotropic metasurface, as shown in Figure 2.3, that can be characterized electromagnetically using a fully populated in-plane conductivity tensor [7]

$$\bar{\bar{\sigma}} = \begin{bmatrix} \sigma_{xx} & \sigma_{xy} \\ \sigma_{yx} & \sigma_{yy} \end{bmatrix}, \tag{2.4}$$

where, the tensor components are complex numbers. In general, a passive metasurface must satisfy that $\mathrm{Re}[\sigma_{xx}] \geq 0$, $\mathrm{Re}[\sigma_{yy}] \geq 0$, and $\mathrm{Re}[\sigma_{xx} + \sigma_{yy}] \geq |\sigma_{xy} + \sigma_{yx}^{*}|$, where '*' denotes the complex conjugate. For uniaxial and reciprocal metasurfaces, the conductivity tensor is diagonal with nondiagonal components $\sigma_{xy} = \sigma_{yx} = 0$ in our reference coordinate system (see Figure 2.3). However, nondiagonal components may appear due to (i) a nonsymmetrical shape with respect to the reference coordinate system [27]; (ii)

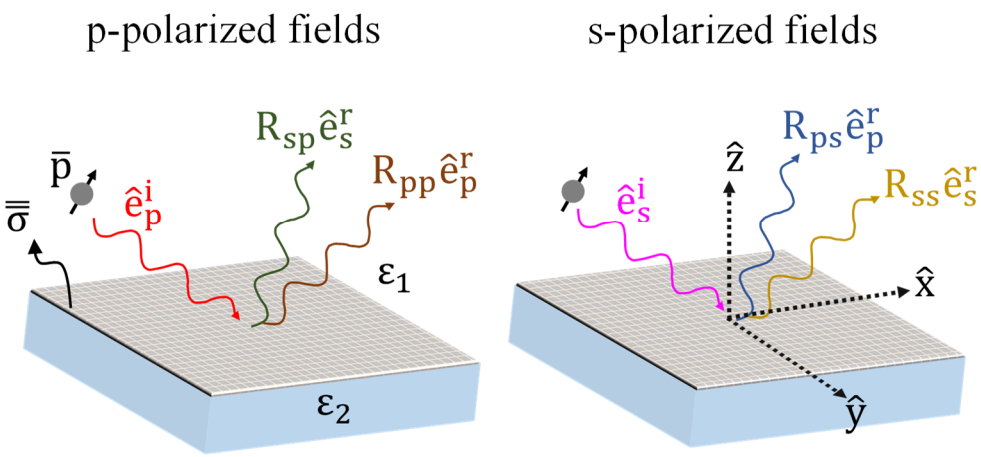

Figure 2.4: Reflected fields from an anisotropic metasurface, defined by in-plane conductivity tensor $\bar{\bar{\sigma}}$, with cross-polarized reflection. The metasurface is standing on a substrate with electrical permittivity ε_2. An electric point source with dipole moment $\bar{p}$ is located in a medium of electrical permittivity ε_1 above the metasurface and radiates TM and transverse electric (TE or s)-polarized electromagnetic waves.

magneto-optical effects in the presence of magnetic field [28], and (iii) nonlocal effects caused by the finite Fermi velocity of electrons in the materials that compose the metasurfaces.

Let me consider an anisotropic metasurface supported by a dielectric substrate of electrical permittivity ε_2 as is shown in Figure 2.4. An electric point emitted having a dipole moment $\bar{p}$ is located above the configuration at a position $\bar{r}_0 = (x_0, y_0, z_0)$ in a medium of electrical permittivity ε_1. Without loss of generality, I assume that the $\hat{x}$ and $\hat{y}$ axes of the coordinate system are tied to the diagonal directions of the conductivity tensor and that there is no magneto-optical effect in the surface. The polarization unit-vectors of the incident and reflected electric field of 'p' and 's' (transverse electric, TE)-polarized waves can be defined as [29]

$$\hat{e}_s^i = -\frac{1}{k_t}\begin{pmatrix} k_y \\ -k_x \\ 0 \end{pmatrix} = -\frac{1}{k_1}\bar{k}_i \times \hat{e}_p^i, \qquad \hat{e}_p^i = \frac{k_{z1}}{k_t k_1}\begin{pmatrix} k_x \\ k_y \\ \frac{k_t^2}{k_{z1}} \end{pmatrix} = \frac{1}{k_0}\bar{k}_i \times \hat{e}_s^i, \tag{2.5a}$$

$$\hat{e}_s^r = -\frac{1}{k_t}\begin{pmatrix} k_y \\ -k_x \\ 0 \end{pmatrix} = -\frac{1}{k_1}\bar{k}_r \times \hat{e}_p^r, \qquad \hat{e}_p^r = \frac{k_{z1}}{k_t k_1}\begin{pmatrix} -k_x \\ -k_y \\ \frac{k_t^2}{k_{z1}} \end{pmatrix} = \frac{1}{k_1}\bar{k}_r \times \hat{e}_s^r, \tag{2.5b}$$

where, '×' is the cross product, k_1 is the wavenumber above the metasurface, $k_t^2 = k_x^2 + k_y^2$, $k_{z1} = \sqrt{k_1^2 - k_t^2}$, and the superscripts 'i' and 'r' denote incident and reflected waves, respectively. The electric fields of 's' and 'p' waves impinging on the metasurface are then given by

$$\bar{E}_s^i = \hat{e}_s^i E_s^{0,i} e^{i\bar{k}_i \cdot \bar{r}} \qquad \text{and} \qquad \bar{E}_p^i = \hat{e}_p^i E_p^{0,i} e^{i\bar{k}_i \cdot \bar{r}}, \tag{2.6}$$

where $E_s^{0,i}$ and $E_p^{0,i}$ are the amplitudes of the incident wave electric fields, $\bar{r} = x\hat{x} + y\hat{y} + z\hat{z}$ is the position vector, 'i' is the imaginary unit, and '·' denotes a dot product. In the case of waves with circular or elliptical polarization, they are decomposed into their 's' and 'p' components, which are then processed following the formulation detailed below and finally added to retrieve the total field.

The goal is to compute the dispersion relation of the metasurfaces which is the key to investigate their electromagnetic response. The total electric field in the media above (medium-1, $z > 0$) and below (medium-2, $z < 0$) the metasurface can be expressed as

$$\bar{E}_1 = \bar{E}_1^0 e^{i\bar{k}_1 \cdot \bar{r}} e^{-i\omega t}, \tag{2.7a}$$

$$\bar{E}_2 = \bar{E}_2^0 e^{i\bar{k}_2 \cdot \bar{r}} e^{-i\omega t}. \tag{2.7b}$$

respectively, where $\bar{k}_2$ is the wavevector in medium 2. I stress that passivity enforces that $\mathrm{Im}[k_{z1}] = \mathrm{Im}\left[\sqrt{k_1^2 - k_t^2}\right]$ and $\mathrm{Im}[k_{z2}] = \mathrm{Im}\left[\sqrt{k_2^2 - k_t^2}\right]$ should be positive and negative, respectively, thus leading

to surface waves having evanescent profile along the $\hat{z}$-axis. Now, I apply the Maxwell's equations to the transverse components of the electric field, magnetic field and wavevector as

Medium-1: Medium-2:

$$\bar{k}_t \cdot (\bar{H}_t \times \hat{z}) = -\omega\varepsilon_1 E_{z1}, \qquad \bar{k}_t \cdot (\bar{H}_t \times \hat{z}) = -\omega\varepsilon_2 E_{z2}, \tag{2.8a}$$

$$H_{z1}\bar{k}_t - k_{z1}\bar{H}_t = -\omega\varepsilon_1(\hat{z} \times \bar{E}_t), \qquad H_{z2}\bar{k}_t - k_{z2}\bar{H}_t = -\omega\varepsilon_2(\hat{z} \times \bar{E}_t), \tag{2.8b}$$

$$\bar{k}_t \cdot (\hat{z} \times \bar{E}_t) = -\omega\mu_0 H_{z1}, \qquad \bar{k}_t \cdot (\hat{z} \times \bar{E}_t) = -\omega\mu_0 H_{z2}, \tag{2.8c}$$

$$E_{z1}\bar{k}_t - k_{z1}\bar{E}_t = -\omega\mu_0(\bar{H}_t \times \hat{z}), \qquad E_{z2}\bar{k}_t - k_{z2}\bar{E}_t = -\omega\mu_0(\bar{H}_t \times \hat{z}), \tag{2.8d}$$

where subscript 't' denotes the lateral or tangential components, $t = \{x, y\}$ to the interface. From Eq. (2.8), the lateral electric field $\bar{E}_t$ and magnetic field $\bar{H}_t$ can be computed as

Medium-1:

$$\bar{H}_t = \frac{\omega\varepsilon_1}{k_{z1}}\left(\bar{\bar{I}} - \frac{\bar{k}_t\bar{k}_t}{k_1^2}\right) \cdot (\hat{z} \times \bar{E}_t) = \bar{\bar{Y}}_1 \cdot (\hat{z} \times \bar{E}_t), \tag{2.9a}$$

$$\bar{E}_t = \frac{\omega\mu_0}{k_{z1}}\left(\bar{\bar{I}} - \frac{\bar{k}_t\bar{k}_t}{k_1^2}\right) \cdot (\bar{H}_t \times \hat{z}) = \bar{\bar{Z}}_1 \cdot (\bar{H}_t \times \hat{z}), \tag{2.9b}$$

Medium-2:

$$\bar{H}_t = \frac{\omega\varepsilon_1}{k_{z2}}\left(\bar{\bar{I}} - \frac{\bar{k}_t\bar{k}_t}{k_2^2}\right)\cdot(\hat{z}\times\bar{E}_t) = \bar{\bar{Y}}_2\cdot(\hat{z}\times\bar{E}_t), \tag{2.9c}$$

$$\bar{E}_t = \frac{\omega\mu_0}{k_{z2}}\left(\bar{\bar{I}} - \frac{\bar{k}_t\bar{k}_t}{k_2^2}\right)\cdot(\bar{H}_t\times\hat{z}) = \bar{\bar{Z}}_2\cdot(\bar{H}_t\times\hat{z}), \tag{2.9d}$$

where $\bar{\bar{I}}$ is the identity matrix, $\bar{k}_t = \hat{x}k_x + \hat{y}k_y$ is the transverse wavevector, $\bar{\bar{Z}}_1 = \frac{\omega\mu_0}{k_{z1}}\left(\bar{\bar{I}} - \frac{\bar{k}_t\bar{k}_t}{k_1^2}\right)$ and $\bar{\bar{Z}}_2 = \frac{\omega\mu_0}{k_{z2}}\left(\bar{\bar{I}} - \frac{\bar{k}_t\bar{k}_t}{k_2^2}\right)$ are the dyadic characteristic impedances of media 1 and 2, respectively. The longitudinal field components are computed by applying the Gauss' laws, $\bar{k}_1\cdot\bar{E}_1 = 0$ and $\bar{k}_2\cdot\bar{E}_2 = 0$. Applying the boundary conditions at $z = 0$ yield as

$$\bar{E}_t\cdot\left(\bar{\bar{Z}}_1\cdot\bar{\bar{Z}}_2\cdot\bar{\bar{\sigma}} + \bar{\bar{Z}}_1 + \bar{\bar{Z}}_2\right) = 0. \tag{2.10}$$

Eq. (2.10) describes the state of the system, and finally the dispersion relation yields

$$\left|\bar{\bar{Z}}_1\cdot\bar{\bar{Z}}_2\cdot\bar{\bar{\sigma}} + \bar{\bar{Z}}_1 + \bar{\bar{Z}}_2\right| = 0, \tag{2.11}$$

and the polarization vectors of the supported modes are the eigenvectors of $\bar{\bar{Z}}_1\cdot\bar{\bar{Z}}_2\cdot\bar{\bar{\sigma}} + \bar{\bar{Z}}_1 + \bar{\bar{Z}}_2$. Note that Eq. (2.11) is general and can be employed to compute the simpler dispersion relation of a free-standing metasurface [see Figure 2.3] by using $\varepsilon_1 = \varepsilon_2 = \varepsilon_0$, $k_1 = k_2 = k_0$ and $k_z = k_{z1} = k_{z2} = \sqrt{k_0^2 - k_t^2}$. These identities lead to the dispersion relation of a free-standing metasurface

$$\begin{aligned} k_0k_z\left\{4 + \eta_0^2\left(\sigma_{xx}\sigma_{yy} - \sigma_{xy}\sigma_{yx}\right)\right\} - 2\eta_0k_0^2\left(\sigma_{xx} + \sigma_{yy}\right) + 2\eta_0\left(k_x^2\sigma_{xx} + k_y^2\sigma_{yy} + \right. \\ \left. k_xk_y\sigma_{xy}\sigma_{yx}\right) = 0. \end{aligned} \tag{2.12}$$

Here, $k_0 = \omega\sqrt{\mu_0\varepsilon_0}$ is the free-space wavenumber with μ_0 and ϵ_0 being the electrical permeability and permittivity, respectively; $\mathrm{Im}[k_z] > 0$ and $\mathrm{Im}[k_z] < 0$ for $z > 0$ and $z < 0$ to impose a decaying or evanescent surface modes in the normal direction to the metasurfaces; and $\eta_0 = \sqrt{\mu_0/\varepsilon_0}$ is the free space impedance. In the case of isotropic surfaces (i.e., $\sigma_{xx} = \sigma_{yy} = \sigma$), Eq. (2.12) can be greatly simplified that provides the dispersion relation or wavenumber of the supported transverse magnetic modes as $k_\rho = k_0\sqrt{1 - \left(\frac{2}{\eta_0\sigma}\right)^2}$ [7,13].

2.2.2 GREEN'S FUNCTION FORMALISM

Here, I develop the scattered dyadic Green's function of an electric point emitter located above an anisotropic metasurface. This formalism enables to compute the excited fields on the metasurface in the physical space by simply multiplying the Green's function with the dipole moment [1].

Following the procedure detailed in Refs. [1,23,29], the scattered dyadic Green's function of an emitter located above such an anisotropic metasurface [see Figure 2.4] is obtained as

$$\bar{\bar{G}}^s(\bar{r},\bar{r}_0) = \frac{i}{8\pi^2}\iint_{-\infty}^{\infty}[R_{ss}\,\bar{\bar{M}}_{ss} + R_{ps}\bar{\bar{M}}_{ps} + R_{sp}\bar{\bar{M}}_{sp} + R_{pp}\bar{\bar{M}}_{pp}]e^{i[k_x(x-x_0)+k_y(y-y_0)+k_{z1}(z+z_0)]}dk_x dk_y, \tag{2.13}$$

where $\bar{\bar{R}} = \begin{bmatrix} R_{ss} & R_{ps} \\ R_{sp} & R_{pp} \end{bmatrix}$ is the anisotropic reflection coefficient tensor of the metasurface. In addition, the M-matrices are defined as $\bar{\bar{M}}_{ss} = \frac{1}{k_{z1}}\hat{e}_s^r \otimes \hat{e}_s^i$, $\bar{\bar{M}}_{ps} = \frac{1}{k_{z1}}\hat{e}_p^r \otimes \hat{e}_s^i$, $\bar{\bar{M}}_{sp} = \frac{1}{k_{z1}}\hat{e}_s^r \otimes \hat{e}_p^i$ and $\bar{\bar{M}}_{pp} = \frac{1}{k_{z1}}\hat{e}_p^r \otimes \hat{e}_p^i$ with $\otimes$ being the vector dyadic product of the polarization unit vectors as is given in Eq. (2.5). The M-matrices read

$$\bar{\bar{M}}_{ss} = \frac{1}{k_{z1}k_t^2}\begin{bmatrix} k_y^2 & -k_x k_y & 0 \\ -k_x k_y & k_x^2 & 0 \\ 0 & 0 & 0 \end{bmatrix}, \qquad \bar{\bar{M}}_{sp} = \frac{1}{k_0 k_t^2}\begin{bmatrix} -k_x k_y & -k_y^2 & -\frac{k_y k_t^2}{k_{z1}} \\ k_x^2 & k_x k_y & \frac{k_x k_t^2}{k_{z1}} \\ 0 & 0 & 0 \end{bmatrix},$$

$$\bar{\bar{M}}_{ps} = \frac{1}{k_0 k_t^2}\begin{bmatrix} k_x k_y & -k_x^2 & 0 \\ k_y^2 & -k_x k_y & 0 \\ -\frac{k_y k_t^2}{k_{z1}} & \frac{k_x k_t^2}{k_{z1}} & 0 \end{bmatrix}, \qquad \bar{\bar{M}}_{pp} = \frac{k_{z1}}{k_0^2 k_t^2}\begin{bmatrix} -k_x^2 & -k_x k_y & -\frac{k_x k_t^2}{k_{z1}} \\ -k_x k_y & -k_y^2 & -\frac{k_y k_t^2}{k_{z1}} \\ \frac{k_x k_t^2}{k_{z1}} & \frac{k_y k_t^2}{k_{z1}} & \frac{k_t^4}{k_{z1}^2} \end{bmatrix}. \tag{2.14}$$

It is useful to derive the reflection coefficient tensor of the metasurfaces in terms of 's' and 'p' waves so it can be integrated in the scattered dyadic Green's function of Eq. (2.13). To this purpose, I first consider $k_y = 0$ for the case where xz is the plane of incidence that leads to $\bar{k}_t = \hat{x}k_x$. Then, to evaluate the wave propagation towards other directions and analyze the complete responses, the xy-plane is rotated counterclockwise considering a rotation dyadic $\bar{\bar{R}}_{rot} = \frac{1}{k_t}\begin{bmatrix} k_x & -k_y \\ k_y & k_x \end{bmatrix}$. This leads to the rotated conductivity tensor of the metasurface as [23,30]

$$\bar{\bar{\sigma}}' = \bar{\bar{R}}_{rot}^{T}\bar{\bar{\sigma}}\bar{\bar{R}}_{rot} =$$

$$\frac{1}{k_t^2}\begin{bmatrix} \sigma_{xx}k_x^2 + \sigma_{yy}k_y^2 + k_x k_y(\sigma_{xy} + \sigma_{yx}) & \sigma_{xy}k_x^2 - \sigma_{yx}k_y^2 - k_x k_y(\sigma_{xx} - \sigma_{yy}) \\ \sigma_{yx}k_x^2 - \sigma_{xy}k_y^2 - k_x k_y(\sigma_{xx} - \sigma_{yy}) & \sigma_{yy}k_x^2 + \sigma_{xx}k_y^2 - k_x k_y(\sigma_{xy} + \sigma_{yx}) \end{bmatrix}, \tag{2.15}$$

where $\bar{\bar{R}}_{rot}^{T}$ is the transpose of $\bar{\bar{R}}_{rot}$.

This rotated conductivity tensor is employed to compute the reflected electric field from the metasurface. Now, I apply the boundary conditions at $z = 0$

$$\hat{z} \times \left(\bar{E}_t^{tr} - \bar{E}_t^{i} - \bar{E}_t^{r}\right) = 0, \tag{2.16a}$$

$$\hat{z} \times \left(\bar{H}_t^{i} + \bar{H}_t^{r} - \bar{H}_t^{tr}\right) = \bar{\bar{\sigma}}' \cdot \bar{E}_t^{tr}. \tag{2.16b}$$

where the superscript 'tr' denotes the transmitted waves. Solving Eq. (2.16), the tangential reflected electric field vector is computed as

$$\bar{E}_t^{r} = -\frac{\bar{\bar{Z}}_1 \cdot \bar{\bar{Z}}_2 \cdot \bar{\bar{\sigma}}' + \bar{\bar{Z}}_1 - \bar{\bar{Z}}_2}{\bar{\bar{Z}}_1 \cdot \bar{\bar{Z}}_2 \cdot \bar{\bar{\sigma}}' + \bar{\bar{Z}}_1 + \bar{\bar{Z}}_2} \cdot \bar{E}_t^{i} = \bar{\bar{R}}_{21} \cdot \bar{E}_t^{i}, \tag{2.17}$$

where $\bar{\bar{R}}_{21} = -\left(\bar{\bar{Z}}_1 \cdot \bar{\bar{Z}}_2 \cdot \bar{\bar{\sigma}}' + \bar{\bar{Z}}_1 + \bar{\bar{Z}}_2\right)^{-1} \cdot \left(\bar{\bar{Z}}_1 \cdot \bar{\bar{Z}}_2 \cdot \bar{\bar{\sigma}}' + \bar{\bar{Z}}_1 - \bar{\bar{Z}}_2\right)$ computes only the transverse components of the reflected electric field. The $\hat{z}$-component of the reflected electric field can easily be computed from the Gauss' laws as $E_z^r = -\frac{k_x}{k_{z1}} E_x^r$.

The reflected electric field can now be decomposed into s and p-polarized waves to analyze the cross-polarized reflection from the metasurface.

<u>s-polarized reflected fields:</u> The $\hat{z}$-component of the electric field vector of s-polarized reflected wave is $E_{z,s}^r = -\frac{k_x}{k_{z1}} E_{x,s}^r = -\frac{k_x}{k_{z1}} R_{21}^{xy} E_{y,s}^i = R_{21,s}^{zy} E_{y,s}^i$ where, $R_{21,s}^{zy} = -\frac{k_x}{k_{z1}} R_{21}^{xy}$. This parameter permits to compute the total reflected s-polarized electric field vector from the metasurface following the identity, $\bar{E}_s^r = \bar{\bar{R}}_{21,s} \cdot \bar{E}_s^i$ where

$$\bar{\bar{R}}_{21,s} = \begin{bmatrix} R_{21}^{xx} & R_{21}^{xy} & 0 \\ R_{21}^{xy} & R_{21}^{yy} & 0 \\ 0 & R_{21,s}^{zy} & 0 \end{bmatrix}. \tag{2.18}$$

Now, the s-polarized reflected electric field is

$$\overline{E}_s^r = \hat{y}R_{21}^{yy}E_{y,s}^i + \hat{x}R_{21}^{yx}\frac{k_{z1}}{k_0}E_{x,p}^i = R_{ss}\overline{E}_s^i + R_{sp}\overline{E}_p^i, \tag{2.19}$$

where $R_{ss} = R_{21}^{yy}$ and $R_{sp} = \frac{k_{z1}}{k_1}R_{21}^{yx}$.

<u>p-polarized reflected fields:</u> The $\hat{z}$-component of the p-polarized reflected electric field vector is $E_{z,p}^r = -\frac{k_x}{k_{z1}}E_{x,p}^r = -\frac{k_x}{k_{z1}}R_{21}^{xx}E_{x,p}^i = -\frac{k_x}{k_{z1}}R_{21}^{xx}\frac{k_{z1}}{k_1}E_p^{0,i} = -R_{21}^{xx}\frac{k_x}{k_1}E_p^{0,i} = -R_{21}^{xx}E_{z,p}^i = R_{21,p}^{zz}E_{z,p}^i$ where $R_{21,p}^{zz} = -R_{21}^{xx}$. This component allows to compute the reflected p-polarized electric field vector from the identity, $\overline{E}_p^r = \overline{\overline{R}}_{21,p} \cdot \overline{E}_p^i$ where

$$\overline{\overline{R}}_{21,p} = \begin{bmatrix} R_{21}^{xx} & R_{21}^{xy} & 0 \\ R_{21}^{xy} & R_{21}^{yy} & 0 \\ 0 & 0 & R_{21,p}^{zz} \end{bmatrix}. \tag{2.20}$$

Now, the p-polarized reflected electric field is

$$\overline{E}_p^r = \hat{x}\left(R_{21}^{xx}E_{x,p}^i + R_{21}^{xy}E_{y,s}^i\right) + \hat{z}\left(R_{21,s}^{zy}E_{y,s}^i + R_{21,p}^{zz}E_{z,p}^i\right) = R_{ps}\overline{E}_s^i + R_{pp}\overline{E}_p^i, \tag{2.21}$$

where $R_{ps} = -\frac{k_1}{k_{z1}}R_{21}^{xy}$ and $R_{pp} = -R_{21}^{xx}$.

Finally, the reflection coefficient tensor of the anisotropic metasurface related to incident s and p-polarized waves yields

$$\overline{\overline{R}} = \begin{bmatrix} R_{21}^{yy} & \frac{k_{z1}}{k_1}R_{21}^{yx} \\ -\frac{k_1}{k_{z1}}R_{21}^{xy} & -R_{21}^{xx} \end{bmatrix}. \tag{2.22}$$

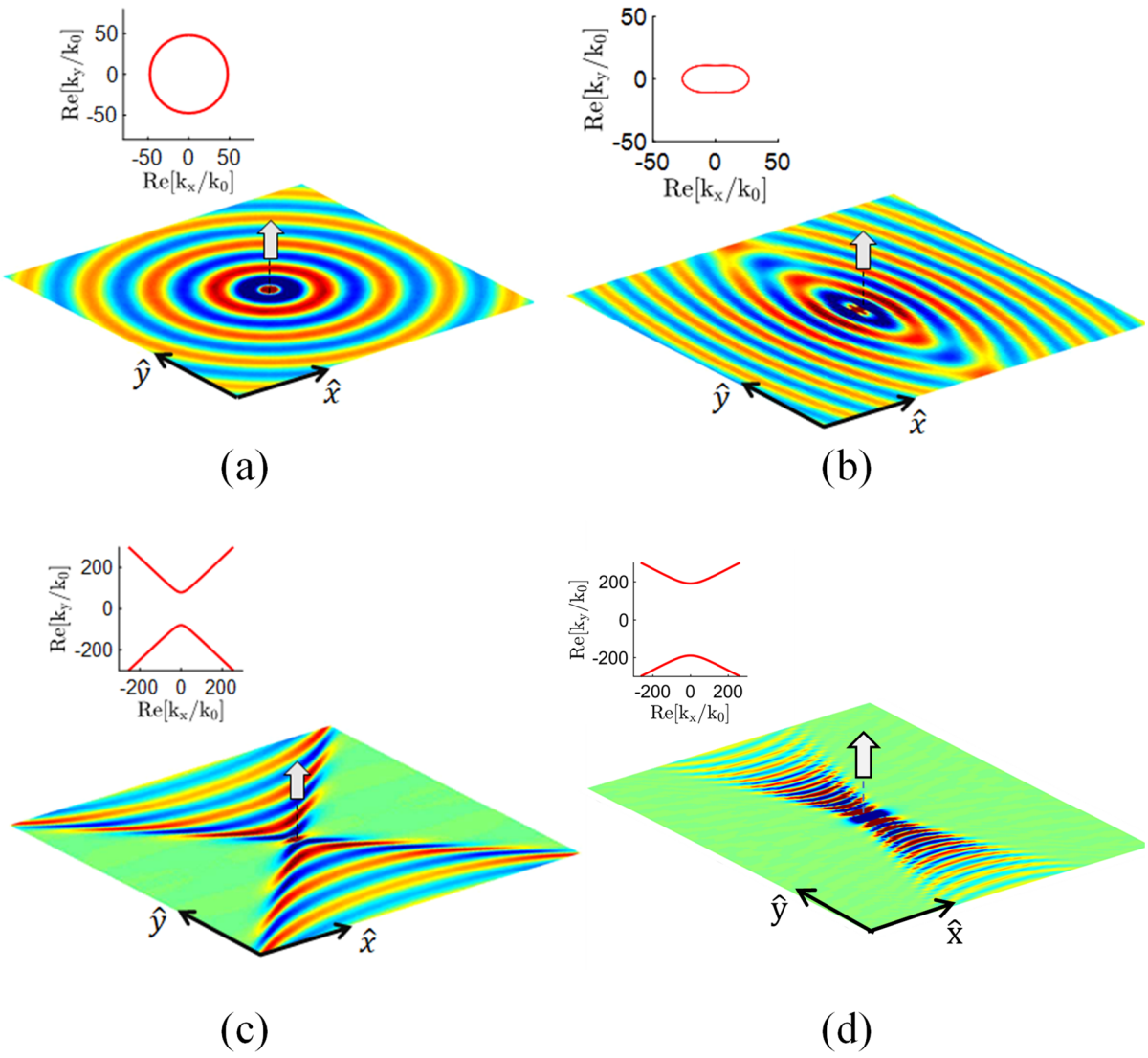

Figure 2.5: E_z field component of surface plasmons excited by a linearly polarized (z-oriented) electric point dipole located above (i) isotropic, (b) elliptic, (c) hyperbolic and (d) extremely anisotropic metasurfaces. The inset above the field shows the isofrequency contours of each topology.

It is important to stress that surface wave poles are located on the integration axis of Eq. (2.13), and Sommerfeld integration techniques are applied by deforming the integration path through the complex plane.

2.2.3 METASURFACE TOPOLOGIES

Anisotropic metasurfaces with different topologies can be realized by analyzing their conductivity tensor components. Figure 2.5 illustrates the field distribution of surface plasmons propagating along different classes of metasurfaces. Specifically, Figure 2.5(a) shows the isotropic topology when $\sigma_{xx} = \sigma_{yy}$ and plasmons propagate along all directions symmetrically on the surface possessing identical properties. Anisotropic responses appear when $\mathrm{Im}[\sigma_{xx}] \neq \mathrm{Im}[\sigma_{yy}]$, and the structure topology depends on the signs of $\mathrm{Im}[\sigma_{xx}]$ and $\mathrm{Im}[\sigma_{yy}]$ that determine the shape of the isofrequency contour. For instance, the metasurface can have (i) an elliptic topology: support quasi-TM surface plasmons when $\mathrm{Im}[\sigma_{xx}] > 0, \mathrm{Im}[\sigma_{yy}] > 0, \mathrm{Im}[\sigma_{xx}] \neq \mathrm{Im}[\sigma_{yy}]$ [see Figure 2.5(b)]; (ii) an hyperbolic topology: when the relative signs of $\mathrm{Im}[\sigma_{xx}]$ and $\mathrm{Im}[\sigma_{yy}]$ are opposite [see Figure 2.5(c)]; and (iii) extremely anisotropic or canalization-like: when $\mathrm{Im}[\sigma_{xx}] \gg \mathrm{Im}[\sigma_{yy}]$ [see Figure 2.5(d)] or $\mathrm{Im}[\sigma_{xx}] \ll \mathrm{Im}[\sigma_{yy}]$. Eq. (2.12) shows that the quasi-TE surface modes exhibit a dispersion relation similar to the free-space having plasmon wavenumber nearly same as the free-space wavenumber. This leads to negligible wave confinement and responses that are of little practical interest. Throughout this work, more emphasize will be put on the unusual features of quasi-TM plasmons supported by metasurface.

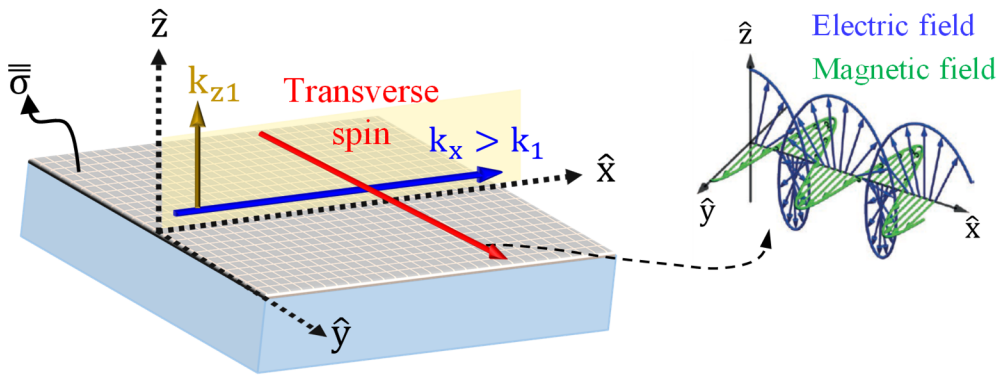

Figure 2.6: Surface plasmon propagating along the $\hat{x}$-axis at a metasurface, defined by optical conductivity tensor $\bar{\bar{\sigma}}$, exhibiting evanescent wavefront along the $\hat{z}$-axis. The inset shows the rotation of the electric and magnetic fields, in the zx-plane, possessing y-directed transverse spin [15].

2.3 PHOTONIC SPIN HALL EFFECT

In this section, I briefly analyze the photonic spin Hall effect that enables directional excitation of SPPs on plasmonic metasurfaces in the presence of an electric point dipole possessing out-of-plane polarization spin. These directional SPPs play a key role to realize recoil optical forces on dipolar nanoparticles located near plasmonic metasurfaces as will be discussed in the following Chapters.

Electrons and photons possess charge as well as spin [1,31]. The spin-orbit interaction of light that appears due to the splitting of opposite spin electrons or photons perpendicular to the incident plane of electromagnetic waves is referred as photonic spin Hall effect [32]. In this phenomenon, the spin or polarization of electromagnetic waves determine the electric field intensity distribution and propagation direction of light [33].

Merging the concept of photonics spin Hall effect with the electromagnetic responses provided by anisotropic metasurfaces has demonstrated unusual abilities of manipulating electromagnetic waves [16,34,35]. One of the most striking phenomena is the tunable and unidirectional excitation of surface plasmons, where the direction of plasmon propagation is controlled by the polarization of the incoming light [34,35]. Such remarkable spin-controlled unidirectional coupling between incoming light and transversely propagating evanescent surface waves is enabled thanks to the spin-properties of evanescent modes in Maxwell's equations [33], and has evoked enormous interest recently [36-41].

Figure 2.6 shows surface plasmons propagating along the $\hat{x}$-axis with transverse wavenumber $k_x > k_1$ that enforces an evanescent wavefront in the $\hat{z}$-direction since k_{z1} becomes imaginary. Following the relation $\bar{k} \cdot \bar{E} = 0$, the transverse electric field component of the plasmon is $E_z = -\left(\frac{k_{z1}}{k_x}\right) E_x = -i\left(\frac{|k_{z1}|}{k_x}\right) E_x$. This relation confirms that the electric field of a linearly polarized (z-polarized) wave rotates in the zx-plane thus generating spin angular momentum along the orthogonal $\hat{y}$-axis [33]. Such transverse spin angular momentum can be computed as [33]

$$\overline{\mathrm{SAM}} = \frac{\mathrm{Re}[\bar{k}]\times\mathrm{Im}[\bar{k}]}{(\mathrm{Re}[\bar{k}])^2} = \frac{(\hat{x}\times\hat{z})k_x k_{z1}}{(\mathrm{Re}[\bar{k}])^2}. \tag{2.23}$$

Eq. (2.23) shows that the transverse spin angular momentum of light is orthogonal to the plasmon wavevector. More importantly, the direction of this transverse spin angular momentum depends on the plasmon propagation direction, and plasmons with $k_x > 0$ and $k_x < 0$ carry transverse spins along $\hat{y}$ and $-\hat{y}$ half spaces, respectively.

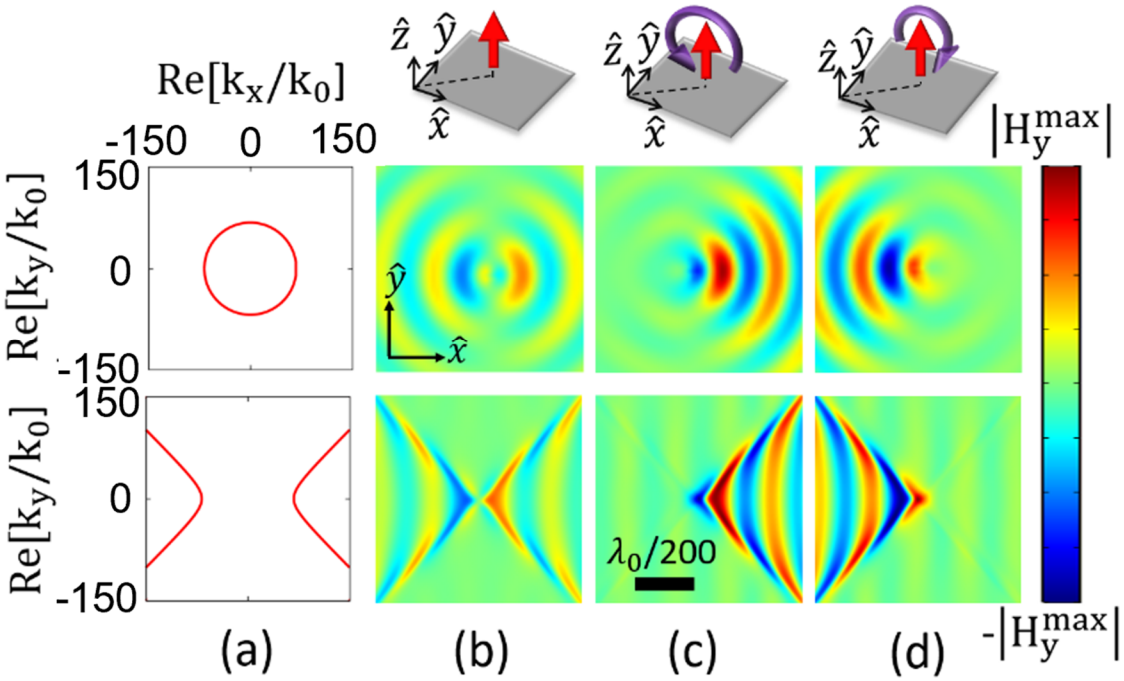

Figure 2.7: Electromagnetic responses of anisotropic metasurfaces and associated photonic spin Hall effect. The metasurfaces are excited by a z-oriented dipole (red arrow) that is located at z_0 =40 nm. The first row corresponds to an isotropic metasurface with $\sigma = 0.05 + i50$ μS and the second row to a hyperbolic metasurface with $\sigma_{xx} = 0.05 + i50$ μS and $\sigma_{yy} = 0.05 - i50$ μS. (a) Isofrequency contour. (b) y-component of the magnetic field of the plasmons excited by a z-oriented dipole. (c) and (d) columns are similar to (b) but considering that the dipole is circularly polarized with respect to the y-axis with given rotation handedness (blue arrows), respectively. The dipole polarization is shown in the insets with a magenta arrow. All plots have identical dimensions and field scale.

Recent years have witnessed growing interests to selectively excite surface plasmons whose spin angular momentum matches with one of the fields radiated by an electric point dipole located nearby the metasurfaces [42,43]. In this case, the plasmon propagation direction depends on the polarization handedness of the dipole. Figure 2.7 shows such responses for the case of isotropic and hyperbolic metasurfaces. Results show that a linearly polarized dipole excites surface plasmons symmetrically on both structures. However, a circularly polarized dipole rotating in the xz-plane excites directional plasmons propagating along the positive or negative x-half spaces. Here, the propagation direction is determined by the interplay between the polarization spin of the dipole and polarization state of the plasmons in the positive and negative x-half spaces of both metasurfaces. Unlike the isotropic one, the directional SPPs supported by the hyperbolic metasurfaces are significantly more confined and possess large spatial wavenumber. In Chapters 5 and 6, the unusual features of the directional hyperbolic surface plasmons enabled by the photonic spin Hall effect will be exploited to obtain giant lateral optical forces on dipoles located in the near field of the structure.

2.4 NUMERICAL SIMULATIONS IN COMSOL MULTIPHYSICS

Full wave simulation in COMSOL Multiphysics is performed to compute the conductivity of ultrathin uniform and nanostructured silver based metasurfaces [see the inset in Figure 2.2(a)]. The frequency dependent electrical permittivity of silver is available in ref-[21]. Scattering boundary conditions are applied to the outer boundaries of the entire geometry. A fine tetrahedral mesh with maximum element size $\lambda_0/70$ is applied to the metasurface. To compute the conductivity tensor, first I consider a normally incident plane wave to the metasurface with electric field polarized along the $\hat{x}$-direction. The simulation permits to numerically calculate the surface current density J_x. Now the $\hat{x}\hat{x}$ component of the conductivity tensor can be easily retrieved from the identity: $\sigma_{xx} = J_x/E_x$, where E_x is composed of the incident and reflected field. In order to compute the $\hat{y}\hat{y}$ component of the conductivity tensor σ_{yy}, I consider a normally incident plane wave to the metasurface with electric field polarized along the $\hat{y}$-direction and apply the identity $\sigma_{yy} = J_y/E_y$, where E_y is the superposition of the incident and the reflected field. I recall that the simulation results

for nanostructured silver based anisotropic metasurface are provided in Figure 2.2. In the case of uniform silver layer, similar procedure is applied to compute the surface conductivity $\sigma_{xx} = \sigma_{yy} = \sigma$ and the results are shown in Figure 2.1(b).

2.5 CHAPTER REFERENCES

[1] Novotny, L. and Hecht, B., 2012. Principles of nano-optics. Cambridge university press.

[2] Pitarke, J.M., Silkin, V.M., Chulkov, E.V. and Echenique, P.M., 2006. Theory of surface plasmons and surface-plasmon polaritons. *Reports on Progress in Physics*, 70(1), p.1.

[3] Zhang, J., Zhang, L. and Xu, W., 2012. Surface plasmon polaritons: physics and applications. *Journal of Physics D: Applied Physics*, 45(11), p.113001.

[4] Wang, C., Zhang, G., Huang, S., Xie, Y. and Yan, H., 2020. The optical properties and plasmonics of anisotropic 2D materials. *Advanced Optical Materials*, 8(5), p.1900996.

[5] Kotov, O.V. and Lozovik, Y.E., 2019. Hyperbolic hybrid waves and optical topological transitions in few-layer anisotropic metasurfaces. *Physical Review B*, 100(16), p.165424.

[6] Gomez-Diaz, J.S., Tymchenko, M. and Alu, A., 2015. Hyperbolic plasmons and topological transitions over uniaxial metasurfaces. *Physical Review Letters*, 114(23), p.233901.

[7] Gomez-Diaz, J.S. and Alu, A., 2016. Flatland optics with hyperbolic metasurfaces. *ACS Photonics*, 3(12), pp.2211-2224.

[8] High, A.A., Devlin, R.C., Dibos, A., Polking, M., Wild, D.S., Perczel, J., De Leon, N.P., Lukin, M.D. and Park, H., 2015. Visible-frequency hyperbolic metasurface. *Nature*, 522(7555), pp.192-196.

[9] Yermakov, O.Y., Permyakov, D.V., Porubaev, F.V., Dmitriev, P.A., Samusev, A.K., Iorsh, I.V., Malureanu, R., Lavrinenko, A.V. and Bogdanov, A.A., 2018. Effective surface conductivity of optical hyperbolic metasurfaces: from far-field characterization to surface wave analysis. *Scientific Reports*, 8(1), pp.1-10.

[10] Huidobro, P.A., Kraft, M., Maier, S.A. and Pendry, J.B., 2016. Graphene as a tunable anisotropic or isotropic plasmonic metasurface. *ACS Nano*, 10(5), pp.5499-5506.

[11] Li, P., Dolado, I., Alfaro-Mozaz, F.J., Casanova, F., Hueso, L.E., Liu, S., Edgar, J.H., Nikitin, A.Y., Vélez, S. and Hillenbrand, R., 2018. Infrared hyperbolic metasurface based on nanostructured van der Waals materials. *Science*, 359(6378), pp.892-896.

[12] Correas-Serrano, D., Gomez-Diaz, J.S., Melcon, A.A. and Alù, A., 2016. Black phosphorus plasmonics: anisotropic elliptical propagation and nonlocality-induced canalization. *Journal of Optics*, 18(10), p.104006.

[13] Correas-Serrano, D., Alù, A. and Gomez-Diaz, J.S., 2017. Plasmon canalization and tunneling over anisotropic metasurfaces. *Physical Review B*, 96(7), p.075436.

[14] Ling, X., Zhou, X., Huang, K., Liu, Y., Qiu, C.W., Luo, H. and Wen, S., 2017. Recent advances in the spin Hall effect of light. *Reports on Progress in Physics*, 80(6), p.066401.

[15] Bliokh, K.Y., Smirnova, D. and Nori, F., 2015. Quantum spin Hall effect of light. *Science*, 348(6242), pp.1448-1451.

[16] Yin, X., Ye, Z., Rho, J., Wang, Y. and Zhang, X., 2013. Photonic spin Hall effect at metasurfaces. *Science*, 339(6126), pp.1405-1407.

[17] Kildishev, A.V., Boltasseva, A. and Shalaev, V.M., 2013. Planar photonics with metasurfaces. *Science*, 339(6125), p.1232009.

[18] Yu, N. and Capasso, F., 2014. Flat optics with designer metasurfaces. *Nature Materials*, 13(2), pp.139-150.

[19] www.comsol.com

[20] Vakil, A. and Engheta, N., 2011. Transformation optics using graphene. *Science*, 332(6035), pp.1291-1294.

[21] Wu, Y., Zhang, C., Estakhri, N.M., Zhao, Y., Kim, J., Zhang, M., Liu, X.X., Pribil, G.K., Alù, A., Shih, C.K. and Li, X., 2014. Intrinsic optical properties and enhanced plasmonic response of epitaxial silver. *Advanced Materials*, 26(35), pp.6106-6110.

[22] Bedeaux, D. and Vlieger, J., 2004. Optical properties of surfaces. Imperial College Press.

[23] Gomez-Diaz, J.S., Tymchenko, M. and Alù, A., 2015. Hyperbolic metasurfaces: surface plasmons, light-matter interactions, and physical implementation using graphene strips. *Optical Materials Express*, 5(10), pp.2313-2329.

[24] Hecht, B., Bielefeldt, H., Novotny, L., Inouye, Y. and Pohl, D.W., 1996. Local excitation, scattering, and interference of surface plasmons. *Physical Review Letters*, 77(9), p.1889.

[25] Novotny, L., Hecht, B. and Pohl, D.W., 1997. Interference of locally excited surface plasmons. *Journal of Applied Physics*, 81(4), pp.1798-1806.

[26] Lakowicz, J.R., 2004. Radiative decay engineering 3. Surface plasmon-coupled directional emission. *Analytical Biochemistry*, 324(2), pp.153-169.

[27] Yermakov, O.Y., Ovcharenko, A.I., Song, M., Bogdanov, A.A., Iorsh, I.V. and Kivshar, Y.S., 2015. Hybrid waves localized at hyperbolic metasurfaces. *Physical Review B*, 91(23), p.235423.

[28] Gusynin, V.P., Sharapov, S.G. and Carbotte, J.P., 2006. Magneto-optical conductivity in graphene. *Journal of Physics: Condensed Matter*, 19(2), p.026222.

[29] Lakhtakia, A., 1992. Green's functions and Brewster condition for a halfspace bounded by an anisotropic impedance plane. *International Journal of Infrared And Millimeter Waves*, 13(2), pp.161-170.

[30] Bilow, H.J., 2003. Guided waves on a planar tensor impedance surface. *IEEE Transactions on Antennas and Propagation*, 51(10), pp.2788-2792.

[31] Yılmaz, S.T., Fallahi, P. and Imamoğlu, A., 2010. Quantum-dot-spin single-photon interface. *Physical Review Letters*, 105(3), p.033601.

[32] Hirsch, J.E., 1999. Spin hall effect. *Physical Review Letters*, 83(9), p.1834.

[33] Bliokh, K.Y., Rodríguez-Fortuño, F.J., Nori, F. and Zayats, A.V., 2015. Spin–orbit interactions of light. *Nature Photonics*, 9(12), pp.796-808.

[34] Huang, L., Chen, X., Bai, B., Tan, Q., Jin, G., Zentgraf, T. and Zhang, S., 2013. Helicity dependent directional surface plasmon polariton excitation using a metasurface with interfacial phase discontinuity. *Light: Science & Applications*, 2(3), pp.e70-e70.

[35] Lin, J., Mueller, J.B., Wang, Q., Yuan, G., Antoniou, N., Yuan, X.C. and Capasso, F., 2013. Polarization-controlled tunable directional coupling of surface plasmon polaritons. *Science*, 340(6130), pp.331-334.

[36] Rodríguez-Fortuño, F.J., Marino, G., Ginzburg, P., O'Connor, D., Martínez, A., Wurtz, G.A. and Zayats, A.V., 2013. Near-field interference for the unidirectional excitation of electromagnetic guided modes. *Science*, 340(6130), pp.328-330.

[37] O'connor, D., Ginzburg, P., Rodríguez-Fortuño, F.J., Wurtz, G.A. and Zayats, A.V., 2014. Spin–orbit coupling in surface plasmon scattering by nanostructures. *Nature Communications*, 5(1), pp.1-7.

[38] Mitsch, R., Sayrin, C., Albrecht, B., Schneeweiss, P. and Rauschenbeutel, A., 2014. Quantum state-controlled directional spontaneous emission of photons into a nanophotonic waveguide. *Nature Communications*, 5(1), pp.1-5.

[39] Le Feber, B., Rotenberg, N. and Kuipers, L., 2015. Nanophotonic control of circular dipole emission. *Nature Communications*, 6(1), pp.1-6.

[40] Söllner, I., Mahmoodian, S., Hansen, S.L., Midolo, L., Javadi, A., Kiršanskė, G., Pregnolato, T., El-Ella, H., Lee, E.H., Song, J.D. and Stobbe, S., 2015. Deterministic photon–emitter coupling in chiral photonic circuits. *Nature Nanotechnology*, 10(9), pp.775-778.

[41] Lefier, Y. and Grosjean, T., 2015. Unidirectional sub-diffraction waveguiding based on optical spin–orbit coupling in subwavelength plasmonic waveguides. *Optics Letters*, 40(12), pp.2890-2893.

[42] Wolf, S.A., Awschalom, D.D., Buhrman, R.A., Daughton, J.M., von Molnár, V.S., Roukes, M.L., Chtchelkanova, A.Y. and Treger, D.M., 2001. Spintronics: a spin-based electronics vision for the future. *Science*, 294(5546), pp.1488-1495.

[43] Jungwirth, T., Wunderlich, J. and Olejník, K., 2012. Spin Hall effect devices. *Nature Materials*, 11(5), pp.382-390.

Chapter 3: Drift-biased Nonreciprocal Graphene Plasmonics

Drift-biased graphene has recently emerged as a promising platform for broadband nonreciprocal plasmonics [1-5]. The resulting nonreciprocal response is remarkably robust since this two-dimensional material simultaneously provides an ultrahigh electron mobility that enables drift-velocities very close to the Fermi velocity [6,7] and a strong plasmonic response in the terahertz and infrared frequency bands [8,9]. Merging drift-biased graphene with the rich functionalities and strong light–matter interactions provided by patterned metasurfaces has opened new routes to manipulate the states supported by the device, allowing new degrees of freedom to tailor its dispersion diagram (two dimensional isofrequency contour) and to excite and steer broadband SPPs immune to backscattering [1].

In this Chapter, I explore the possibilities enabled by drift-biased graphene to tailor the isofrequency contour of the supported modes, and apply it to construct broadband and unidirectional plasmonic hyperlens. First, I briefly review the electromagnetic modeling of drift-biased graphene conductivity using a nonlocal approach. This model relies on the Doppler shift that the surface waves experience due to the drifting electrons, and negative Landau damping that might lead to plasmon amplification. Using a dedicated Green's function formalism [see Chapter 2], I investigate the properties of surface plasmons excited on the structure in the presence of a nearby dipolar source. Then, I propose a new approach to tailor the isofrequency contour of the modes supported by graphene: applying two drift-biases on the graphene sheet that are orthogonal to each other. This simple technique tailors the modal dispersion of the supported plasmons to a great extent in an unprecedented manner, thus permitting to dynamically steer and canalize one-way plasmons towards desired directions within the plane. This technique avoids the need of nanopatterning the two-dimensional layer [1] or its ground plane and permits to obtain nonreciprocal, broadband, dynamic, and flat modal dispersions that canalize surface plasmons toward desired directions in the plane. Finally, I investigate the capabilities of this platform to resolve the presence of two sources

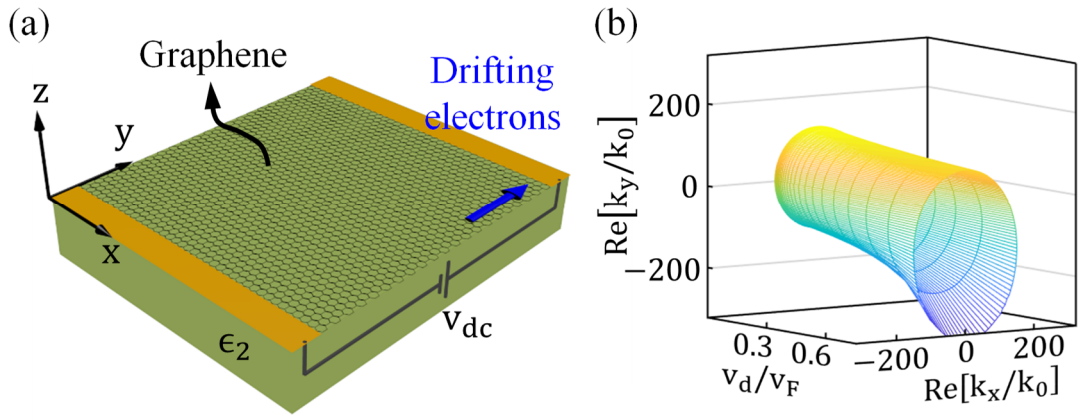

Figure 3.1: A graphene sheet, standing on a substrate of electrical permittivity ε_2, is electrical biased with dc voltage V_{dc} thus inducing drifting electrons. (a) Schematic of the configuration. (b) Three-dimensional view of the isofrequency contour of the structure as a function of drift velocity $\bar{v}_d = \hat{y}v_d$ assuming $\varepsilon_2 = 3.8$. Operation frequency is 21 THz and graphene's chemical potential and relaxation time are set to 0.1eV and 0.5 ps, respectively.

located in the near field in terms of subwavelength resolution and operation frequency. I also determine the velocity that drifting electrons must acquire to achieve an optimum resolution. I exploit the orthogonality between the voltage sources and drifting electrons to generate effectively superluminal currents traveling diagonally along the surface and explore the potential response of such a platform using the semi-classical formalism. Here, superluminal refers to the fact that the speed of light in graphene is compared to the Fermi velocity, and electrons drift at a speed faster than the Fermi velocity. Even though the feasibility of a superluminal drift regime in graphene is not yet determined, results suggest that it would significantly enhance the platform performance. I then take advantage of spin–orbit interactions to construct broadband and unidirectional planar hyperlenses for near-field sources with specific field polarization distribution.

3.1 NONLOCAL CONDUCTIVITY MODEL OF DRIFT-BIASED GRAPHENE

Let me consider a graphene sheet, standing on a substrate of relative electrical permittivity ε_2, is biased with a longitudinal voltage V_{dc} that induces drifting electrons with velocity $\bar{v}_d = v_d\hat{e}_c$ along the sheet, where $\hat{e}_c$ is the unit-vector that defines the current direction within the plane. The schematic of this

configuration is depicted in Figure 3.1(a). As described in [1-3], drifting electrons introduce a Doppler shift in the wavevectors thus enabling different responses for SPPs propagating along and against the drift. In the presence of drift-bias, graphene's conductivity becomes nonlocal, and it can be expressed as [1-3]

$$\sigma_d\left(\omega, v_d^x, v_d^y, k_x, k_y\right) = \frac{\omega}{\omega - \bar{k}_\rho \cdot \bar{v}_d}\sigma_g\left(\omega - \bar{k}_\rho \cdot \bar{v}_d\right), \tag{3.1}$$

where $\omega = 2\pi f$ is the oscillation frequency, $\bar{k}_\rho = \hat{x}k_x + \hat{y}k_y$ is the in-plane wavenumber of the surface modes, $\bar{v}_d = \hat{x}v_d^x + \hat{y}v_d^y$, and σ_g is graphene's conductivity computed using a nonlocal approach [10,11]. Eq. (3.1) accounts for a drift-induced Doppler shift in the momentum space proportional to the velocity of the drifting electrons ($\sim k_x v_d^x + k_y v_d^y$) as well as a negative Landau damping expressed through the factor $\frac{\omega}{\omega - k_x v_d^y - k_y v_d^y}$ that might lead to plasmon amplification [3]. Incorporating Eq. (3.1) in the nonlocal and anisotropic Green's function framework (see Chapter 2) permits to calculate the modal dispersion of drift-biased graphene as well as its electromagnetic response to point sources.

For the sake of simplicity, I assume that the dc-bias is applied along $\hat{y}$-axis of the reference coordinate system that leads to $\bar{v}_d = \hat{y}v_d$. The graphene sheet is supported by hexagonal boron nitride (i.e., $\varepsilon_2 \approx 3.8$) [1]. Figure 3.1(b) shows the isofrequency contour of the structure as a function of the drift velocity v_d in three-dimensional fashion. In the absence of drifting electrons, the purely circular shape of the isofrequency contour (IFC) confirms that graphene exhibits an isotropic and reciprocal response [9]. The applied drift bias breaks the symmetry of the supported eigenstates and leads to effectively anisotropic and nonreciprocal metasurfaces. These structures support SPPs with larger wavenumbers propagating in the opposite of drift (negative y half space) than those propagating towards the electrons drifting direction. The asymmetry further increases with the amount of v_d. In the orthogonal directions to the drift, these metasurfaces display nearly symmetric behavior and SPPs propagating in the positive and negative x half spaces possess equal wavenumber. Note that nonlocality due to the finite velocity of electrons in graphene is a key ingredient in

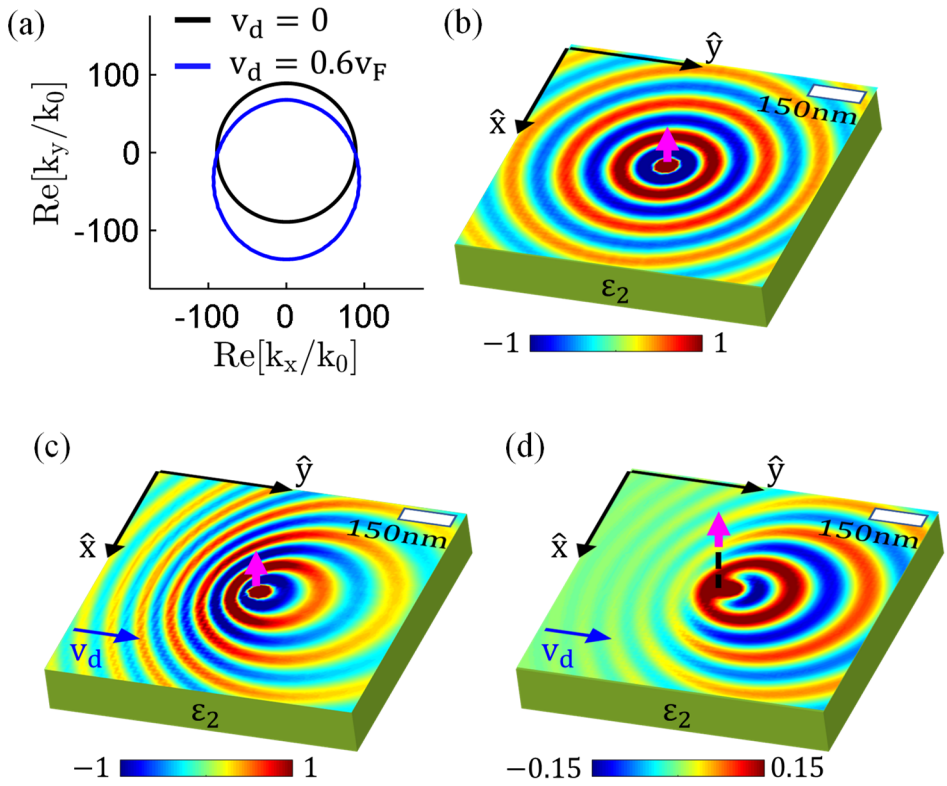

Figure 3.2: A linearly polarized electric point dipole (magenta arrow) polarized along $\hat{z}$ is located, in free space, above an electrical biased graphene sheet. (a) Isofrequency contour of the metasurface without (black line) and with (blue line) drift velocity, $v_d = 0.6v_F$. Normalized z-component of the electric field of the excited surface plasmons on graphene when (b) there is no drift, and (c) $v_d = 0.6v_F$ keeping the dipole position $z_0 = 30$ nm above the sheet. (d) Excited surface plasmons when the dipole is moved to $z_0 = 60$ nm keeping $v_d = 0.6v_F$. Remaining parameters are as in Figure 3.1.

this response. Without considering nonlocal effects, the isofrequency contour may show an open shape in one axis, that would completely forbit wave propagation in that direction.

3.2 ELECTROMAGNETIC RESPONSE OF NONRECIPROCAL SURFACE PLASMONS

Let me consider a linearly polarized dipole (i.e., $\bar{p} = \hat{z}$) located at a distance z_0 from the graphene sheet. Figure 3.2(a) shows the isofrequency contours of unbiased and drift-biased graphene metasurface with $v_d = 0.6v_F$. Figure 3.2(b)-(d) depict the z-component of the plasmon electric field excited on these surfaces. Specifically, Figure 3.2(b) shows that plasmons are excited symmetrically on the unbiased sheet thus confirming the reciprocal responses. Figure 3.2(c)-(d) show the excited surface plasmons for different

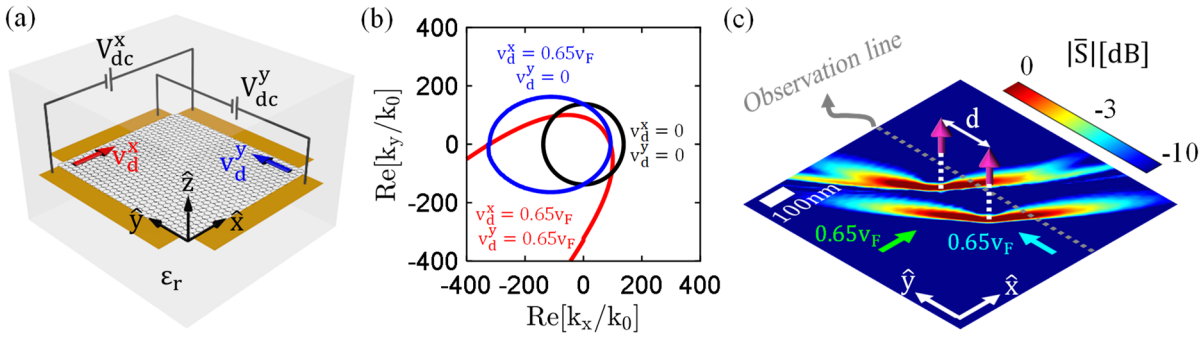

Figure 3.3: Proposed planar hyperlensing platform based on drift-biased graphene. (a) Schematic. A graphene sheet embedded in hBN is electrically biased with two longitudinal dc voltages, V_{dc}^{x} and V_{dc}^{y}, that generate orthogonal drifting electrons moving along the $\hat{x}$ and $\hat{y}$ axes with velocities v_d^x and v_d^y, respectively. (b) Influence of the drifting electron velocity on the isofrequency contour of the structure. (black) No bias; (blue) $\bar{v}_d = 0.65v_F\hat{x} + 0.0\hat{y}$; (red) $\bar{v}_d = 0.65v_F\hat{x} + 0.65v_F\hat{y}$. (c) Excitation of surface waves (normalized magnitude of the Poynting vector $\bar{S}$ in dB) by two $\hat{z}$-oriented dipoles separated by a distance $d = \lambda_0/100$ (λ_0 is the wavelength) along the $\hat{y}$ axis and located at 15nm over the surface. Operation frequency is 15 THz, and graphene's chemical potential and relaxation time are set to 0.1eV and 0.5 ps.

position of the dipole keeping the electron drift velocity $\bar{v}_d = \hat{y}0.6v_F$ fixed. Specifically, when the dipole is very close to the metasurface [see panel-(c)], the evanescent fields radiated by the dipole are efficiently coupled to the structure and excite surface plasmons with all possible supported modes. It is obvious that the plasmons flowing against the drifting electrons are more confined than the ones propagating in the opposite direction. As the distance between the metasurface and the dipole increases [see panel-(d)], larger wavenumbers radiated by the dipole are quickly filtered out by free space and do not effectively couple to surface modes in the negative y half space. Instead, radiated fields with smaller wavenumbers are coupled to the sheet and plasmons favorably propagate toward the electron drifting direction.

In the following, I consider the case when a dipole is very close to the surface, aiming to take advantage of the strong near-field coupling between the dipole and the metasurfaces, and I propose the use of this platform as a planar plasmonic hyperlens with ultra-subwavelength resolution over a broadband frequency.

3.3 BROADBAND AND UNIDIRECTIONAL PLASMONIC HYPERLENSING

Let me consider a drift-biased graphene metasurface with two orthogonal longitudinal dc-biases [see Figure 3.3(a)]. Here, the additional dc-bias provides an extra degree of freedom to manipulate the isofrequency contours of the metasurfaces in unprecedented ways. Note that Eq. (3.1) can be readily applied to model this device assuming that the orthogonal drift currents on graphene layer do not interact with each other.

Figure 3.3(b) shows the isofrequency contours of the supported modes for several biasing conditions. I recall that in the absence of any drift-bias, graphene exhibits an isotropic response associated to surface plasmons (black line). Applying a longitudinal bias along the $\hat{x}$-axis induces drifting electrons on graphene that breaks the symmetry of the eigenstates and leads to an effectively anisotropic and nonreciprocal modal response. In case of drifting electrons with velocity $v_d^x = 0.65v_F$ (blue line), plasmons propagating along the drift (positive k_x half space) travel significantly faster than other modes, exhibiting a moderate field confinement and low-loss. On the contrary, plasmons propagating against the drift (negative k_x half space) are extremely confined and lossy. The resulting isofrequency contour acquires a closed elliptical shape that is symmetric with respect to the direction orthogonal to the drift-axis (i.e., $\hat{y}$) and whose center has been shifted in the momentum space toward the direction opposite to the drift. Applying an additional drift bias of similar magnitude on the $\hat{y}$ direction [red line in Figure 3.3(b)] permits to further manipulate the supported states by (i) decreasing the field confinement and loss of certain states; and (ii) and flattening the IFC along the directions of the applied bias. This response arises due to the interplay between nonlocality and nonreciprocity: the effective drift bias generates a strong nonreciprocal response whereas nonlocality imposes that SPPs must be supported at all directions within the plane. The ultra-confined states that appear in directions opposite to the effective drift elongates and significantly flattens the isofrequency contour of the device, thus enabling the use of drift-biased graphene to canalize SPPs. It is important to remark the key role played by nonlocality to determine the platform dispersion as well as the direction of energy flow: if this phenomenon is not considered, the IFC would exhibit an open shape in the momentum space that

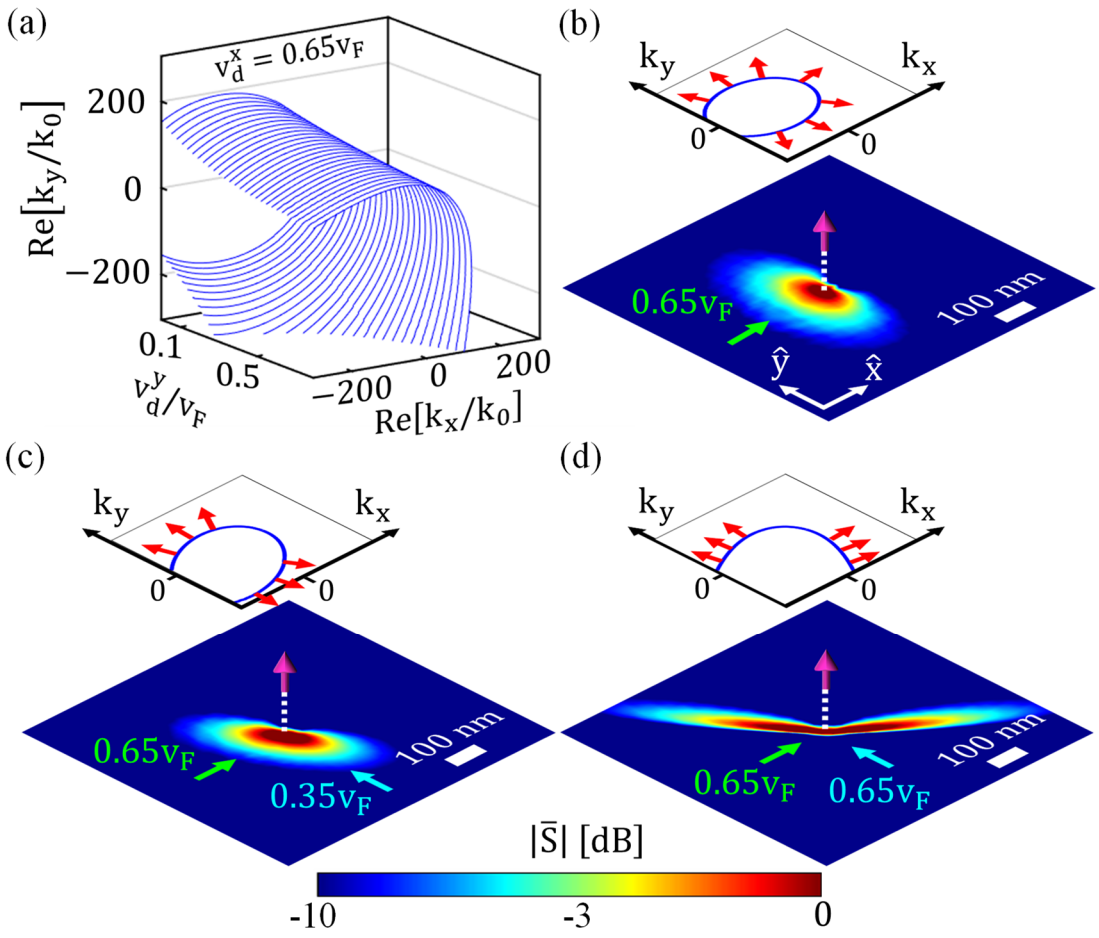

Figure 3.4: Properties of the surface plasmons supported by a graphene layer biased with a drift velocity $v_d^x = 0.65v_F$ along the $\hat{x}$ axis versus the velocity of drifting electrons flowing along the orthogonal direction $\hat{y}$, v_d^y. (a) Isofrequency contour. (b-d) Normalized magnitude of the Poynting vector $\bar{S}$ (in dB) excited by a $\hat{z}$-oriented dipole located at 15 nm above the surface. Results are computed on the metasurface for (b) $v_d^y = 0$; (c) $v_d^y = 0.35v_F$; and (d) $v_d^y = 0.65v_F$. Each panel contains an inset illustrating the metasurface isofrequency contour and the direction of energy flow (red arrow). Other parameters are as in Figure 3.3.

would prevent the propagation of SPPs in directions opposite to the drifting electrons. The strong influence of nonlocality in drift-biased graphene plasmonics is in full agreement with recent works that have discussed how nonlocal effects prevent the presence of truly unidirectional plasmons at homogeneous magnetic interfaces [12-14] by closing the IFC. To illustrate the application of the proposed platform in hyperlensing, Figure 3.3(c) shows the excitation of surface waves by two *z*-oriented dipoles separated by a

distance d=200 nm ($\sim\lambda_0/100$ where λ_0 is the free space wavelength) along the $\hat{y}$ axis and located 15 nm over the graphene surface. Results shows that plasmons are excited only along directions close to those defined by the applied bias and they travel without any apparent diffraction, demonstrating strong capability for subwavelength imaging. Remarkably, the platform provides a strong nonreciprocal response and prevents any wave propagation in the surface but collimated plasmonic beams. In the following, I investigate the performance of this platform in terms of applied drift bias, resolution, operation frequency, and polarization.

Figure 3.4 studies the properties of surface plasmons supported by a graphene layer that is biased with a drift velocity $v_d^x = 0.65v_F$ along the $\hat{x}$-axis versus the velocity of drifting electrons traveling toward the orthogonal direction, v_d^y. Specifically, Figure 3.4(a) shows the evolution of the isofrequency contour in the momentum-space versus v_d^y. Results show the capability of this platform to manipulate the isofrequency contour in a dynamic manner by adjusting the voltages applied to the orthogonal DC sources. For sufficiently larger values of the drift velocity ($v_d^y > 0.6v_F$), the isofrequency contour acquires the quasi-flat response typical of media operating in the canalization regime [15,16]. Figure 3.4(b)-(d) show the normalized magnitude of the Poynting vector excited by a z-oriented dipole located at 15nm above the graphene layer when it is biased with different drift velocities. In the different panels, the insets show the

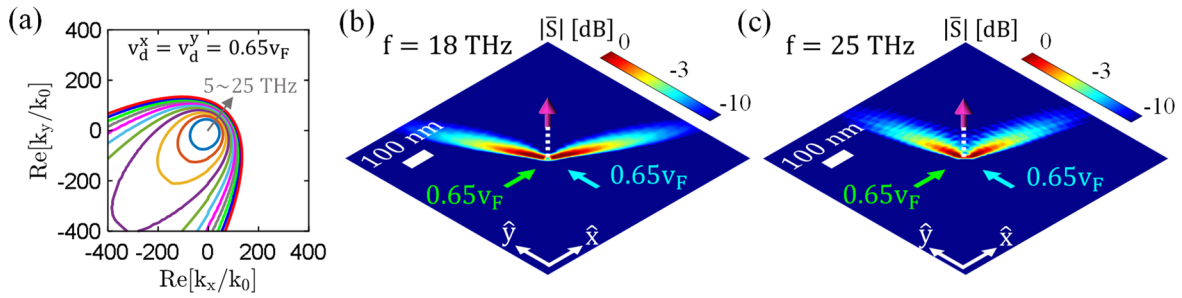

Figure 3.5: Broadband response of the proposed planar hyperlensing platform. The structure is biased with a drift velocity $\bar{v}_d = 0.65v_F\hat{x} + 0.65v_F\hat{y}$ (a) Isofrequency contour at different frequencies. (b-c) Normalized magnitude of the Poynting vector $\bar{S}$ (in dB) excited by a $\hat{z}$-oriented dipole located at 15nm above the surface. Results are computed on the metasurface at (b) 18 THz and (c) 25 THz. Other parameters are as in Figure 3.3.

isofrequency contours of the surface and the direction of energy flow (red arrows). Results clearly illustrate how the quality of the canalization (inversely proportional to the plasmon beamwidth) and propagation distance of the excited surface plasmons significantly increase with the velocity of the drifting electrons flowing along the $\hat{y}$ direction, in full agreement with the qualitative analysis of the isofrequency contour.

One of the most remarkable properties of the proposed hyperlensing platform is the broadband response, covering from the terahertz/far-infrared band to the mid-infrared. Figure 3.5(a) shows the isofrequency contours of the supported modes from 5 to 25 THz, a frequency region in which intraband contributions dominate the electromagnetic response of graphene. Results show that flat isofrequency contours, associated to strong canalization responses, can be obtained over a very broad frequency region (roughly from 11 to 25 THz). Figure 3.5(b)-(c) further confirm this response, showing the magnitude of Poynting vector on the drift-biased graphene layer when it is excited by a z-oriented emitter oscillating at 18 and 25 THz, respectively. It should be noted that strong canalization responses are not found at frequencies lower than 10 THz, which I attribute to the lower confinement and larger loss of SPPs supported in this band. However, it might be possible to achieve canalization in these frequencies by increasing the

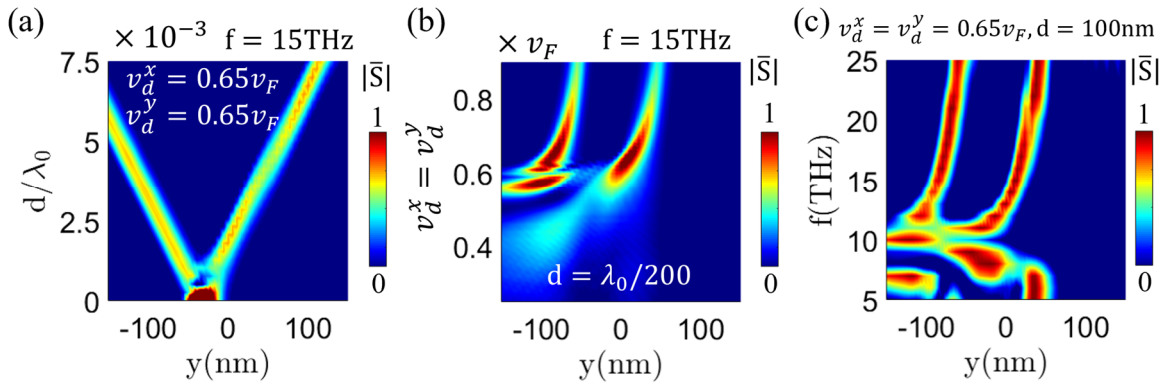

Figure 3.6: Performance the proposed planar hyperlensing platform. Results show the normalized magnitude of the Poynting vector $\bar{S}$ (in dB) excited by two $\hat{z}$-oriented dipoles separated by a sub-wavelength distance d along the $\hat{y}$ axis computed at a distance x_0=50 nm (gray observation line in Fig. 3.3c) versus (a) separation distance d, keeping $\bar{v}_d = 0.65v_F\hat{x} + 0.65v_F\hat{y}$ and f=15THz; (b) drift velocity $\bar{v}_d = v_d^x\hat{x} + v_d^y\hat{y}$, keeping $v_d^x = v_d^y$, d=$\lambda_0/200$(~100 nm) and f=15 THz; and (c) frequency, keeping $\bar{v}_d = 0.65v_F\hat{x} + 0.65v_F\hat{y}$ and d=100 nm. Other parameters are as in Figure 3.3.

graphene quality (using relaxation times > 0.75 ps) [17] or reducing the chemical potential, which in turn would adjust the overall frequency region in which plasmon canalization is supported.

Figure 3.6 investigates and determines the capability of drift-biased graphene to resolve the presence of emitters separated by ultra-subwavelength distances. Specifically, I consider the scenario shown in Figure 3.3(c) and study the power of the surface plasmons excited by two emitters at a fixed distance from them [x_0=50nm, observation line in Figure 3.3(c)] versus the (a) separation distance d between the sources; (b) applied drift-velocity; and (c) operation frequency. The performance of the platform is remarkable: it offers resolution larger than $\sim\lambda_0/500$ and enables ultra-subwavelength imaging; requires realistic drift-velocities ($v_d^x = v_d^y = 0.65v_F$ and $|\bar{v}_d| \approx 0.92v_F$) that have already been experimentally demonstrated in hexagonal boron nitride encapsulated graphene [6,7]; and can easily resolve the presence of emitters separated by 100nm that oscillate from 12 to 25 THz [see Figure 3.6(c)]. Such response can be enhanced further by increasing the applied orthogonal bias voltages [see Figure 3.6(b)] up to a point in which the platform may become superluminal in the sense that the effective drifting electrons move faster than the electron Fermi velocity (i.e., $|\bar{v}_d| > v_F$). In this scenario, electrons move orthogonally along the $\hat{x}$ and $\hat{y}$

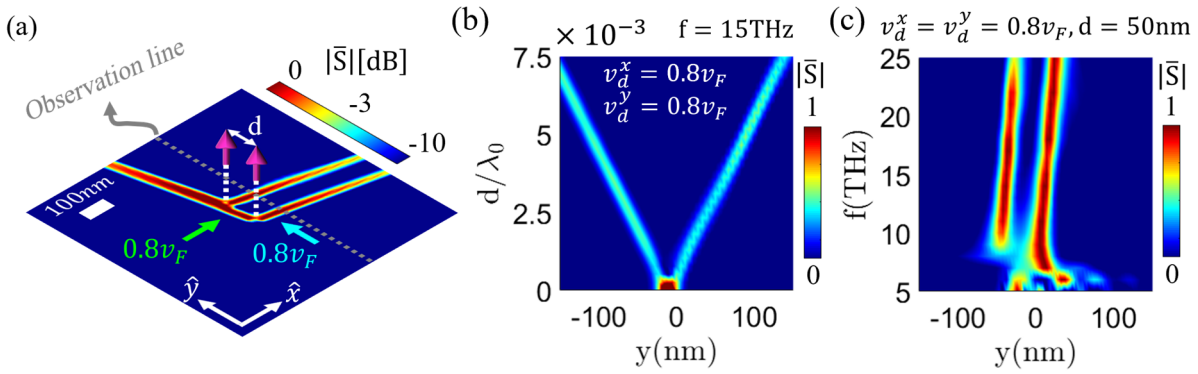

Figure 3.7: Performance of the hyperlensing platform in a superluminal case. Graphene is biased with an effective drift current $\bar{v}_d = 0.8v_F\hat{x} + 0.8v_F\hat{y}$ ($|\bar{v}_d| \approx 1.13v_F$). (a) Excitation of surface waves (magnitude of the Poynting vector $\bar{S}$ in dB) by two $\hat{z}$-oriented dipoles separated by a distance $d = \lambda_0/200$ along the $\hat{y}$ axis and located at 15nm over the surface. (b)-(c) Response of the platform computed at a distance x_0=50 nm (gray observation line panel a) versus (b) separation distance d, keeping f=15 THz; and (c) frequency, keeping separation distance as d=50nm. Other parameters are as in Figure 3.3.

axes with a velocity slower than v_F and generate an electromagnetic response similar to the one created by an effectively superluminal motion of electrons drifting diagonally along the metasurface. Although an effectively superluminal regime has not yet been experimentally realized in graphene, I consider this regime as a futuristic possibility and explore its potential performance. Figure 3.7 shows the hyperlensing response of the platform when it is biased with an effective current $\bar{v}_d = 0.8v_F\hat{x} + 0.8v_F\hat{y}$ ($|\bar{v}_d| \approx 1.13v_F$). Results confirm the presence of extremely canalized surface plasmons as well as a subwavelength resolution $>\lambda_0/1800$ over a large bandwidth. It should be noted that these properties can be further tuned by applying a gate-bias, allowing a dynamic control of the hyperlens performance.

The intrinsic nonreciprocal response of drift-biased graphene can be exploited in this platform to put forward unidirectional hyperlenses. To this purpose, one can exploit spin-orbit interactions [18-21] and match the field polarization spin of dipolar sources or a field distribution image with the transverse spin of a subset of the modes supported by drift-bias graphene, thus enabling plasmon canalization toward a unique direction within the plane. This possibility is explored in Figure 3.8, which shows the excitation of surface waves by two closely located, circularly-polarized emitters. Results show that sources with an out-of-plane dipole moment spin rotating along the $\hat{x}$-axis ($\bar{p} = \hat{x} + i\hat{z}$) excite surface plasmons canalized along the $\hat{x}$-

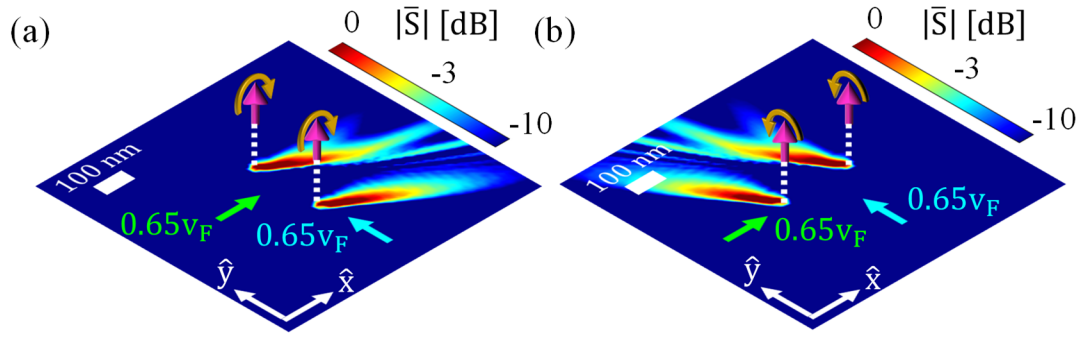

Figure 3.8: Unidirectional hyperlensing exploiting the photonic spin Hall effect. Normalized magnitude of the Poynting vector $\bar{S}$ (in dB) excited by two circularly polarized dipoles separated by a distance $d = \lambda_0/100$ and located at 15nm over the surface. Results are computed on the metasurface at 15THz when the emitters have a dipole moment with an out-of-plane polarization spin defined by (a) $\bar{p} = \hat{x} + i\hat{z}$, rotating along the $\hat{x}$-axis; and (b) $\bar{p} = \hat{y} + i\hat{z}$, along the $\hat{y}$-axis. Other parameters are as in Figure 3.3.

axis, whereas sources with a spin rotating along the $\hat{y}$-axis ($\bar{p} = \hat{y} + i\hat{z}$) excite plasmons canalized toward the orthogonal direction, $\hat{y}$. It should be stressed that the spin-locking does not deteriorate the overall performance of the hyperlensing platform, which maintains its response in terms of resolution and bandwidth.

3.4 CHAPTER CONCLUSIONS

In summary, I have put forward a platform to achieve broadband and unidirectional plasmon hyperlensing based on a graphene layer longitudinally biased with two orthogonal dc-voltages. This approach exploits the interplay between nonreciprocity and nonlocality to flatten the isofrequency contour of the supported modes and enable canalization of surface plasmons toward the direction defined by the applied biases. The proposed platform merges nonreciprocal and canalization responses over a simple structure, avoiding the presence of magnetic bias or the need of nanostructured surfaces, and exhibits a remarkable response in terms of resolution (up to $\sim\lambda_0/1000$) and broadband response (roughly from 10 to 25 THz, keeping a resolution larger than $\lambda_0/500$ in the entire range) while requiring realistic drift-bias. Besides, unidirectional canalization can be achieved using emitters or field images with an out-ot-plane polarization spin that rotates against the desired direction of propagation. The platform response is tunable with a gate bias which might lead to a dynamic control and steering of canalized plasmons. In terms of practical implementation, it should be stressed that recent experiments have demonstrated graphene embedded in hexagonal boron nitride supporting drift-currents with velocities very close to the Fermi velocity ($v_d \approx 0.95v_F$) at room temperature [6,7], a response enabled by the reduced carrier scattering with surface optical phonons in hexagonal boron nitride. I envision that the unidirectional hyperlensing may trigger exciting applications in sub-diffractive imaging, sensing, as well as in the excitation, routing, and processing of plasmons over a broad frequency range.

3.5 CHAPTER REFERENCES

[1] Correas-Serrano, D. and Gomez-Diaz, J.S., 2019. Nonreciprocal and collimated surface plasmons in drift-biased graphene metasurfaces. *Physical Review B*, 100(8), p.081410.

[2] Morgado, T.A. and Silveirinha, M.G., 2021. Active graphene plasmonics with a drift-current bias. *ACS Photonics*, 8(4), pp.1129-1136.

[3] Morgado, T.A. and Silveirinha, M.G., 2017. Negative Landau damping in bilayer graphene. *Physical Review Letters*, 119(13), p.133901.

[4] Dong, Y., Xiong, L., Phinney, I.Y., Sun, Z., Jing, R., McLeod, A.S., Zhang, S., Liu, S., Ruta, F.L., Gao, H. and Dong, Z., 2021. Fizeau drag in graphene plasmonics. *Nature*, 594(7864), pp.513-516.

[5] Zhao, W., Zhao, S., Li, H., Wang, S., Wang, S., Utama, M., Kahn, S., Jiang, Y., Xiao, X., Yoo, S. and Watanabe, K., 2021. Efficient Fizeau drag from Dirac electrons in monolayer graphene. *Nature*, 594(7864), pp.517-521.

[6] Dorgan, V.E., Behnam, A., Conley, H.J., Bolotin, K.I. and Pop, E., 2013. High-field electrical and thermal transport in suspended graphene. *Nano Letters*, 13(10), pp.4581-4586.

[7] Ramamoorthy, H., Somphonsane, R., Radice, J., He, G., Kwan, C.P. and Bird, J.P., 2016. "Freeing" graphene from its substrate: Observing intrinsic velocity saturation with rapid electrical pulsing. *Nano Letters*, 16(1), pp.399-403.

[8] Grigorenko, A.N., Polini, M. and Novoselov, K.S., 2012. Graphene plasmonics. *Nature Photonics*, *6*(11), pp.749-758.

[9] Garcia de Abajo, F.J., 2014. Graphene plasmonics: challenges and opportunities. *ACS Photonics*, 1(3), pp.135-152.

[10] Correas-Serrano, D., Gomez-Diaz, J.S., Tymchenko, M. and Alù, A., 2015. Nonlocal response of hyperbolic metasurfaces. *Optics Express*, 23(23), pp.29434-29448.

[11] Lovat, G., Hanson, G.W., Araneo, R. and Burghignoli, P., 2013. Semiclassical spatially dispersive intraband conductivity tensor and quantum capacitance of graphene. *Physical Review B*, 87(11), p.115429.

[12] Muruato, A.E., Fontes-Garfias, C.R., Ren, P., Garcia-Blanco, M.A., Menachery, V.D., Xie, X. and Shi, P.Y., 2020. A high-throughput neutralizing antibody assay for COVID-19 diagnosis and vaccine evaluation. *Nature Communications*, 11(1), pp.1-6.

[13] Mann, S.A., Sounas, D.L. and Alu, A., 2019. Nonreciprocal cavities and the time–bandwidth limit. *Optica*, 6(1), pp.104-110.

[14] Gangaraj, S.A.H. and Monticone, F., 2019. Do truly unidirectional surface plasmon-polaritons exist?. *Optica*, 6(9), pp.1158-1165.

[15] Correas-Serrano, D., Alù, A. and Gomez-Diaz, J.S., 2017. Plasmon canalization and tunneling over anisotropic metasurfaces. *Physical Review B*, 96(7), p.075436.

[16] Gomez-Diaz, J.S., Tymchenko, M. and Alù, A., 2015. Hyperbolic metasurfaces: surface plasmons, light-matter interactions, and physical implementation using graphene strips. *Optical Materials Express*, 5(10), pp.2313-2329.

[17] Dean, C.R., Young, A.F., Meric, I., Lee, C., Wang, L., Sorgenfrei, S., Watanabe, K., Taniguchi, T., Kim, P., Shepard, K.L. and Hone, J., 2010. Boron nitride substrates for high-quality graphene electronics. *Nature Nanotechnology*, 5(10), pp.722-726.

[18] Bliokh, K.Y., Rodríguez-Fortuño, F.J., Nori, F. and Zayats, A.V., 2015. Spin–orbit interactions of light. *Nature Photonics*, 9(12), pp.796-808.

[19] Cardano, F. and Marrucci, L., 2015. Spin–orbit photonics. *Nature Photonics*, 9(12), pp.776-778.

[20] Rodríguez-Fortuño, F.J., Marino, G., Ginzburg, P., O'Connor, D., Martínez, A., Wurtz, G.A. and Zayats, A.V., 2013. Near-field interference for the unidirectional excitation of electromagnetic guided modes. *Science*, 340(6130), pp.328-330.

[21] Bliokh, K.Y., Smirnova, D. and Nori, F., 2015. Quantum spin Hall effect of light. *Science*, 348(6242), pp.1448-1451.

Chapter 4: Theory of Optical Forces at Nanoscale

Light carries energy and momentum, and can exert actual forces on objects. The fundamental principle of these forces relies on the momentum conservation law that found significant importance in classical electrodynamics [1]. When light is scattered or absorbed by an object, the change of momentum via absorption or scattering is transferred to a mechanical motion of that object. The presence of these optical forces was first reported in the pioneering seminal work of Prof. Ashkin in 1970 [2] that led to the 2018 Nobel Prize in Physics "*for groundbreaking inventions in the field of laser physics*" [3].

The goal of this Chapter is to calculate optical forces induced on a spherical Rayleigh particle (radius $a < \lambda_0/20$ where λ_0 is the wavelength [1,4]) upon illumination of plane waves, and unveil and describe the underlying mechanisms that sustain such forces. First, I review the classical electrodynamics to derive the general expression of optical forces exerted on an arbitrary object following the momentum conservation law [1]. The net forces can be accurately computed using the Maxwell's stress tensor. In the small object or Rayleigh limit, Lorentz force model within dipole approximation can be directly applied to rigorously model such forces. Then, I derive a comprehensive theoretical framework to compute the resulting forces when the particle is located near reciprocal plasmonic metasurfaces. Later, I extend my analysis to model the forces when the surface is nonreciprocal in the presence of an external in-plane momentum bias. My theory is based on a semi-classical Green's function formalism that models and understands the electromagnetic interaction between the surface and an electric point dipole located above it, and neglects other potential sources of forces such as thermal or quantum fluctuations [5-7]. The proposed theory is general in the sense that it can be readily applied to any type of structures, including bulk or two-dimensional materials, provided by that the adequate Green's function of the system is available. Finally, I detail the full-wave simulation procedure to compute such optical forces using Maxwell's stress tensor method in COMSOL Multiphysics [8].

Throughout my theoretical development, I also derive analytical approximated expressions for lateral optical forces. To this purpose, I analytical solve scattered dyadic Green's function of the system based complex integration technique [9] combined with Residue theorem [10]. These analytical solution reveals that the dispersion relation of a plasmonic system suffices to determine lateral forces, shedding light into the underlying mechanisms that control these forces and facilitating the easy and accurate design of plasmonic platforms capable of manipulating nanoparticles.

4.1 FORMALISM OF OPTICAL FORCES

In this section, I review the Maxwell's stress tensor and dipole approximation models to compute optical forces on a quasi-stationary object (i.e., Doppler shift effects are negligible) assuming monochromatic light at optical frequency ω.

4.1.1 MAXWELL'S STRESS TENSOR

The conservation law of linear momentum is a direct consequence of the combination of Maxwell's equations and Lorentz force law. Together, they form the foundation of classical electromagnetics. On one hand, the Maxwell's equations in free space are expressed as [1]

$$\nabla \times \overline{\mathrm{E}} = -\mu_0 \frac{\mathrm{d}}{\mathrm{dt}} \overline{\mathrm{H}}, \tag{4.1a}$$

$$\nabla \times \overline{\mathrm{H}} = \varepsilon_0 \frac{\mathrm{d}}{\mathrm{dt}} \overline{\mathrm{E}} + \bar{\mathrm{J}}, \tag{4.1b}$$

$$\nabla \cdot \overline{\mathrm{E}} = \frac{1}{\varepsilon_0} \rho, \tag{4.1c}$$

$$\nabla \cdot \overline{\mathrm{H}} = 0, \tag{4.1d}$$

where $\overline{E}$ and $\overline{H}$ are the electric and magnetic fields of an electromagnetic wave, respectively; ε_0 and μ_0 are the permittivity and permeability of free space, respectively; and $\overline{J}$ and ρ are the electric current density (per unit area) and charge density (per unit volume). Lorentz force law reads as [1,11]

$$\overline{F} = \int_V (\rho\overline{E} + \mu_0\overline{J} \times \overline{H})dV, \tag{4.2}$$

where the electric charges are enclosed in a volume V. The Lorentz force law satisfies the charge conservation law [1]

$$\nabla \cdot \overline{J} + \frac{d}{dt}\rho = 0, \tag{4.3}$$

that is deduced from Maxwell's equations.

Let me perform a vector cross product of Eq. (4.1a) and (4.1b) with $\varepsilon_0\overline{E}$ and $\mu_0\overline{H}$, respectively. The superposition of these two terms yields to [1]

$$\varepsilon_0(\nabla \times \overline{E}) \times \overline{E} + \mu_0(\nabla \times \overline{H}) \times \overline{H} = \mu_0\overline{J} \times \overline{H} + \mu_0\varepsilon_0 \frac{d}{dt}(\overline{E} \times \overline{H}). \tag{4.4}$$

The two quantities in the left-hand side of Eq. (4.4) can be explicitly written as [1]

$$\varepsilon_0(\nabla \times \overline{E}) \times \overline{E} = \nabla \cdot \left[\varepsilon_0\overline{E} \otimes \overline{E} - \frac{\varepsilon_0}{2}|\overline{E}|^2\overline{\overline{I}}\right] - \rho\overline{E}, \tag{4.5a}$$

$$\mu_0(\nabla \times \overline{H}) \times \overline{H} = \nabla \cdot \left[-\mu_0\overline{H} \otimes \overline{H} - \frac{\mu_0}{2}|\overline{H}|^2\overline{\overline{I}}\right], \tag{4.5b}$$

where $\overline{E} \otimes \overline{E}$ and $\overline{H} \otimes \overline{H}$ are the vector dyadic products; $|\overline{E}|$ and $|\overline{H}|$ are the electric and magnetic field amplitudes, respectively; and $\overline{\overline{I}}$ is a diagonal unit tensor. These identities allow to reformulate Eq. (4.4) as

$$\nabla \cdot \left[\varepsilon_0 \bar{E} \otimes \bar{E} - \mu_0 \bar{H} \otimes \bar{H} - \frac{1}{2}(\varepsilon_0 |\bar{E}|^2 + \mu_0 |\bar{H}|^2)\bar{\bar{I}}\right] = \mu_0 \bar{J} \times \bar{H} + \mu_0 \varepsilon_0 \frac{d}{dt}(\bar{E} \times \bar{H}) + \rho \bar{E}. \quad (4.6)$$

The element in the left-hand side of Eq. (4.6) is the electromagnetic momentum density defined as the Maxwell's stress tensor in free space [1,11]

$$\bar{\bar{T}} = \nabla \cdot \left[\varepsilon_0 \bar{E} \otimes \bar{E} - \mu_0 \bar{H} \otimes \bar{H} - \frac{1}{2}(\varepsilon_0 |\bar{E}|^2 + \mu_0 |\bar{H}|^2)\bar{\bar{I}}\right]. \quad (4.7)$$

In case that the current and charge sources are embedded in an arbitrary medium, the Maxwell's stress tensor can be calculated following the similar procedure [Eqs. (4.1)-(4.7)] considering the electric permittivity and permeability of that medium.

Let me consider that all the sources (i.e., ρ and $\bar{J}$) are fully enclosed in the domain V. The volume integral of Eq. (4.6) leads to

$$\int_V \nabla \cdot \bar{\bar{T}} dV = \mu_0 \varepsilon_0 \int_V \frac{d}{dt}(\bar{E} \times \bar{H}) dV + \int_V \frac{d}{dt}(\rho \bar{E} + \mu_0 \bar{J} \times \bar{H}) dV. \quad (4.8)$$

This integral in Eq. (4.8) can be transformed into surface integral following the divergence theorem [1] as

$$\int_V \nabla \cdot \bar{\bar{T}} dV = \int_S \bar{\bar{T}} \cdot \hat{n}\, dS, \quad (4.9)$$

where S represents the surface of the domain V, dS is infinitesimal surface element, and $\hat{n}$ is the outward normal unit vector to it. Therefore, Eq. (4.8) can be reformulated as

$$\int_S \bar{\bar{T}} \cdot \hat{n}\, dS = \mu_0 \varepsilon_0 \int_V \frac{d}{dt}(\bar{E} \times \bar{H}) dV + \int_V \frac{d}{dt}(\rho \bar{E} + \mu_0 \bar{J} \times \bar{H}) dV. \quad (4.10)$$

Here, the first term in the right-hand side of Eq. (4.10) represents the electromagnetic momentum of the field within the volume V. Note that the time-averaged quantity (i.e., average over one oscillation period)

of this field momentum is strictly zero [1]. Therefore, the remaining component corresponds to the time-averaged mechanical force exerted on the object [see Eq. (4.2)].

Finally, the time-averaged optical forces read as

$$\langle \bar{F} \rangle = \frac{1}{2} \mathrm{Re}\left[\int_S \bar{\bar{T}} \cdot \hat{n} \, dS \right]. \tag{4.11}$$

Note that Eq. (4.11) can be applied to calculate optical forces on any arbitrary object enclosed by a surface S. The force entirely depends on the electromagnetic momentum density or Maxwell's stress tensor that is evaluated from the total electric and magnetic fields on the surface.

4.1.2 DIPOLE APPROXIMATION

An alternative approach to compute optical forces on a small particle with relative permittivity ε_p, within the Rayleigh limit, is the dipole approximation [1,11-13]. Here, the particle can be modelled as an electric point dipole with two oppositely charged atoms separated by a small distance $d \ll \lambda_0$. The optical forces exerted on the particle when it is located in free space can be computed as [1,11]

$$\bar{F} = (\bar{p} \cdot \nabla)\bar{E} + \mu_0 \frac{d}{dt} \bar{p} \times \bar{H}, \tag{4.12}$$

where $\bar{p} = \alpha_0 \cdot \bar{E}$ is the dipole moment; $\alpha_0 = \frac{\alpha'}{1 - i\frac{\alpha' k_0^3}{6\pi\varepsilon_0}}$ is the dynamic electrical polarizability of the particle with $\alpha' = 4\pi\varepsilon_0 a^3 \frac{\varepsilon_p - \varepsilon_0}{\varepsilon_p + 2\varepsilon_0}$ [1]; k_0 is free space wavenumber; and $\bar{E}$ and $\bar{H}$ are the electric and magnetic fields at the dipole position, respectively. Note that eq. (4.12) is completely general and can be applied to any dipolar spherical Rayleigh objects including metallic and dielectric particles whose response is not dominated by higher order multipoles. Eq. (4.12) shows that the forces are composed of two elements: the first one $(\bar{p} \cdot \nabla)\bar{E}$ appears from the inhomogeneous electric field, and the remaining one is the familiar Lorentz force. The later component can be reformulated as

$$\mu_0 \frac{d}{dt}\bar{p} \times \bar{H} = \bar{p} \times (\nabla \times \bar{E}) + \mu_0 \frac{d}{dt}(\bar{p} \times \bar{H}). \tag{4.13}$$

Therefore, Eq. (4.12) yields to

$$\bar{F} = (\bar{p} \cdot \nabla)\bar{E} + \bar{p} \times (\nabla \times \bar{E}) + \mu_0 \frac{d}{dt}(\bar{p} \times \bar{H}) = \bar{p} \cdot \nabla\bar{E} + \mu_0 \frac{d}{dt}(\bar{p} \times \bar{H}). \tag{4.14}$$

In Eq. (4.14), the time-averaged quantity of $\frac{d}{dt}(\bar{p} \times \bar{H}) = \frac{d}{dt}(\bar{\bar{\alpha}} \cdot \bar{E} \times \bar{H})$ is strictly zero.

Finally, the time-averaged optical forces acting on the particle read as [1,11-16]

$$\langle \bar{F} \rangle = \frac{1}{2} \mathrm{Re}\{\bar{p}^* \cdot \nabla \bar{E}\}. \tag{4.15}$$

In the following, I employ Eq. (4.15) to develop a theoretical framework to compute optical forces on a Rayleigh particle located near plasmonic surfaces.

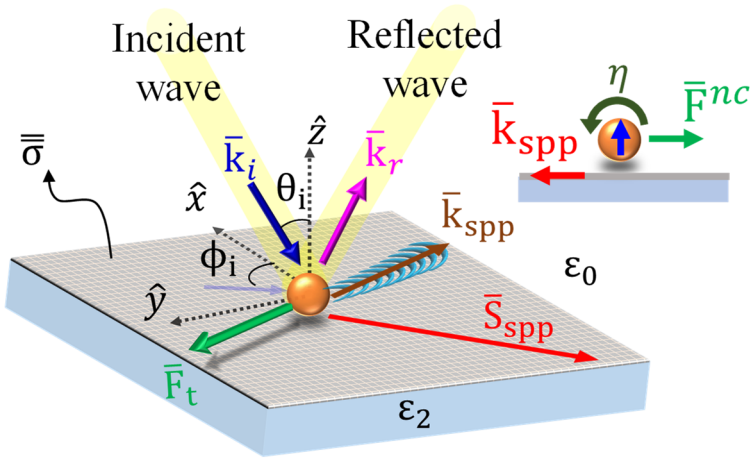

Figure 4.1: Schematic of the configuration. Lateral optical forces induced on an electrically polarizable Rayleigh particle (gold sphere) located in free space at a distance z_0 over an anisotropic metasurface characterized by a conductivity tensor $\bar{\bar{\sigma}}$. The metasurface is supported by a substrate of relative permittivity ε_2 and is illuminated by a plane wave. The scattered light excites directional surface plasmons — with wavevector $\bar{k}_{spp}$ and Poynting vector $\bar{S}_{spp}$— and exert a lateral optical force F_t on the particle. Inset shows the directions of dipole polarization spin η, excited surface plasmons and the induced nonconservative lateral recoil force $\bar{F}^{nc}$.

4.2 THEORETICAL FRAMEWORK: FORCES ABOVE RECIPROCAL SURFACES

Let me consider a non-magnetic, electrically polarizable, and dipolar Rayleigh particle of radius a located above a reciprocal metasurface characterized by a conductivity tensor $\overline{\overline{\sigma}}$ (see Figure 4.1), and is illuminated by light. The particle is suspended in free space, and the metasurface is supported by a substrate with relative permittivity ε_2. During the scattering process, the total electric field at the dipole position is computed as $\overline{\mathrm{E}} = \overline{\mathrm{E}}^0 + \overline{\mathrm{E}}^{\mathrm{s}}$. Here, $\overline{\mathrm{E}}^0 = \overline{\mathrm{E}}^{\mathrm{i}} + \overline{\mathrm{E}}^{\mathrm{r}}$ corresponds to the electric field of the standing wave formed above the metasurface due to the superposition of the incident electric field ($\overline{\mathrm{E}}^{\mathrm{i}}$) and the one reflected ($\overline{\mathrm{E}}^{\mathrm{r}}$) from the surface, and $\overline{\mathrm{E}}^{\mathrm{s}}$ is the field scatted by the particle that couples to the metasurface in the form of surface plasmons.

The total optical forces [see Eq. (4.15)] can be decomposed into conservative (i.e., $\overline{\mathrm{F}}^{\mathrm{c}}$) and nonconservative recoil (i.e., $\overline{\mathrm{F}}^{\mathrm{nc}}$) components. On one hand, nonconservative refers to the fact that part of the incoming energy is dissipated, absorbed, or scattered to originate mechanical motion on the object. On the other hand, conservative forces exhibit centrosymmetric behavior with examples including the radiation pressure or gradient forces. These components read as

$$\overline{\mathrm{F}}^{\mathrm{c}} = \frac{1}{2}\mathrm{Re}\{\bar{\mathrm{p}}^* \cdot \nabla \overline{\mathrm{E}}^0\}, \tag{4.16a}$$

$$\overline{\mathrm{F}}^{\mathrm{nc}} = \frac{1}{2}\mathrm{Re}\{\bar{\mathrm{p}}^* \cdot \nabla \overline{\mathrm{E}}^{\mathrm{s}}\}. \tag{4.16b}$$

The field scattered by the particle can be computed from the scattered dyadic Green's function $\overline{\overline{\mathrm{G}}}^{\mathrm{s}}$ of the system at the particle position as [1,12,13]

$$\overline{\mathrm{E}}^{\mathrm{s}} = \omega^2 \mu_0 \overline{\overline{\mathrm{G}}}^{\mathrm{s}} \cdot \bar{\mathrm{p}}. \tag{4.17}$$

In reciprocal systems, $\overline{\overline{\mathrm{G}}}^{s}$ is a purely diagonal tensor at the particle position [1,12,13,17], and Eq. (4.17) simplifies to

$$\bar{E}^s = \omega^2 \mu_0 \begin{bmatrix} G^s_{xx} p_x \\ G^s_{yy} p_y \\ G^s_{zz} p_z \end{bmatrix}. \tag{4.18}$$

It is important to stress that in the case when the incident light is a plane wave, the conservative force component $\bar{F}^c$ [see Eq. (4.16a)] leads to well-known radiation pressure pointing toward the direction of the wavefront (will be discussed in Chapter 5); whereas in the case of a structured light or focused laser beam such as Gaussian beams, this component leads to the gradient force that acts toward the maximum electric field intensity (will be discussed in Chapter 6), as in common optical tweezers [2,11,18]. On the other hand, the nonconservative recoil force [Eq. (4.16b)] depends on the properties of the surface plasmons excited on the metasurface during the scattering process. The plasmon properties are related to the fields scattered by the dipole that are expressed through the dyadic Green's function as shown in Eq. (4.18).

4.2.1 EFFECTIVE DIPOLE MOMENT

To compute the total optical forces, one needs to compute the electric dipole moment acquired by the particle [see Eq. (4.15)]. This dipole moment is computed from the local electric field at the particle position as [12,13,17]

$$\bar{p} = \alpha_0 \{\bar{E}^0 + \bar{E}^s\}, \tag{4.19}$$

Substituting the expression of scattered $\bar{E}^s$ in Eq. (4.19) yields the dipole moment components to

$$\begin{bmatrix} p_x \\ p_y \\ p_z \end{bmatrix} = \alpha_0 \begin{bmatrix} E^0_x + \omega^2 \mu_0 G^s_{xx} p_x \\ E^0_y + \omega^2 \mu_0 G^s_{yy} p_y \\ E^0_z + \omega^2 \mu_0 G^s_{zz} p_z \end{bmatrix}. \tag{4.20}$$

The solution of Eq. (4.20) leads to the compact form expressions of the dipole moment components as

$$p_x = \frac{\alpha_0}{1-\alpha_0\omega^2\mu_0 G^s_{xx}} E^0_x = \alpha_{xx} E^0_x, \tag{4.21a}$$

$$p_y = \frac{\alpha_0}{1-\alpha_0\omega^2\mu_0 G^s_{yy}} E^0_y = \alpha_{yy} E^0_y, \tag{4.21b}$$

$$p_z = \frac{\alpha_0}{1-\alpha_0\omega^2\mu_0 G^s_{zz}} E^0_z = \alpha_{zz} E^0_z. \tag{4.21c}$$

Following the identity $\bar{p} = \bar{\bar{\alpha}} \cdot \bar{E}^0$ [1,12,13], the effective polarizability tensor of the particle $\bar{\bar{\alpha}}$ reads

$$\bar{\bar{\alpha}} = \begin{bmatrix} \frac{\alpha_0}{1-\alpha_0\omega^2\mu_0 G^s_{xx}} & 0 & 0 \\ 0 & \frac{\alpha_0}{1-\alpha_0\omega^2\mu_0 G^s_{yy}} & 0 \\ 0 & 0 & \frac{\alpha_0}{1-\alpha_0\omega^2\mu_0 G^s_{zz}} \end{bmatrix}. \tag{4.22}$$

I recall that in the absence of the metasurface platform, the dipole polarizability is purely scalar and transfers to the dynamic polarizability α_0 of free-standing particle as detailed in section 4.1.

4.2.2 NONCONSERVATIVE RECOIL OPTICAL FORCE

The nonconservative recoil optical force [Eq. (4.16b)] components are

$$F^{nc}_x = \frac{1}{2}\mathrm{Re}\left\{\bar{p}^* \cdot \frac{d}{dx}\bar{E}^s\right\}, \tag{4.23a}$$

$$F^{nc}_y = \frac{1}{2}\mathrm{Re}\left\{\bar{p}^* \cdot \frac{d}{dy}\bar{E}^s\right\}, \tag{4.23b}$$

$$F^{nc}_z = \frac{1}{2}\mathrm{Re}\left\{\bar{p}^* \cdot \frac{d}{dz}\bar{E}^s\right\}, \tag{4.23c}$$

Let me first simplify the lateral components of the nonconservative forces. This requires computing the x and y-derivatives of the scattered fields [Eq. (4.17)] at the dipole position. Even though $\bar{\bar{G}}^s$ is a purely

diagonal tensor at the dipole position, the spatial derivatives of the off-diagonal components might not be zero. Therefore, it is important to consider the fully populated Green's function and calculate the associated derivatives as

$$\frac{\mathrm{d}}{\mathrm{dx}}\overline{\mathrm{E}}^{\mathrm{s}} = \omega^2\mu_0\begin{bmatrix} \mathrm{p_x}\frac{\mathrm{d}}{\mathrm{dx}}\mathrm{G}^{\mathrm{s}}_{\mathrm{xx}} + \mathrm{p_y}\frac{\mathrm{d}}{\mathrm{dx}}\mathrm{G}^{\mathrm{s}}_{\mathrm{xy}} + \mathrm{p_z}\frac{\mathrm{d}}{\mathrm{dx}}\mathrm{G}^{\mathrm{s}}_{\mathrm{xz}} \\ \mathrm{p_x}\frac{\mathrm{d}}{\mathrm{dx}}\mathrm{G}^{\mathrm{s}}_{\mathrm{yx}} + \mathrm{p_y}\frac{\mathrm{d}}{\mathrm{dx}}\mathrm{G}^{\mathrm{s}}_{\mathrm{yy}} + \mathrm{p_z}\frac{\mathrm{d}}{\mathrm{dx}}\mathrm{G}^{\mathrm{s}}_{\mathrm{yz}} \\ \mathrm{p_x}\frac{\mathrm{d}}{\mathrm{dx}}\mathrm{G}^{\mathrm{s}}_{\mathrm{zx}} + \mathrm{p_y}\frac{\mathrm{d}}{\mathrm{dx}}\mathrm{G}^{\mathrm{s}}_{\mathrm{zy}} + \mathrm{p_z}\frac{\mathrm{d}}{\mathrm{dx}}\mathrm{G}^{\mathrm{s}}_{\mathrm{zz}} \end{bmatrix}, \tag{4.24a}$$

$$\frac{\mathrm{d}}{\mathrm{dy}}\overline{\mathrm{E}}^{\mathrm{s}} = \omega^2\mu_0\begin{bmatrix} \mathrm{p_x}\frac{\mathrm{d}}{\mathrm{dy}}\mathrm{G}^{\mathrm{s}}_{\mathrm{xx}} + \mathrm{p_y}\frac{\mathrm{d}}{\mathrm{dy}}\mathrm{G}^{\mathrm{s}}_{\mathrm{xy}} + \mathrm{p_z}\frac{\mathrm{d}}{\mathrm{dy}}\mathrm{G}^{\mathrm{s}}_{\mathrm{xz}} \\ \mathrm{p_x}\frac{\mathrm{d}}{\mathrm{dy}}\mathrm{G}^{\mathrm{s}}_{\mathrm{yx}} + \mathrm{p_y}\frac{\mathrm{d}}{\mathrm{dy}}\mathrm{G}^{\mathrm{s}}_{\mathrm{yy}} + \mathrm{p_z}\frac{\mathrm{d}}{\mathrm{dy}}\mathrm{G}^{\mathrm{s}}_{\mathrm{yz}} \\ \mathrm{p_x}\frac{\mathrm{d}}{\mathrm{dy}}\mathrm{G}^{\mathrm{s}}_{\mathrm{zx}} + \mathrm{p_y}\frac{\mathrm{d}}{\mathrm{dy}}\mathrm{G}^{\mathrm{s}}_{\mathrm{zy}} + \mathrm{p_z}\frac{\mathrm{d}}{\mathrm{dy}}\mathrm{G}^{\mathrm{s}}_{\mathrm{zz}} \end{bmatrix}. \tag{4.24b}$$

In the case of a reciprocal system, exactly at the dipole position, it can be shown that $\frac{\mathrm{d}}{\mathrm{dx}}\mathrm{G}^{\mathrm{s}}_{\mathrm{xx}} = \frac{\mathrm{d}}{\mathrm{dx}}\mathrm{G}^{\mathrm{s}}_{\mathrm{xy}} = \frac{\mathrm{d}}{\mathrm{dx}}\mathrm{G}^{\mathrm{s}}_{\mathrm{yx}} = \frac{\mathrm{d}}{\mathrm{dx}}\mathrm{G}^{\mathrm{s}}_{\mathrm{yy}} = \frac{\mathrm{d}}{\mathrm{dx}}\mathrm{G}^{\mathrm{s}}_{\mathrm{yz}} = \frac{\mathrm{d}}{\mathrm{dx}}\mathrm{G}^{\mathrm{s}}_{\mathrm{zy}} = \frac{\mathrm{d}}{\mathrm{dx}}\mathrm{G}^{\mathrm{s}}_{\mathrm{zz}} = \frac{\mathrm{d}}{\mathrm{dy}}\mathrm{G}^{\mathrm{s}}_{\mathrm{xx}} = \frac{\mathrm{d}}{\mathrm{dy}}\mathrm{G}^{\mathrm{s}}_{\mathrm{xy}} = \frac{\mathrm{d}}{\mathrm{dy}}\mathrm{G}^{\mathrm{s}}_{\mathrm{xz}} = \frac{\mathrm{d}}{\mathrm{dy}}\mathrm{G}^{\mathrm{s}}_{\mathrm{yx}} = \frac{\mathrm{d}}{\mathrm{dy}}\mathrm{G}^{\mathrm{s}}_{\mathrm{yy}} = \frac{\mathrm{d}}{\mathrm{dy}}\mathrm{G}^{\mathrm{s}}_{\mathrm{zx}} = \frac{\mathrm{d}}{\mathrm{dy}}\mathrm{G}^{\mathrm{s}}_{\mathrm{zz}} = 0$ [12,13,17]. These identities hold independently to the metasurface topologies for any reciprocal system, and allow to simplify Eq. (4.24) to

$$\frac{\mathrm{d}}{\mathrm{dx}}\overline{\mathrm{E}}^{\mathrm{s}} = \omega^2\mu_0\begin{bmatrix} \mathrm{p_z}\frac{\mathrm{d}}{\mathrm{dx}}\mathrm{G}^{\mathrm{s}}_{\mathrm{xz}} \\ 0 \\ \mathrm{p_x}\frac{\mathrm{d}}{\mathrm{dx}}\mathrm{G}^{\mathrm{s}}_{\mathrm{zx}} \end{bmatrix}, \tag{4.25a}$$

$$\frac{\mathrm{d}}{\mathrm{dy}}\overline{\mathrm{E}}^{\mathrm{s}} = \omega^2\mu_0\begin{bmatrix} 0 \\ \mathrm{p_z}\frac{\mathrm{d}}{\mathrm{dy}}\mathrm{G}^{\mathrm{s}}_{\mathrm{yz}} \\ \mathrm{p_y}\frac{\mathrm{d}}{\mathrm{dy}}\mathrm{G}^{\mathrm{s}}_{\mathrm{zy}} \end{bmatrix}, \tag{4.25b}$$

which permits to express the nonconservative lateral recoil forces as

$$F_x^{nc} = \frac{\omega^2\mu_0}{2}\mathrm{Re}\left\{p_x^* p_z \frac{d}{dx}G_{xz}^s + p_z^* p_x \frac{d}{dx}G_{zx}^s\right\}, \tag{4.26a}$$

$$F_y^{nc} = \frac{\omega^2\mu_0}{2}\mathrm{Re}\left\{p_y^* p_z \frac{d}{dy}G_{yz}^s + p_z^* p_y \frac{d}{dy}G_{zy}^s\right\}. \tag{4.26b}$$

Moreover, exactly at the dipole position, it can be shown that $\frac{d}{dx}G_{xz}^s = -\frac{d}{dx}G_{zx}^s$ and $\frac{d}{dy}G_{yz}^s = -\frac{d}{dy}G_{zy}^s$ [12,13,17]. This allows to reformulate the lateral recoil forces as

$$F_x^{nc} = \frac{\omega^2\mu_0}{2}\mathrm{Re}\left\{(p_x^* p_z - p_z^* p_x)\frac{d}{dx}G_{xz}^s\right\}, \tag{4.27a}$$

$$F_y^{nc} = \frac{\omega^2\mu_0}{2}\mathrm{Re}\left\{(p_y^* p_z - p_z^* p_y)\frac{d}{dy}G_{yz}^s\right\}. \tag{4.27b}$$

Applying the identities $p_x^* p_z - p_z^* p_x = 2i\mathrm{Im}\{p_x^* p_z\}$ and $p_y^* p_z - p_z^* p_y = 2i\mathrm{Im}\{p_y^* p_z\}$ to Eq. (4.27) where 'Im' is the imaginary part of a complex number, I obtain

$$F_x^{nc} = -\frac{k_0^2}{\varepsilon_0}\mathrm{Im}[p_x^* p_z]\mathrm{Im}\left[\frac{d}{dx}G_{xz}^s\right], \tag{4.28a}$$

$$F_y^{nc} = -\frac{k_0^2}{\varepsilon_0}\mathrm{Im}[p_y^* p_z]\mathrm{Im}\left[\frac{d}{dy}G_{yz}^s\right]. \tag{4.28b}$$

Now, the total power radiated by the dipole – which is a measure of the dipole amplitude – in free space reads as [1,12]

$$P_{rad} = \frac{c_0 k_0^4}{12\pi\varepsilon_0}|\bar{p}|^2 = \frac{c_0 k_0^4}{12\pi\varepsilon_0}\left(|p_x|^2 + |p_y|^2 + |p_z|^2\right). \tag{4.29}$$

The amount of power radiated by the xz and yz-components of the dipole yield [12]

$$P_{rad}^{xz} = \frac{c_0 k_0^4}{12\pi\varepsilon_0}(|p_x|^2 + |p_z|^2), \tag{4.30a}$$

$$P_{rad}^{yz} = \frac{c_0 k_0^4}{12\pi\varepsilon_0}\left(|p_y|^2 + |p_z|^2\right). \tag{4.30b}$$

This power allows to reformulate the lateral recoil forces as

$$F_x^{nc} = -\frac{12\pi}{c_0 k_0^2} P_{rad}^{xz} \frac{\mathrm{Im}[p_x^* p_z]}{|p_x|^2+|p_z|^2} \mathrm{Im}\left[\frac{d}{dx} G_{xz}^s\right], \tag{4.31a}$$

$$F_y^{nc} = -\frac{12\pi}{c_0 k_0^2} P_{rad}^{yz} \frac{\mathrm{Im}[p_y^* p_z]}{|p_y|^2+|p_z|^2} \mathrm{Im}\left[\frac{d}{dy} G_{yz}^s\right]. \tag{4.31b}$$

Moreover, the particle polarization spin or helicity around the lateral axis (i.e., x and y) can be defined as [12,13]

$$\eta_y = -2\frac{\mathrm{Im}[p_x^* p_z]}{|p_x|^2+|p_z|^2} = \frac{|p_{\sigma+}^y|^2 - |p_{\sigma-}^y|^2}{|p_{\sigma+}^y|^2 + |p_{\sigma-}^y|^2}, \tag{4.32a}$$

$$\eta_x = -2\frac{\mathrm{Im}[p_y^* p_z]}{|p_y|^2+|p_z|^2} = \frac{|p_{\sigma+}^x|^2 - |p_{\sigma-}^x|^2}{|p_{\sigma+}^x|^2 + |p_{\sigma-}^x|^2}. \tag{4.32b}$$

These quantities are equal to zero in case of linearly polarized dipoles, and to ± 1 for circularly polarized rotating dipoles (with respect to the lateral axis) in opposite directions [12].

Finally, the nonconservative lateral recoil forces are

$$F_x^{nc} = \frac{6\pi}{c_0 k_0^2} P_{rad}^{xz} \eta_y \mathrm{Im}\left[\frac{d}{dx} G_{xz}^s\right], \tag{4.33a}$$

$$F_y^s = \frac{6\pi}{c_0 k_0^2} P_{rad}^{yz} \eta_x \mathrm{Im}\left[\frac{d}{dy} G_{yz}^s\right]. \tag{4.33b}$$

Eq. (4.33) shows that the origin of the nonconservative lateral recoil forces above reciprocal surfaces is the dipole polarization spin or helicity (see inset in Figure 4.1). For instance, a quasi-circularly polarized dipole excites directionally propagating surface plasmons on the metasurface thanks to the photonic spin-Hall effect [19-22]. To compensate for the momentum surge, the particle experiences lateral recoil forces acting in the opposite of plasmon propagation direction. The strength of such forces depends on the imaginary part of the off-diagonal components of the Green's function which is directly proportional to the fourth power of the plasmon wavenumber supported by the metasurface as will be discussed soon. Intuitively, this implies that with an adequately designed plasmonic structure that supports surface modes with very large wavenumber, the strength of the lateral recoil forces can be significantly enhanced (will be discussed further in Chapter 5 and 6). Note that the lateral recoil forces completely vanish for linearly polarized particles (i.e., $\eta_x \to 0$, $\eta_y \to 0$). This is because the lack of spin in the scattered field by the dipole cannot excited direction surface plasmons, rather plasmons are symmetrically excited within the surface and the momentum imbalance completely vanishes.

Now, it is instructive to simplify the vertical component of the nonconservative forces following Eq. (4.23c). Here, the z-derivatives of the off-diagonal Green's function tensor components are strictly zero at the dipole position, i.e., $\frac{d}{dz}G^s_{xy} = \frac{d}{dz}G^s_{xz} = \frac{d}{dz}G^s_{yx} = \frac{d}{dz}G^s_{yz} = \frac{d}{dz}G^s_{zx} = \frac{d}{dz}G^s_{zy} = 0$ [12]. These identities allow to reformulate the vertical recoil force component as

$$F^s_z = \frac{\omega^2\mu_0}{2}\sum_{n=x,y,z}|p_n|^2 \mathrm{Re}\left\{\frac{d}{dz}G^s_{nn}\right\}. \tag{4.34}$$

Taking into account the power radiated by the dipole [see (Eq. 4.29)], Eq. (4.34) can be simplified to

$$F^s_z = \frac{6\pi}{c_0 k_0^2}\sum_{n=x,y,z} P^n_{rad}\mathrm{Re}\left\{\frac{d}{dz}G^s_{nn}\right\}. \tag{4.35}$$

Note that the expressions of the lateral and vertical nonconservative recoil forces, shown in Eqs. (4.31) and (4.35), are general and hold for any linear and reciprocal metasurfaces. These formalisms can also be

readily applied to compute optical forces on nanoparticles located above bulk materials [12,17]. In that case, one needs to accurately model the scattered dyadic Green's function of the system considering the electric permittivity tensor of the material as done in ref-[12,17]. In Chapter 5 and 6, I will employ these formalisms to investigate giant lateral optical forces and stable optical trapping of nanoparticles located near anisotropic and hyperbolic metasurfaces.

4.2.3 CONSERVATIVE OPTICAL FORCE

The conservative optical force exerted on the particle depends on the electric field gradient of the standing wave formed above the metasurface as shown in Eq. (4.16a). These components read

$$F_x^c = \frac{1}{2}\,\mathrm{Re}\left\{\bar{p}^* \cdot \frac{d}{dx}\bar{E}^0\right\}, \tag{4.36a}$$

$$F_y^c = \frac{1}{2}\,\mathrm{Re}\left\{\bar{p}^* \cdot \frac{d}{dy}\bar{E}^0\right\}, \tag{4.36b}$$

$$F_z^c = \frac{1}{2}\,\mathrm{Re}\left\{\bar{p}^* \cdot \frac{d}{dz}\bar{E}^0\right\}. \tag{4.36c}$$

Let me first simplify the lateral components. To this purpose, I perform the x and y-derivatives of the electric field of the standing wave as follows:

$$\frac{d}{dx}\bar{E}^0 = ik_x\bar{E}^0, \qquad \text{and} \qquad \frac{d}{dy}\bar{E}^0 = ik_y\bar{E}^0. \tag{4.37}$$

Now, the dot products inside the real parts of the expressions in Eq. (4.36a-b) yield to

$$\bar{p}^* \cdot \frac{d}{dx}\bar{E}^0 = ik_x \sum_{n=x,y,z} \bar{p}_n^* E_n^0 = ik_x \sum_{n=x,y,z} \alpha_{nn}^* |E_n^0|^2, \tag{4.38a}$$

$$\bar{p}^{*} \cdot \frac{d}{dy}\bar{E}^{0} = ik_{y}\sum_{n=x,y,z}\bar{p}_{n}^{*}E_{n}^{0} = ik_{y}\sum_{n=x,y,z}\alpha_{nn}^{*}|E_{n}^{0}|^{2}. \tag{4.38b}$$

The real parts of these quantities are expressed as

$$\mathrm{Re}\left\{\bar{p}^{*} \cdot \frac{d}{dx}\bar{E}^{0}\right\} = k_{x}\sum_{n=x,y,z}\mathrm{Im}\{\alpha_{nn}\}|E_{n}^{0}|^{2}, \tag{4.39a}$$

$$\mathrm{Re}\left\{\bar{p}^{*} \cdot \frac{d}{dy}\bar{E}^{0}\right\} = k_{y}\sum_{n=x,y,z}\mathrm{Im}\{\alpha_{nn}\}|E_{n}^{0}|^{2}, \tag{4.39b}$$

These identities reformulate the lateral conservative force components as

$$F_{x}^{c} = \frac{1}{2}\,k_{x}\sum_{n=x,y,z}\mathrm{Im}\{\alpha_{nn}\}|E_{n}^{0}|^{2}, \tag{4.40a}$$

$$F_{y}^{c} = \frac{1}{2}\,k_{y}\sum_{n=x,y,z}\mathrm{Im}\{\alpha_{nn}\}|E_{n}^{0}|^{2}. \tag{4.40b}$$

Eq. (4.40) confirms that the conservative lateral forces are completely determined by the properties of the standing wave formed above the surface.

Now, the vertical conservative force component is calculated using the z-derivative of the electric field of the standing wave as

$$\frac{d}{dz}\bar{E}^{0} = -ik_{z}\bar{E}^{i} + ik_{z}\bar{E}^{r} = ik_{z}\left[\bar{E}^{r} - \bar{E}^{i}\right]. \tag{4.41}$$

Note that this derivative is not similar to the ones with respect to the lateral direction [see Eq. (4.37)]. This is because the incident and reflected electric fields propagate in opposite directions, and the k_{z} is negative and positive in the former and later cases, respectively (see Figure 4.1). Finally, the conservative vertical force reads as

$$F_z^c = \frac{1}{2}\mathrm{Re}\{ik_z \sum_{n=x,y,z} p_n^* \cdot \{\bar{E}_n^r - \bar{E}_n^i\}\}. \tag{4.42}$$

I stress that this force can be negative or positive depending on the interplay between the incident and the reflected fields. Therefore, the conservative vertical force may attract or repel the particle toward or away from the metasurface as will be discussed in Chapter 6.

4.2.4 ANALYTICAL MODEL OF NONCONSERVATIVE LATERAL FORCES

The lateral components of the nonconservative optical forces depend on the imaginary parts of the spatial derivatives of the Green's functions off-diagonal components, i.e., $\mathrm{Im}\left[\frac{d}{dx}G_{xz}^s\right]$ and $\mathrm{Im}\left[\frac{d}{dx}G_{xz}^s\right]$ at the particle position [see Eq. (4.33)]. To develop an analytical formalism of these forces, it is required to get an analytical or compact form expressions of the associated derivatives as will be discussed now.

Let me begin the analytical treatment by transforming the scattered dyadic Green's function (see Chapter 2) into polar coordinates (k'_ρ, k'_ϕ) using the identities $k_x = k'_\rho \cos k'_\phi$ and $k_y = k'_\rho \sin k'_\phi$, thus yielding

$$\bar{\bar{G}}^s = \int_0^{2\pi} \bar{\bar{N}}(k'_\phi) dk'_\phi, \tag{4.43a}$$

$$\bar{\bar{N}}(k'_\phi) = \int_0^{\infty} \frac{\bar{\bar{X}}_s(k'_\rho, k'_\phi)}{M(k'_\rho, k'_\phi) D(k'_\rho, k'_\phi)} e^{i2k'_z z_0} dk'_\rho, \tag{4.43b}$$

where $\bar{k}' = k'_\rho \hat{\rho} + k'_\phi \hat{\phi} + k'_z \hat{z}$ is the wavevector in polar coordinates; $\bar{\bar{X}}_s(k'_\rho, k'_\phi)$ is a tensor that includes the reflection and cross-coupling of propagative and evanescent waves; $D(k'_\rho, k'_\phi)$ represents the dispersion relation of the system and determines the response of the supported surface plasmons; and $M(k'_\rho, k'_\phi)$ is associated to the medium surrounding the structure. In reciprocal systems, Eq. (4.43) exhibits a symmetrical behavior in both physical and momentum spaces. Eq. (4.43) and associated spatial derivatives are usually

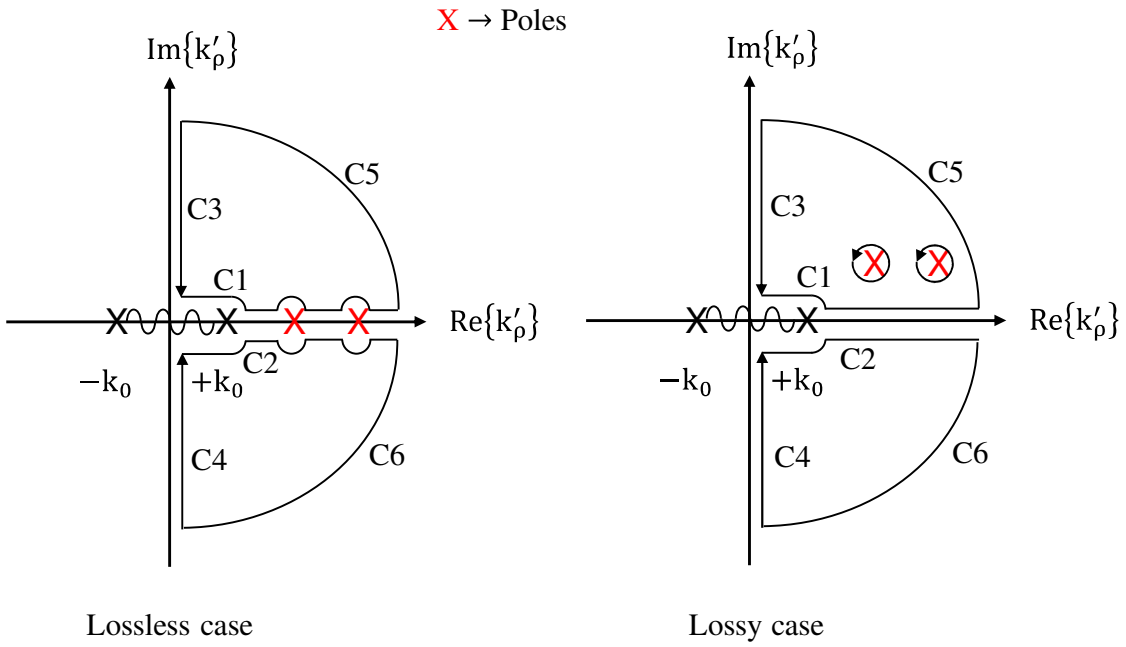

Figure 4.2: Integration path in the complex plane for lossless and lossy platforms using the integration along the imaginary axis technique. Poles are represented with a red X.

solved through numerical techniques involving integration in the complex plane that are time-consuming and conceal the mechanisms governing recoil optical forces

To derive analytical solutions of the Green's function, I first consider the integral along k'_ρ shown in Eq. (4.43b) using the imaginary axis integration technique [23]. There, the real-axis integration path is deformed into the complex plane using an elliptical path to avoid the branch cut or surface wave poles and adequately capture their response. Figure 4.2 shows this integration strategy in the complex plane for a fixed k'_ϕ. Here, integration paths C1 and C2 capture the pole response along the real axis of k'_ρ, C3 and C4 computes the integration along the imaginary axis of k'_ρ, C5 and C6 are used to enclose the integration contour. First, I stress that the Jordan's lemma is satisfied [24] and therefore the integral around paths C5 and C6 when $k'_\rho \to \infty$ are strictly zero. Second, it can be shown [23] that the integrals around paths C1 and C2 are identical but with opposite sign, thus cancelling each other. Third, the dynamic part of the Green's function tensor is solely determined by the surface modes supported by the platform [23] that appear in the

form of poles in Figure 4.2 (red X). Assuming a lossless platform, the pole response is a real quantity that can be obtained analytically through the residue theorem [24]. These poles will control the response of lateral recoil forces in the platform. And forth, the integral around the path C3 and C4 leads to a non-zero purely imaginary quantity associated to the quasi-static response of the Green's function. Even though this integral is not analytical along the imaginary axis of k'_ρ, it is well-behaved and can be quickly integrated using numerical routines [25]. It should also be noted the integration contour has been deformed to avoid the brunch-cut from $-k_0$ to $+k_0$.

Let me consider that k_ρ is the wavenumber of the surface mode supported by the metasurface for a specific azimuthal direction k'_ϕ. This wavenumber can easily be calculated by solving the dispersion relation of the system (see Chapter 2). The residues of the associated derivatives in Eq. (4.33) at k_ρ can be computed as

$$N_{\frac{d}{dx}G^s_{xz}}\left(k'_\phi\right) = -\frac{\eta_0\sigma_{xx}k_\rho^2\left(k_0^2-k_\rho^2\right)^{3/2}\left(2\sqrt{k_0^2-k_\rho^2}+\eta_0\sigma_{xx}k_0\right)}{32\varepsilon_r\pi k_0^2\left\{4\eta_0\sigma_{xx}k_0^2-3\eta_0\sigma_{xx}k_\rho^2+k_0\sqrt{k_0^2-k_\rho^2}\left(4+\eta_0^2\sigma_{xx}^2\right)\right\}}e^{-2z_0\sqrt{k_\rho^2-k_0^2}}, \tag{4.44a}$$

$$N_{\frac{d}{dy}G^s_{yz}}\left(k'_\phi\right) = -\frac{\eta_0\sigma_{yy}k_\rho^2\left(k_0^2-k_\rho^2\right)^{3/2}\left(2\sqrt{k_0^2-k_\rho^2}+\eta_0\sigma_{yy}k_0\right)}{32\varepsilon_r\pi k_0^2\left\{4\eta_0\sigma_{yy}k_0^2-3\eta_0\sigma_{yy}k_\rho^2+k_0\sqrt{k_0^2-k_\rho^2}\left(4+\eta_0^2\sigma_{yy}^2\right)\right\}}e^{-2z_0\sqrt{k_\rho^2-k_0^2}}. \tag{4.44b}$$

Here, η_0 is the free space impedance, and ε_r is the average relative permittivity of the media above and below the metasurface. Even though Eq. (4.44) is analytical, these expressions are lengthy and difficult to work with. To further simplify them and gain physical insight into the problem, I consider that the platform operates in the non-retarded regime assuming that $k_\rho \gg k_0$ [1,12,13]. This permits to directly link the conductivity along x and y directions with the wavenumber of the modes supported therein as $\sigma_{xx} \approx i\omega\varepsilon_0\frac{2}{k_x}$ and $\sigma_{yy} \approx i\omega\varepsilon_0\frac{2}{k_y}$ [1], where k_x and k_y are the wavenumber of the supported surface plasmons along x and y-directions of the reference coordinate system. As a result, Eq. (4.44) is greatly simplified to

$$N_{\frac{d}{dx}G_{xz}^{s}}\left(k_{\phi}'\right) = -i\frac{1}{8\varepsilon_r\pi^2k_0^2}k_x^4e^{-2z_0\sqrt{k_x^2-k_0^2}}, \tag{4.45a}$$

$$N_{\frac{d}{dy}G_{yz}^{s}}\left(k_{\phi}'\right) = -i\frac{1}{8\varepsilon_r\pi^2k_0^2}k_y^4e^{-2z_0\sqrt{k_y^2-k_0^2}}, \tag{4.45b}$$

Next, the spatial derivatives of the Green's functions required in Eq. (4.33) to calculate lateral recoil forces can be computed at the particle position by performing the following integrals along k_{ϕ}':

$$\mathrm{Im}\left\{\frac{d}{dx}G_{xz}^{s}\right\} = \int_0^{2\pi}\frac{1}{8\varepsilon_r\pi k_0^2}k_x^4e^{-2z_0\sqrt{k_x^2-k_0^2}}dk_{\phi}', \tag{4.46a}$$

$$\mathrm{Im}\left\{\frac{d}{dy}G_{yz}^{s}\right\} = \int_0^{2\pi}\frac{1}{8\varepsilon_r\pi k_0^2}k_y^4e^{-2z_0\sqrt{k_y^2-k_0^2}}dk_{\phi}'. \tag{4.46b}$$

These equations can be readily applied to compute lateral recoil forces above any anisotropic metasurfaces.

Now, for the sake of simplicity, I assume that the metasurface is isotropic in nature (i.e., $\sigma_{xx} = \sigma_{yy}$) and supports surface plasmons with identical wavenumber within any directions k_{ϕ}' of the metasurface. This allows to solve the integration in Eq. (4.46) by simply multiplying the integrand with a factor of 2π [1]. This leads to

$$\mathrm{Im}\left\{\frac{d}{dx}G_{xz}^{s}\right\} = \frac{1}{8\varepsilon_rk_0^2}\left[k_x^4e^{-2z_0\sqrt{k_x^2-k_0^2}}\right], \tag{4.47a}$$

$$\mathrm{Im}\left\{\frac{d}{dy}G_{yz}^{s}\right\} = \frac{1}{8\varepsilon_rk_0^2}\left[k_y^4e^{-2z_0\sqrt{(k_y^-)^2-k_0^2}}\right]. \tag{4.47b}$$

Finally, the analytical expression of nonconservative lateral forces are

$$F_x^{nc} \approx \frac{3\pi P_{rad}^{xz}\eta_y}{4c_0\varepsilon_r}\left(\frac{k_x}{k_0}\right)^4 e^{-2z_0\sqrt{k_x^2-k_0^2}}, \tag{4.48a}$$

$$F_y^{nc} \approx \frac{3\pi P_{rad}^{yz}\eta_x}{4c_0\varepsilon_r}\left[\left(\frac{k_y}{k_0}\right)^4 e^{-2z_0\sqrt{k_y^2-k_0^2}}\right]. \tag{4.48b}$$

Eq. (4.48) confirms that the strength of nonconservative lateral optical forces is directly proportional to the fourth power of the wavenumber of the surface plasmons supported by the metasurface, whereas the direction is solely determined the dipole helicity as mentioned before.

Note that ref-[12] also develops a similar analytical expressions of the nonconservative recoil forces, but considering isotropic plasmonic metasurfaces. This approach relies on the image dipole theory and the quasi-static approximation that holds very well when the dipole is located in the surface near field.

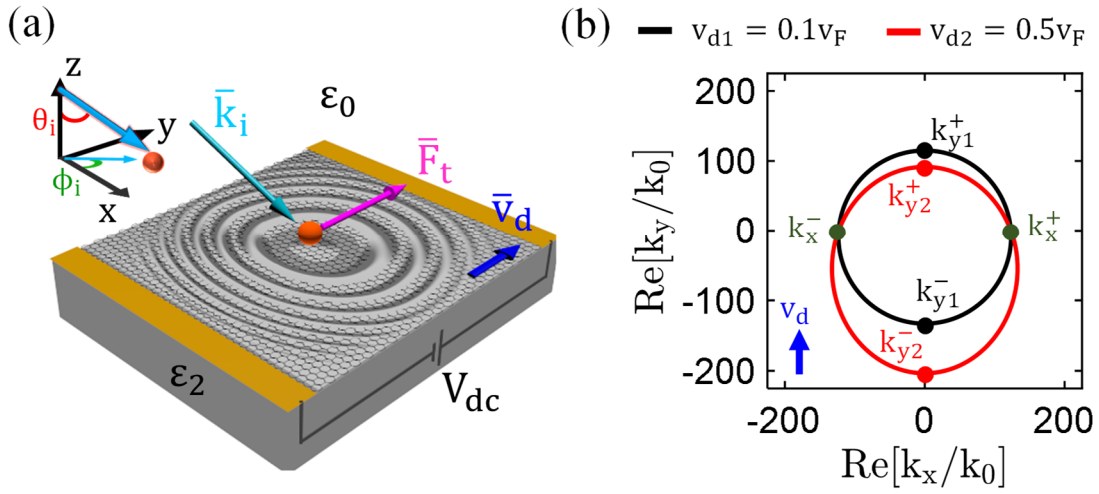

Figure 4.3: Manipulating lateral recoil optical forces using nonreciprocal plasmonic states. (a) Schematic of the configuration. Lateral optical forces (magenta) are exerted on a Rayleigh particle (orange) located over a drift-biased graphene transferred over hexagonal boron nitride upon illumination with a plane wave (cyan). (b) IFC of the states supported by graphene at $\lambda_0 = 14\ \mu m$ for two velocities of drifting electrons. k_y^+ and k_y^- denote the supported states along and against the applied drift. Graphene's Fermi velocity is $v_F = 10^6\ m/s$, and graphene's chemical potential and relaxation time are set to $\mu_c = 0.1eV$ and $\tau = 0.3$ ps, respectively.

However, my approach based on the residue theorem is general and Eq. (4.48) holds very well away from the near field as will be shown in Chapter 7.

4.3 THEORETICAL FRAMEWORK: FORCES ABOVE NONRECIPROCAL SURFACES

In this section, I extend the theoretical framework developed in section 4.2 to the case when an external in-plane momentum bias is applied to the metasurface (see Figure 4.3a). This bias breaks the symmetry of the surface mode thus resulting in a nonreciprocal response as shown in Figure 4.3(b). It can be obtained in practice by applying a parallel magnetic bias [36,37] or drift-current bias [38-44]. The applied bias breaks the amplitude symmetry of the surface modes along the bias axis; whereas the polarization symmetry is broken in the orthogonal lateral axis (see Chapter 3). Note that the broken symmetry modifies the Green's function in such a way that its components and associated spatial derivatives might not be strictly zero at the dipole position as found in the reciprocal case. This is confirmed in Figures 4.4-4.7 that show the spatial distribution of the scattered dyadic Green's function in the case of nonreciprocal metasurfaces and compare the response with the reciprocal one.

Throughout this derivation, I consider that the external bias is applied along $\hat{y}$-axis of the reference coordinate system aiming to simplify the mathematical analysis. In the case when the bias is applied along any other direction within the plane, the resulting response can be captured by applying an adequate coordinate rotation.

Let me begin with the scattered electric field $\overline{\mathrm{E}}^{\mathrm{s}} = \omega^2\mu_0\overline{\overline{\mathrm{G}}}^{\mathrm{s}} \cdot \bar{\mathrm{p}}$ [1]. Exactly at the dipole position, the Green's function is not diagonal anymore due to the broken system symmetry that introduces non-zero off-diagonal terms (i.e., $\mathrm{G}^{\mathrm{s}}_{\mathrm{yz}}$ and $\mathrm{G}^{\mathrm{s}}_{\mathrm{zy}}$). Therefore, the scattered field at the dipole position modifies to

$$\overline{\mathrm{E}}^{\mathrm{s}} = \omega^2\mu_0 \begin{bmatrix} \mathrm{G}^{\mathrm{s}}_{\mathrm{xx}}\mathrm{p}_{\mathrm{x}} \\ \mathrm{G}^{\mathrm{s}}_{\mathrm{yy}}\mathrm{p}_{\mathrm{y}} + \mathrm{G}^{\mathrm{s}}_{\mathrm{yz}}\mathrm{p}_{\mathrm{z}} \\ \mathrm{G}^{\mathrm{s}}_{\mathrm{zy}}\mathrm{p}_{\mathrm{y}} + \mathrm{G}^{\mathrm{s}}_{\mathrm{zz}}\mathrm{p}_{\mathrm{z}} \end{bmatrix}. \tag{4.49}$$

The appearance of these off-diagonal components (see Figures 4.4-4.7) modifies the dipole moment acquired by the particle and the optical forces as will be discussed below.

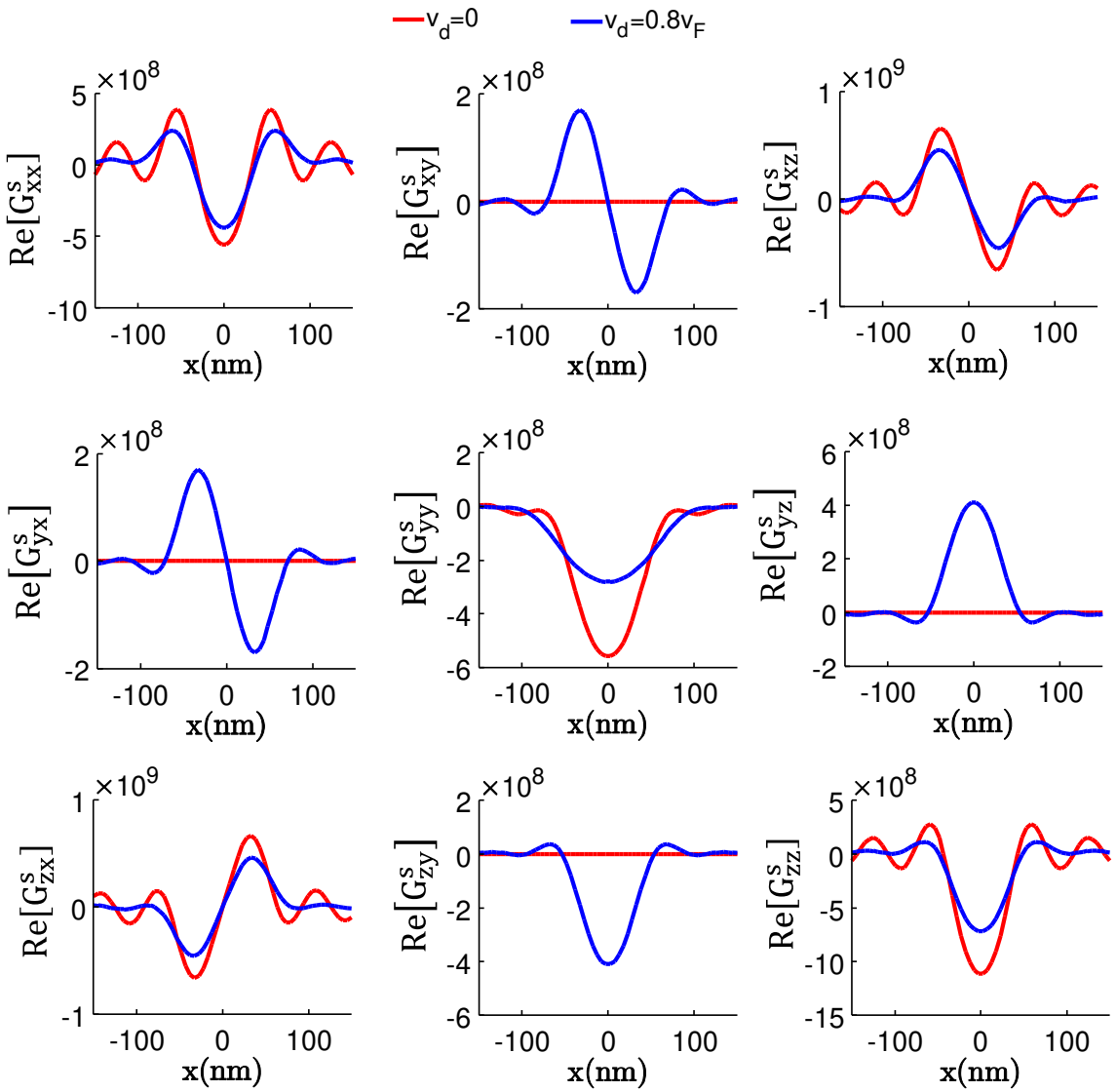

Figure 4.4: Real parts of the scattered dyadic Green's function tensor components of a reciprocal (red) and nonreciprocal (blue) graphene based metasurface. Responses are computed in the orthogonal lateral direction of the applied bias considering the dipole is located at $\bar{r} = \{x, 0, 30\ \text{nm}\}$ above the surface. Other parameters are as in Figure 4.3.

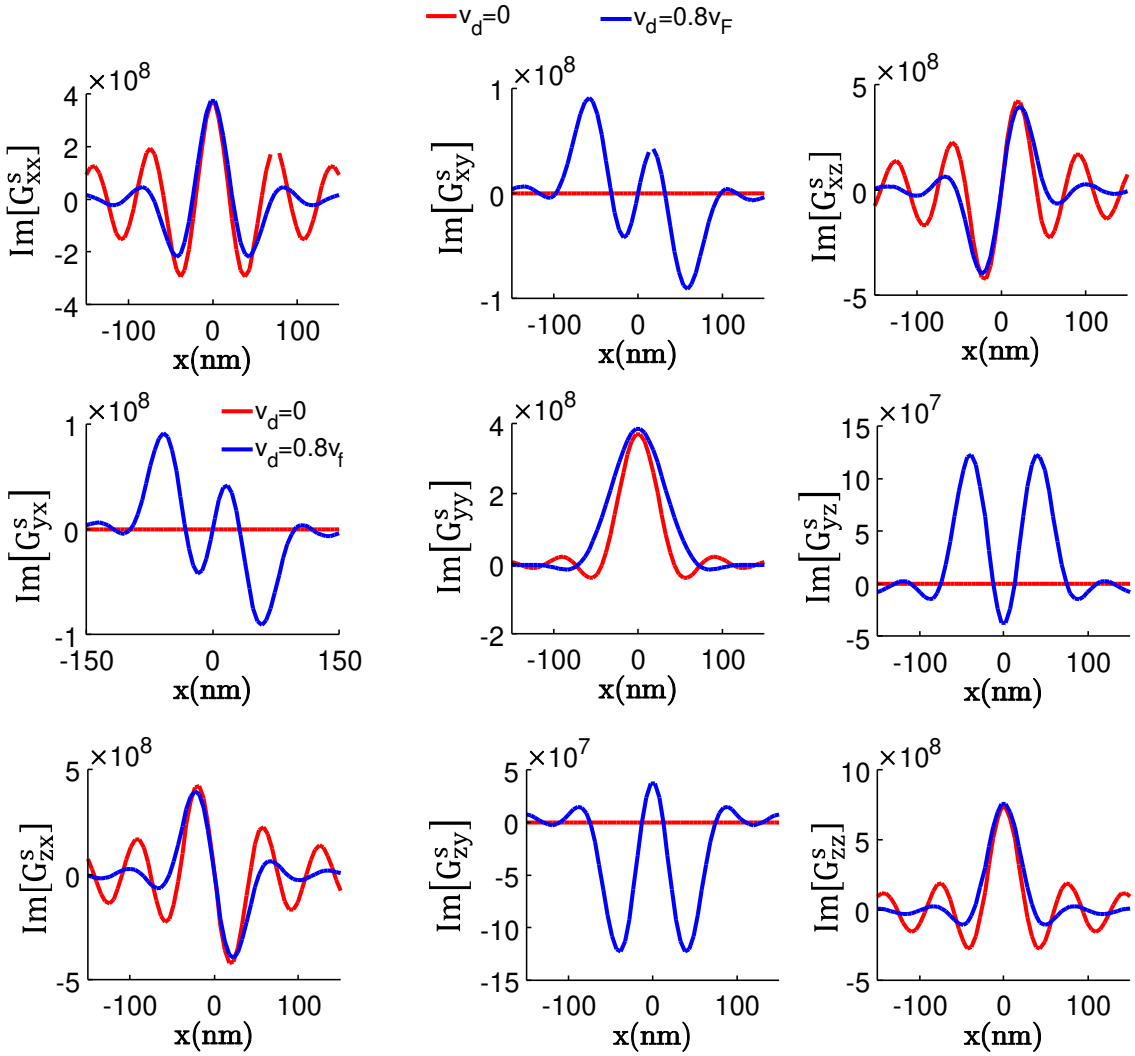

Figure 4.5: Imaginary parts of the scattered dyadic Green's function tensor components of a reciprocal (red) and nonreciprocal (blue) graphene based metasurface. Responses are computed in the orthogonal lateral direction of the applied bias considering the dipole is located at $\bar{r} = \{x, 0, 30\ \text{nm}\}$ above the surface. Other parameters are as in Figure 4.3.

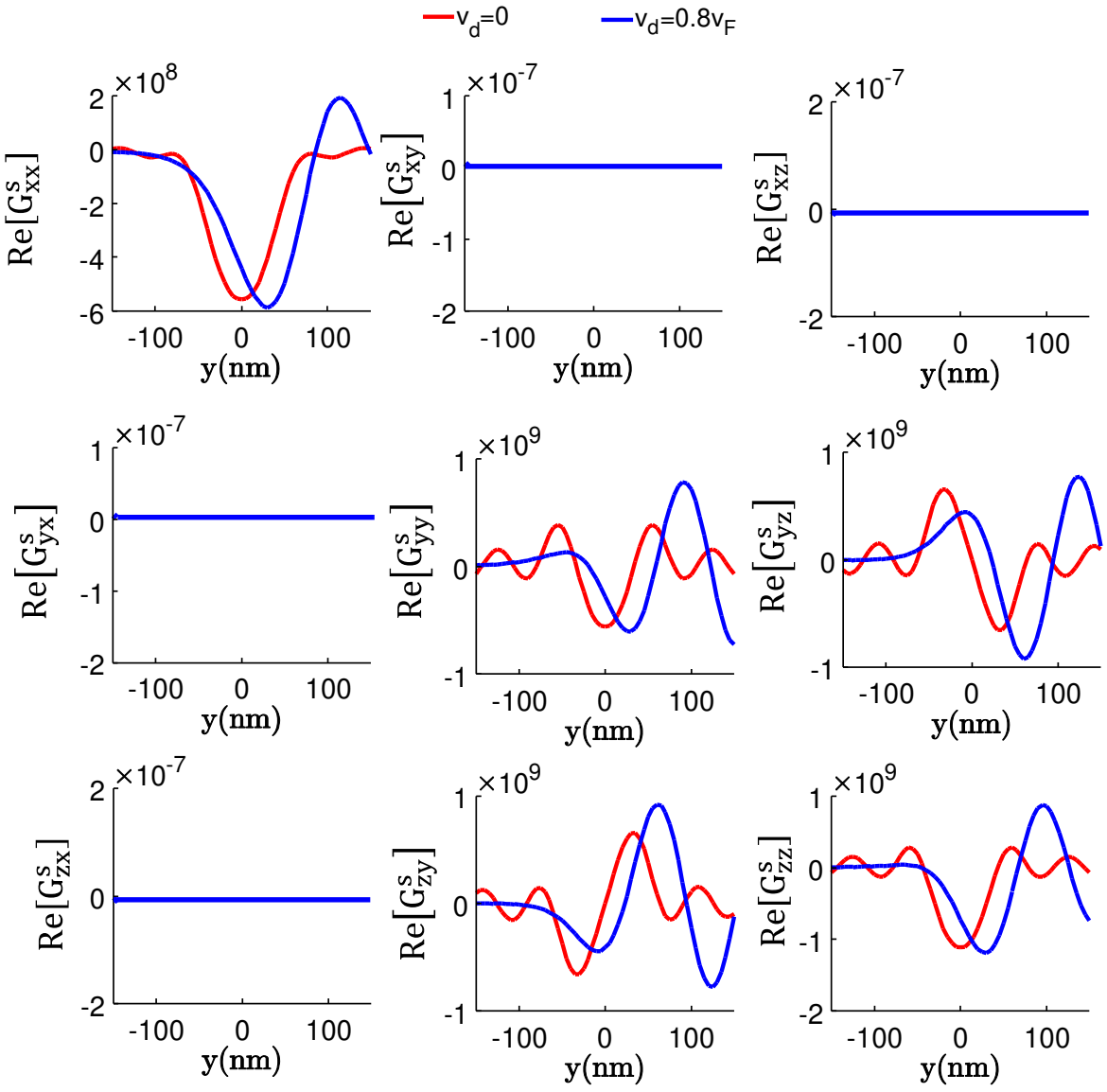

Figure 4.6: Real parts of the scattered dyadic Green's function tensor components of a reciprocal (red) and nonreciprocal (blue) graphene based metasurface. Responses are computed along the direction of the applied bias considering the dipole is located at $\bar{r} = \{0, y, 30\ \text{nm}\}$ above the surface. Other parameters are as in Figure 4.3.

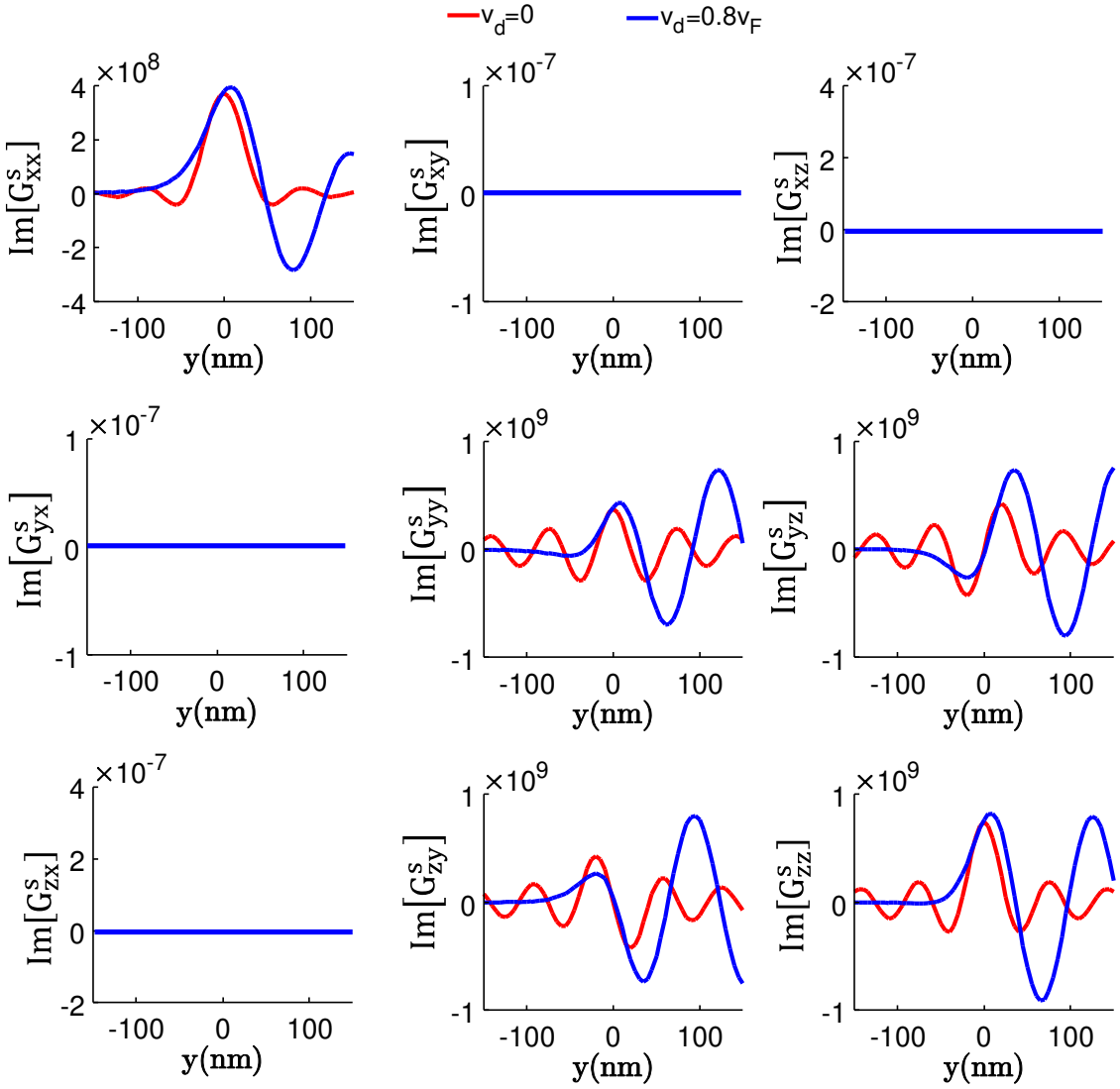

Figure 4.7: Imaginary parts of the scattered dyadic Green's function tensor components of a reciprocal (red) and nonreciprocal (blue) graphene based metasurface. Responses are computed along the direction of the applied bias considering the dipole is located at $\bar{r} = \{0, y, 30\ \text{nm}\}$ above the surface. Other parameters are as in Figure 4.3.

4.3.1 EFFECTIVE DIPOLE MOMENT

The effective dipole moment acquired by the particle is computed as $\bar{p} = \alpha_0(\overline{E}^0 + \overline{E}^s)$ [see Eq. (4.19)]. Substituting the expression $\overline{E}^s(\bar{r}_0, \bar{r}_0)$ as expressed in Eq. (4.49) to the dipole moment expression yields to the following set of equations:

$$(1 - \omega^2\mu_0\alpha_0 G^s_{xx})p_x = \alpha_0 E^0_x, \tag{4.50a}$$

$$\left(1 - \omega^2\mu_0\alpha_0 G^s_{yy}\right)p_y - \omega^2\mu_0\alpha_0 G^s_{yz}p_z = \alpha_0 E^0_y, \tag{4.50b}$$

$$-\omega^2\mu_0\alpha_0 G^s_{zy}p_y + (1 - \omega^2\mu_0\alpha_0 G^s_{zz})p_z = \alpha_0 E^0_z. \tag{4.50c}$$

Now, the effective dipole moment components acquired by the particle are computed by solving the set of equations in Eq. (4.50) that leads to

$$p_x = \frac{E^0_x\alpha_0}{1-\omega^2\mu_0\alpha_0 G^s_{xx}(\bar{r}_0,\bar{r}_0)}, \tag{4.51a}$$

$$p_y = \frac{E^0_y\alpha_0\left(1-\omega^2\mu_0\alpha_0 G^s_{zz}\right)+E^0_z\omega^2\mu_0\alpha_0^2 G^s_{yz}}{\left(1-\omega^2\mu_0\alpha_0 G^s_{yy}\right)\left(1-\omega^2\mu_0\alpha_0 G^s_{zz}\right)-\omega^4\mu_0^2\alpha_0^2 G^s_{yz}G^s_{zy}}, \tag{4.51b}$$

$$p_z = \frac{E^0_y\omega^2\mu_0\alpha_0^2 G^s_{zy}+E^0_z\alpha_0\left(1-\omega^2\mu_0\alpha_0 G^s_{yy}\right)}{\left(1-\omega^2\mu_0\alpha_0 G^s_{yy}\right)\left(1-\omega^2\mu_0\alpha_0 G^s_{zz}\right)-\omega^4\mu_0^2\alpha_0^2 G^s_{yz}G^s_{zy}}. \tag{4.51c}$$

Following the identity $\bar{p} = \overline{\overline{\alpha}} \cdot \overline{E}^0$, the nonzero elements of the effective dipole polarizability tensor $\overline{\overline{\alpha}}$ of the particle can be expressed

$$\alpha_{xx} = \frac{\alpha_0}{1-\omega^2\mu_0\alpha_0 G^s_{xx}}, \tag{4.52a}$$

$$\alpha_{yy} = \frac{\alpha_0\left(1-\omega^2\mu_0\alpha_0 G^s_{zz}\right)}{\left(1-\omega^2\mu_0\alpha_0 G^s_{yy}\right)\left(1-\omega^2\mu_0\alpha_0 G^s_{zz}\right)-\omega^4\mu_0^2\alpha_0^2 G^s_{yz}G^s_{zy}}, \tag{4.52b}$$

$$\alpha_{zz} = \frac{\alpha_0\left(1-\omega^2\mu_0\alpha_0 G^s_{yy}\right)}{\left(1-\omega^2\mu_0\alpha_0 G^s_{yy}\right)\left(1-\omega^2\mu_0\alpha_0 G^s_{zz}\right)-\omega^4\mu_0^2\alpha_0^2 G^s_{yz}G^s_{zy}}, \tag{4.52c}$$

$$\alpha_{yz} = \frac{\omega^2\mu_0\alpha_0^2 G^s_{yz}}{\left(1-\omega^2\mu_0\alpha_0 G^s_{yy}\right)\left(1-\omega^2\mu_0\alpha_0 G^s_{zz}\right)-\omega^4\mu_0^2\alpha_0^2 G^s_{yz}G^s_{zy}}, \tag{4.52d}$$

$$\alpha_{zy} = \frac{\omega^2\mu_0\alpha_0^2 G^s_{zy}}{\left(1-\omega^2\mu_0\alpha_0 G^s_{yy}\right)\left(1-\omega^2\mu_0\alpha_0 G^s_{zz}\right)-\omega^4\mu_0^2\alpha_0^2 G^s_{yz}G^s_{zy}}. \tag{4.52e}$$

Note that the nondiagonal components α_{yz} and α_{zy} completely vanish in the absence of the applied bias [see Eq. (4.22)].

In summary, the following table compares the zero and non-zero elements of the effective dipole polarizability tensors for reciprocal and nonreciprocal systems:

Reciprocal	Nonreciprocal
$\bar{\bar{\alpha}} = \begin{bmatrix} \alpha_{xx} & 0 & 0 \\ 0 & \alpha_{yy} & 0 \\ 0 & 0 & \alpha_{zz} \end{bmatrix}$	$\bar{\bar{\alpha}} = \begin{bmatrix} \alpha_{xx} & 0 & 0 \\ 0 & \alpha_{yy} & \alpha_{yz} \\ 0 & \alpha_{zy} & \alpha_{zz} \end{bmatrix}$

Table 4.1: Zero and non-zero elements of the effective dipole polarizability tensor for reciprocal and nonreciprocal structures. Nonreciprocity is obtained by applying an in-plane momentum bias along the $\hat{y}$-axis of the platform.

4.3.2 NONCONSERVATIVE RECOIL FORCE

The nonconservative recoil force components exerted on the particle can be computed from Eq. (4.23). Let me first derive the lateral components. To this purpose, it is required to compute the x and y-derivatives of the scattered dyadic Green's function components at the particle position as shown in Eq. (4.24). In the presence of an external bias applied along $\hat{y}$-axis (see Figure 4.3a), the following derivatives are strictly

zero at the particle position: $\frac{d}{dx}G^s_{xx} = \frac{d}{dx}G^s_{yy} = \frac{d}{dx}G^s_{yz} = \frac{d}{dx}G^s_{zy} = \frac{d}{dx}G^s_{zz} = \frac{d}{dy}G^s_{xy} = \frac{d}{dy}G^s_{xz} = \frac{d}{dy}G^s_{yx} = \frac{d}{dy}G^s_{zx} = 0$. Note that some derivatives were strictly zero in the reciprocal system at the dipole position, i.e., $\frac{d}{dx}G^s_{xy}$, $\frac{d}{dx}G^s_{yx}$, $\frac{d}{dy}G^s_{xx}$, $\frac{d}{dy}G^s_{yy}$, $\frac{d}{dy}G^s_{zz}$, are not zero anymore in the nonreciprocal system.

Following the similar procedure described above, see Eqs. (4.25)-(4.28), and taking into account the nonzero derivatives, the nonconservative lateral recoil forces can be simplified to

$$F_x^{nc} = \frac{k_0^2}{\varepsilon_0}\left[\mathrm{Re}\{p_x^* p_y\}\,\mathrm{Re}\left\{\frac{d}{dx}G^s_{xy}\right\}\right] - \frac{k_0^2}{\varepsilon_0}\mathrm{Im}\{p_x^* p_z\}\,\mathrm{Im}\left\{\frac{d}{dx}G^s_{xz}\right\}, \tag{4.53a}$$

$$F_y^{nc} = \frac{k_0^2}{2\varepsilon_0}\sum_{n=x,y,z}|p_n|^2\mathrm{Re}\left\{\frac{d}{dy}G^s_{nn}\right\} - \frac{k_0^2}{\varepsilon_0}\mathrm{Im}[p_y^* p_z]\mathrm{Im}\left\{\frac{d}{dy}G^s_{yz}\right\}. \tag{4.53b}$$

Let me decompose Eq. (4.53) as $F_x^{nc} = F_x^{nr-p} + F_x^s$ and $F_y^{nc} = F_y^{nr-a} + F_y^s$. Here, superscripts 'a' and 'p' refer to amplitude and polarization, respectively, and 'nr' and 's' refer to nonreciprocity and spin, respectively. Here, F_x^{nr-p} and F_y^{nr-a} are the lateral recoil forces that appear due to the broken symmetry in polarization and amplitude of the surface modes supported by the nonreciprocal structure, respectively; and F_x^s and F_y^s are recoil components that appears due to the dipole polarization spin and they are similar to the ones as found above reciprocal systems (see Eq. 4.28). All of these force components can be explicitly expressed as

$$F_x^{nr-p} = \frac{k_0^2}{\varepsilon_0}\left[\mathrm{Re}\{p_x^* p_y\}\,\mathrm{Re}\left\{\frac{d}{dx}G^s_{xy}\right\}\right], \tag{4.54a}$$

$$F_x^s = -\frac{k_0^2}{\varepsilon_0}\mathrm{Im}\{p_x^* p_z\}\,\mathrm{Im}\left\{\frac{d}{dx}G^s_{xz}\right\}, \tag{4.54b}$$

$$F_y^{nr-a} = \frac{k_0^2}{2\varepsilon_0}\sum_{n=x,y,z}|p_n|^2\mathrm{Re}\left\{\frac{d}{dy}G^s_{nn}\right\}, \tag{4.54c}$$

$$F_y^s = -\frac{k_0^2}{\varepsilon_0}\mathrm{Im}\left[p_y^* p_z\right]\mathrm{Im}\left\{\frac{d}{dy}G_{yz}^s\right\}. \tag{4.54d}$$

Finally, taking into account the power radiated by the dipole as expressed in Eqs. (4.29)-(4.30), and the polarization spin of the dipole as in Eq. (4.32), the lateral components can be simplified to

$$F_x^{nr-p} = \frac{6\pi}{c_0 k_0^2} P_{rad}^{xy} \chi_{xy} \mathrm{Re}\left\{\frac{d}{dx}G_{xy}^s\right\}, \tag{4.55a}$$

$$F_x^s = \frac{6\pi}{c_0 k_0^2} P_{rad}^{xz} \eta_y \mathrm{Im}\left\{\frac{d}{dx}G_{xz}^s\right\}, \tag{4.55b}$$

$$F_y^{nr-a} = \frac{6\pi}{c_0 k_0^2} \sum_{n=x,y,z} P_{rad}^{n} \mathrm{Re}\left\{\frac{d}{dy}G_{nn}^s\right\}, \tag{4.55c}$$

$$F_y^s = \frac{6\pi}{c_0 k_0^2} P_{rad}^{yz} \eta_x \mathrm{Im}\left\{\frac{d}{dy}G_{yz}^s\right\}. \tag{4.55d}$$

Here, $P_{rad}^{xy} = \frac{c_0 k_0^4}{12\pi\varepsilon_0}\left(|p_x|^2 + |p_y|^2\right)$ and $P_{rad}^{n} = \frac{c_0 k_0^4}{12\pi\varepsilon_0}(|p_n|^2)$ are the amount of power radiated by the xy and n-components of the dipole in free space; and $\chi_{xy} = 2\frac{\mathrm{Re}\{p_x^* p_y\}}{|p_x|^2+|p_y|^2}$ is the dipole's in-plane polarization factor [45]. I recall that the excitation of surface plasmons with different wavenumber (polarization) profiles within the plane gives rise to F_y^{nr-a} (F_x^{nr-p}) that is always directed along (orthogonal) to the bias axis. In case that the external bias is applied vertically to the surface, such as magneto-optical structures shown in ref-[45], F_y^{nr-a} completely vanishes due to the lack of broken symmetry in the plasmon amplitude. F_x^{nr-p} still appears there since the vertical bias breaks the polarization symmetry. This force is zero when the particle acquires a dipole moment oriented along or orthogonal to the applied vertical bias (i.e., $\chi_{xy} = 0$), and is maximum when the dipole is linearly polarized at an angle 45^0 with respect to the bias axis – a state that favors the polarization conversion process of the scattered fields. In Chapter 7 and 8, I will employ Eq.

(55) to investigate lateral optical forces and nanoscale manipulation of optical traps induced on nanoparticles located above nonreciprocal surfaces with in-plane momentum bias.

Now, I derive the vertical component of the nonconservative forces using Eq. (4.23c). Due to the broken symmetry of the system in the presence of applied bias along $\hat{y}$-direction, the z-derivative of the scattered dyadic Green's function at the dipole position is not a diagonal tensor anymore, as found in the reciprocal case (see section 4.2). The only derivatives that are strictly zero are $\frac{d}{dz}G^s_{xy} = \frac{d}{dz}G^s_{yx} = 0$. In addition, the following identities hold exactly at the particle position: $\frac{d}{dz}G^s_{xz} = -\frac{d}{dz}G^s_{zx}$ and $\frac{d}{dz}G^s_{yz} = -\frac{d}{dz}G^s_{zy}$. These allow to simplify the nonconservative vertical force components (i.e., $F^{nc}_z = F^{nr}_z + F^s_z$) as

$$F^s_z = \frac{6\pi}{c_0 k_0^2}\sum_{n=x,y,z} P^n_{rad}\mathrm{Re}\left\{\frac{d}{dz}G^s_{nn}\right\}, \tag{4.56a}$$

$$F^{nr}_z = \frac{6\pi}{c_0 k_0^2}P^{xz}_{rad}\eta_y \mathrm{Im}\left\{\frac{d}{dz}G^s_{xz}\right\} + \frac{6\pi}{c_0 k_0^2}P^{yz}_{rad}\eta_x \mathrm{Im}\left\{\frac{d}{dz}G^s_{yz}\right\}. \tag{4.56b}$$

Here, F^{nr}_z is the vertical force component that appears due to the broken symmetry of the nonreciprocal system, and F^s_z is the common recoil component found above reciprocal structures [see Eq. (4.35)]. Here, F^{nr}_z possesses an interesting feature: Eq. (4.56b) shows that it depends on the polarization spin or helicity of the dipole. This component can be negative or positive thus acting toward or away from the metasurface as a function of the dipole rotation handedness which may open up new possibilities to levitate non-magnetic nanoparticles away from the structure, where the standard levitation techniques rely on the use of extremely anisotropic structures [46] or magnetic particles near a plasmonic surface [47].

4.3.3 CONSERVATIVE OPTICAL FORCE

Eq. (4.16) can be directly applied to compute the conservative optical forces exerted on the particle. The lateral components of these forces read as

$$F_x^c = \frac{1}{2}\mathrm{Re}\left[ik_x\left\{\alpha_{yz}^* E_z^{0^*} E_y^0 + \alpha_{zy}^* E_y^{0^*} E_z^0 + \sum_{n=x,y,z} \alpha_{nn}^* |E_n^0|^2\right\}\right], \tag{4.57a}$$

$$F_y^c = \frac{1}{2}\mathrm{Re}\left[ik_y\left\{\alpha_{yz}^* E_z^{0^*} E_y^0 + \alpha_{zy}^* E_y^{0^*} E_z^0 + \sum_{n=x,y,z} \alpha_{nn}^* |E_n^0|^2\right\}\right]. \tag{4.57b}$$

Note that the off-diagonal dipole polarizability components [see Eq. 4.52(d-e)] fulfills the following identity: $\alpha_{yz} = -\alpha_{zy}$. Applying $E_z^{0^*} E_y^0 - E_y^{0^*} E_z^0 = 2\mathrm{Im}\left[E_z^{0^*} E_y^0\right]$, Eq. (4.57) can be reformulated as

$$F_x^c = \frac{1}{2}k_x\left[2\mathrm{Im}\{\alpha_{yz}\}\mathrm{Im}\left\{E_z^{0^*} E_y^0\right\} + \sum_{n=x,y,z} \mathrm{Im}\{\alpha_{nn}\}|E_n^0|^2\right], \tag{4.58a}$$

$$F_y^c = \frac{1}{2}k_y\left[2\mathrm{Im}\{\alpha_{yz}\}\mathrm{Im}\left\{E_z^{0^*} E_y^0\right\} + \sum_{n=x,y,z} \mathrm{Im}\{\alpha_{nn}\}|E_n^0|^2\right]. \tag{4.58b}$$

Finally, the vertical component of conservative forces can be computed using Eq. (4.42). There, it is required to plug in the modified dipole moment [see Eq. (4.51)] in the presence of the applied bias.

4.3.4 ANALYTICAL MODEL OF LATERAL RECOIL FORCE DUE TO BROKEN SYMMETRY IN AMPLITUDE

To compute the analytical formalism of nonconservative lateral force (i.e., F_y^{nr-a}) due the broken symmetry in amplitude, it is needed to analytically solve the y-derivatives of the Green's function diagonal components [see Eq. (4.55c)]. To this purpose, I employ the similar approach as detailed in section 4.2.4.

The integral along k_ρ' of the Green's function spatial derivatives at the particle position can be analytically computed as

$$N_{\frac{d}{dy}G_{xx}^s}\left(k_\phi'\right) = i\frac{\eta_0 k_\rho^2 \sin k_\phi'[A_{xx}+B_{xx}]}{D_{xx}} e^{-2z_0\sqrt{k_\rho^2-k_0^2}}, \tag{4.59a}$$

$$N_{\frac{d}{dy}G_{yy}^s}\left(k_\phi'\right) = -i\frac{\eta_0 k_\rho^2 \sin k_\phi'[A_{yy}+B_{yy}]}{D_{yy}} e^{-2z_0\sqrt{k_\rho^2-k_0^2}}, \tag{4.59b}$$

$$N_{\frac{d}{dy}G_{zz}^{S}}\left(k'_{\phi}\right) = -\frac{\eta_0 k_\rho^3 \sin k_\phi [A_{zz}+B_{zz}+C_{zz}]}{D_{zz}} e^{-2z_0\sqrt{k_\rho^2-k_0^2}}. \tag{4.59c}$$

The associated terms in Eq. (4.59) are given by

$$A_{xx} = 2\sigma_{xx}\cos\left(2k'_{\phi}\right)\left\{4k_0^4 - \left(2k_0^2 - k_\rho^2\right)\left(2k_\rho^2 - i\eta_0\sigma_{yy}k_0k_\rho\right)\right\}, \tag{4.60a}$$

$$B_{xx} = k_\rho^2\{-\left(3\sigma_{xx}+\sigma_{yy}\right)\left(2k_0^2-k_\rho^2\right) - i2\eta_0\sigma_{xx}\sigma_{yy}k_0k_\rho + k_\rho^2\left(\sigma_{xx} - \sigma_{yy}\right)\cos\left(4k'_{\phi}\right)\}, \tag{4.60b}$$

$$D_{xx} = 64\varepsilon_r\pi k_0^2\{\eta_0\left(\sigma_{xx}+\sigma_{yy}\right)\left(4k_0^2-3k_\rho^2\right) + 3\eta_0k_\rho^2\left(\sigma_{yy}-\sigma_{xx}\right)\cos\left(2k'_{\phi}\right) + i2k_0k_\rho\left(4+\eta_0^2\sigma_{xx}\sigma_{yy}\right)\}, \tag{4.60c}$$

$$A_{yy} = 2\sigma_{yy}\cos\left(2k'_{\phi}\right)\left\{4k_0^4 - \left(2k_0^2 - k_\rho^2\right)\left(2k_\rho^2 - i\eta_0\sigma_{xx}k_0k_\rho\right)\right\}, \tag{4.60d}$$

$$B_{yy} = k_\rho^2\{\left(\sigma_{xx}+3\sigma_{yy}\right)\left(2k_0^2-k_\rho^2\right) + i2\eta_0\sigma_{xx}\sigma_{yy}k_0k_\rho + k_\rho^2\left(\sigma_{xx} - \sigma_{yy}\right)\cos\left(4k'_{\phi}\right)\}, \tag{4.60e}$$

$$D_{yy} = 64\varepsilon_r\pi k_0^2\{\eta_0\left(\sigma_{xx}+\sigma_{yy}\right)\left(4k_0^2-3k_\rho^2\right) + 3\eta_0k_\rho^2\left(\sigma_{yy}-\sigma_{xx}\right)\cos\left(2k'_{\phi}\right) + i2k_0k_\rho\left(4+\eta_0^2\sigma_{xx}\sigma_{yy}\right)\}, \tag{4.60f}$$

$$A_{zz} = \eta_0 \sigma_{xx} \sigma_{yy} k_0 \cos^4 k'_\phi, \tag{4.60g}$$

$$B_{zz} = \sigma_{yy}\left(i2k_\rho + \eta_0 \sigma_{xx} k_0 \sin^2 k'_\phi\right) \sin^2 k'_\phi, \tag{4.60h}$$

$$C_{zz} = 2\sigma_{xx}\left(ik_\rho + \eta_0 \sigma_{yy} k_0 \sin^2 k'_\phi\right) \cos^2 k'_\phi, \tag{4.60i}$$

$$D_{zz} = 16\varepsilon_r \pi k_0^2 \left\{2\eta_0\left(\sigma_{xx} + \sigma_{yy}\right) + \frac{k_0\left(4+\eta_0^2 \sigma_{xx}\sigma_{yy}\right)}{ik_\rho} + 2\eta_0\left(\sigma_{xx} - \sigma_{yy}\right)\cos\left(2k'_\phi\right)\right\}. \tag{4.60j}$$

Assuming that the platform operates in the nonretarded regime (i.e., $k_\rho \gg k_0$) [1,12], Eq. (4.59) greatly simplifies to

$$N_{\frac{d}{dy}G^s_{xx}}\left(k'_\phi\right) \approx -i\frac{k_\rho^6 \sin^3 k'_\phi \cos^4 k'_\phi \left(\cos^2 k'_\phi + \sin k'_\phi\right)}{192\pi\varepsilon_r k_0^2 \left(3\cos k'_\phi + 3\sin k'_\phi - 2\sqrt{2}\right)} e^{-2z_0\sqrt{k_\rho^2 - k_0^2}}, \tag{4.61a}$$

$$N_{\frac{d}{dy}G^s_{yy}}\left(k'_\phi\right) \approx -i\frac{k_\rho^6 \sin^5 k'_\phi \cos^2 k'_\phi \left(\sin k'_\phi + \cos k'_\phi\right)}{96\pi\varepsilon_r k_0^2 \left(3\cos k'_\phi + 3\sin k'_\phi - 2\sqrt{2}\right)} e^{-2z_0\sqrt{k_\rho^2 - k_0^2}}, \tag{4.61b}$$

$$N_{\frac{d}{dy}G^s_{zz}}\left(k'_\phi\right) \approx -i\frac{k_\rho^6 \sin^3 k'_\phi \cos^2 k'_\phi \left(\sin k'_\phi + \cos k'_\phi\right)}{96\pi\varepsilon_r k_0^2 \left(3\cos k'_\phi + 3\sin k'_\phi - 2\sqrt{2}\right)} e^{-2z_0\sqrt{k_\rho^2 - k_0^2}}. \tag{4.61c}$$

Now the spatial derivatives of the Green's function associated with F_y^{nr-a} [see Eq. (4.55c)] can be computed at the particle position by performing the following integrals along k'_ϕ:

$$\mathrm{Re}\left\{\frac{d}{dy} G^s_{xx}\right\} = \int_0^{2\pi} \frac{k_\rho^6 \sin^3 k'_\phi \cos^4 k'_\phi \left(\cos^2 k'_\phi + \sin k'_\phi\right)}{192\varepsilon_r k_0^2 \left(3\cos k'_\phi + 3\sin k'_\phi - 2\sqrt{2}\right)} e^{-2z_0\sqrt{k_\rho^2 - k_0^2}} dk'_\phi, \tag{4.62a}$$

$$\mathrm{Re}\left\{\frac{\mathrm{d}}{\mathrm{dy}}\mathrm{G}_{\mathrm{yy}}^{\mathrm{s}}\right\}=\int_0^{2\pi}\frac{\mathrm{k}_\rho^6\sin^5\mathrm{k}_\phi'\cos^2\mathrm{k}_\phi'\left(\sin\mathrm{k}_\phi'+\cos\mathrm{k}_\phi'\right)}{96\varepsilon_\mathrm{r}\mathrm{k}_0^2\left(3\cos\mathrm{k}_\phi'+3\sin\mathrm{k}_\phi'-2\sqrt{2}\right)}\mathrm{e}^{-2\mathrm{z}_0\sqrt{\mathrm{k}_\rho^2-\mathrm{k}_0^2}}\mathrm{dk}_\phi', \tag{4.62b}$$

$$\mathrm{Re}\left\{\frac{\mathrm{d}}{\mathrm{dy}}\mathrm{G}_{\mathrm{zz}}^{\mathrm{s}}\right\}=\int_0^{2\pi}\frac{\mathrm{k}_\rho^6\sin^3\mathrm{k}_\phi'\cos^2\mathrm{k}_\phi'\left(\sin\mathrm{k}_\phi'+\cos\mathrm{k}_\phi'\right)}{96\varepsilon_\mathrm{r}\mathrm{k}_0^2\left(3\cos\mathrm{k}_\phi'+3\sin\mathrm{k}_\phi'-2\sqrt{2}\right)}\mathrm{e}^{-2\mathrm{z}_0\sqrt{\mathrm{k}_\rho^2-\mathrm{k}_0^2}}\mathrm{dk}_\phi'. \tag{4.62c}$$

where again the relationship between k_ρ and k_ϕ' is implicit and given by the dispersion relation of the platform. Note that these expressions are strictly zero in case of reciprocal devices, due to the polar symmetry of the platform response.

It should be stressed that Eq. (4.62) captures the fundamental physics of the problem: lateral recoil forces only depend on the dispersion relation of the modes supported by the platform. Additionally, as shown in Figure 4.8 for a specific example, the integrands of these functions exhibit a smooth behavior versus k_ϕ' and thus can easily be integrated using numerical routines [25]. Interestingly, a close look into Eqs. (4.61)-(4.62) reveals that $\mathrm{Re}\left\{\frac{\mathrm{d}}{\mathrm{dy}}\mathrm{G}_{\mathrm{xx}}^{\mathrm{s}}\right\}$ is strictly zero along/against the bias direction, whereas the terms $\mathrm{Re}\left\{\frac{\mathrm{d}}{\mathrm{dy}}\mathrm{G}_{\mathrm{yy}}^{\mathrm{s}}\right\}$ and $\mathrm{Re}\left\{\frac{\mathrm{d}}{\mathrm{dy}}\mathrm{G}_{\mathrm{zz}}^{\mathrm{s}}\right\}$ are minimum/maximum along/against such direction. The former response is expected because in $\mathrm{Re}\left\{\frac{\mathrm{d}}{\mathrm{dy}}\mathrm{G}_{\mathrm{xx}}^{\mathrm{s}}\right\}$ the bias is applied in the direction orthogonal to the xx-tensor component

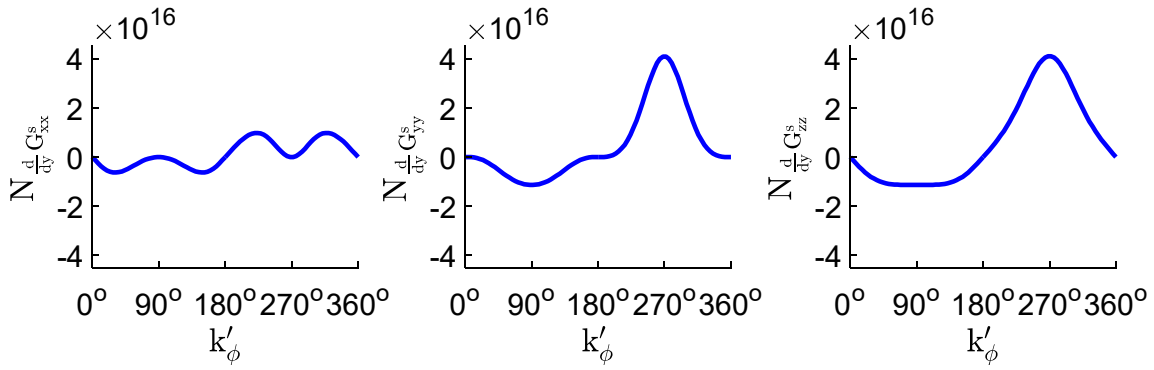

Figure 4.8: Residue of $\frac{\mathrm{d}}{\mathrm{dy}}\mathrm{G}_{\mathrm{xx}}^{\mathrm{s}}$ (left panel), $\frac{\mathrm{d}}{\mathrm{dy}}\mathrm{G}_{\mathrm{yy}}^{\mathrm{s}}$ (middle panel), and $\frac{\mathrm{d}}{\mathrm{dy}}\mathrm{G}_{\mathrm{zz}}^{\mathrm{s}}$ (right panel) at k_ρ versus k_ϕ' in the case of drift-biased nonreciprocal graphene. Results are computed using Eq. (4.61) keeping $\bar{\mathrm{v}}_\mathrm{d}=0.5\mathrm{v}_\mathrm{F}$. Other parameters are as in Figure 4.3.

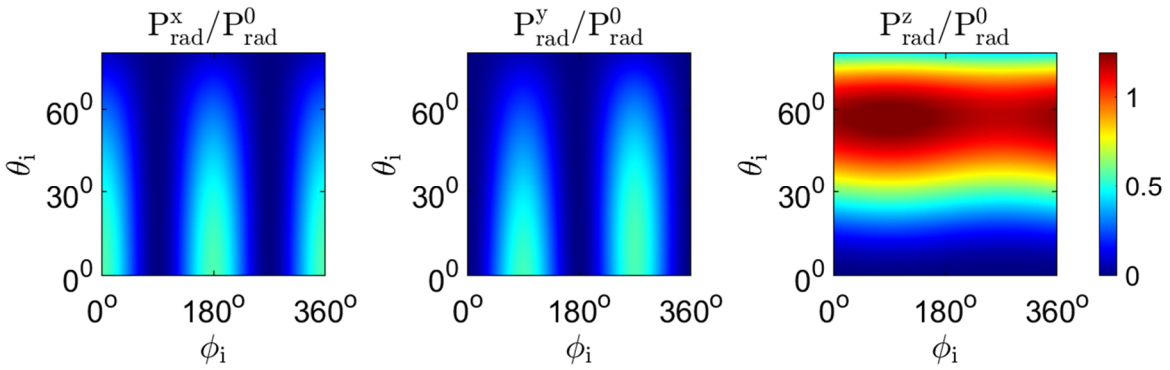

Figure 4.9: Amount of power radiated by the x, y and z-components of a polarized nanoparticle, P^x_{rad} (left panel), P^y_{rad} (middle panel) and P^z_{rad} (right panel), normalized with respect to the power scattered by the same particle when illuminated in free space (P^0_{rad}). Results are computed as a function of incident angles θ_i and ϕ_i of a transverse magnetic polarized incoming light. Other parameters are as in Figure 4.3.

of the Green's function and therefore yields an exact zero along the y-direction. The latter response appears because the momentum of the supported modes along/against the bias is minimum/maximum (see Chapter 3). Additionally, Eq. (4.62) reveals a dependence $\propto k_\rho^6$ with the supported states and therefore it is expected that those with larger momentum will dominate the overall response of the platform. These arguments permit to simplify (Eq. 4.55c) and obtain and approximate analytical expression. To this purpose, I consider first that the power scattered by the particle in the direction orthogonal to the bias is not dominant, i.e., $P^x_{rad} \leq P^y_{rad}$ and $P^x_{rad} \leq P^z_{rad}$. This condition is relatively general and appears in many scenarios (see Figure 4.9). One exception occurs when a plane wave quasi-vertically illuminates the platform with a polarization aligned in the direction orthogonal to the bias (x-axis in this case). Assuming the common situations, Eq. (4.55c) can be approximated as

$$F_y^{nr-a} \approx \frac{6\pi}{c_0 k_0^2}\left[P^y_{rad}\mathrm{Re}\left\{\frac{d}{dy}G^s_{yy}\right\} + P^z_{rad}\mathrm{Re}\left\{\frac{d}{dy}G^s_{zz}\right\}\right], \tag{4.63}$$

where I have assumed that $P^y_{rad}\mathrm{Re}\left\{\frac{d}{dy}G^s_{yy}\right\} \gg P^x_{rad}\mathrm{Re}\left\{\frac{d}{dy}G^s_{xx}\right\}$ and $P^z_{rad}\mathrm{Re}\left\{\frac{d}{dy}G^s_{zz}\right\} \gg P^x_{rad}\mathrm{Re}\left\{\frac{d}{dy}G^s_{xx}\right\}$. To calculate the real part of the spatial derivatives of the Green's function tensor, I evaluate Eqs. (4.62b-c)

along and against the bias direction. This approximation assumes a delta function at these directions and is justified due to the $\propto k_\rho^6$ dependence on the momentum of the supported states. Since the momentum of the states along and against the bias are maximum in their respective semi-plane of the momentum space, they are expected to dominate the response of the platform. Following this strategy, the spatial derivatives of the Green's function required in Eq. (4.63) can be computed analytically as

$$\mathrm{Re}\left\{\frac{d}{dy}G_{yy}^{s}\right\} \approx \frac{1}{16\varepsilon_r k_0^2}\left[\left(k_y^-\right)^4 e^{-2z_0\sqrt{\left(k_y^-\right)^2-k_0^2}} - \left(k_y^+\right)^4 e^{-2z_0\sqrt{\left(k_y^+\right)^2-k_0^2}}\right], \tag{4.64a}$$

$$\mathrm{Re}\left\{\frac{d}{dy}G_{zz}^{s}\right\} \approx \frac{1}{16\varepsilon_r k_0^2}\left[\left(k_y^-\right)^4 e^{-2z_0\sqrt{\left(k_y^-\right)^2-k_0^2}} - \left(k_y^+\right)^4 e^{-2z_0\sqrt{\left(k_y^+\right)^2-k_0^2}}\right], \tag{4.64b}$$

where, k_y^- and k_y^+ are the plasmon wavenumber against and along the drifting electrons, respectively, as shown in Figure 4.3(b). Substituting the compact form expression of these derivatives into Eq. (4.63), the nonreciprocity-induced recoil force acting along the external bias direction yields

$$F_y^{nr-a} \approx \frac{6\pi P_{rad}^{yz}}{8\varepsilon_r c_0}\left[\left(\frac{k_y^-}{k_0}\right)^4 e^{-2z_0\sqrt{\left(k_y^-\right)^2-k_0^2}} - \left(\frac{k_y^+}{k_0}\right)^4 e^{-2z_0\sqrt{\left(k_y^+\right)^2-k_0^2}}\right]. \tag{4.65}$$

Eq. (4.65) confirms that F_y^{nr-a} originates to compensate for the momentum imbalance of the asymmetric surface plasmons excited on the metasurface during the scattering process. In the reciprocal system, this force components completely vanishes (i.e., F_y^{nr-a}) since $k_y^+ = k_y^-$. The accuracy of this expression will be discussed further in Chapters 7 and 8.

4.3.5 Analytical model of lateral recoil force due to broken symmetry in polarization

To compute the analytical formalism of nonconservative lateral recoil force (i.e., F_y^{nr-p}) due the broken symmetry in polarization, it is required to analytically solve the x-derivatives of the Green's function off-

diagonal diagonal component [see Eq. (4.55a)], i.e., $\mathrm{Re}\left\{\frac{\mathrm{d}}{\mathrm{dx}}\mathrm{G}_{\mathrm{xy}}^{\mathrm{s}}\right\}$. To this purpose, I again follow the analysis detailed in section 4.2.4.

First, the integral along k_{ρ}' of this derivative at the particle position can be analytically computed as

$$\mathrm{N}_{\frac{\mathrm{d}}{\mathrm{dx}}\mathrm{G}_{\mathrm{xy}}^{\mathrm{s}}}\left(\mathrm{k}_{\phi}'\right) = \mathrm{i}\frac{\eta_0\mathrm{k}_{\rho}^2\cos\mathrm{k}_{\phi}'\sin\left(2\mathrm{k}_{\phi}'\right)\left[\mathrm{A}_{\mathrm{xy}}+\mathrm{B}_{\mathrm{xy}}+\mathrm{C}_{\mathrm{xy}}\right]}{\mathrm{D}_{\mathrm{xy}}}\mathrm{e}^{-2\mathrm{z}_0\sqrt{\mathrm{k}_{\rho}^2-\mathrm{k}_0^2}}, \tag{4.66}$$

where

$$\mathrm{A}_{\mathrm{xy}} = 2\mathrm{k}_0^3\sigma_{\mathrm{yy}}\left(2\mathrm{k}_0 + \mathrm{i}\eta_0\mathrm{k}_{\rho}\sigma_{\mathrm{xx}}\right), \tag{4.67a}$$

$$\mathrm{B}_{\mathrm{xy}} = -\mathrm{k}_0\mathrm{k}_{\rho}^2\sigma_{\mathrm{yy}}\left(4\mathrm{k}_0 + \mathrm{i}\eta_0\mathrm{k}_{\rho}\sigma_{\mathrm{xx}}\right), \tag{4.67b}$$

$$\mathrm{C}_{\mathrm{xy}} = \mathrm{k}_{\rho}^4\left\{\sigma_{\mathrm{xx}} + \sigma_{\mathrm{yy}} + \left(\sigma_{\mathrm{xx}} - \sigma_{\mathrm{yy}}\right)\cos\left(2\mathrm{k}_{\phi}'\right)\right\}, \tag{4.67c}$$

$$\mathrm{D}_{\mathrm{xy}} = 32\pi\varepsilon_{\mathrm{r}}\mathrm{k}_0^2\left[\eta_0\left(\sigma_{\mathrm{xx}} + \sigma_{\mathrm{yy}}\right)\left(4\mathrm{k}_0^2 - 3\mathrm{k}_{\rho}^2\right) + \mathrm{k}_{\rho}\left\{\mathrm{i}8\mathrm{k}_0 - 3\eta_0\mathrm{k}_{\rho}\left(\sigma_{\mathrm{xx}} - \sigma_{\mathrm{yy}}\right)\cos\left(2\mathrm{k}_{\phi}'\right)\right\}\right]. \tag{4.67d}$$

Operating the platform within the nonretarded regime $\mathrm{k}_{\rho} \gg \mathrm{k}_0$, Eq. (4.66) simplifies to

$$\mathrm{N}_{\frac{\mathrm{d}}{\mathrm{dx}}\mathrm{G}_{\mathrm{xy}}^{\mathrm{s}}}\left(\mathrm{k}_{\phi}'\right) \approx -\mathrm{i}\frac{\mathrm{k}_{\rho}^4\cos\mathrm{k}_{\phi}'\sin\left(2\mathrm{k}_{\phi}'\right)}{32\pi\varepsilon_{\mathrm{r}}\mathrm{k}_0^2}\mathrm{e}^{-2\mathrm{z}_0\sqrt{\mathrm{k}_{\rho}^2-\mathrm{k}_0^2}}. \tag{4.68}$$

where again the $\mathrm{k}_{\rho} - \mathrm{k}_{\phi}'$ relation is determined by the dispersion relation of the system. Then, the spatial derivative of the Green's functions required in Eq. (4.55a) to calculate lateral recoil forces can be computed at the particle position by performing the following integral along k_{ϕ}':

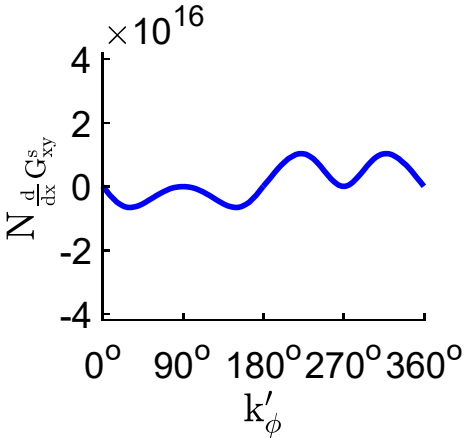

Figure 4.10: Residue of $\frac{d}{dx}G_{xy}^{s}$ at k_ρ versus k'_ϕ in the case of drift-biased nonreciprocal graphene. Results are computed using Eq. (4.68) keeping $v_d = 0.5v_F$. Other parameters are as in Figure 4.3.

$$\mathrm{Re}\left\{\frac{d}{dx}G_{xy}^{s}\right\} = \int_0^{2\pi} \frac{k_\rho^4 \cos k'_\phi \sin(2k'_\phi)}{32\varepsilon_r k_0^2} e^{-2z_0\sqrt{k_\rho^2 - k_0^2}} dk'_\phi. \tag{4.69}$$

Again, the integrand of this function exhibits a smooth behavior versus k'_ϕ (see Figure 4.10) and can be integrated using standard numerical techniques [25]. Importantly, Eq. (4.69) reveals a dependence $\propto k_\rho^4$ with the momentum of the supported states, two orders of magnitude smaller than the one found in Eq. (4.62) for recoil forces arising from the broken symmetry of the system in amplitude.

Finally, the lateral recoil force acting in the orthogonal direction of the external bias yields

$$F_x^{nr-p} \approx \frac{3\pi P_{rad}^{xy}\chi_{xy}}{16\varepsilon_r c_0 k_0^4} \int_0^{2\pi} k_\rho^4 \cos k_\phi \sin(2k'_\phi)\, e^{-2z_0\sqrt{k_\rho^2 - k_0^2}} dk'_\phi. \tag{4.70}$$

Note that Eq. (4.70) is completely general and holds for any directions of the incident light. The accuracy of this expression and its use in realistic platforms will be discussed in Chapter 7.

4.3.6 ANALYTICAL MODEL OF DIPOLE SPIN-INDUCED LATERAL RECOIL FORCE

The dipole polarization spin-induced nonconservative lateral recoil forces share identical expressions for reciprocal and nonreciprocal as shown in Eqs. (4.33) and (4.55), respectively. The analytical model of these forces in the case of reciprocal system has been developed in section 4.2.4. In the presence of the in-plane momentum bias, the broken symmetry of the nonreciprocal system slightly modifies these analytical formalisms as detailed below.

My analytical model begins with Eq. (4.46) that can be readily applied to nonreciprocal systems with in-plane momentum bias. Eq. (4.46) can be easily integrated over k'_{ϕ} thus yielding

$$\mathrm{Im}\left\{\frac{d}{dx}G^{s}_{xz}\right\} \approx \frac{1}{16\varepsilon_r k_0^2}\left[(k_x^-)^4 e^{-2z_0\sqrt{(k_x^-)^2-k_0^2}} + (k_x^+)^4 e^{-2z_0\sqrt{(k_x^+)^2-k_0^2}}\right], \tag{4.71a}$$

$$\mathrm{Im}\left\{\frac{d}{dy}G^{s}_{yz}\right\} \approx \frac{1}{16\varepsilon_r k_0^2}\left[(k_y^-)^4 e^{-2z_0\sqrt{(k_y^-)^2-k_0^2}} + (k_y^+)^4 e^{-2z_0\sqrt{(k_y^+)^2-k_0^2}}\right], \tag{4.71b}$$

where k_x^- and k_x^+ are the plasmon wavenumber in the negative and positive k_x-half spaces, respectively, in the direction orthogonal to the external bias as shown in Figure 4.3(b). These identities allow to write the spin-induced lateral recoil force analytically in a general form as

$$F_x^s \approx \frac{3\pi P_{rad}^{xz}\eta_y}{8c_0\varepsilon_r}\left[\left(\frac{k_x^+}{k_0}\right)^4 e^{-2z_0\sqrt{(k_x^+)^2-k_0^2}} + \left(\frac{k_x^-}{k_0}\right)^4 e^{-2z_0\sqrt{(k_x^-)^2-k_0^2}}\right], \tag{4.72a}$$

$$F_y^s \approx \frac{3\pi P_{rad}^{yz}\eta_x}{8c_0\varepsilon_r}\left[\left(\frac{k_y^+}{k_0}\right)^4 e^{-2z_0\sqrt{(k_y^+)^2-k_0^2}} + \left(\frac{k_y^-}{k_0}\right)^4 e^{-2z_0\sqrt{(k_y^-)^2-k_0^2}}\right]. \tag{4.72b}$$

Note that Eq. (4.72) is general and holds for any directions of the incoming light. In the case of reciprocal surfaces, $k_x^- = k_x^+$ and $k_y^- = k_y^+$, and Eq. (4.72) results in to the one as expressed in Eq. (4.48). The accuracy of these analytical models will be further discussed in Chapter 7 and 8.

4.4 NUMERICAL FRAMEWORK IN COMSOL MULTIPHYSICS

The total optical forces exerted on a nanoparticle located near *reciprocal* structures can be computed numerically by full wave simulation using the electromagnetic wave frequency domain solver available in COMSOL Multiphysics 5.5 [8]. This commercial software uses Maxwell's stress tensor method (see section 4.1.1) to compute the total optical forces. Unfortunately, COMSOL Multiphysics does not allow to study light-matter interactions provided by nonreciprocal structures in the presence of external momentum bias, and the resulting optical forces cannot be evaluated. In the following, I detail the numerical procedure to compute optical forces above reciprocal surfaces.

Let me consider a nanoparticle located above a homogeneous metasurface that is illuminated with light. The metasurface can be characterized as a two-dimensional sheet with the provided complex conductivity. Scattering boundary conditions (SBC) should be imposed to the boundaries surrounding the entire geometry to avoid the reflection of incident light impinging the boundaries. Perfectly matched layers should be used to prevent potential reflections of the excited surface modes from the boundaries with SBC. A fine

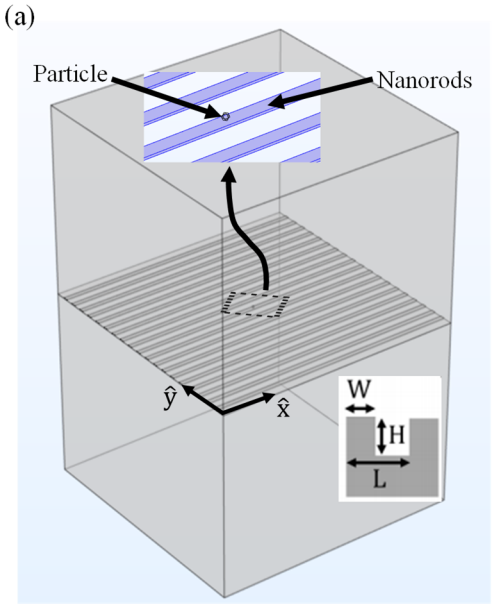

Figure 4.11: Domain of simulation to compute optical forces on nanoparticles located above nanostructured metal based hyperbolic metasurface performed in COMSOL Multiphysics.

tetrahedral mesh should be applied to discretize the entire geometry, with a denser mesh around the particle surface and the metasurface to properly capture their electromagnetic interaction.

The optical forces induced on the particle can be directly computed using the Maxwell's stress tensor formulation [see Eq. (4.11)] considering a spherical surface that surrounds the particle at 1nm of distance. Figure 4.11 shows an example of the domain of the simulation considering a nanoparticle located above nanostructured metal based hyperbolic metasurface. Note that similar numerical models are common in the literature [12,13,17]. To develop symmetric mesh throughout the entire geometry and get rid of possible numerical noise affecting the induced forces, one should divide the entire geometry into four equal quadrants, impose tetrahedral mesh to the domains in an arbitrary quadrant, and then copy the mesh to the domains in the remaining quadrants. The particle surface, the stress tensor surface, and the metasurface should be finely meshed to capture the interactions among them. Finally, the integration of the Maxwell's stress tensor should be performed along the stress tensor surface to compute the induced optical forces.

In Chapter 5 and 6, I will follow the approaches described above to compute lateral force and optical trapping response on nanoparticles located near nanostructured silver under illumination with a plane wave and Gaussian laser beam. The electrical properties of silver can be modelled considering the frequency-dependent complex permittivity from Ref – [48].

4.5 CHAPTER REFERENCES

[1] Novotny, L. and Hecht, B., 2012. *Principles of nano-optics*. Cambridge university press.

[2] Ashkin, A., 1970. Acceleration and trapping of particles by radiation pressure. *Physical Review Letters*, *24*(4), p.156.

[3] Ashkin, A., Mourou, G. and Strickland, D., 2018. The Nobel Prize in Physics for groundbreaking inventions in the field of laser physics.

[4] Young, A.T., 1982. Rayleigh scattering. *Physics Today*, *35*(1), pp.42-48.

[5] Intravaia, F., Koev, S., Jung, I.W., Talin, A.A., Davids, P.S., Decca, R.S., Aksyuk, V.A., Dalvit, D.A. and López, D., 2013. Strong Casimir force reduction through metallic surface nanostructuring. *Nature Communications*, *4*(1), pp.1-8.

[6] Bennett, R., 2015. Spontaneous decay rate and Casimir-Polder potential of an atom near a lithographed surface. *Physical Review A*, *92*(2), p.022503.

[7] Novotny, L. and Henkel, C., 2008. Van der Waals versus optical interaction between metal nanoparticles. *Optics Letters*, *33*(9), pp.1029-1031.

[8] www.comsol.com

[9] Mosig, J.R. and Melcón, A.A., 2003. Green's functions in lossy layered media: Integration along the imaginary axis and asymptotic behavior. *IEEE Transactions on Antennas and Propagation*, *51*(12), pp.3200-3208.

[10] Mitrinovic, D.S. and Keckic, J.D., 1984. *The Cauchy Method of Residues: Theory And Applications* (Vol. 9). Springer Science & Business Media.

[11] Kemp, B.A., 2015. Macroscopic theory of optical momentum. *Progress in Optics*, *60*, pp.437-488.

[12] Rodríguez-Fortuño, F.J., Engheta, N., Martínez, A. and Zayats, A.V., 2015. Lateral forces on circularly polarizable particles near a surface. *Nature Communications*, *6*(1), pp.1-8.

[13] Girón-Sedas, J.A. and Rodríguez-Fortuño, F.J., 2020. Strong recoil optical forces on dipoles via high-k plasmons excitation in thin metallic films. *Applied Physics Letters*, *117*(18), p.181106.

[14] Paul, N.K. and Kemp, B.A., 2016. Optical manipulation of small particles on the surface of a material. *Journal of Optics*, *18*(8), p.085402.

[15] Paul, N.K. and Kemp, B.A., 2015. Push-pull phenomenon of a dielectric particle in a rectangular waveguide. *Progress In Electromagnetics Research*, *151*, pp.73-81.

[16] Paul, N.K. and Kemp, B.A., 2016. Optical pulling force on a particle near the surface of a dielectric slab waveguide. *Optical Engineering*, *55*(1), p.015106.

[17] Petrov, M.I., Sukhov, S.V., Bogdanov, A.A., Shalin, A.S. and Dogariu, A., 2016. Surface plasmon polariton assisted optical pulling force. *Laser & Photonics Reviews*, *10*(1), pp.116-122.

[18] Ashkin, A., Dziedzic, J.M., Bjorkholm, J.E. and Chu, S., 1986. Observation of a single-beam gradient force optical trap for dielectric particles. *Optics Letters*, *11*(5), pp.288-290.

[19] Bliokh, K.Y., Smirnova, D. and Nori, F., 2015. Quantum spin Hall effect of light. *Science*, *348*(6242), pp.1448-1451.

[20] Petersen, J., Volz, J. and Rauschenbeutel, A., 2014. Chiral nanophotonic waveguide interface based on spin-orbit interaction of light. *Science*, *346*(6205), pp.67-71.

[21] Lodahl, P., Mahmoodian, S., Stobbe, S., Rauschenbeutel, A., Schneeweiss, P., Volz, J., Pichler, H. and Zoller, P., 2017. Chiral quantum optics. *Nature*, *541*(7638), pp.473-480.

[22] Antognozzi, M., Bermingham, C.R., Harniman, R.L., Simpson, S., Senior, J., Hayward, R., Hoerber, H., Dennis, M.R., Bekshaev, A.Y., Bliokh, K.Y. and Nori, F., 2016. Direct measurements of the extraordinary optical momentum and transverse spin-dependent force using a nano-cantilever. *Nature Physics*, *12*(8), pp.731-735.

[23] Mosig, J.R. and Melcón, A.A., 2003. Green's functions in lossy layered media: Integration along the imaginary axis and asymptotic behavior. *IEEE Transactions on Antennas and Propagation*, *51*(12), pp.3200-3208.

[24] Mitrinovic, D.S. and Keckic, J.D., 1984. *The Cauchy method of residues: theory and applications* (Vol. 9). Springer Science & Business Media.

[25] Press, W.H., Teukolsky, S.A., Vetterling, W.T. and Flannery, B.P., 1996. *Numerical Recipes in Fortran 90: Numerical recipes in Fortran 77V. 2. Numerical recipes in Fortran 90*. Cambridge University Press.

[36] Gangaraj, S.A.H., Hanson, G.W., Silveirinha, M.G., Shastri, K., Antezza, M. and Monticone, F., 2019. Unidirectional and diffractionless surface plasmon polaritons on three-dimensional nonreciprocal plasmonic platforms. *Physical Review B*, *99*(24), p.245414.

[37] Lin, X., Xu, Y., Zhang, B., Hao, R., Chen, H. and Li, E., 2013. Unidirectional surface plasmons in nonreciprocal graphene. *New Journal of Physics*, *15*(11), p.113003.

[38] Correas-Serrano, D. and Gomez-Diaz, J.S., 2019. Nonreciprocal and collimated surface plasmons in drift-biased graphene metasurfaces. *Physical Review B*, *100*(8), p.081410.

[39] Paul, N.K. and Gomez-Diaz, J.S., 2021. Broadband and unidirectional plasmonic hyperlensing in drift-biased graphene. *Applied Physics Letters*, *118*(9), p.091107.

[40] Morgado, T.A. and Silveirinha, M.G., 2017. Negative Landau damping in bilayer graphene. *Physical Review Letters*, *119*(13), p.133901.

[41] Morgado, T.A. and Silveirinha, M.G., 2021. Active graphene plasmonics with a drift-current bias. *ACS Photonics*, *8*(4), pp.1129-1136.

[42] Dong, Y., Xiong, L., Phinney, I.Y., Sun, Z., Jing, R., McLeod, A.S., Zhang, S., Liu, S., Ruta, F.L., Gao, H. and Dong, Z., 2021. Fizeau drag in graphene plasmonics. *Nature*, *594*(7864), pp.513-516.

[43] Zhao, W., Zhao, S., Li, H., Wang, S., Wang, S., Utama, M., Kahn, S., Jiang, Y., Xiao, X., Yoo, S. and Watanabe, K., 2021. Efficient Fizeau drag from Dirac electrons in monolayer graphene. *Nature*, *594*(7864), pp.517-521.

[44] Bliokh, K.Y., Rodríguez-Fortuño, F.J., Bekshaev, A.Y., Kivshar, Y.S. and Nori, F., 2018. Electric-current-induced unidirectional propagation of surface plasmon-polaritons. *Optics Letters*, *43*(5), pp.963-966.

[45] Girón-Sedas, J.A., Kingsley-Smith, J.J. and Rodríguez-Fortuño, F.J., 2019. Lateral optical force on linearly polarized dipoles near a magneto-optical surface based on polarization conversion. *Physical Review B*, *100*(7), p.075419.

[46] Rodríguez-Fortuño, F.J., Vakil, A. and Engheta, N., 2014. Electric levitation using ϵ-near-zero metamaterials. *Physical Review Letters*, *112*(3), p.033902.

[47] Kingsley-Smith, J.J., Picardi, M.F. and Rodríguez-Fortuño, F.J., 2020. Optical magnetic dipole levitation using a plasmonic surface. *Nano Letters*, *20*(10), pp.7094-7099.

[48] Wu, Y., Zhang, C., Estakhri, N.M., Zhao, Y., Kim, J., Zhang, M., Liu, X.X., Pribil, G.K., Alù, A., Shih, C.K. and Li, X., 2014. Intrinsic optical properties and enhanced plasmonic response of epitaxial silver. *Advanced Materials*, *26*(35), pp.6106-6110.

.

Chapter 5: Giant Lateral Optical Forces Above Hyperbolic Metasurfaces

Light-induced forces have led to many exciting applications in nanotechnology and bioengineering by trapping, pushing, pulling, binding, and manipulating nanoparticles and biological samples [1-11]. Recently, the emergence of nano-optical plasmonic configurations has been exploited to boost the strength of optical forces at the nanoscale by exciting surface plasmon polaritons [12-15], which are confined electromagnetic waves traveling along dielectric-metal interfaces [16]. In fact, illuminating an electric, non-magnetic, located above a metallic surface like gold or silver with light induces optical forces on the particle that compensate the momentum of the directional SPPs excited in the scattering process, leading to a strong dependence between the induced forces and the wavenumber of the plasmons supported by the surface [17]. Such response has been further enhanced taking advantage of the quantum spin-Hall effect of light [18-22], exploiting the spin of circularly polarized incoming waves to control the excitation of directional plasmons and, in turn, the direction of the induced forces [23,24]. Over the years, a wide variety of devices have been put forward to shape these forces and merge them with other techniques such as surface-enhanced Raman spectroscopy (SERS) [25-29] or photoluminescence [30,31], aiming to select and handle nanoparticles after their individual characterization. Despite recent advances in this field [17,23,32,33], the exponential growth of nanophotonics and bioengineering is continuously imposing challenging demands to enhance the strength and control the direction of the forces induced on nanoparticles using low-intensity laser beams.

In a related context, hyperbolic metasurfaces [34-43] –which are ultrathin surfaces that exhibit metallic or dielectric responses as a function of the electric field polarization– have recently gathered considerable attention from the scientific community [37-39]. These structures significantly enhance the available local density of states, support the propagation of ultra-confined surface plasmons, and have empowered an ample set of near-field functionalities such as boosting the spontaneous emission rate of emitters located nearby [37], an unusual spin-control of light [40,41], or a wavelength-dependent routing of SPPs.

Hyperbolic metasurfaces can easily be realized using ultrathin nanostructured composites made of hexagonal boron nitride [36], silver [34], gold [42], graphene [40,43] and other two-dimensional materials [44,45]. Even though the bulk version of hyperbolic metasurfaces, hyperbolic metamaterials [46-48], have already been suggested to provide new knobs to augment optical forces [49-51], their relatively weak near-field interactions with external dipoles [52] and challenging fabrication process have hindered the use of hyperbolic structures in practical applications.

In this Chapter, I show that replacing standard plasmonic surfaces with hyperbolic or extremely anisotropic metasurfaces enhances the strength of the lateral optical forces induced on Rayleigh particles located nearby by several orders of magnitude. The enabling mechanisms are illustrated in Figure 4.1 in Chapter 4. Upon adequate plane wave illumination, the particle gets polarized [53] and behaves as an out-of-plane circularly polarized electric dipole that excites directional SPPs on the surface thanks to the

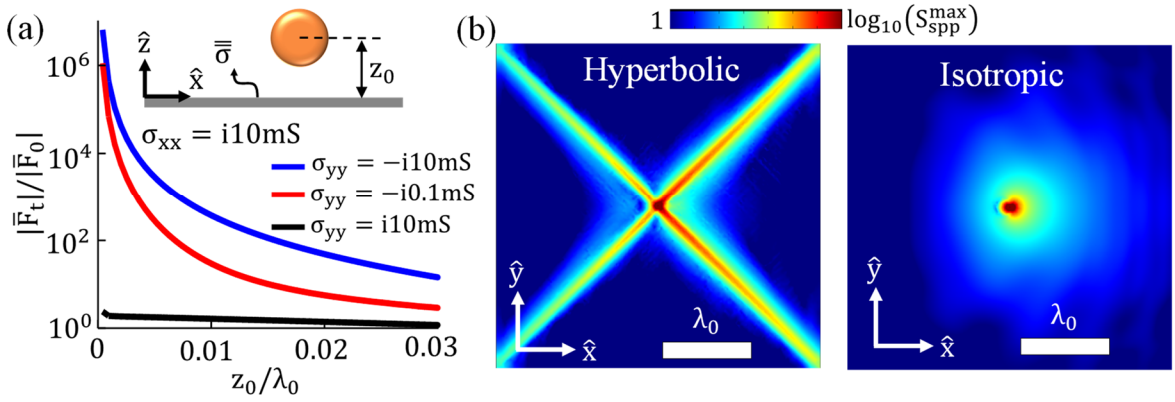

Figure 5.1: Lateral optical forces induced on an electrically polarizable Rayleigh particle located in free space at a distance z_0 over an anisotropic metasurface characterized by a conductivity tensor (see schematic in Figure 4.1 in Chapter 4). (a) Lateral optical forces induced on the particle versus its distance above isotropic (black line; with $\sigma_{xx} = \sigma_{yy} = i10$ mS), σ-near zero (red line; $\sigma_{xx} = i10$ mS, $\sigma_{yy} = -i0.1$ mS), and hyperbolic (blue line; $\sigma_{xx} = i10$ mS, $\sigma_{yy} = -i10$ mS) metasurfaces. Results are normalized with respect to the free-space scattering force $\bar{F}_0$. (b) Absolute magnitude of the normalized Poynting vector of the excited SPPs on the hyperbolic (left) and isotropic (right) metasurfaces. The particle is located at z_0=1 μm, has a radius $a = 15$ nm, relative permittivity $\varepsilon_p = 3$, and is illuminated by a TM plane wave at 8 THz coming from $\theta_i = 35^0$ and $\phi_i = 0^0$.

photonic spin-Hall effect [54,55] (see Figure 4.1 in Chapter 4). Due to the momentum conservation, a lateral

recoil force that strongly depends on the wavevector of the excited modes [17,23] is induced on the particle. Since the SPPs supported by hyperbolic metasurfaces possess very high wavenumbers compared to isotropic surfaces, the induced recoil forces over these structures are dramatically enhanced. Figure 5.1(a) shows that such enhancement is maximum in the very near field of the metasurface and progressively lessens as the nanoparticle moves away from it. In the following, I apply the formalism developed in Chapter 4 to compute the lateral optical forces acting on polarizable Rayleigh particles over anisotropic metasurfaces and describe the physical mechanisms that enable them. Then, I numerically demonstrate the presence of giant lateral optical forces over realistic hyperbolic metasurfaces made of nanostructured silver and an array of graphene strips, enabling a unique platform to route and trap nanoparticles with low-intensity laser beams.

5.1 ENHANCEMENT OF LATERAL OPTICAL FORCES

Let me consider a non-magnetic, electrically polarizable, and dielectric Rayleigh particle located at a distance z_0 over a reciprocal, linear, and anisotropic metasurface defined by the diagonal conductivity tensor $\overline{\overline{\sigma}} = \sigma_{xx}\hat{x}\hat{x} + \sigma_{yy}\hat{y}\hat{y}$ and is illuminated by a plane wave, as shown in Figure 4.1. The total lateral forces exerted on the particle can be computed from the radiation pressure and spin-induced recoil components as detailed in Chapter 4. These two components read as

$$F_t^0 = \frac{1}{2}k_t\left[\mathrm{Im}\{\alpha_{xx}\}|E_x^0|^2 + \mathrm{Im}\{\alpha_{yy}\}\left|E_y^0\right|^2 + \mathrm{Im}\{\alpha_{zz}\}|E_z^0|^2\right], \tag{5.1}$$

$$F_t^s = \frac{6\pi}{c_0 k_0^2}P_{rad}^{tz}\eta_m \mathrm{Im}\left[\frac{d}{dt}G_{tz}^s(\bar{r}_0, \bar{r}_0)\right], \tag{5.2}$$

Eq. (5.2) confirms that two mechanisms dominate the lateral recoil forces induced on the particle: (i) the helicity of the polarization induced on the particle; and (ii) the wavenumber of the supported plasmons, indirectly expressed in Eq. (5.2) through the imaginary part of the spatial derivative of the Green's function out of plane cross-terms at the particle position. It should be noted that Eq. (5.2) is general and applies to any surface provided the adequate Green's function. For instance, it can be applied to analyze isotropic plasmonic surfaces, as done in Ref. [17,23]. There, the helicity of the particle polarization was exploited to

convert the spin of incident circularly polarized light into lateral optical forces acting on the particles. In this Chapter, I replace such surfaces with hyperbolic metasurfaces aiming to significantly enhance the available density of states and, in turn, the strength of the induced lateral optical forces.

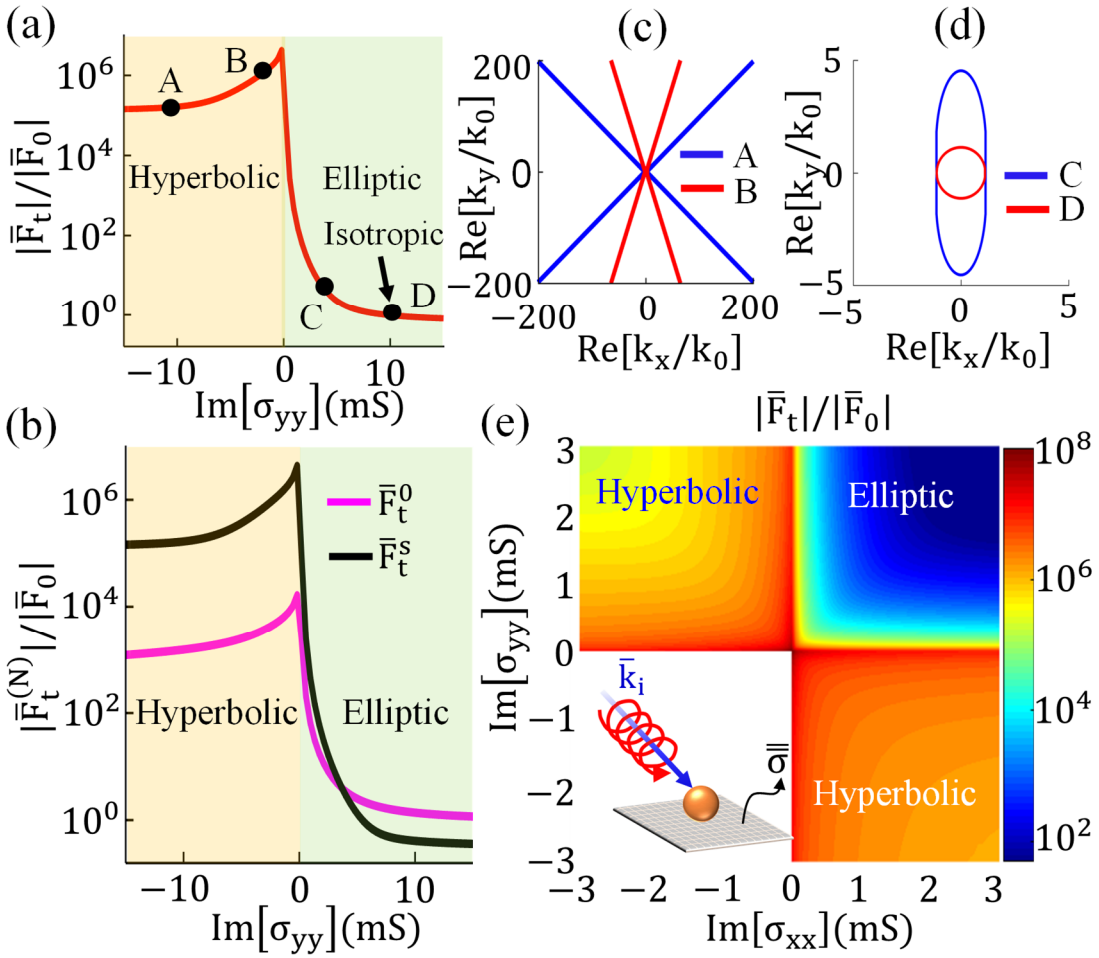

Figure 5.2: Influence of the metasurface topology on the lateral optical forces induced on a Rayleigh particle located 40nm above the metasurface and illuminated by a RHCP plane wave. (a) Forces induced on the particle versus the metasurface conductivity along the y axis, σ_{yy}, for a fixed $\sigma_{xx} = i10$ mS. (b) Contributions to the lateral optical force: radiation pressure ($\bar{F}_t^0$, magenta) and interaction force ($\bar{F}_t^s$, black). (c), (d) Isofrequency contours of the A, B, C, and D metasurface topologies shown in panel (a). (e) Lateral forces versus the conductivity components of a lossless anisotropic metasurface. Results are normalized with respect to the free-space scattering force F_0. Other parameters are as in Figure 5.1.

Figure 5.2 illustrates the influence of the metasurface anisotropy on the lateral forces acting on a Rayleigh particle located nearby under circularly polarized plane wave illumination. According to Eq. (5.2), such anisotropy bounds the maximum force attainable over a metasurface. Specifically, Figure 5.2(a) shows the lateral force $\bar{F}_t$ induced on the particle placed over a lossless metasurface with $\sigma_{xx} = i10$ mS (i.e., metallic response, similar to $\mathrm{Re}[\varepsilon_{xx}]<0$ in a bulk material) versus the conductivity along the y direction, σ_{yy}, thus analyzing all possible elliptical and hyperbolic topologies of the metasurfaces and going through its topological transition [35,37]. Figure 5.2(b) depicts a similar analysis but detailing the lateral radiation pressure ($\bar{F}_t^0$) and recoil ($\bar{F}_t^s$) force that compose $\bar{F}_t$. Results, normalized with respect to the free-space scattering force $\bar{F}_{\mathbf{0}}$, confirm a very large enhancement of the induced forces due to the strongly dominant response of the recoil force over hyperbolic metasurfaces (i.e., when $\mathrm{sign}\{\mathrm{Im}[\sigma_{xx}]\} \neq \mathrm{sign}\{\mathrm{Im}[\sigma_{yy}]\}$). Note that these metasurfaces support surface modes with high wavenumbers (see Figure 5.2c) that are directionally excited by the scattering from the polarized particle thanks to the spin-Hall effect, providing a giant recoil force. Maximum enhancement is found near the topological transition of the metasurface ($\mathrm{Im}[\sigma_{yy}] \approx 0$), which is a topology known to maximize the density of states [37]. However, the induced optical forces decrease for elliptical metasurfaces ($\mathrm{sign}\{\mathrm{Im}[\sigma_{xx}]\} = \mathrm{sign}\{\mathrm{Im}[\sigma_{yy}]\}$) due to the reduced density of states they provide and the limited wavenumber of the supported surface modes (see Figure 5.2d). Figure 5.2(e) shows the complete response exploring the lateral forces that appear over an anisotropic metasurface whose conductivity tensor components are simultaneously varied. The second and fourth quadrants of the figure show the response of hyperbolic metasurfaces, confirming enhancements larger than 6 orders of magnitude over the free space scattering force. Importantly, such enhancement is robust against moderate deviations in the metasurface anisotropy, thus alleviating potential fabrication challenges when realizing specific designs. The first quadrant of Figure 5.2(e) corresponds to elliptical metasurfaces that support transverse magnetic (TM) plasmons ($\mathrm{Im}[\sigma_{yy}] > 0$ and $\mathrm{Im}[\sigma_{xx}] > 0$) and provides significantly weaker optical forces than hyperbolic metasurfaces. In bulk media, similar plasmons are supported by materials whose real part of their relatively permittivity is negative [16]. It should be emphasized that as

the conductivity along one axis decreases, the induced forces increase due to the additional density of states provided by the structure and the larger wavenumbers of the supported SPPs. The limiting case appears again at the metasurface topological transition, where the induced optical forces reach their maximum value. Finally, the metasurfaces engineered in the third quadrant of Figure 5.2e support elliptical transverse electric (TE) surface modes weakly bounded to the surface and unable to induce significant optical forces on particles located nearby.

The strength and direction of the resulting lateral forces depend on the direction of the incident plane wave. Figure 5.3 investigates this scenario for the case of hyperbolic (top row) and extremely anisotropic, σ-near zero, (bottom row) metasurfaces. In the former case, the strength of the induced force is maximum

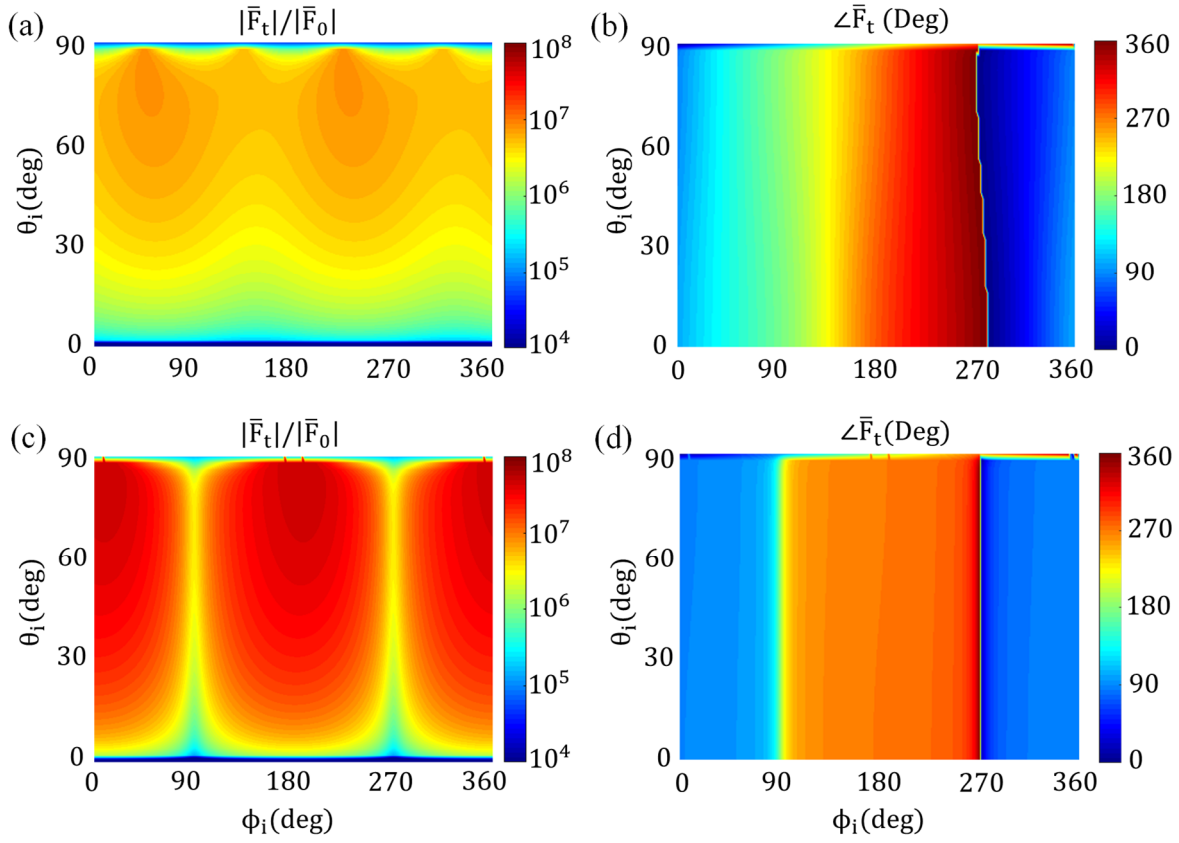

Figure 5.3: Influence of the direction of a RHCP plane wave on the strength (left column) and direction (right column) of the lateral forces induced on a particle located 40 nm above lossless hyperbolic ($\sigma_{xx} =$ i0.5 mS, $\sigma_{yy} =$ $-$ i0.5 mS, top row) and extremely anisotropic ($\sigma_{xx} =$ i0.5 mS, $\sigma_{yy} =$ $-$ i0.01 mS, bottom row) metasurfaces. Other parameters are as in Figure 5.1.

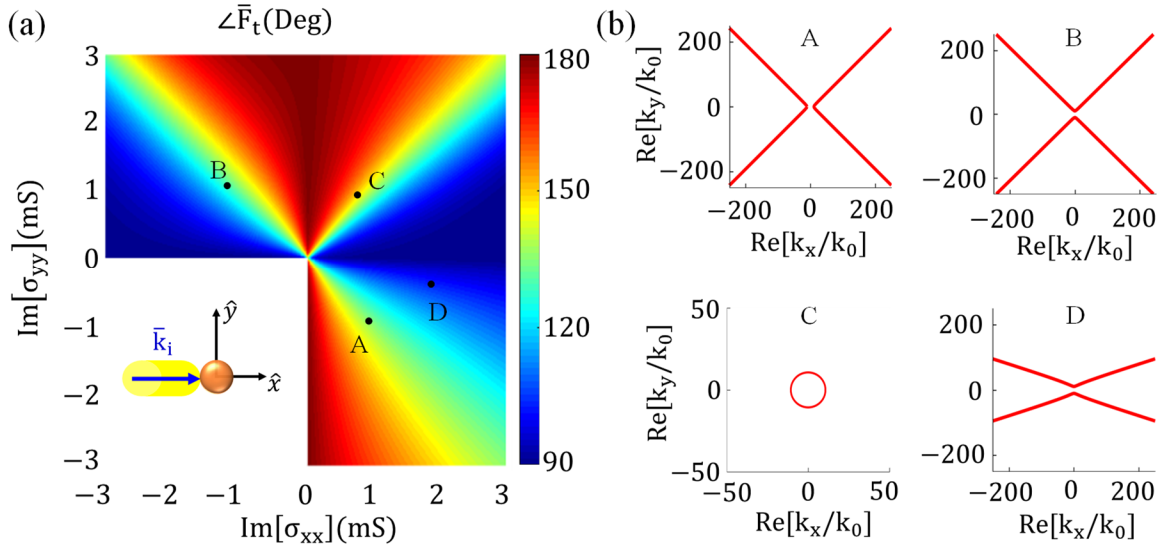

Figure 5.4: Influence of the metasurface anisotropy on the direction of the lateral optical forces induced on a Rayleigh particle located 40nm over the metasurface and illuminated by a RHCP plane wave coming from $\phi_i = 0^0$, $\theta_i = 35^0$ following the reference system shown in Fig. 1a of the main paper. Panel (b) depicts the isofrequency contours of the A, B, C and D metasurfaces shown in panel (a). Other parameters are as in Figure 5.1.

when the direction of the incident wave is aligned with the hyperbolic branches of the surface that exhibit similar polarization [45] ($\phi_i \approx 45^0, 225^0$ in this case), being significantly weaker along the orthogonal branches. In the latter, the force is maximum when the wave is aligned towards the canalization angle ($\phi_i = 0^0, 180^0$ in this case). In addition, it can be observed that the elevation of the plane wave (i.e., θ_i) also affects the strength of the induced force, finding its maximum relatively far away from the normal direction. Figure 5.4 completes this study by illustrating the influence of the metasurface anisotropy on the direction of the lateral force induced on the particle.

5.2 UNDERLYING MECHANISMS

The lateral recoil force as expressed in Eq. (5.2) depends on three main mechanisms: (i) the helicity of the particle polarization η_t along the t axis (with t={x,y}); (ii) the density of states provided by the metasurface; and (iii) the power radiated by the dipole.

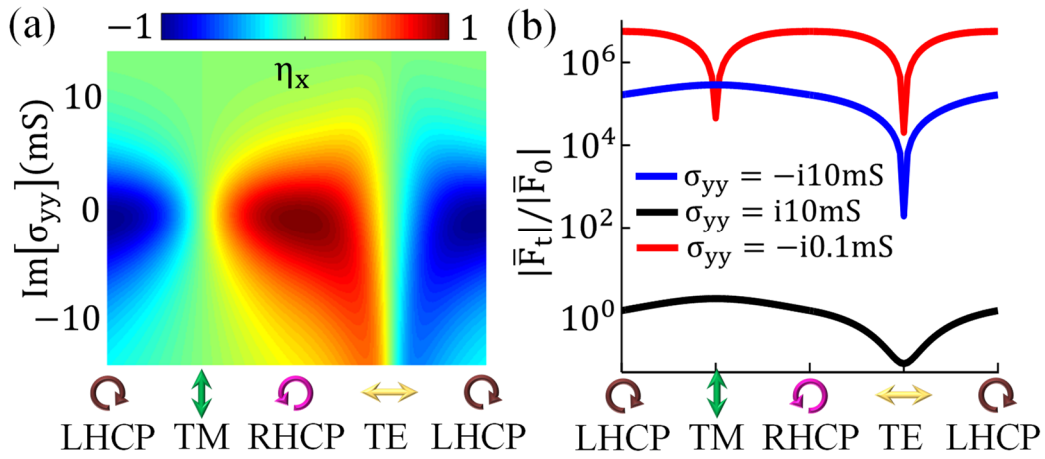

Figure 5.5: Influence of the polarization of an incident plane wave on the lateral optical forces induced on a Rayleigh particle located 40nm above a lossless anisotropic metasurface. (a) Particle polarization helicity with respect to the x direction (see Figure 5.1a). Results are plotted versus the metasurface conductivity along the y axis, σ_{yy}, for a fixed $\sigma_{xx} = i10$ mS. (b) Lateral forces induced on the particle when it is located above isotropic (black; with $\sigma_{xx} = \sigma_{yy} = i10$ mS), σ-near zero (red; $\sigma_{xx} = i10$ mS, $\sigma_{yy} = -i0.1$ mS), and hyperbolic (blue; $\sigma_{xx} = i10$ mS, $\sigma_{yy} = -i10$ mS) metasurfaces. The incoming plane wave has an axial ratio equal to 1 and polarization states that follows a circular trajectory on the Poincaré sphere. Other parameters are as in Figure 5.1.

5.2.1 HELICITY OF PARTICLE POLARIZATION

An important mechanism that originates recoil forces over reciprocal metasurfaces is the in-plane helicity of the polarization acquired by the particle. Specifically, the polarization spin around the x (y) axis induces optical forces towards the orthogonal axis within the plane, y (x), with a direction determined by the rotation handedness (see Eq. (5.2)). The maximum strength of the induced forces appears when the helicity is ± 1, corresponding to circularly polarized dipoles. In practice, the helicity depends on the direction and polarization state of the incoming plane wave, the anisotropy of the metasurfaces, and the distance between the particle and the structure.

As happens in the case of standard plasmonic surfaces [23], the polarization of the incident light plays a key role to tailor the helicity and to control the strength of the forces. To illustrate this behavior, Figure 5.5 shows the dipole polarization helicity around the x axis, η_x, versus the polarization state of the incoming

light and the metasurface conductivity value along the y axis, keeping constant the surface conductivity on the orthogonal axis (σ_{xx}). For the sake of simplicity, the incident light is aligned in this example with the x axis ($\phi_i = 0$), thus avoiding cross-polarization components on the reflected waves. The resulting helicity η_x is zero when the total electric field does not simultaneously exhibit components along the y and z axis to induce a spin around x, as happens in this case with incident TE and TM waves. On the contrary, plane waves with elliptical and right/left handed circular polarization (RHCP/LHCP) possess these field components and thus might polarize the particle with a desired spin. Interestingly, the helicity increases as $|\sigma_{yy}|$ gets closer to zero because the metasurface becomes almost transparent there and the particle acquires

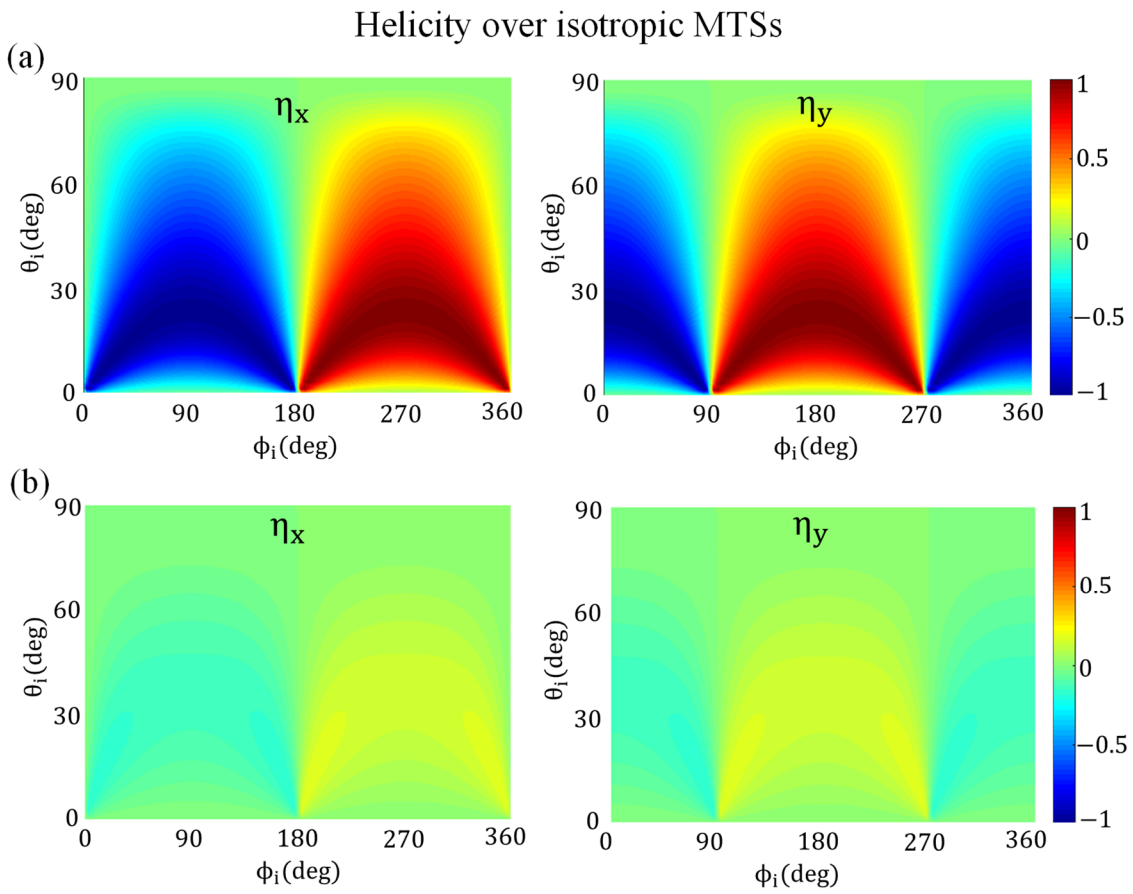

Figure 5.6: In-plane helicity of a Rayleigh particle located above an isotropic metasurface defined with a diagonal conductivity tensor of (a) $\sigma_{xx} = \sigma_{yy} = i10$ mS and (b) $\sigma_{xx} = \sigma_{yy} = i0.5$ mS versus the direction of propagation (θ_i, ϕ_i) of a TM-polarized incident plane wave. The particle is in free space at a distance $z_0 = \lambda_0/37$=1 μm over the metasurface, and other parameters are as in Figure 5.1.

the polarization of the incident light. As $|\sigma_{yy}|$ increases, the fields reflected from the structure interfere with the incident wave, thus altering the particle polarization. In such cases, the helicity can be enhanced by simply changing the angle of incidence of the incoming light. Note that the helicity around the y axis is only affected by the TM component of the incident light and therefore is constant $(\eta_y \approx -0.71)$ for all incident polarizations, except for purely TE waves, where it is strictly zero. Figure 5.5(b) shows the lateral optical forces induced on the particle versus the polarization of the incoming light. As expected, the induced lateral forces are minimum for incident TE waves $(|\bar{F}_t^s| = 0, |\bar{F}_t| = |\bar{F}_t^0|)$, whereas their maximum strength

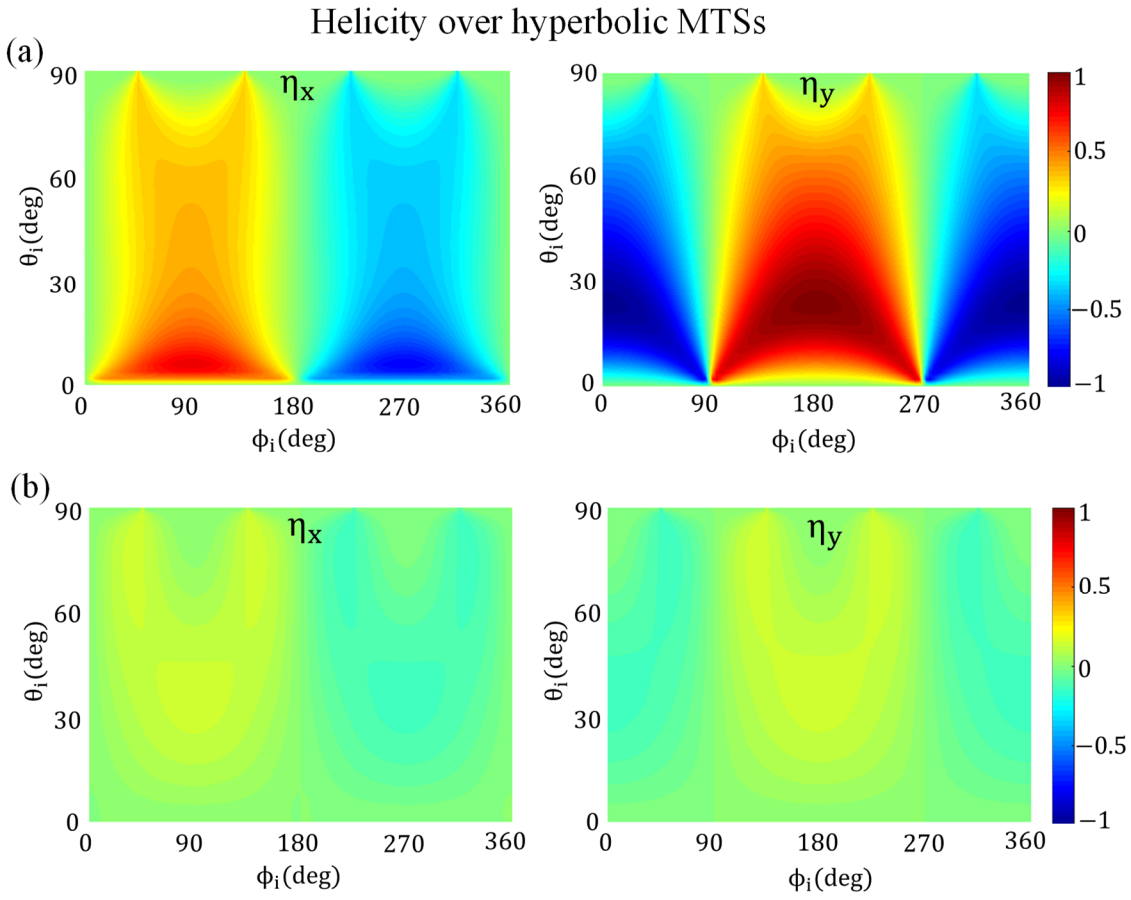

Figure 5.7: In-plane helicity of a Rayleigh particle located above an hyperbolic metasurface defined with a diagonal conductivity tensor of (a) $\sigma_{xx} = i10$ mS, $\sigma_{yy} = -i10$ mS and (b) $\sigma_{xx} = i0.5$ mS, $\sigma_{yy} = -i0.5$ mS versus the direction of propagation (θ_i, ϕ_i) of a TM-polarized incident plane wave. The particle is in free space at a distance $z_0 = \lambda_0/37$=1 μm over the metasurface, and other parameters are as in Figure 5.1.

depends on the interplay between the polarization states and the metasurface anisotropy. Overall, plane waves with specific combination of polarization state and angle of incidence should be used to adequately polarize the particle and maximize the strength of the induced optical forces.

Figures 5.6-5.8 explore the helicity of the particle polarization versus the direction of propagation of an incident plane wave with TM polarization considering isotropic, hyperbolic, and σ-near zero (i.e., an example of extremely anisotropic metasurface operated at this topological transition) metasurfaces, respectively. In all cases, the metasurface conductivity along the x axis, σ_{xx}, is kept constant and the

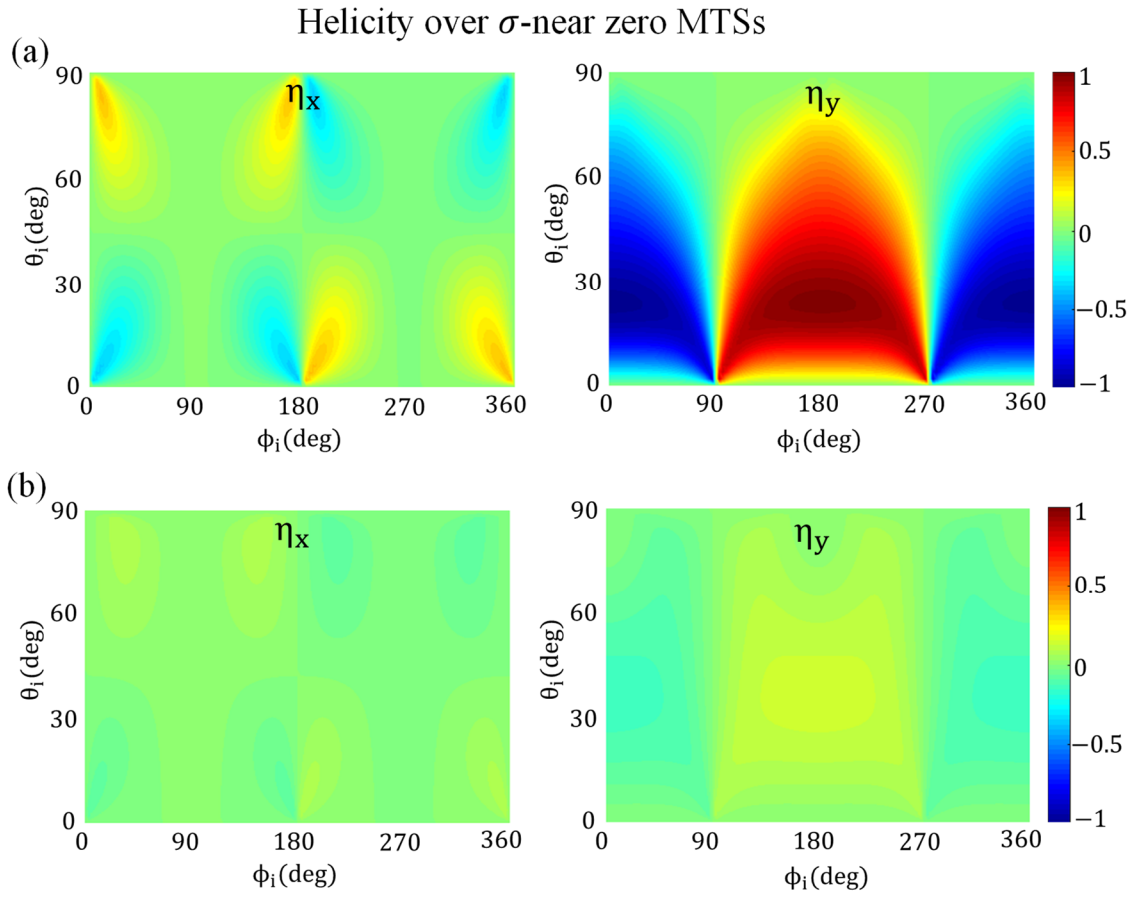

Figure 5.8: In-plane helicity of a Rayleigh particle located above an extremely anisotropic metasurface defined with a diagonal conductivity tensor of (a) $\sigma_{xx} = i10$ mS, $\sigma_{yy} = -i0.05$ mS and (b) $\sigma_{xx} = i0.5$ mS, $\sigma_{yy} = -i0.05$ mS versus the direction (θ_i, ϕ_i) of a TM-polarized incident plane wave. The particle is in free space at a distance $z_0 = \lambda_0/37$=1 μm over the metasurface, and other parameters are as in Figure 5.1.

different metasurface topologies are obtained by modifying the σ_{yy} component of the conductivity tensor. Figure 5.6 considers a particle located above an isotropic metasurface. In this case, the total in-plane helicity is independent of the azimuthal angle (ϕ_i) of the incoming wave (similar as in Ref. [23]). This is shown in the figure by the alternance in the maximum/minimum values of the particle polarization helicity with respect to the x and y axis. Specifically, when the incident plane wave is aligned towards the x axis ($\phi_i = 0°$), the helicity with respect to this axis is zero –there is no field along y that can induce the spin– but maximum along the y-axis. This situation is reversed when the incoming wave is aligned towards the y axis ($\phi_i = 90°$), because there the x-component of the incoming wave electric field vanishes. Figure 5.7 considers that the particle is located now over a hyperbolic metasurface. In this case, the helicity along the y axis is quite similar to the previous case because the metasurfaces have identical σ_{xx} values and the cross-polarization is small. However, note that the helicity along the x axis is reversed (i.e., it goes from RHCP to LHCP and vice-versa) with respect to the isotropic case, which is due to the polarization change (from inductive to capacitive) of the σ_{yy} conductivity component of the hyperbolic metasurface. In the last

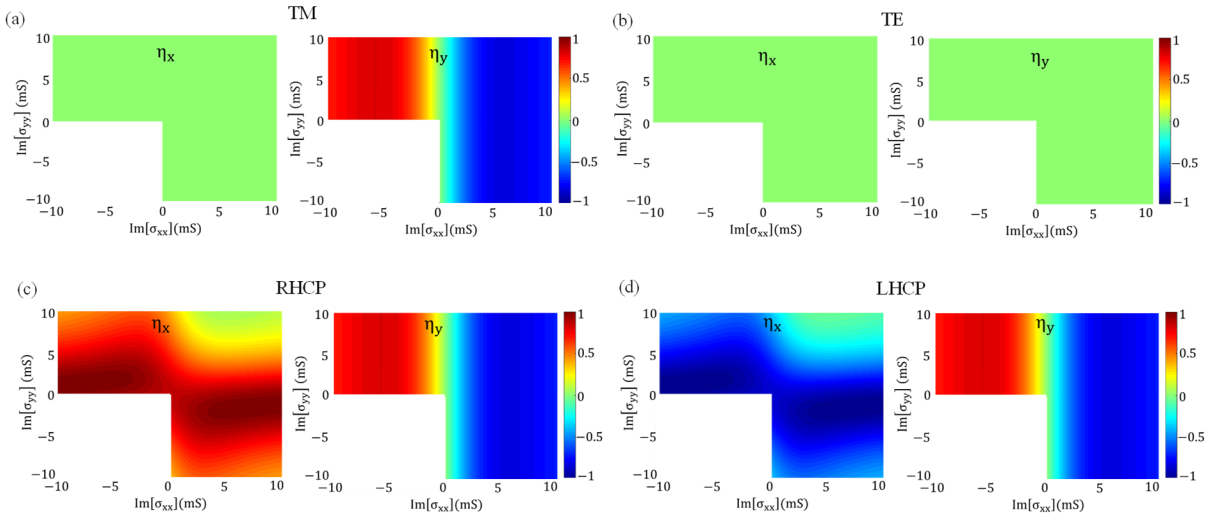

Figure 5.9: In-plane helicity of a Rayleigh particle located above an anisotropic metasurface versus the components of its diagonal conductivity tensor. The particle is illuminated by a plane wave coming from the direction $\theta_i = 35^0$ and $\phi_i = 0^0$ (the reference system is shown in Fig. 1a of the main paper) with a (a) TM; (b) TE; (c) RHCP; and (d) LHCP polarization. The particle is in free space at a distance $z_0 = \lambda_0/37$=1 μm over the metasurface, and other parameters are as in Figure 5.1.

example, Figure 5.8 considers the case of a particle over a σ-near zero metasurface. While the helicity along the y-axis again resembles the previous examples, its value along the x-axis is significantly damped. This is due to the near zero value of the σ_{yy} conductivity component, which prevents strong reflections of waves with this polarization. It should also be noted that larger conductivity values lead to higher helicity of the particle polarization.

Figure 5.9 investigates the helicity of a Rayleigh particle located above an anisotropic metasurface versus the components of the metasurface diagonal conductivity tensor. For the sake of simplicity, the particle is illuminated by a plane wave coming from the direction $\theta_i = 35^0$ and $\phi_i = 0^0$ (i.e., along the x axis). Panel (a) considers the case of an incoming wave with TM polarization. Results confirm that helicity around the x-axis is always zero. As noted above, this is because at $\phi_i = 0^0$ the y-component of the incident wave electric field is strictly zero and therefore it cannot induce any spin along the x-axis [54]. This scenario is different for the helicity along the y axis, which can take values up to $+1$ and -1 (i.e., RHCP and LHCP, respectively) for a wide variety of σ_{xx} conductivity components – I stress that σ_{yy} is not relevant in this case, since the TM wave does not have an electric field along the y direction. Panel (b) considers the case of an incident plane wave with TE polarization. In this case, the helicity is always zero independently of the metasurface topology. This is because TE waves do not exhibit any 'z' component (see Chapter 2) and therefore they cannot provide any in-plane spin angular momentum. Panels (c) and (d) consider the case of incoming plane waves with RHCP and LHCP, respectively. Results confirm that the helicity of the particle polarization around the x axis acquires similar polarization as the incoming CP waves possesses, which occurs due to the very small reflection from the metasurface. However, the other in-plane component of the helicity (along the y-axis) presents a response that depends on the σ_{xx} of the metasurface conductivity, similarly to what happens when the particle is illuminated by a TM plane wave. This response appears because only the TM component of the incoming CP waves interacts with the metasurface, and therefore the reflected waves acquire such polarization.

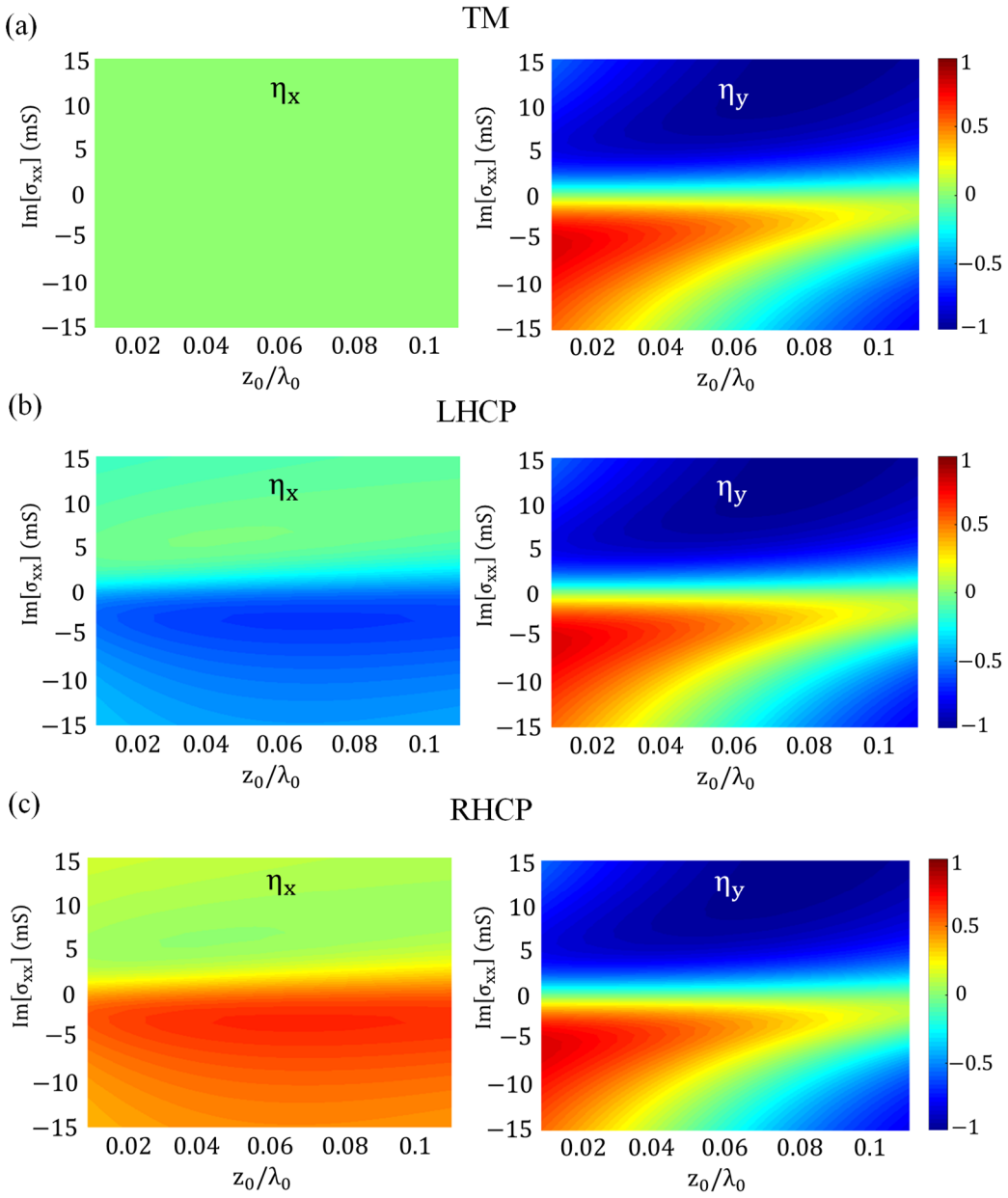

Figure 5.10: In-plane helicity of a Rayleigh particle versus its distance z_0 over an anisotropic metasurface and the σ_{xx} component of the surface conductivity. The conductivity along the y direction is kept constant and equal to σ_{yy} =i10 mS. The particle is illuminated by a plane wave coming from the direction $\theta_i = 35^0$ and $\phi_i = 0^0$ (reference system is shown in Fig. 1a of the main paper) with a (a) TM; (b) RHCP; and (c) LHCP. The particle is in free space at a distance $z_0 = \lambda_0/37$=1 μm over the metasurface, and other parameters are as in Figure 5.1.

Finally, Figure 5.10 depicts the smooth variation of the in-plane helicity versus the distance between the particle and the metasurface, considering different conductivity values of the surface along the x axis. It should be noted that this variation is more pronounced in case of hyperbolic metasurfaces because the free space behaves as a filter for the evanescent spectrum which dominate the response of these structures.

5.2.2 WAVENUMBER OF THE SUPPORTED SPPS

The main mechanism that enables giant lateral recoil force over anisotropic metasurfaces is related to the wavenumber of the surface plasmons supported by the structure, expressed in Eq. (5.2) through the spatial derivative of the scattered Green's function, and associated to the local density of states. It is important to stress that the recoil force can be expressed analytically in terms of the plasmon wavenumber when the metasurface is isotropic as detailed in Chapter 4. In the case of hyperbolic metasurfaces, such analytical treatment becomes much complicated, and it is beyond the scope of this thesis. However, the strength of the recoil force always directly depends on the plasmon wavenumber independent of the metasurface topologies.

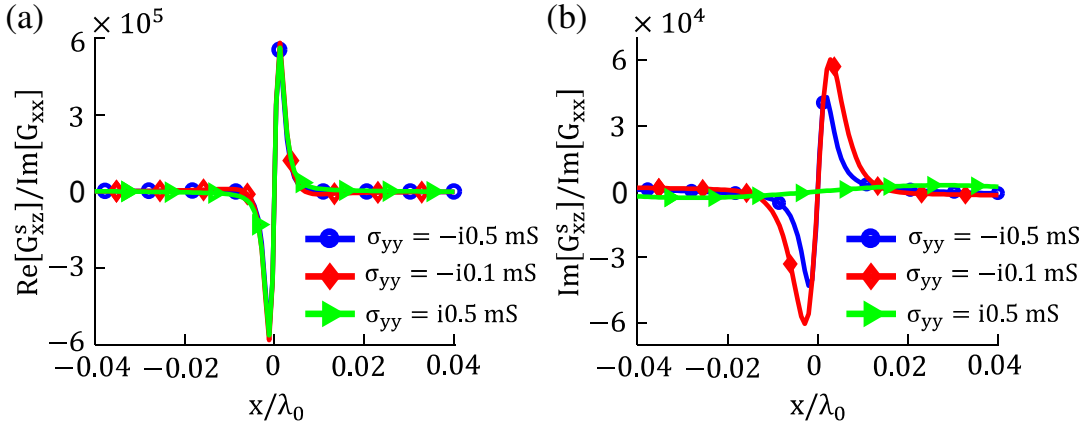

Figure 5.11: xz-component of the scattered Green's function tensor of an emitter located at $\bar{r}_0 = 0\hat{x} + 0\hat{y} + 40\hat{z}$ (nm) over an anisotropic metasurface, plotted along an observation line that goes through the x-axis and crosses the source position. (a) Real part. (b) Imaginary part. Results are computed for hyperbolic ($\sigma_{xx} = i0.5$ mS and $\sigma_{yy} = -i0.5$ mS, blue line), extremely anisotropic ($\sigma_{xx} = i0.5$ mS and $\sigma_{yy} = -i0.05$ mS, red line) and isotropic ($\sigma_{xx} = i0.5$ mS and $\sigma_{yy} = i0.5$ mS , green line) metasurfaces, and are normalized with respect to the imaginary part of the free space Green's function. Operation frequency is set to 8 THz.

Let me consider an electric point dipole located above an anisotropic metasurface. Figure 5.11 shows the real and imaginary part of the $G^s_{xz}(\bar{r}, \bar{r}_0)$, i.e., the xz component of the scattered dyadic Green's function, plotted along the x axis -and crossing through the source position- for three different lossless metasurfaces: isotropic, hyperbolic, and σ-near zero. Results are normalized with respect to the imaginary part of the free-space Green's function $G^0(\bar{r}, \bar{r}_0)$ [16] to avoid the singular behavior of the function at the emitter location. Panel (a) shows that the real component of $G^s_{xz}(\bar{r}, \bar{r}_0)$ is an odd function with respect to the source position, with similar behavior for the three metasurfaces considered here due to their identical conductivity along the x axis, σ_{xx}. Panel (b) plots a similar study for the imaginary component of the Green's function, i.e., $\mathrm{Im}[G^s_{xz}(\bar{r}, \bar{r}_0)]$. This function is also odd, crossing through zero at the source position. Very importantly, the slope of such crossing is determined by the metasurface anisotropy and the wavenumber of the supported modes. The inset of Figure 5.11(b) confirms that the slope of $\mathrm{Im}[G^s_{xz}(\bar{r}, \bar{r}_0)]$ at the source position is significantly steeper as the topology of the metasurface changes from isotropic to hyperbolic/σ-near zero.

Figure 5.12 shows the spatial derivate of $\mathrm{Im}[G^s_{xz}(\bar{r}, \bar{r}_0)]$ along the x direction at exactly the source position, $\bar{r}_0$. Results (normalized with respect to the imaginary part of the free space Green's function to

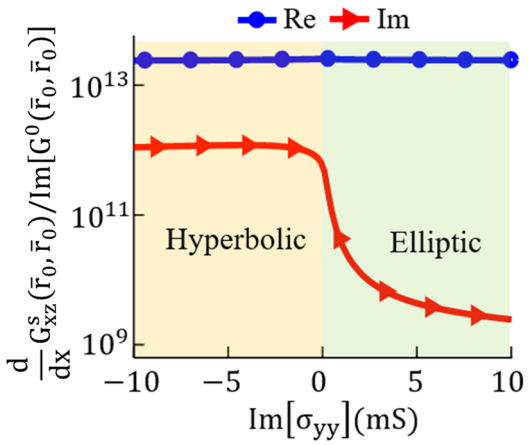

Figure 5.12: Real and imaginary parts of the G^s_{xz} spatial derivative along x, computed at exactly the source position. The emitter is located at $\bar{r}_0 = 0\hat{x} + 0\hat{y} + 40\hat{z}$ (nm) over an anisotropic metasurface. Results are plotted versus the metasurface conductivity along the y-axis (σ_{yy}), keeping σ_{xx}=i0.5 mS, and the operation frequency is 8 THz.

avoid the influence of the source singularity) are plotted versus the conductivity along the y axis (σ_{yy}), keeping σ_{xx} constant. As expected, the real part of the function does not depend on the metasurface topology. However, the imaginary part of the derivative drastically increases –several orders of magnitude– when the metasurface topology changes from isotropic to hyperbolic, a response related to the significant enhancement of the density of states provided by these structures. This is fully consistent with the analysis in Chapter 4: the imaginary part of the derivative enhances dramatically with the plasmon wavenumber.

I stress that the lateral forces induced on particles near anisotropic metasurfaces are directly proportional to the term $\mathrm{Im}\left[\frac{dG^{S}_{xz}(\bar{r},\bar{r}_0)}{dx}\right]$, as explicitly described in Eq. (5.2). Therefore, by tailoring this parameter through the metasurface anisotropy, the induced optical forces can be significantly boosted.

5.2.3 POWER RADIATED BY THE PARTICLE

The last parameter that controls the interaction force is related to the total power radiated by the dipole moment induced on the particle. Figure 5.13 investigates such power versus the metasurface response

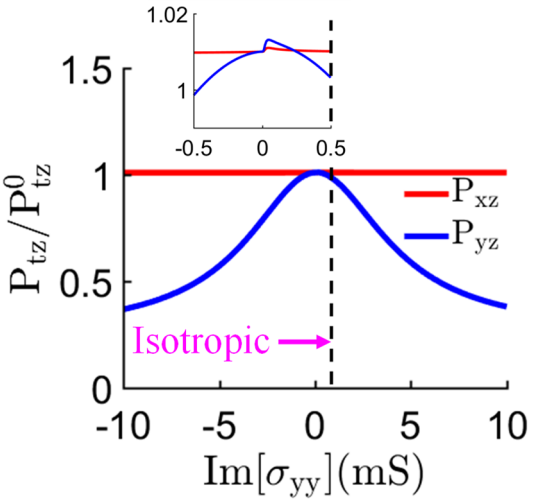

Figure 5.13: Total power radiated by the xz and yz components of the polarized particle versus the σ_{yy} component of the metasurface keeping σ_{xx} fixed at i0.5 mS. The power is computed assuming that the particle has been polarized in the presence of the metasurface and then radiates in free space. Results are normalized with respect to the power radiated by the same particle when it is polarized in free space. Other parameters are as in Figure 5.1.

(similarly as in Figure 5.12). Results are normalized with respect to the power radiated by the same particle when it is polarized in free-space. It can be observed that the presence of the anisotropic metasurface modifies the total amount of radiated power, but only up to a limited extend. Specifically, the dipole radiates slightly more power when the structure presents a σ-near-zero response and decreases when the absolute value of one component of the metasurface conductivity tensor increases. Similar responses can be found for other configurations.

This study demonstrates that the power radiated by the dipole moment components involved in the recoil force does not significantly increase due to the presence of extremely anisotropy or hyperbolic metasurface. In particular, the enhancement of optical forces acting over Rayleigh particles located near anisotropic and hyperbolic metasurfaces can only be attributed to the density of states provided by such structures.

5.3 ADDITIONAL FEATURE OF LATERAL AND VERTICAL FORCES

In this section, I explore the influence of metasurface loss and particle properties on the total lateral force response to assess the viability of hyperbolic metasurfaces in practice.

5.3.1 INFLUENCE OF PLATFORM LOSS

The presence of loss in anisotropic metasurfaces reduces the strength of the optical forces induced on Rayleigh particles located nearby. To explore the loss influence, Figure 5.14 plots the total lateral forces induced on a particle versus the amount of loss of the metasurface, considering hyperbolic and σ-near zero topologies. Results confirm that the force strength decreases with larger loss. This response arises because the isofrequency contour of anisotropic metasurface shrinks as loss increases (see panels (b) and (c) in the figure), thus limiting the local density of states provided by the structure.

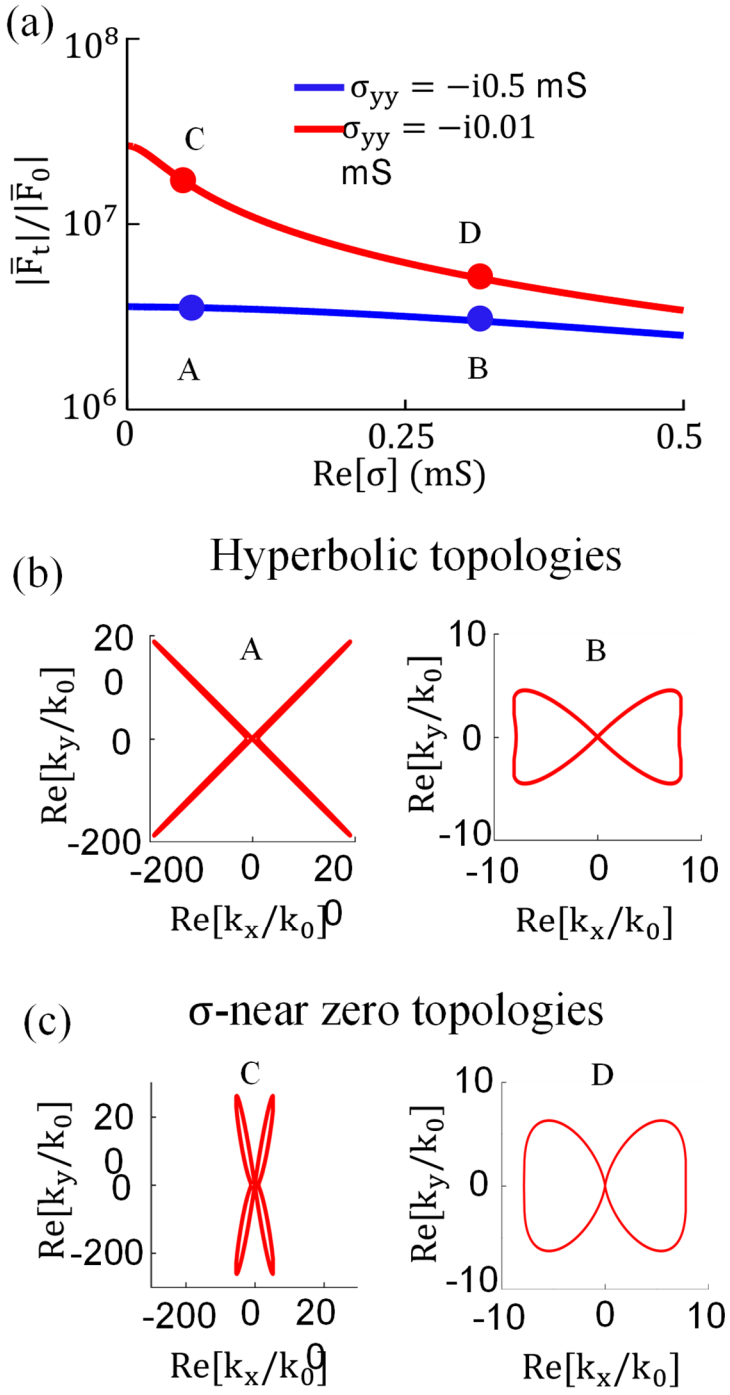

Figure 5.14: Influence of loss in the strength of the lateral forces induced on a Rayleigh particle located 40nm over hyperbolic (blue line; σ_{xx} = i0.5 mS, $\sigma_{yy} = -i0.5$ mS) and σ-near-zero (red line; σ_{xx} = i0.5 mS, $\sigma_{yy} = -i0.01$ mS) metasurfaces. Results are normalized with respect to the free space scattering force. Panel (c) and (d) illustrate the isofrequency contour of the metasurfaces highlighted in panel (b). Other parameters are as in Figure 5.1.

5.3.2 INFLUENCE OF PARTICLE PROPERTIES

The enhancement of the lateral optical forces induced on Rayleigh particles located over anisotropic metasurfaces as a function of the size and relatively permittivity of the particles is shown in Figure 5.15. Intuitively, the enhancement becomes smaller for larger particles due to the increased electrical distance between the particle and the metasurface. In addition, such enhancement is not sensitive to the electrical properties such as relative permittivity of the particle.

5.4 LATERAL FORCES ABOVE REALISTIC CONFIGURATION

Hyperbolic metasurfaces operating in the visible spectrum – frequency range in which optical tweezers are usually operated – have been experimentally realized using single-crystal silver nanostructures [34]. Here, I numerically investigate the lateral optical forces acting on an electric Rayleigh particle located over such structure when it is illuminated by a plane wave with RHCP polarization, as illustrated in Figure 5.16(a). Figure 5.16(b) depicts the strength of the induced forces, normalized with respect to the power radiated by the dipole in free space when it is polarized in the absence of the metasurface, versus frequency

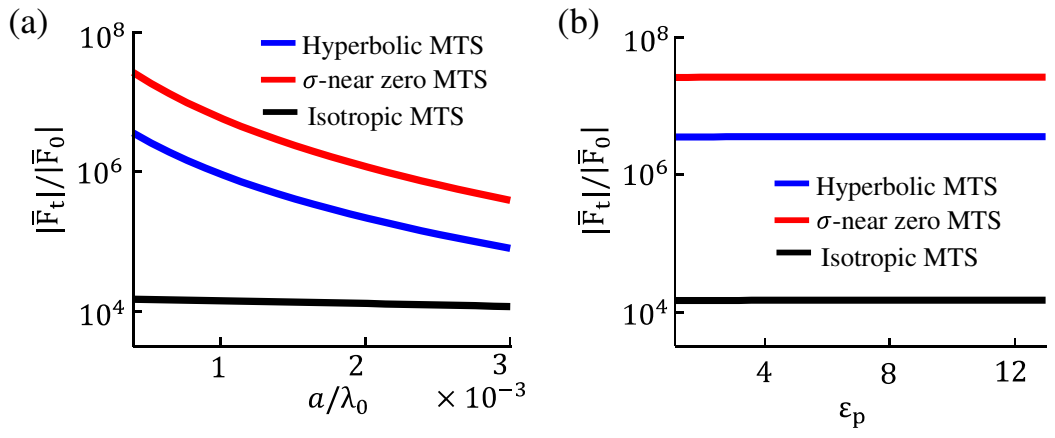

Figure 5.15: Strength of the lateral optical forces induced on a Rayleigh particle located at z_0=r+25nm (being r the particle radius) over hyperbolic (blue line; $\sigma_{xx} = i0.5$ mS, $\sigma_{yy} = -i0.5$ mS), σ-near zero (red line; $\sigma_{xx} = i0.5$ mS, $\sigma_{yy} = -i0.01$ mS) and isotropic (black line; $\sigma_{xx} = \sigma_{yy} = i0.5$ mS) metasurfaces. Results are plotted versus the particle (a) radius, keeping the permittivity fixed to $\varepsilon_p = 3$; and (b) relative permittivity, keeping the radius fixed to a = 15 nm. Other parameters are as in Figure 5.1.

and compares it to the one obtained when the hyperbolic metasurface is replaced with bulk silver [57]. Numerical results obtained using COMSOL Multiphysics [58] confirm that the hyperbolic structure induces lateral optical forces with a strength more than three orders of magnitude larger than silver over a broadband

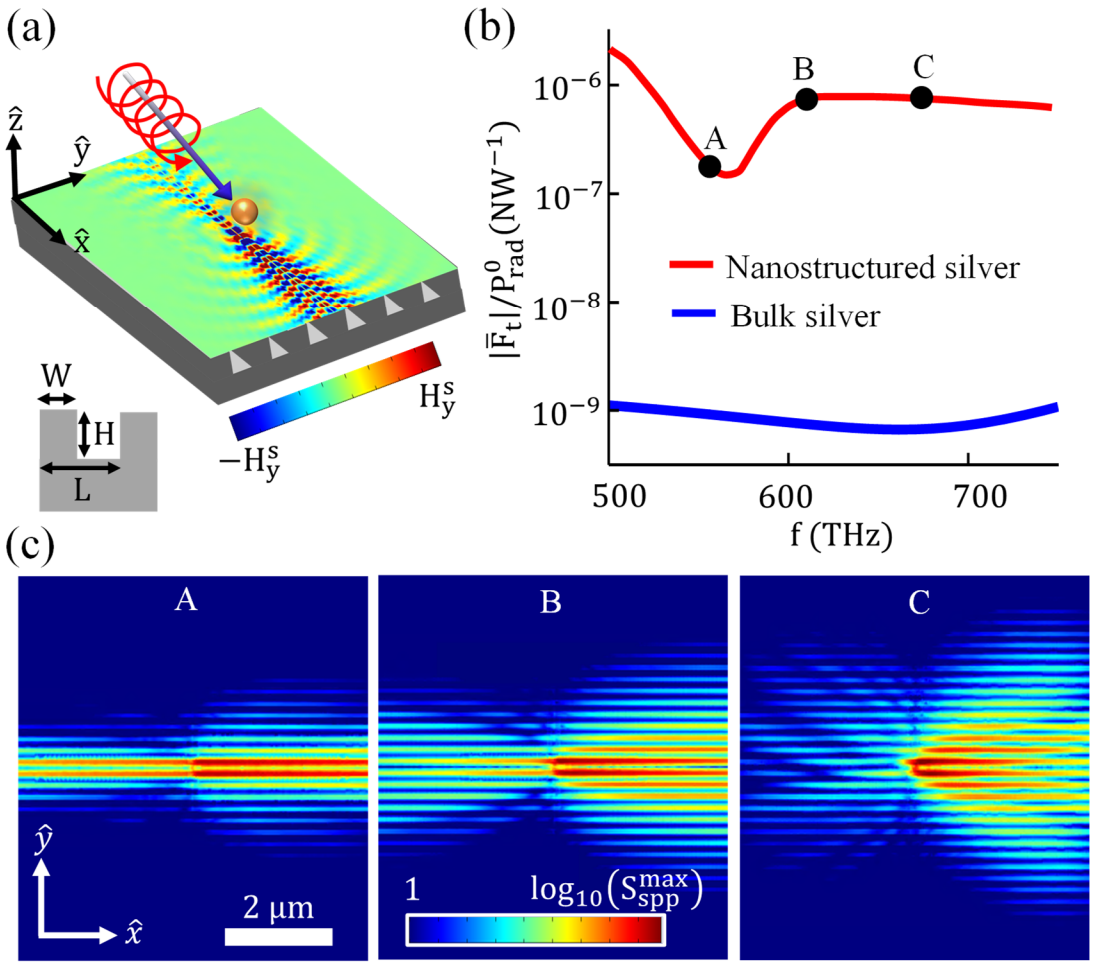

Figure 5.16: Lateral optical forces on a Rayleigh particle located 25 nm above nanostructured silver. (a) 3D schematic, showing an incident RHCP plane wave coming from $\theta_i = 35^0$ and $\phi_i = 0^0$. Superimposed field plot illustrates the y-component of the magnetic field excited on the structure (not to scale) at 612 THz due to the scattering process. (b) Lateral optical forces induced on the particle, normalized with respect to the power radiated by the particle when it is polarized in free space, plotted versus frequency. Results obtained when the particle is located above bulk silver are included for comparison purposes. (c) Absolute magnitude of the normalized Poynting vector on the metasurface at the operation frequencies shown in panel (b). The particle has a radius r=15 nm and relative permittivity $\varepsilon_p = 3$. The metasurface dimensions are W = 120 nm, H=80 nm, and L = 180 nm.

frequency range (from 500 to 750 THz). It is important to highlight that such enhancement is independent

to the electrical properties of the dipolar particles and that similar responses can be obtained using light with different polarization states and coming from other directions. Figure 5.16(c) illustrates the magnitude of the Poynting vector of the fields scattered by the particle plotted exactly on top of the metasurface at

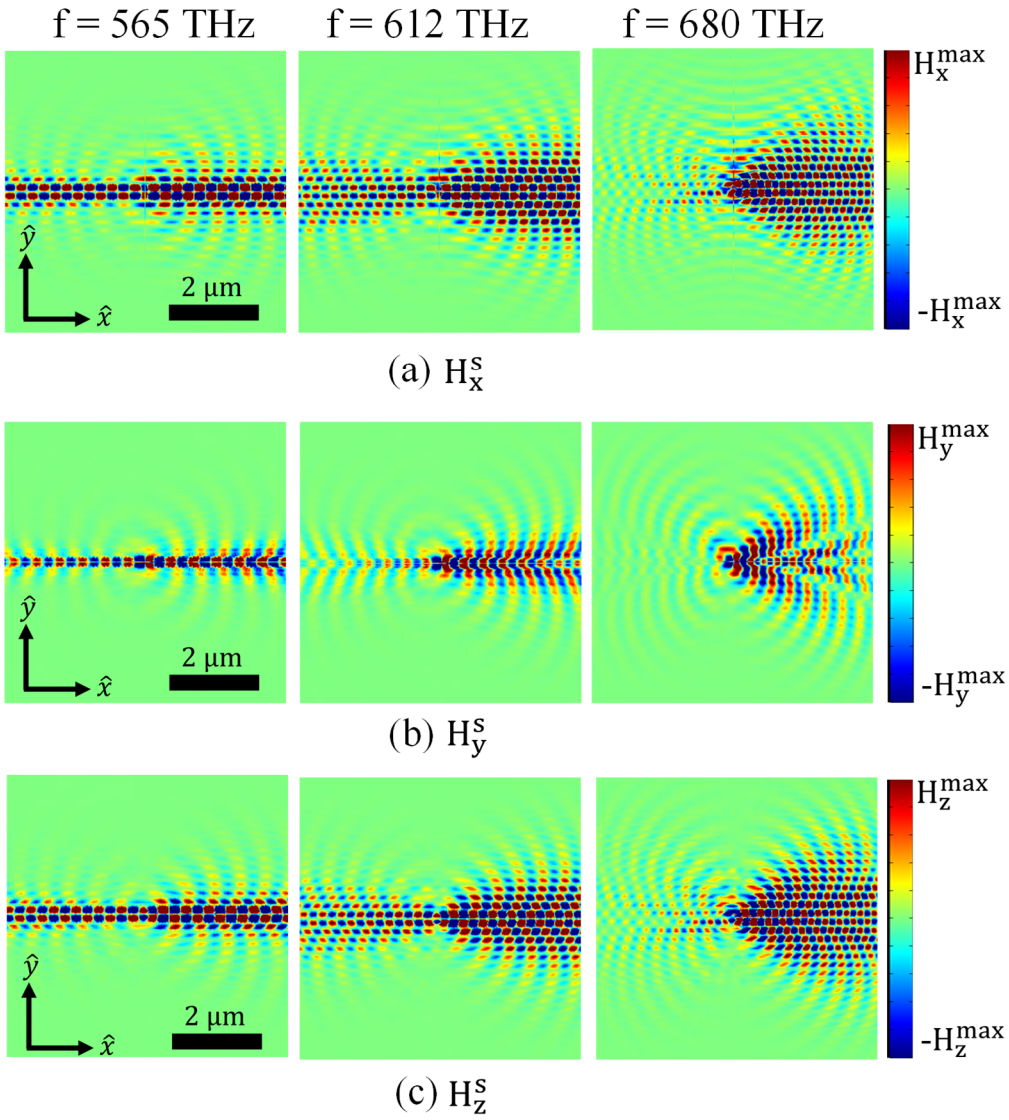

Figure 5.17: Magnetic field components (H_x^s-top row, H_y^s-middle row and H_z^s-bottom row) of the surface modes excited by the light scattered on a particle located above the nanostructured silver surface. Results are computed for different operation frequencies, 565 THz (left column), 612 THz (middle column), and 680 THz (right column). The particle is illuminated by a right-handed circularly polarized incident plane wave coming from $\phi_i = 0^0$, $\theta_i = 35^0$. Other parameters are as in Figure 5.16. Results have been obtained with COMSOL Multiphysics.

different operation frequencies, confirming the directional excitation of highly confined surface modes. Inspecting these power plots, it is easy to observe the evolution of the metasurface topology from σ-near-zero to hyperbolic as frequency increases. Remarkably, the strength of the reported forces is even larger (up to 11 times) than the one found over bulk silver at its plasmonic resonance – located in the near ultraviolet at ~890 THz [16]. Note that the silver nanostructure considered here is designed to operate at visible frequencies [34] and it does not behave as a homogeneous metasurface in that band. Besides, such strength is comparable to the one appearing on strongly chiral particles in the presence of evanescent fields [59]. For the sake of completeness, Figure 5.17 shows the magnetic-field components of the surface modes excited by the scattering process at different frequencies. Inspecting these scattered fields, it is clear the evolution of the metasurface topology from σ-near zero to hyperbolic as frequency increases.

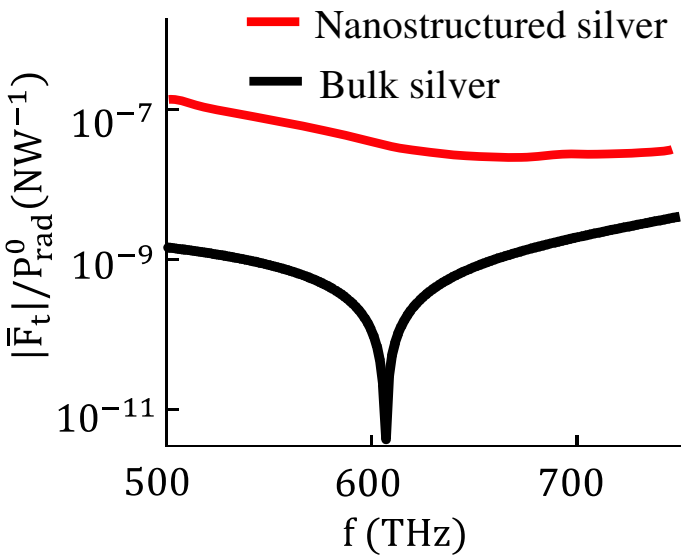

Figure 5.18: Normalized lateral optical forces on a Rayleigh particle located 25 nm above the nanostructured silver surface, computed with COMSOL Multiphysics. The particle is illuminated with an incident TM plane wave coming from $\theta_i = 35^0$ and $\phi_i = 0^0$. Results obtained when the particle is located above bulk silver are included for comparison purposes. Other parameters are as in Figure 5.16.

It is instructive to analyze the response of lateral forces induced on the particle versus the azimuthal angle of incidence ϕ_i and polarization state of the incoming plane wave. Figure 5.18 plots the force strength when the polarization of the wave (still aligned along the x axis, i.e., $\phi_i = 0°$) is changed to TM. Results confirm that, even though the forces induced on the particle are still significantly larger than those found over bulk silver, their strength have diminished almost two orders of magnitude with respect to the case where the particle was illuminated with CP light. This response appears because the y-component of the local electric field acting on the particle is strictly zero (note that there is no cross-polarization at the surface), thus vanishing the helicity of the polarization around the x axis (see Figure 5.9) and therefore nulling the y-component of the induced force. In addition, the incident and reflected TM wave cannot effectively polarize the particle in the yz plane, thus leading to a limited overall strength of the lateral force. Figure 5.19 shows the forces induced on the particle versus the azimuthal angle of incidence for several polarization states of the incident plane wave. In case of incident TM waves, the strength of the forces increases with the azimuthal angle of incidence. This enhancement appears because the local electric field

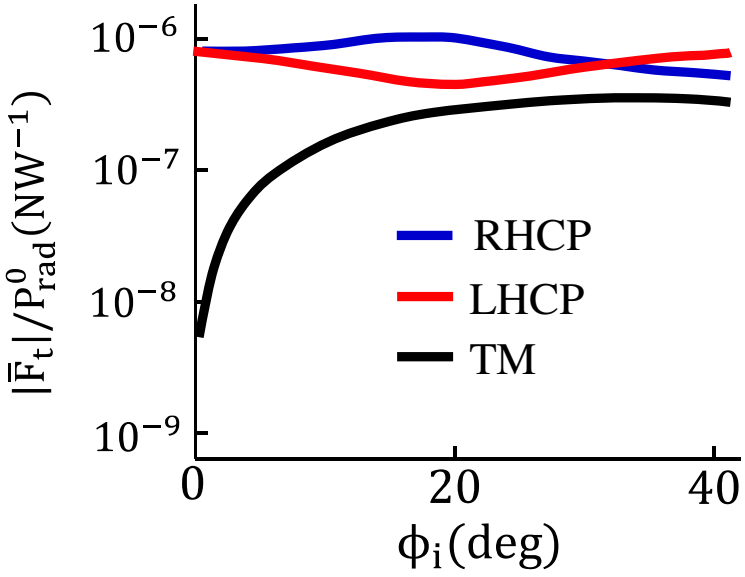

Figure 5.19: Strength of the normalized lateral optical forces induced on a Rayleigh particle located 25nm above the nanostructured silver surface versus the azimuthal angle of incidence ϕ_i of a plane wave at 650 THz coming from $\theta_i = 35^0$. Results, computed with COMSOL Multiphysics, are plotted for different polarization states of the wave, including RHCP (blue line), LHCP (red line), and TM (black line). Other parameters are as in Figure 5.16.

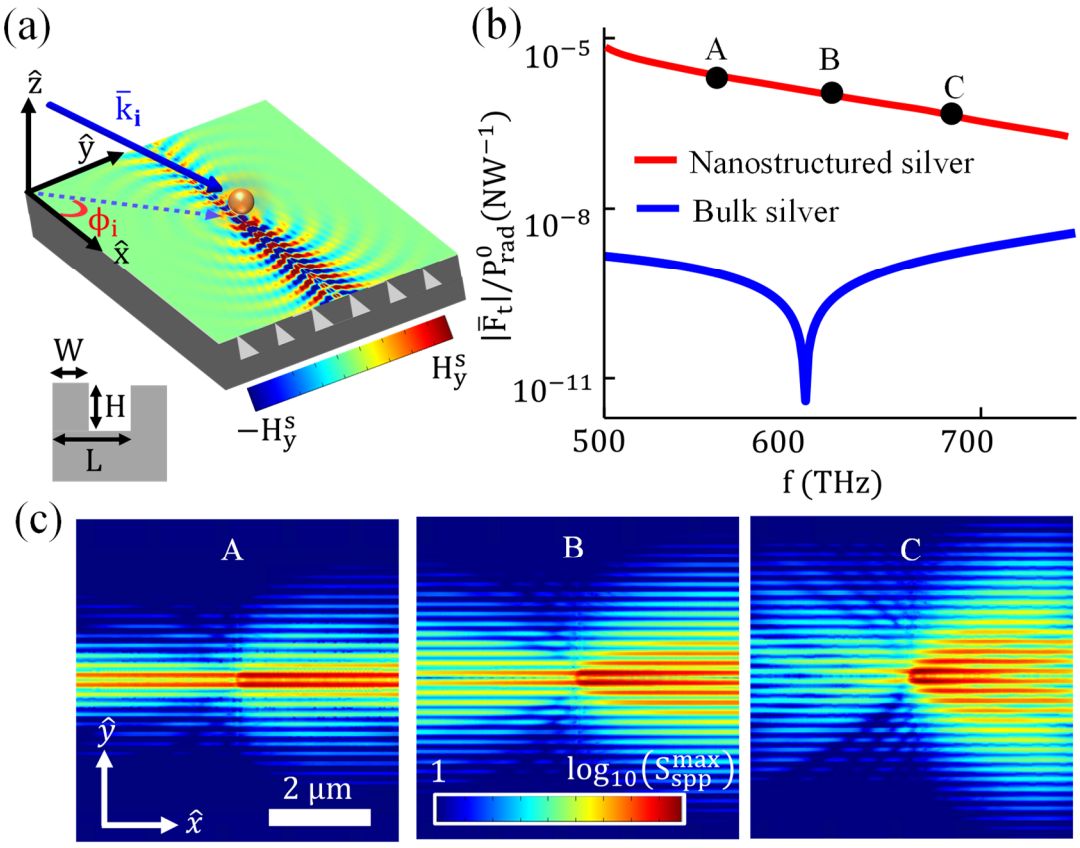

Figure 5.20: Lateral optical forces on a Rayleigh particle located 25 nm above the nanostructured silver surface. Results have been obtained with COMSOL Multiphysics. (a) 3D schematic, showing an incident TM plane wave coming from $\theta_i = 35^0$ and $\phi_i = 25^0$. Superimposed field plot illustrates the y-component of the magnetic field excited on the structure at 612 THz due to the scattering process. (b) Normalized lateral optical forces induced on the particle versus frequency. Additional data when the particle is located above bulk silver is included for comparison purposes. (c) Absolute magnitude of the normalized Poynting vector on the metasurface at the operation frequencies shown in panel (b). Other parameters are as in Figure 5.16.

has now all three components, enabling a more effective out-of-plane polarization of the particle. It should also be noted that incident plane waves with RHCP and LHCP induce optical forces on the particle with a smooth dependence on the azimuthal angle of incidence. Note that this study has been carried out at 650THz, where the nanostructured silver surface exhibits an almost σ-near zero topology.

Figure 5.20 illustrates the lateral optical forces induced on a Rayleigh particle located over the nanostructured silver surface when it is illuminated with a TM plane wave coming from $\phi_i = 25°$. Results

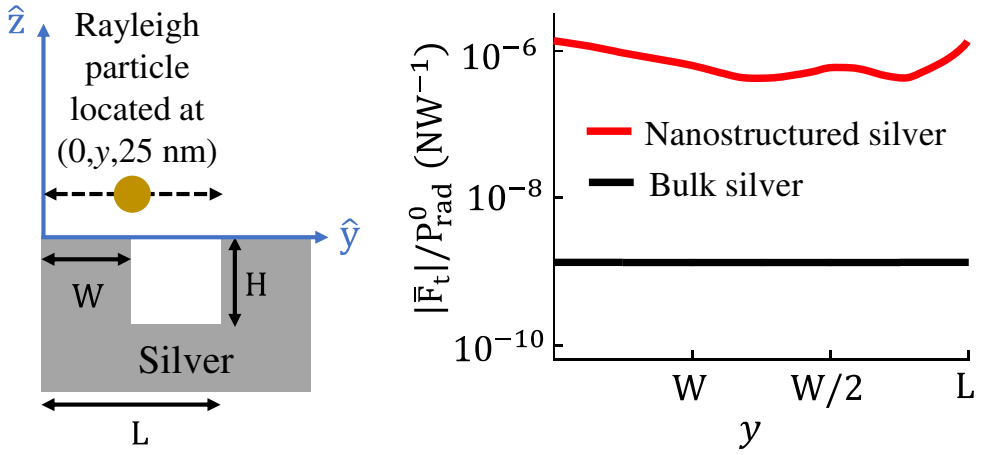

Figure 5.21: Lateral optical forces, normalized by the power radiated by the dipole when it is polarized in free space, induced on a Rayleigh particle versus its position over a strip within a periodically nanostructured silver structure that behaves as a hyperbolic metasurfaces. Operation frequency is 750 THz. Other parameters are as in Figure 5.16.

confirm that the induced forces are three orders of magnitude larger than over bulk silver for a broad frequency band. This study highlights that the strength of the forces found over hyperbolic and extremely anisotropic metasurface can be maximized by employing laser beams with adequate sets of polarization state and angle of incidence.

Finally, Figure 5.21 shows the optical forces induced on Rayleigh particle versus its position over one strip within the periodically nanostructured silver structure. Results confirm that the induced forces barely depend on the position of the particle within the surface.

5.5 CHAPTER CONCLUSIONS

In conclusion, I have reported a giant enhancement of lateral optical forces acting on electrically polarizable Rayleigh particles located near hyperbolic and extremely anisotropic metasurfaces. The enhancement is enabled by the interplay between the increased density of states provided by these structures and the in-plane helicity of the polarization acquired by the particle. Theoretical and numerical results confirm that the induced optical forces are broadband, robust against fabrication tolerances, and quite

resilient to loss. Hyperbolic and extremely anisotropic metasurfaces can be realized in different frequency bands to provide boosted lateral optical forces, using, for instance, nanostructured silver in the visible or nanostructured graphene in the terahertz and infrared bands. My analysis is based on a classical electromagnetic approach that neglects other potential source of forces such as fluctuation induced, thermal, or quantum [65-67]. However, the very large enhancement of the reported optical forces and the fact that they appear over a broad frequency band strongly suggest that this response is of fundamental nature. In addition, I expect that anisotropic metasurfaces will also greatly influence fluctuation-induced forces since they depend on the same scattering problem analyzed here. These findings might have significant implications in practice. In particular, hyperbolic metasurfaces seem ideal candidates to construct highly performing nano-optical tweezers to precisely manipulate and trap nanoparticles as well as assembling them through optical binding, allowing to significantly reduce the intensity of the required laser beams and to prevent damaging due to photoheating. Furthermore, the large density of states provided by these structures will boost phenomena such as SERS and photoluminescence, finding exciting applications in fields such as nanophotonics, bioengineering and biochemistry.

5.6 CHAPTER REFERENCES

[1] Ashkin, A., 1970. Acceleration and trapping of particles by radiation pressure. *Physical Review Letters*, *24*(4), p.156.

[2] Ashkin, A., Dziedzic, J.M., Bjorkholm, J.E. and Chu, S., 1986. Observation of a single-beam gradient force optical trap for dielectric particles. *Optics Letters*, *11*(5), pp.288-290.

[3] Ashkin, A. and Dziedzic, J.M., 1987. Optical trapping and manipulation of viruses and bacteria. *Science*, *235*(4795), pp.1517-1520.

[4] Ashkin, A., Dziedzic, J.M. and Yamane, T., 1987. Optical trapping and manipulation of single cells using infrared laser beams. *Nature*, *330*(6150), pp.769-771.

[5] Chen, J., Ng, J., Lin, Z. and Chan, C.T., 2011. Optical pulling force. *Nature Photonics*, *5*(9), pp.531-534.

[6] Svoboda, K. and Block, S.M., 1994. Biological applications of optical forces. *Annual Review of Biophysics And Biomolecular Structure*, *23*(1), pp.247-285.

[7] Grier, D.G., 2003. A revolution in optical manipulation. *Nature*, *424*(6950), pp.810-816.

[8] Grzegorczyk, T.M., Kemp, B.A. and Kong, J.A., 2006. Stable optical trapping based on optical binding forces. *Physical Review Letters*, *96*(11), p.113903.

[9] Dholakia, K. and Zemánek, P., 2010. Colloquium: Gripped by light: Optical binding. *Reviews Of Modern Physics*, *82*(2), p.1767.

[10] Juan, M.L., Gordon, R., Pang, Y., Eftekhari, F. and Quidant, R., 2009. Self-induced back-action optical trapping of dielectric nanoparticles. *Nature Physics*, *5*(12), pp.915-919.

[11] Gómez-Medina, R. and Sáenz, J.J., 2004. Unusually strong optical interactions between particles in quasi-one-dimensional geometries. *Physical Review Letters*, *93*(24), p.243602.

[12] Maragò, O.M., Jones, P.H., Gucciardi, P.G., Volpe, G. and Ferrari, A.C., 2013. Optical trapping and manipulation of nanostructures. *Nature Nanotechnology*, *8*(11), pp.807-819.

[13] Juan, M.L., Righini, M. and Quidant, R., 2011. Plasmon nano-optical tweezers. *Nature Photonics*, *5*(6), pp.349-356.

[14] Volpe, G., Quidant, R., Badenes, G. and Petrov, D., 2006. Surface plasmon radiation forces. *Physical Review Letters*, *96*(23), p.238101.

[15] Righini, M., Zelenina, A.S., Girard, C. and Quidant, R., 2007. Parallel and selective trapping in a patterned plasmonic landscape. *Nature Physics*, *3*(7), pp.477-480.

[16] Novotny, L. and Hecht, B., 2012. *Principles of nano-optics*. Cambridge university press.

[17] Petrov, M.I., Sukhov, S.V., Bogdanov, A.A., Shalin, A.S. and Dogariu, A., 2016. Surface plasmon polariton assisted optical pulling force. *Laser & Photonics Reviews*, *10*(1), pp.116-122.

[18] Bliokh, K.Y., Smirnova, D. and Nori, F., 2015. Quantum spin Hall effect of light. *Science*, *348*(6242), pp.1448-1451.

[19] Petersen, J., Volz, J. and Rauschenbeutel, A., 2014. Chiral nanophotonic waveguide interface based on spin-orbit interaction of light. *Science*, *346*(6205), pp.67-71.

[20] Lodahl, P., Mahmoodian, S., Stobbe, S., Rauschenbeutel, A., Schneeweiss, P., Volz, J., Pichler, H. and Zoller, P., 2017. Chiral quantum optics. *Nature*, *541*(7638), pp.473-480.

[21] Antognozzi, M., Bermingham, C.R., Harniman, R.L., Simpson, S., Senior, J., Hayward, R., Hoerber, H., Dennis, M.R., Bekshaev, A.Y., Bliokh, K.Y. and Nori, F., 2016. Direct measurements of the extraordinary optical momentum and transverse spin-dependent force using a nano-cantilever. *Nature Physics*, *12*(8), pp.731-735.

[22] Magallanes, H. and Brasselet, E., 2018. Macroscopic direct observation of optical spin-dependent lateral forces and left-handed torques. *Nature Photonics*, *12*(8), pp.461-464.

[23] Rodríguez-Fortuño, F.J., Engheta, N., Martínez, A. and Zayats, A.V., 2015. Lateral forces on circularly polarizable particles near a surface. *Nature Communications*, *6*(1), pp.1-8.

[24] Sukhov, S., Kajorndejnukul, V., Naraghi, R.R. and Dogariu, A., 2015. Dynamic consequences of optical spin–orbit interaction. *Nature Photonics*, *9*(12), pp.809-812.

[25] Thurn, R. and Kiefer, W., 1984. Raman-microsampling technique applying optical levitation by radiation pressure. *Applied Spectroscopy*, *38*(1), pp.78-83.

[26] Xie, C., Dinno, M.A. and Li, Y.Q., 2002. Near-infrared Raman spectroscopy of single optically trapped biological cells. *Optics Letters*, *27*(4), pp.249-251.

[27] Petrov, D.V., 2007. Raman spectroscopy of optically trapped particles. *Journal of Optics A: Pure and Applied Optics*, *9*(8), p.S139.

[28] Cherney, D.P. and Harris, J.M., 2010. Confocal Raman microscopy of optical-trapped particles in liquids. *Annual Review Of Analytical Chemistry*, *3*, pp.277-297.

[29] Kong, L., Lee, C., Earhart, C.M., Cordovez, B. and Chan, J.W., 2015. A nanotweezer system for evanescent wave excited surface enhanced Raman spectroscopy (SERS) of single nanoparticles. *Optics Express*, *23*(5), pp.6793-6802.

[30] Reece, P.J., Paiman, S., Abdul-Nabi, O., Gao, Q., Gal, M., Tan, H.H. and Jagadish, C., 2009. Combined optical trapping and microphotoluminescence of single InP nanowires. *Applied Physics Letters*, *95*(10), p.101109.

[31] Wang, F., Toe, W.J., Lee, W.M., McGloin, D., Gao, Q., Tan, H.H., Jagadish, C. and Reece, P.J., 2013. Resolving stable axial trapping points of nanowires in an optical tweezers using photoluminescence mapping. *Nano letters*, *13*(3), pp.1185-1191.

[32] Wang, S.B. and Chan, C.T., 2014. Lateral optical force on chiral particles near a surface. *Nature Communications*, *5*(1), pp.1-8.

[33] Wang, S. and Chan, C.T., 2016. Strong optical force acting on a dipolar particle over a multilayer substrate. *Optics Express*, *24*(3), pp.2235-2241.

[34] High, A.A., Devlin, R.C., Dibos, A., Polking, M., Wild, D.S., Perczel, J., De Leon, N.P., Lukin, M.D. and Park, H., 2015. Visible-frequency hyperbolic metasurface. *Nature*, *522*(7555), pp.192-196.

[35] Gomez-Diaz, J.S., Tymchenko, M. and Alù, A., 2015. Hyperbolic metasurfaces: surface plasmons, light-matter interactions, and physical implementation using graphene strips. *Optical Materials Express*, *5*(10), pp.2313-2329.

[36] Li, P., Dolado, I., Alfaro-Mozaz, F.J., Casanova, F., Hueso, L.E., Liu, S., Edgar, J.H., Nikitin, A.Y., Vélez, S. and Hillenbrand, R., 2018. Infrared hyperbolic metasurface based on nanostructured van der Waals materials. *Science*, *359*(6378), pp.892-896.

[37] Gomez-Diaz, J.S., Tymchenko, M. and Alu, A., 2015. Hyperbolic plasmons and topological transitions over uniaxial metasurfaces. *Physical Review Letters*, *114*(23), p.233901.

[38] Kildishev, A.V., Boltasseva, A. and Shalaev, V.M., 2013. Planar photonics with metasurfaces. *Science*, *339*(6125), p.1232009.

[39] Smalley, J.S.T., Vallini, F., Montoya, S.A., Ferrari, L., Shahin, S., Riley, C.T., Kanté, B., Fullerton, E.E., Liu, Z. and Fainman, Y., 2017. Luminescent hyperbolic metasurfaces. *Nature Communications*, *8*(1), pp.1-8.

[40] Gomez-Diaz, J.S. and Alu, A., 2016. Flatland optics with hyperbolic metasurfaces. *ACS Photonics*, *3*(12), pp.2211-2224.

[41] Yermakov, Y., Ovcharenko, A.I., Bogdanov, A.A., Iorsh, I.V., Bliokh, K.Y. and Kivshar, Y.S., 2016. Spin control of light with hyperbolic metasurfaces. *Physical Review B*, *94*(7), p.075446.

[42] Yermakov, O.Y., Permyakov, D.V., Porubaev, F.V., Dmitriev, P.A., Samusev, A.K., Iorsh, I.V., Malureanu, R., Lavrinenko, A.V. and Bogdanov, A.A., 2018. Effective surface conductivity of optical hyperbolic metasurfaces: from far-field characterization to surface wave analysis. *Scientific Reports*, *8*(1), pp.1-10.

[43] Gusynin, V.P. and Sharapov, S.G., 2006. Transport of Dirac quasiparticles in graphene: Hall and optical conductivities. *Physical Review B*, *73*(24), p.245411.

[44] Correas-Serrano, D., Gomez-Diaz, J.S., Melcon, A.A. and Alù, A., 2016. Black phosphorus plasmonics: anisotropic elliptical propagation and nonlocality-induced canalization. *Journal of Optics*, *18*(10), p.104006.

[45] Correas-Serrano, D., Alù, A. and Gomez-Diaz, J.S., 2017. Plasmon canalization and tunneling over anisotropic metasurfaces. *Physical Review B*, *96*(7), p.075436.

[46] Poddubny, A., Iorsh, I., Belov, P. and Kivshar, Y., 2013. Hyperbolic metamaterials. *Nature Photonics*, *7*(12), pp.948-957.

[47] Iorsh, I.V., Mukhin, I.S., Shadrivov, I.V., Belov, P.A. and Kivshar, Y.S., 2013. Hyperbolic metamaterials based on multilayer graphene structures. *Physical Review B*, *87*(7), p.075416.

[48] Drachev, V.P., Podolskiy, V.A. and Kildishev, A.V., 2013. Hyperbolic metamaterials: new physics behind a classical problem. *Optics Express*, *21*(12), pp.15048-15064.

[49] Ginis, V., Tassin, P., Soukoulis, C.M. and Veretennicoff, I., 2013. Enhancing optical gradient forces with metamaterials. *Physical Review Letters*, *110*(5), p.057401.

[50] Zhao, R., Tassin, P., Koschny, T. and Soukoulis, C.M., 2010. Optical forces in nanowire pairs and metamaterials. *Optics Express*, *18*(25), pp.25665-25676.

[51] Bogdanov, A.A., Shalin, A.S. and Ginzburg, P., 2015. Optical forces in nanorod metamaterial. *Scientific Reports*, *5*(1), pp.1-9.

[52] Miller, O.D., Johnson, S.G. and Rodriguez, A.W., 2014. Effectiveness of thin films in lieu of hyperbolic metamaterials in the near field. *Physical Review Letters*, *112*(15), p.157402.

[53] Zemánek, P., Jonáš, A., Šrámek, L. and Liška, M., 1999. Optical trapping of nanoparticles and microparticles by a Gaussian standing wave. *Optics Letters*, *24*(21), pp.1448-1450.

[54] Rodríguez-Fortuño, F.J., Marino, G., Ginzburg, P., O'Connor, D., Martínez, A., Wurtz, G.A. and Zayats, A.V., 2013. Near-field interference for the unidirectional excitation of electromagnetic guided modes. *Science*, *340*(6130), pp.328-330.

[55] O'connor, D., Ginzburg, P., Rodríguez-Fortuño, F.J., Wurtz, G.A. and Zayats, A.V., 2014. Spin–orbit coupling in surface plasmon scattering by nanostructures. *Nature Communications*, *5*(1), pp.1-7.

[56] Lakhtakia, A., 1992. Green's functions and Brewster condition for a halfspace bounded by an anisotropic impedance plane. *International Journal of Infrared And Millimeter Waves*, *13*(2), pp.161-170.

[57] Wu, Y., Zhang, C., Estakhri, N.M., Zhao, Y., Kim, J., Zhang, M., Liu, X.X., Pribil, G.K., Alù, A., Shih, C.K. and Li, X., 2014. Intrinsic optical properties and enhanced plasmonic response of epitaxial silver. *Advanced Materials*, *26*(35), pp.6106-6110.

[58] www.comsol.com

[59] Hayat, A., Mueller, J.B. and Capasso, F., 2015. Lateral chirality-sorting optical forces. *Proceedings of the National Academy of Sciences*, *112*(43), pp.13190-13194.

[60] Garcia de Abajo, F.J., 2014. Graphene plasmonics: challenges and opportunities. *ACS Photonics*, *1*(3), pp.135-152.

[61] Gómez-Díaz, J.S. and Perruisseau-Carrier, J., 2013. Graphene-based plasmonic switches at near infrared frequencies. *Optics Express*, *21*(13), pp.15490-15504.

[62] Esquius-Morote, M., Gómez-Dı, J.S. and Perruisseau-Carrier, J., 2014. Sinusoidally modulated graphene leaky-wave antenna for electronic beamscanning at THz. *IEEE Transactions on Terahertz Science and Technology*, *4*(1), pp.116-122.

[63] Gómez-Díaz, J.S., Esquius-Morote, M. and Perruisseau-Carrier, J., 2013. Plane wave excitation-detection of non-resonant plasmons along finite-width graphene strips. *Optics Express*, *21*(21), pp.24856-24872.

[64] Chen, P.Y., Huang, H., Akinwande, D. and Alu, A., 2014. Graphene-based plasmonic platform for reconfigurable terahertz nanodevices. *ACS Photonics*, *1*(8), pp.647-654.

[65] Intravaia, F., Koev, S., Jung, I.W., Talin, A.A., Davids, P.S., Decca, R.S., Aksyuk, V.A., Dalvit, D.A. and López, D., 2013. Strong Casimir force reduction through metallic surface nanostructuring. *Nature Communications*, *4*(1), pp.1-8.

[66] Bennett, R., 2015. Spontaneous decay rate and Casimir-Polder potential of an atom near a lithographed surface. *Physical Review A*, *92*(2), p.022503.

[67] Novotny, L. and Henkel, C., 2008. Van der Waals versus optical interaction between metal nanoparticles. *Optics Letters*, *33*(9), pp.1029-1031.

Chapter 6: Engineering Optical Traps Above Anisotropic Metasurfaces

Optical trapping of small particles in the micrometer range has triggered numerous applications in microbiology [1-3], colloidal dynamics [4], and lab-on-a-chip applications [5], among many others [6-9]. In conventional optical tweezers [10-13], an optical trap is set through a tightly focused laser beam that confines the particle near the higher electric field intensity. There, the gradient of the electric field intensity that surrounds the particle generates the required trapping forces. Unfortunately, it is challenging to extend this approach to trap particles whose size is particularly in the nanometer range as (i) the gradient force significantly lessens with the third power of the particle size [14]; and (ii) the thermal fluctuation induced motion of the particles increases [15,16], thus favoring them to escape from the trap. As a result, stable trapping demands high-intensity and tightly focused laser beams that may damage the nanoparticles due to photoheating.

In this context, recoil force has recently been exploited to trap nanoparticles near bulk metals using a linearly polarized Gaussian beam [17]. This elegant approach takes advantage of the peculiar distribution of the electric field within the beam: the components parallel to the surface are even-symmetric with respect to the laser beam axis whereas the out-of-plane component is odd-symmetric. The interplay between even/odd symmetries of the in-/out-of- plane electric field components enforces that the nanoparticle acquires an out-of-plane polarization spin with a rotation handedness always pointing away from the beam axis that excites SPPs toward this direction. This response holds independently of the particle position within the beam. The combination of recoil force coming from the excitation of directional SPPs in the scattering process together with gradient force originating from the Gaussian beam generates an optical trap located exactly at the beam axis [17]. Unfortunately, this platform might not be suitable for many practical applications because it requires specific laser sources operating at wavelengths very close to the intrinsic plasmon resonance frequency of metals. As the laser operation frequency is shifted away from such

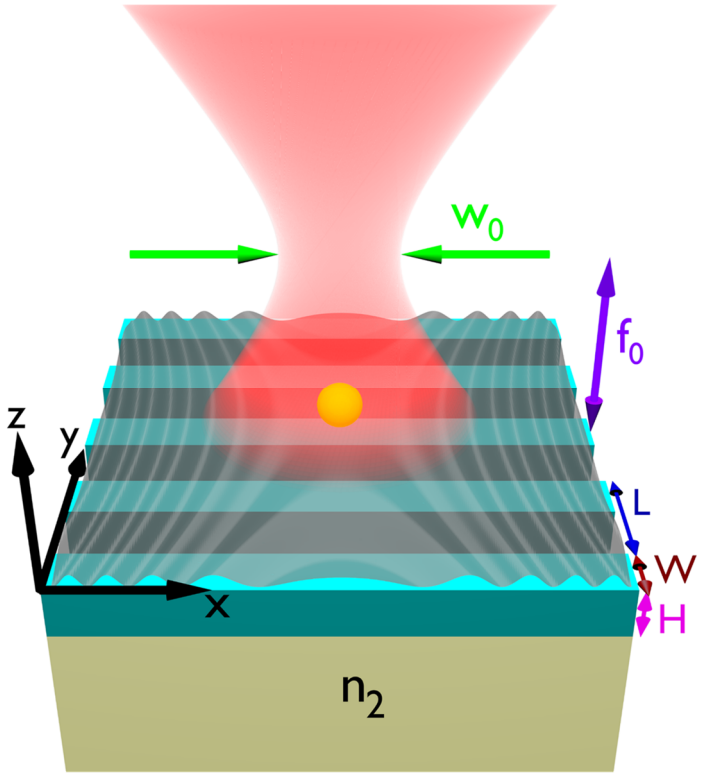

Figure 6.1: Hyperbolic optical trap created by illuminating a Rayleigh particle (yellow) located above an ultrathin anisotropic metasurface (cyan) with a p-polarized Gaussian beam (red). The beam has waist w_0 and has been focused at a distance f_0 normal to the surface. During the light scattering process, the particle excites highly confined surface plasmons (grey) on the metasurface propagating away from the beam axis where the optical trap is generated. The hyperbolic metasurface is constructed using subwavelength metallic rods with width W, height H and periodicity L, and is supported by a medium of refractive index n_2.

resonance, the presence of the metals does not play a significant role on the force acting on the particle and the trap performance becomes similar to a common optical tweezer governed by gradient force originating from the Gaussian beam. In addition, the performance of this approach in terms of potential distribution, trap depth, and minimum beam intensity required to achieve stable optical trapping has not yet been investigated. The calculation of these parameters is challenging due to the intrinsic nonconservative nature of the recoil force, which prevents the use of common theoretical approaches based on the definition of potential energy in the case of conservative force fields [18].

In this Chapter, I propose stable optical trapping of nanoparticles using ultrathin anisotropic and hyperbolic metasurfaces illuminated with low-intensity Gaussian beams. This platform, illustrated in Figure

6.1, permits to engineer optical traps in which giant, nonconservative recoil force coming from the directional excitation of ultra-confined SPPs determines the overall performance of the traps. The incident Gaussian beam enforces that the nanoparticle acquires an adequate out-of-plane polarization spin and set the optical trap at its axis. Strikingly, and in stark contrast with the case of bulk metals studied in Ref. [17], the properties of the traps are directly linked with the anisotropic and broadband features of the supported SPPs, and can be modified by tailoring the electromagnetic response of the metasurface. In general, and compared to traps set over common isotropic surfaces (bulk metal and uniform thin layers), the proposed optical traps exhibit (i) *significantly larger trapping forces*, associated to the high momentum of the supported plasmons; and (ii) *a broadband response*, in the sense that stable trapping can be set with beams oscillating at any frequency within a wide range in which anisotropic metasurfaces supports SPPs. To investigate this platform, explore its practical viability, and compare its performance with respect to other configurations, I develop a rigorous theoretical formalism based on (i) the Lorentz force within the dipole approximation merged with anisotropic Green's functions [18] to compute the trapping forces; and (ii) the Helmholtz decomposition method [19] to compute the potential energy of nonconservative forces. I validate the results using full-wave numerical simulations performed in COMSOL Multiphysics [20]. My approach permits to calculate the spatial potential distribution of the trap, including the trap depth, and allows to elucidate the minimum beam intensity required to achieve stable optical trapping. I have applied my formulation to explore the trapping response using three realistic configurations, namely a bulk silver substrate, a uniform and thin silver layer, and an array of densely packed silver nanostrips [21] that behaves as a hyperbolic metasurface. Numerical results reveal an outstanding trap performance of nanostructured silver over an ultra-wide frequency band ranging from the visible to the infrared (IR). Compared to the case of a thin silver layer or bulk silver, the nanostructured configuration greatly enhances the trap depth over the entire band that in turn reduces the beam intensity required to achieve stable optical trapping. It should be noted that at the plasmon resonance, the thin silver layer exhibits better performance than the bulk or nanostructured silver. This response appears because the nanostructured configuration does not exhibit a hyperbolic response at that wavelength. Next, I explore the asymmetrical potential distribution of the traps

as the topology of nanostructured silver layer evolves from elliptical to hyperbolic regimes going through its topological transition, and reveal the presence of local potential barriers that might appear along precise directions within the surface. Such potential barriers arise over anisotropic surfaces thanks to its rotationally asymmetric response, exhibit larger energy than the trap depth, and might be useful to predict the direction taken by an energetic particle to escape from the trap. This response is in stark contrast with the rotationally symmetrical and smooth potential distribution of traps set over thin and bulk metals which are isotropic in nature. These results position anisotropic and hyperbolic metasurfaces as promising candidates to trap and manipulate nanoparticles using low-intensity laser sources operating in the visible and near-IR band, and might lead to important applications in a wide variety of fields ranging from physics and chemistry to bioengineering.

6.1 NON-PARAXIAL MODEL OF GAUSSIAN BEAM

The common paraxial approximation to model a Gaussian beam is valid when the electric field does not change its amplitude significantly within one wavelength along the propagation direction [22,23]. However, for a tightly focused beam possessing waist in the order of wavelength or smaller, as the one

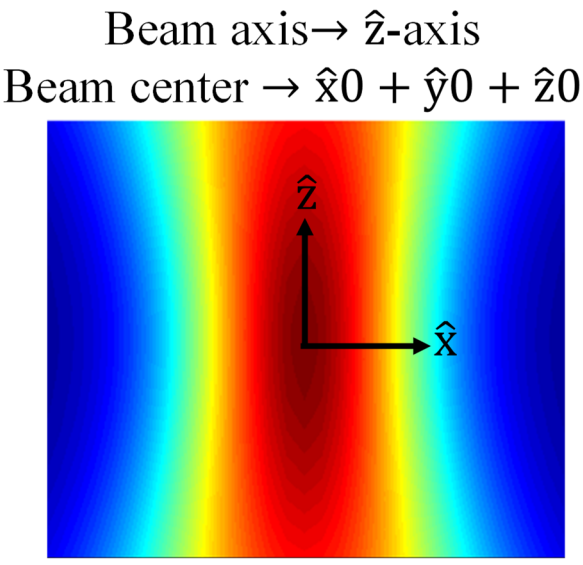

Figure 6.2: Example of electric field intensity distribution of a Gaussian beam in the xz-plane showing the beam axis and the beam center. The beam exhibits a similar response in the yz-plane.

employed in the proposed platform, this approximation is not valid. In that case, a more general non-paraxial model [22,23] should be used to describe the beam. Here, I review this formulation to model a linearly polarized Gaussian beam incoming to the metasurface and its reflection. This model does not include the presence of the emitter, as its presence would be negligible in the overall reflection process.

The electric field of a p-polarized (i.e., transverse magnetic) Gaussian beam employed in the proposed platform possesses x and y components (in-plane) that are even-symmetric with respect to the beam axis, whereas the z component (out-of-plane) is odd-symmetric [17]. The non-paraxial incident electric field vector components of such a normally incident Gaussian wave can be expressed as [18]

$$E_{x,inc}^{GW}(\bar{r}) = \frac{w_0^2}{4\pi}\iint_{-k_1}^{k_1} \frac{k_x k_{z1}}{k_t k_1} e^{-\frac{k_t^2 w_0^2}{4}} e^{ik_{z1}f_0} e^{i(k_x x + k_y y - k_{z1} z)} dk_x dk_y, \tag{6.1a}$$

$$E_{y,inc}^{GW}(\bar{r}) = \frac{w_0^2}{4\pi}\iint_{-k_1}^{k_1} \frac{k_y k_{z1}}{k_t k_1} e^{-\frac{k_t^2 w_0^2}{4}} e^{ik_{z1}f_0} e^{i(k_x x + k_y y - k_{z1} z)} dk_x dk_y, \tag{6.1b}$$

$$E_{z,inc}^{GW}(\bar{r}) = \frac{w_0^2}{4\pi}\iint_{-k_1}^{k_1} \frac{k_t}{k_1} e^{-\frac{k_t^2 w_0^2}{4}} e^{ik_{z1}f_0} e^{i(k_x x + k_y y - k_{z1} z)} dk_x dk_y, \tag{6.1c}$$

where w_0 and f_0 are the beam waist and focus position, respectively; and k_1 is the wavenumber in the medium above the surface with a transverse component $\bar{k}_t = \hat{x}k_x + \hat{y}k_y$ and a vertical component $k_{z1} = \sqrt{k_1^2 - k_t^2}$. A phase shift $e^{ik_{z1}f_0}$ is introduced as a measure of tuning the laser focus position f_0 along the $\hat{z}$-axis [17,18]. Note that the integration limits in Eq. (6.1) are set to $\pm k_1$, because the propagative modes dominate the response of the beam, and the influence of evanescent spectrum is negligible [17]. Figure 6.2 shows the electric field intensity distribution of the beam propagating in free space in the xz-plane (see the coordinate system in Figure 6.1) indicating the center and the beam axis. Note that the intensity distribution is completely symmetric in the radial direction.

The reflected electric field vector components from the anisotropic surface are computed as

$$E_{x,ref}^{GW}(\bar{r}) - \frac{w_0^2}{4\pi}\iint_{-k_1}^{k_1}\left(R_{sp}\frac{k_y}{k_t} + R_{pp}\frac{k_x k_{z1}}{k_t k_1}\right)e^{-\frac{k_t^2 w_0^2}{4}}e^{ik_{z1}f_0}e^{i(k_x x + k_y y + k_{z1} z)}dk_x dk_y, \quad (6.2a)$$

$$E_{y,ref}^{GW}(\bar{r}) = \frac{w_0^2}{4\pi}\iint_{-k_1}^{k_1}\left(-R_{sp}\frac{k_x}{k_t} + R_{pp}\frac{k_y k_{z1}}{k_t k_1}\right)e^{-\frac{k_t^2 w_0^2}{4}}e^{ik_{z1}f_0}e^{i(k_x x + k_y y + k_{z1} z)}dk_x dk_y, \quad (6.2b)$$

$$E_{z,ref}^{GW}(\bar{r}) = \frac{w_0^2}{4\pi}\iint_{-k_1}^{k_1} R_{pp}\frac{k_t}{k_1}e^{-\frac{k_t^2 w_0^2}{4}}e^{ik_{z1}f_0}e^{i(k_x x + k_y y + k_{z1} z)}dk_x dk_y. \quad (6.2c)$$

Here, R_{pp} and R_{sp} are the Fresnel reflection coefficients that characterize the reflection of 'p' and 's'-polarized waves from the anisotropic surface when it is illuminated with 'p'-polarized waves [31]. In most scenarios, the total fields described in Eq. (6.2) keep a similar symmetry as the incident Gaussian beam in free space, as discussed below, and polarize the particle with the desired handedness to enable optical trapping. It should be noted that the symmetry of these fields may change when the Gaussian beam is focused well below the metasurface. In that case, the particle may acquire an out-of-plane polarization spin with rotation handedness pointing toward the beam axis and the recoil force becomes an "anti-trapping"

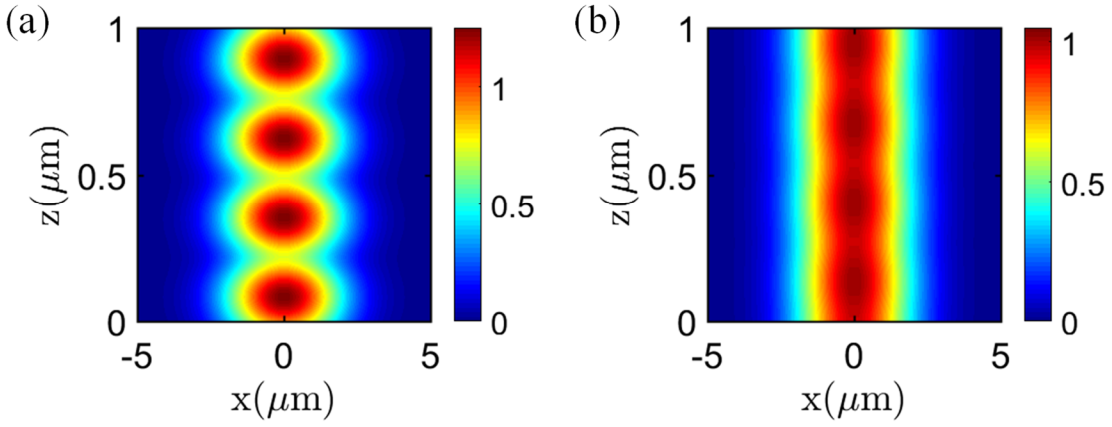

Figure 6.3: Electric field intensity distribution of the standing wave formed due to the superposition of the incident Gaussian beam and the reflected one from (a) hyperbolic metasurface; and (b) bulk silver. The beam waist is $w_0 = 2$ μm, it is focused at $f_0 = z = 0$, and its operation wavelength is 540 nm. The metasurface is constructed using nanostructured silver (see Figure 4.1) with parameters W = 60 nm, L = 180 nm, H = 10 nm, and $n_2 = 1.05$.

force [17]. The intensity distribution of the standing wave (i.e., superposition of the incident Gaussian beam and the reflected one) formed above a nanostructured silver layer and above bulk silver is shown in Figure 6.3. Here, the incident beam is focused exactly at $z = 0$. Results show that an intensity hotspot is formed above $z = 0$ even though the incident beam is focused exactly on the surface. Such standing waves may exert a repulsive vertical gradient force on the nanoparticle that will be discussed later in this Chapter.

6.2 THEORETICAL FRAMEWORK

Let me consider an isotropic, non-magnetic, and electrically polarizable spherical Rayleigh particle located at a position $\bar{r}_0 = (x_0, y_0, z_0)$ above an anisotropic metasurface defined by a conductivity tensor $\bar{\bar{\sigma}}^{eff} = \sigma_{xx}^{eff}\hat{x}\hat{x} + \sigma_{yy}^{eff}\hat{y}\hat{y}$, as shown in Figure 6.1. The ultrathin metasurface is placed in the plane $z = 0$, lying on the interface between two media with refractive indices n_1 (top) and n_2 (bottom). The particle is illuminated by a normally incident Gaussian beam, i.e., the beam axis is aligned with the $\hat{z}$-axis (see Figure 6.2), that has a beam waist w_0 and is focused at a distance f_0. The focus position f_0 is defined as the vertical distance between the metasurface and the center of the Gaussian beam [17], and it is positive (negative) when the beam is focused above (below) the metasurface. Following the theoretical development in Chapter 4, the total optical forces on the particle are composed of conservative gradient and nonconservative recoil components. The gradient force reads as

$$\bar{F}_{grad} = \frac{1}{2}\mathrm{Re}\begin{bmatrix} p_x^* \frac{d}{dx}E_x^{GW} + p_y^* \frac{d}{dx}E_y^{GW} + p_z^* \frac{d}{dx}E_z^{GW} \\ p_x^* \frac{d}{dy}E_x^{GW} + p_y^* \frac{d}{dy}E_y^{GW} + p_z^* \frac{d}{dy}E_z^{GW} \\ p_x^* \frac{d}{dz}E_x^{GW} + p_y^* \frac{d}{dz}E_y^{GW} + p_z^* \frac{d}{dz}E_z^{GW} \end{bmatrix}, \tag{6.3}$$

where $\bar{E}^{GW}$ is the superposition of the electric field of the standing wave formed due to the incident laser beam and its reflection from the metasurface. The nonconservative recoil force exerted on the particle yields to

$$\bar{F}_{rec} = \begin{bmatrix} -2\mathrm{Im}[p_x^* p_z]\mathrm{Im}\left[\frac{d}{dx}G_{xz}^s\right] \\ -2\mathrm{Im}[p_y^* p_z]\mathrm{Im}\left[\frac{d}{dx}G_{yz}^s\right] \\ \frac{\omega^2\mu_0}{2}\mathrm{Re}\left\{|p_x|^2\frac{d}{dz}G_{xx}^s(\bar{r}_0,\bar{r}_0) + |p_y|^2\frac{d}{dz}G_{yy}^s(\bar{r}_0,\bar{r}_0) + |p_z|^2\frac{d}{dz}G_{zz}^s(\bar{r}_0,\bar{r}_0)\right\} \end{bmatrix}. \quad (6.4)$$

Let me analyze these gradient and recoil forces in the context of optical trapping. Eq. (6.3) shows that the conservative gradient force always acts toward the higher electric field intensity of the standing wave [24-26]. The nonconservative recoil force shown in Eq. (6.4) appears to compensate the momentum of the directional SPPs excited on the surface [27-30]. These two force components have a very different origin: the gradient force depends on the gradient of the electric field intensity surrounding the particle, and thus varies with the type of beam employed. For instance, in the case of plane waves, this term would lead to a radiation pressure pointing toward the direction of the wavefront; whereas in the case of a Gaussian beam, this component leads to gradient force pointing towards the beam center, as in common optical tweezers [12]. On the other hand, the recoil force mostly depends on the properties of the surface plasmons supported by the metasurface. Besides, this force also depends on the effective dipole polarization spin or helicity acquired by the particle. For a given distance between the particle and the metasurface, the recoil force is maximized (strictly zero) when the particle acquires a quasi-circular (linear) polarization state. Using a properly focused Gaussian beam, the particle acquires an out-of-plane polarization spin with rotation handedness against the beam axis and the resultant recoil force is directed towards the beam axis. In the case of isotropic metasurfaces, this force points exactly towards the beam axis independently of the particle position within the beam [17]. However, in the case of anisotropic metasurfaces, the direction of the recoil force may not point towards the beam axis due to the broken rotational symmetry of the system [i.e., $G_{xz}^s(\bar{r}_0) \neq G_{yz}^s(\bar{r}_0)$ in Eq. (4.8)]. As discussed below, the recoil force will then push the particle towards the beam axis following a parabolic trajectory. In addition, Eq. (6.4) unveils that the strength of the recoil force depends on the imaginary part of the spatial derivative of scattered Green's functions out-of-plane tensor component, which measures the momentum of the excited directional plasmons.

6.2.1 TRAP STIFFNESS

An important parameter that defines the performance of an optical trap is the trap stiffness, which measures the restoring force that acts on the nanoparticle to bring it back to a stable position within the trap – similar to the spring constant in a common mechanical system. This parameter is more significant in Brownian systems, where particles suspended in liquids may acquire random motion due to the continuous collision with the moving fluid molecules. The stiffness of a trap set over a surface can be approximated as [31]

$$\kappa(\phi) = -\frac{F_\rho(\rho,\phi)}{\rho}\bigg|_{\rho\to 0} \tag{6.5}$$

where $F_\rho(\rho,\phi)$ denotes the radial component of the lateral forces evaluated at a position (ρ,ϕ) defined in polar coordinate system. In Eq. (6.5), I assume that the tangential force component is significantly weaker than the radial one, as happens in the plasmonic systems considered here. In most cases considered in the literature [12,17], for instance, the force generated by Gaussian beam in free-space or over common plasmonic materials, the trap stiffness is isotropic in the sense that it has polar symmetry and therefore provides an identical response in all directions: $\kappa(\phi) = \kappa$. This is different in the case of traps set over anisotropic metasurfaces: the restoring force that a nanoparticle experiences towards the trap depends on the direction through which the particle is trying to escape. Traps with anisotropic stiffness are useful to predict the probable direction followed by the particle when it acquires enough energy to escape from the trap.

6.2.2 TRAP POTENTIAL

The trap potential is arguably the most important parameter that defines the performance of an optical trap [32,33]. Here, I will focus on the trap potential energy and trap depth, which is a quantitative measure of how long the particle remains confined within the trap. In the case of conservative forces, such as the gradient force originating from a Gaussian beam [13], the trapping potential U of a conservative vector force $\bar{F}_c$ can be obtained as $U_c(\bar{r}) = -\int_{-\infty}^{\bar{r}} \bar{F}_c(\bar{r}') \cdot d\bar{r}'$ [21]. This potential represents the energy required

to move a particle from a reference location with zero energy (considered here to be in the infinite) to the position defined by the vector $\bar{r}$. Conservative forces are free of solenoidal components and thus the path chosen in the integral is not relevant: any trajectory from infinite to $\bar{r}$ provides identical potential energy. This situation is different in the case of nonconservative vector forces because they possess a solenoidal component [34]. Nonconservative forces may arise in many scenarios, for instance in certain optomechanical systems [35], using structured or evanescent fields [36], or when a nanoparticle is illuminated near a plasmonic surface [27-30]. In such cases, choosing different paths to move the particle from a reference location to a position $\bar{r}$ will lead to different potential energies due to the presence of the solenoidal force component. As a result, it is not possible to use direct integration methods to compute the potential energy. To avoid this issue, I apply here the Helmholtz decomposition method to compute the trapping potential of nonconservative forces [19]. Following this approach, I express the force field as [34-36]

$$\bar{F}(\bar{r}) = -\nabla U + \nabla \times \bar{A} \tag{6.6}$$

where, U is the potential energy, $\bar{A}$ is the vector potential, and ∇U and $\nabla \times \bar{A}$ denote the conservative and nonconservative (solenoidal) force components, respectively. Taking the divergence of Eq. (6.6) and applying the identity $\nabla \cdot (\nabla \times \bar{A}) = 0$ permit me to find the potential energy through the differential equation [34]

$$-\nabla^2 U = \nabla \cdot \bar{F} \text{ on } \Omega \tag{6.7}$$

that is subjected to the Neumann boundary conditions [37]

$$\nabla U \cdot \hat{\rho} = \bar{F} \cdot \hat{\rho} \text{ on } d\Omega \tag{6.8}$$

where $\hat{\rho}$ is a unit vector pointing outwards with respect to the boundary of the domain Ω. This numerical approach is valid when the force field is defined over a bounded region Ω with a smooth boundary condition $d\Omega$. The platform considered here fulfils these conditions: the domain is defined by the Gaussian beam

impinging over the metasurface, and the boundary conditions are related to the negligible force acting on the particle when it is located very far away from the beam axis.

I will explore the potential distribution of optical traps set using Gaussian beams over isotropic surfaces, for instance ultrathin and bulk metals, and reveal that they are defined by a spatially rotational symmetric function centered at the beam axis. In stark contrast, the trapping potential over anisotropic metasurfaces illuminated with a Gaussian beam lacks such rotational polar symmetry. In both cases, the trap depth is unique and is defined as the potential difference between the energy computed at the beam axis and at a position located in infinite with zero energy. Strikingly, and as further detailed below, the intrinsic anisotropy of the metasurface gives rise to *local potential barriers* with larger potential difference than the trap depth. As a result, the particle might acquire enough energy to escape from the trap but not to overcome such potential barriers and thus will follow a special route within the plane to avoid them. Finally, it should be noted that stable optical trapping appears when the trap depth is larger than $10k_BT$, where k_B is the Boltzmann constant and T is temperature. If this condition is not fulfilled, mechanisms such as thermal fluctuation [38,39] and Brownian motion [12,32,36] may provide enough energy to the particle to quickly escape from the trap. Thus, the minimum laser beam intensity required to achieve stable trapping is the one required to generate an optical trap with a potential depth $\geq 10k_BT$ [18].

6.3 ENABLING MECHANISM OF OPTICAL TRAPPING

In this section, I investigate the mechanisms that enable lateral trapping forces on a nanoparticle located near an ultrathin metasurface when illuminated by a p-polarized Gaussian beam. To this purpose, I first analyze the out-of-plane dipole polarization spin or helicity acquired by the particle that enables excitation of directional SPPs on the platform. Then, I analyze the recoil and gradient forces acting on a nanoparticle versus its position with respect to the beam axis, unveiling the mechanisms that conform the optical trap. I also compare the force response when the nanostructured silver is replaced by a pristine thin silver.

Let me consider a spherical gold nanoparticle of radius $a = 15\text{nm}$ located at $\bar{r}_0 = (x_0, y_0, a)$. The metasurface is constructed using nanostructured and periodic silver rods [21] with width W= 60 nm, height

H = 10nm and periodicity L = 180nm (see Figure 6.1) patterned over a porous polymer with refractive index $n_2 = 1.05$ [30]. The subwavelength thickness and periodicity of the layer allow to characterize it using an effective in-plane conductivity tensor [40-43], as discussed in Chapter 2, with negligible out-of-plane polarizability [44,45]. Even though the use of different substrates might change the particle polarizability and the density of states provided by the structure, the overall response will not be significantly affected. I have carefully verified the accuracy of my model using full-wave numerical simulations as well as the dispersive hyperbolic response of the surface. For comparison purposes, I employ ultrathin silver with identical properties as the one employed on the nanostructured metasurface [21].

6.3.1 DIPOLE HELICITY

I begin the analysis considering that the Gaussian beam is operating at $\lambda_0 = 540\text{nm}$. At this wavelength, the nanostructured silver layer behaves as a hyperbolic metasurface (see Chapter 2). For the sake of simplicity, I first assume that the nanoparticle is located along the metallic rods (i.e., the $\hat{x}$-axis). In this situation, the polarization state acquired by the particle can be computed from dipole moment $\bar{p}(x_0)=[p_{xr}(|x_0|) + ip_{xi}(|x_0|)]\hat{x} + [\mp p_{zr}(|x_0|) \mp ip_{zi}(|x_0|)]\hat{z}$, where the subscripts 'r' and 'i' denote the real and imaginary components of a complex number, and the upper (lower) sign appears when the particle is located in the negative (positive) portion of the $\hat{x}$-axis. I stress the symmetry of the electric dipole magnitude with respect to the beam axis, i.e., $|\bar{p}(x_0)| = |\bar{p}(-x_0)|$. This dipole can be expressed as a linear combination of two fundamental emitters that have opposite out-of-plane polarization rotation handedness with respect to the surface. The dipole moments of these emitters are $\bar{p}_1(x_0)=p_{xr}(|x_0|)\hat{x} \mp ip_{zi}(|x_0|)\hat{z}$ and $\bar{p}_2(x_0)=ip_{xi}(|x_0|)\hat{x} \mp p_{zr}(|x_0|)\hat{z}$. The excitation of $\bar{p}_1$ ($\bar{p}_2$) depends on the real (imaginary) and imaginary (real) parts of the in-plane and out-of-plane electric field components of the standing wave created over the surface. Focusing the incident p-polarized Gaussian beam close to the metasurface ensures that the real part of the in-plane electric field components is much stronger than the other ones. As a result, the dipole $\bar{p}_1$ is

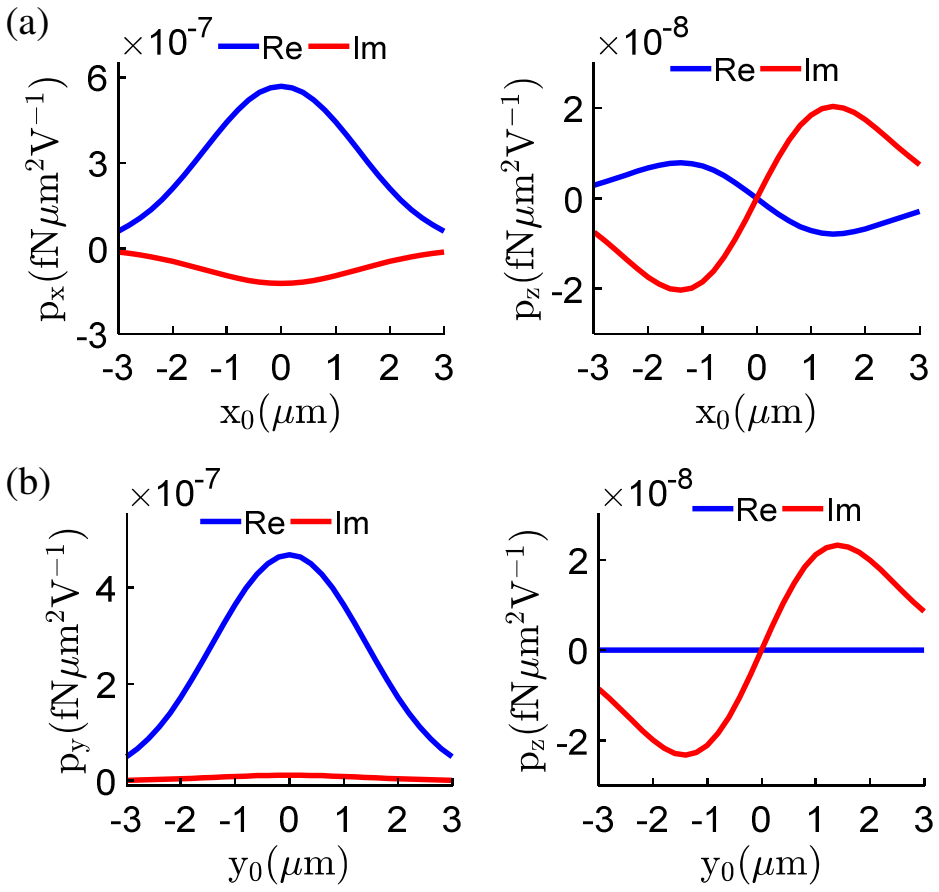

Figure 6.4: Dipole moment components p_x, p_y and p_z induced on a gold nanoparticle located above nanostructured silver based metasurface when illuminated by a normally incident 'p'-polarized Gaussian beam. Results are computed versus particle position (a) x_0, keeping $y_0 = 0$ fixed; and (b) y_0, keeping $x_0 = 0$ fixed. Note that $p_x = 0$ and $p_y = 0$ for panels (a) and (b), respectively. The gold nanoparticle has a radius $a = 15$nm and is located in free space at a distance $z_0 = a$ over the metasurface described in Figure 6.1. Other parameters are as in Figure 6.3.

strongly excited and dominates the scattering processes, thus generating SPPs that propagate in the radial direction against the beam axis.

To explain this scenario, Figures 6.4-6.6 show the characteristics of dipole moment induced on the particle as a function of its position (x_0, y_0) with laser beam focused at $f_0 = 0$ and waist is $w_0 = 2\mu$m and Figure 6.7 displays the real and imaginary parts of the electric field components of the standing wave. Specifically, Figure 6.4(a) shows the in-plane, p_x and out of plane, p_z dipole moment components versus

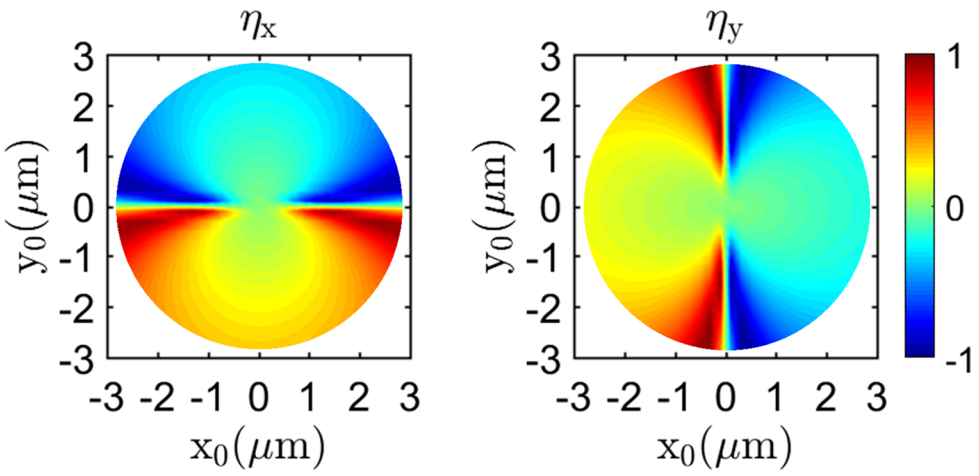

Figure 6.5: Helicity of the particle induced around x (left panel) and y (right panel)-axes computed as a function of dipole position in the xy-plane above the hyperbolic metasurface. Other parameters are as in Figures 6.3 and 6.4.

x_0 keeping $y_0 = 0$ fixed. In this case, $p_y = 0$ and the responses are computed as a function of the electric field intensity available at the beam center. Results show that p_x and p_z exhibit even and odd symmetries versus the particle position with respect to the beam axis (i.e., $x_0 = 0$), respectively. The value of p_z is strictly zero when it is located along the beam axis. This is because $E_{z,inc}^{GW}$ and $E_{z,ref}^{GW}$ vanish at this position as shown in Figure 6.7 and the particle behaves as a purely linearly polarized dipole. As the particle is moved away from the beam axis, the appearance of $E_{z,inc}^{GW}$ and $E_{z,ref}^{GW}$ induce an out-of-plane polarization component, p_z. The interplay between p_x and p_z induces a polarization spin on the particle with a rotation handedness against the beam axis as shown in Figures 6.5 and 6.6. Following a similar approach, Figure 6.4(b) shows the in-plane (p_y) and out of plane (p_z) dipole moment components versus y_0 keeping $x_0 = 0$ fixed. In this case, $p_x = 0$, and p_y and p_z exhibit even and odd symmetries with respect to the beam axis, respectively. The dipole helicity, a measure of out-of-plane polarization spin acquired by the particle, around the $\hat{\rho} = (x, y)$ axis can be computed from the dipole moment as $\eta_\rho = -2\frac{\mathrm{Im}[p_\rho^* p_z]}{|p_\rho|^2 + |p_z|^2}$ [8]. Figure 6.5 show the dipole helicity as a function of its position over the xy-plane of the surface. This confirms that the

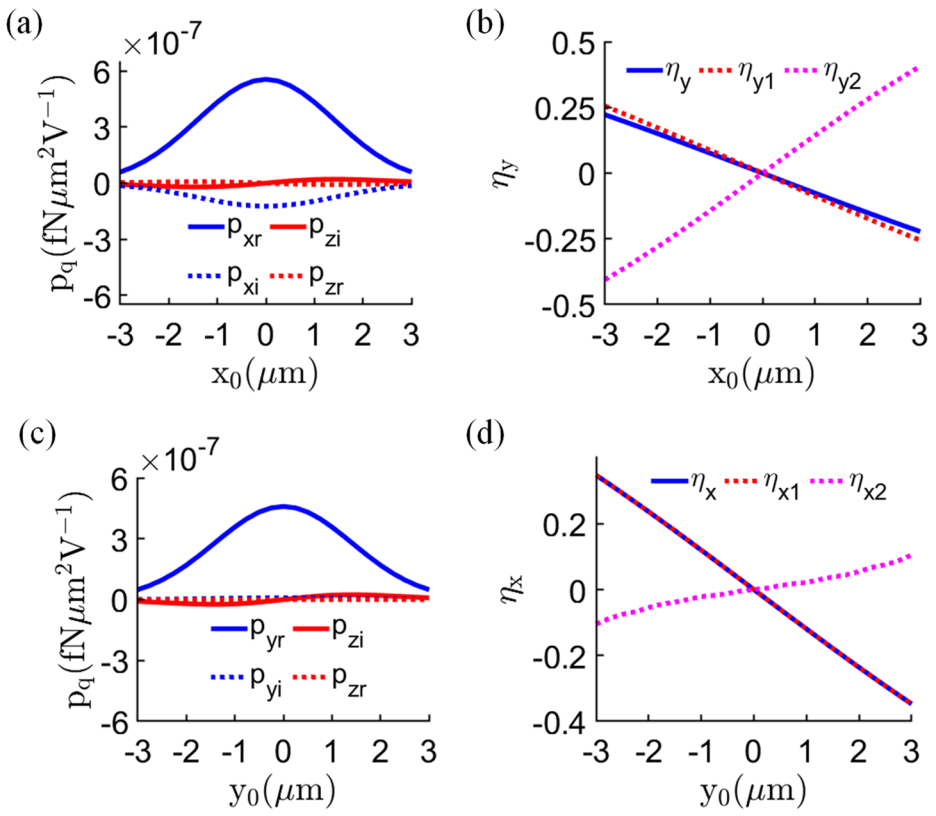

Figure 6.6: Dipole moment components of the two fundamental emitters $\bar{p}_1(t_0)=p_{\rho r}(|t_0|)\hat{t} \mp ip_{zi}(|t_0|)\hat{z}$ and $\bar{p}_2(t_0)=ip_{\rho i}(|t_0|)\hat{t} \mp p_{zr}(|t_0|)\hat{z}$, with $t = \{x, y\}$, as a function of particle position. (a) In-plane and out-of-plane dipole moment components of the two emitters ($\bar{p}_1$: solid lines and $\bar{p}_2$: dotted lines). (b) Out-of-plane polarization spin of net dipole moment (blue solid line), emitter $\bar{p}_1$ (red dotted line) and emitter $\bar{p}_2$ (magenta dotted line) versus x_0 keeping $y_0 = 0$ fixed. Panel (c)-(d) show the similar study versus y_0 keeping $x_0 = 0$ fixed. Other parameters are as in Figures 6.3 and 6.4.

dipole always acquires spin with rotation handedness against the beam axis independent to the particle position.

In a parallel development, the dipole moment $\bar{p}$ induced on the particle (Figure 6.4) can be decomposed into two fundamental emitters with opposite spin as $\bar{p} = \bar{p}_1 + \bar{p}_2$. First, I consider the case when the dipole is located along the metallic rods of the structure (with $y_0 = 0$). There, the fundamental emitters are $\bar{p}_1(x_0)=p_{xr}(|x_0|)\hat{x} \mp ip_{zi}(|x_0|)\hat{z}$, with a spin rotating against the beam axis, and $\bar{p}_2(x_0)=ip_{xi}(|x_0|)\hat{x} \mp p_{zr}(|x_0|)\hat{z}$, with a spin rotating towards the beam axis. In these equations, the negative (positive) sign

appears when the particle is in the negative (positive) part of the $\hat{x}$-axis, and the subscripts 'r' and 'i' denote the real and imaginary components of a complex number, respectively. Figure 6.6(a) shows the dipole moment components of these two emitters as a function of particle position x_0. Results confirm that the dipole moment magnitude of the emitter $\bar{p}_1$ is much stronger than the one of dipole $\bar{p}_2$. Figure 6.6(b) displays the particle total helicity (blue solid line) together with the helicities associated with the dipoles $\bar{p}_1$ (red dotted line) and $\bar{p}_2$ (magenta dotted line) versus the particle position x_0. It is clear that both the particle and the emitter $\bar{p}_1$ possess a similar polarization spin that rotates against the beam axis and generates recoil trapping force, whereas the emitter $\bar{p}_2$ possesses a polarization spin that rotates in the opposite direction and generates anti-trapping recoil force. I remark that the latter forces are negligible because the emitter $\bar{p}_2$ is weakly excited. A similar study is shown in Figure 6.6(c-d) when the particle is located across the nanorods of the structure (with $x_0 = 0$). In this case, the particle net dipole moment $\bar{p}$ is decomposed as $\bar{p}_1(y_0)=p_{yr}(|y_0|)\hat{y} \mp ip_{zi}(|y_0|)\hat{z}$ and $\bar{p}_2(y_0)=ip_{yi}(|y_0|)\hat{y} \mp p_{zr}(|y_0|)\hat{z}$. Results confirm that the dipole moment magnitude of the emitter $\bar{p}_1$ is always stronger than the one of dipole $\bar{p}_2$. I also stress that the net dipole polarization spin follows the one of dipole $\bar{p}_1$. I stress that the electric field $\left(\bar{E}^{GW} = \bar{E}^{GW}_{inc} + \bar{E}^{GW}_{ref}\right)$

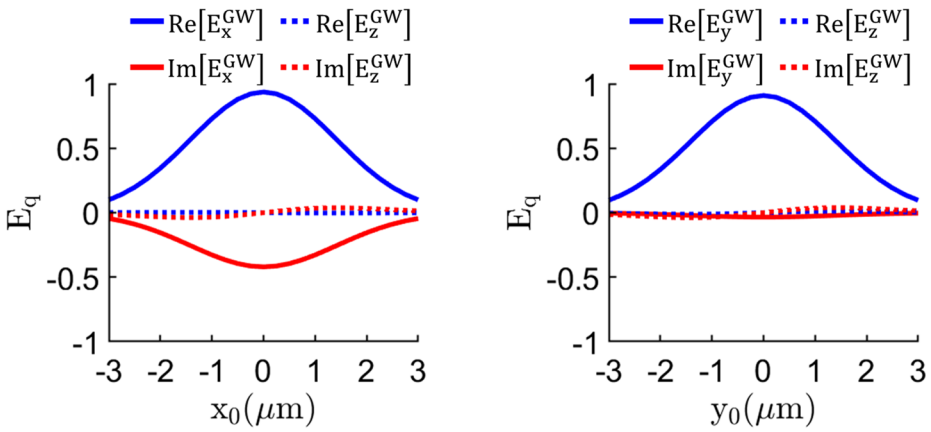

Figure 6.7: Real and imaginary part of the in-plane (E_x^{GW} and E_y^{GW}) and out-of-plane (E_z^{GW}) electric field components of the standing wave formed above nanostructured silver due the superposition of the incident Gaussian beam and the one reflected from the surface. Results are computed as a function of particle position x_0 (left panel) and y_0(right panel) keeping $y_0 = 0$ and $x_0 = 0$, respectively. Other parameters are as in Figure 6.3.

of the standing wave plays a key role that enables strong excitation of the emitter $\bar{p}_1$. To investigate this scenario, Figure 6.7 displays the real and imaginary parts of the electric field components of the standing wave as a function of particle position when the incident Gaussian beam is focused at the metasurface ($f_0 = 0$). Results show that the real parts of the in-plane electric field components (E_x^{GW} and E_y^{GW}) dominate, which in turn ensure a strong excitation of the dipole $\bar{p}_1$.

6.3.2 DIRECTIONAL SPPS AND TRAPPING FORCE

The response of the SPPs excited on the metasurface depends on polarization state acquired by the dipole. Figure 6.8(a) shows the power of the SPPs launched on the metasurface for several particle positions along the nanorods (i.e., $y_0 = 0$). When the particle is located away from the beam axis (i.e., $x_0 \neq 0$), it mostly scatters evanescent waves with a transverse spin that excites directional plasmons with wavevectors pointing away from the beam axis, associated with a "trapping" recoil force acting toward the beam axis. When the particle is located exactly on the axis of the Gaussian beam, it acquires a linear polarization $\bar{p}(x_0 = 0) = p_x(x_0 = 0)\hat{x}$ (see Figure 6.4a) and scatters waves without any specific spin that excites SPPs propagating symmetrically through the surface. As a result, the recoil force vanishes, and an optical trap is set at $x_0 = 0$. It is important to note the role of the dipole $\bar{p}_2(x_0)$: it excites directional plasmons propagating towards the beam axis (see Figure 6.6b) that result into "anti-trapping" recoil force [17]. In the case shown in Figure 6.8(a), the magnitude of this emitter is very small (see Figure 6.6) and thus it barely contributes to the excitation of SPPs. In a more general case, it is possible to engineer trapping or anti-trapping recoil forces by controlling the strength of the orthogonal dipoles that characterize the electromagnetic response of the particle. This can be done by manipulating the properties (focusing, polarization, etc.) of the incident Gaussian beam.

The total optical forces exerted on the nanoparticle are determined by the superposition of gradient and recoil forces. Figure 6.8(b) shows the x-component of the total (blue solid line) and recoil (red solid line) forces versus the particle position along the $\hat{x}$-axis. For the sake of comparison, it also shows these forces arising when the nanostructured layer is replaced by a thin silver layer (dashed lines) of similar thickness.

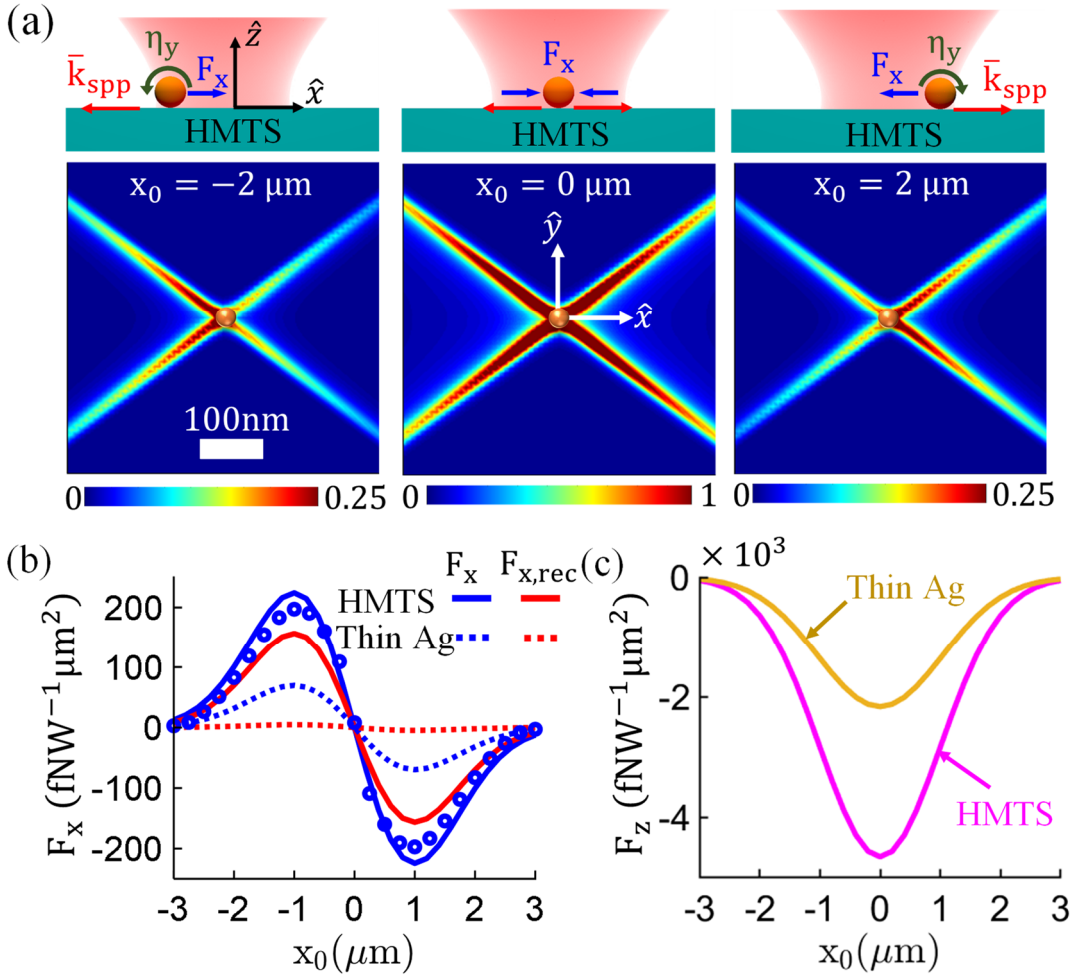

Figure 6.8: Trapping Rayleigh particles over a nanostructured metasurface with a Gaussian beam. (a) Normalized power of the surface plasmons excited on the surface when the particle is located in different positions with respect to the beam axis. The top inset illustrates the dipole polarization spin that rotates against the beam axis, direction of the plasmon wavevector, and the recoil forces acting on the particle. (b) Total lateral forces F_x (blue solid line) and recoil forces $F_{x,rec}$ (red solid line) exerted on the nanoparticle versus its position with respect to the beam axis. Results obtained above actual nanostructured silver using COMSOL Multiphysics (markers) are included for validation. Dotted lines correspond to the forces acting on the nanoparticle when the metasurface is replaced by a thin silver layer of identical thickness as the nanostructured metasurface. (c) Attractive vertical forces F_z acting on the nanoparticle as a function of its position x_0 with respect to the beam axis. Other parameters are as in Figures 6.3 and 6.4.

Results show that the recoil force strength over nanostructured silver is more than an order of magnitude (~40 times) larger than the one found over the thin layer. This enhancement appears thanks to the large

wavenumber (momentum) of the surface plasmons excited over the nanostructured surface. As a result, the trapping mechanism is very different in both platforms: above the thin silver layer, the trap is dominated by the gradient force generated from the Gaussian beam and its reflection from the surface; above the nanostructured silver layer, the trap is primarily determined by the strong recoil force originating from the directional excitation of hyperbolic surface plasmons. Overall, the hyperbolic response of nanostructured silver enhances the total lateral force strength over six times with respect to the nonpatterned case. This example highlights how anisotropic metasurfaces can enable plasmon-assisted optical traps at desired wavelengths determined by the surface properties. Figure 6.8(c) compares the vertical forces acting on the particle when it is located over these two configurations. In both cases, the total vertical force is always attractive, pushes the particle towards the surface, and exhibits a maximum strength near the trapping position. Note that a nanoparticle located above a bulk silver substrate experiences a repulsive vertical force due to the dominant contribution of the gradient component as will be discussed later, whereas the lateral components exhibit a similar response as in the case of thin silver. Numerical full-wave simulations performed in COMSOL Multiphysics (markers) are included in Figure 6.8(b). Results are obtained considering realistic nanostructured silver and applying the Maxwell's stress tensor formalism. This study

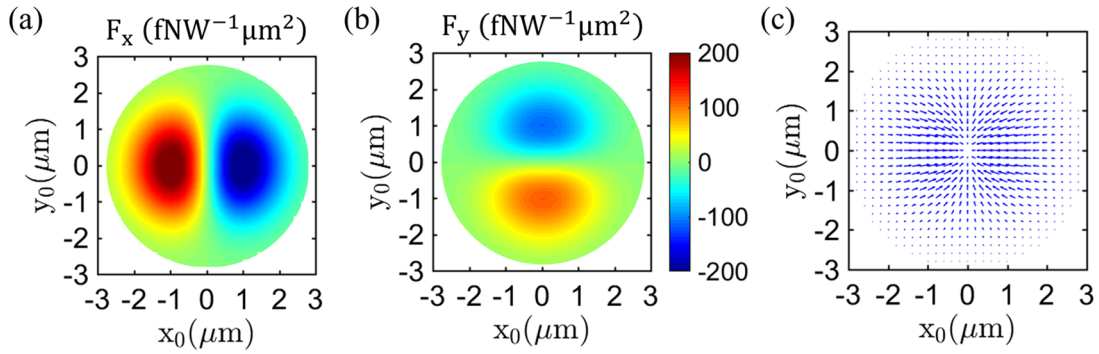

Figure 6.9: Optical trapping of a Rayleigh particle located above a hyperbolic metasurface when it is illuminated with a Gaussian beam. (a)-(b) Lateral components of the total force acting on the nanoparticle versus its position (x_0, y_0) with respect to the beam axis. (c) Quiver plot detailing the direction of the lateral forces. Other parameters are as in Figures 6.3 and 6.4.

shows that the effective medium approach can be applied to model the trap response of hyperbolic structures even though the particle is in the near field with more detail provided later in this Chapter.

Although the study above has been focused on nanoparticles located along the metallic rods of the nanostructure ($\hat{x}$-axis in the coordinate system of Figure 6.1), the underlying mechanisms hold independently of the particle position within the surface. Figure 6.9 explores this scenario and shows the components of the lateral forces acting on the particle as well as a quiver plot indicating the force direction. Results confirm that an optical trap is created exactly at the beam axis. Furthermore, this analysis reveals the intrinsic anisotropy of the metasurface: the strength of the recoil force exerted on the nanoparticle lacks rotational symmetry. This asymmetry appears because SPPs travelling towards different directions within the surface possess different momentum and spin, and the resulting force might not be directly directed towards the beam center. Instead, the particle would follow a parabolic trajectory towards the trap, as shown in Figure 6.9(c). Note that the recoil force is significantly larger than gradient force for all particle positions and thus dominates the trap performance.

The success of optical trapping using nonconservative recoil forces relies on the interplay between radial and polar (solenoidal) components. The radial component attracts the nanoparticle toward the beam axis and the polar component rotates the particle around the beam axis. In the case when the solenoidal

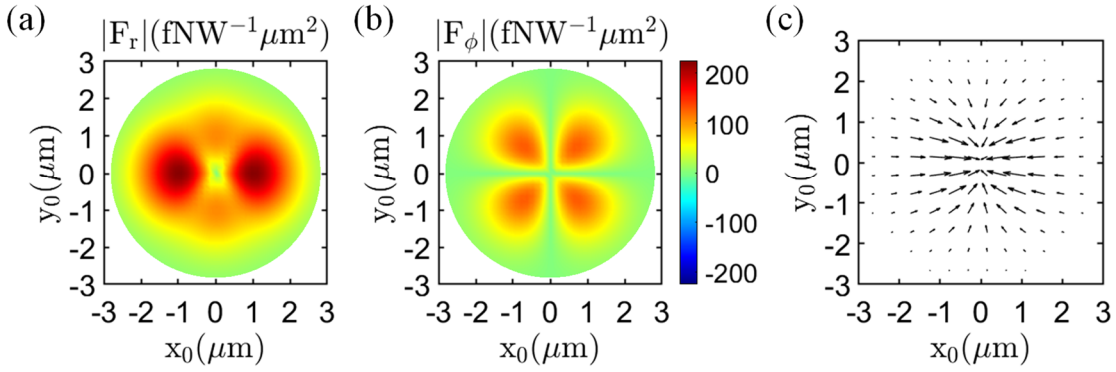

Figure 6.10: Optical trapping of a Rayleigh particle located above a hyperbolic metasurface when it is illuminated with a Gaussian beam. Radial (a) and polar (b) components of the total lateral forces acting on the nanoparticle versus its position (x_0, y_0) with respect to the beam axis. (c) Quiver plot detailing the direction of the lateral forces. Other parameters are as in Figures 6.3 and 6.4.

component outperforms the radial one, the particle will spin around the trap through a circular or elliptical trajectory, and will be kicked out of the trap. The radial and polar components of the lateral trapping forces can be computed from the x and y-components as $\bar{F}_r = \hat{x}F_x \cos\phi + \hat{y}F_y \sin\phi$ and $\bar{F}_\phi = -\hat{x}F_x \sin\phi + \hat{y}F_y \cos\phi$. Here, ϕ is the angle between the $\hat{x}$-axis and $\bar{F}_r$ computed in a counterclockwise direction. Figure 6.10(a)-(b) shows the strength of radial and polar components of net lateral forces, $\bar{F} = \hat{r}F_r + \hat{\phi}F_\phi$ above nanostructured silver as a function of particle position (x_0, y_0, a) computed at 540nm operation wavelength. Results show that the radial force strength is much stronger (4~5 times) than the polar one, and the interplay between them draws the nanoparticle toward the trapping position through a parabolic trajectory as can be seen from the quiver plot as shown in Figure 6.10(c).

6.4 STABILITY OF OPTICAL TRAPS

In this section, I explore the performance of the optical traps induced on nanoparticles located above nanostructured silver. I investigate key parameters of the trap including trap depth and stiffness, spatial potential distribution, local potential barriers, and the laser beam intensity needed to achieve stable trapping versus the wavelength of the incoming beam. As the wavelength increases, the metasurface topology evolves from an anisotropic elliptical to a hyperbolic regime going through a topological transition, which permits to study how the different light-matter interactions enabled by these regimes conform the properties of the optical trap. During this study, I compare the performance of the proposed traps to the one found using Gaussian beams in free-space [11-12], bulk metals [17], and thin films, aiming to highlight the pros and cons of this platform with respect to other configurations and to assess its practical viability.

6.4.1 TRAPPING POTENTIAL

Figure 6.11(a) shows the potential depth of the traps engineered over nanostructured silver versus the wavelength of the incident Gaussian beam. Results have been normalized with respect to the beam intensity available at the focus position. This figure highlights *the extreme bandwidth in which optical traps with very large potentials can be set*, covering the band from around 300nm to over 2μm, and how the trap depth

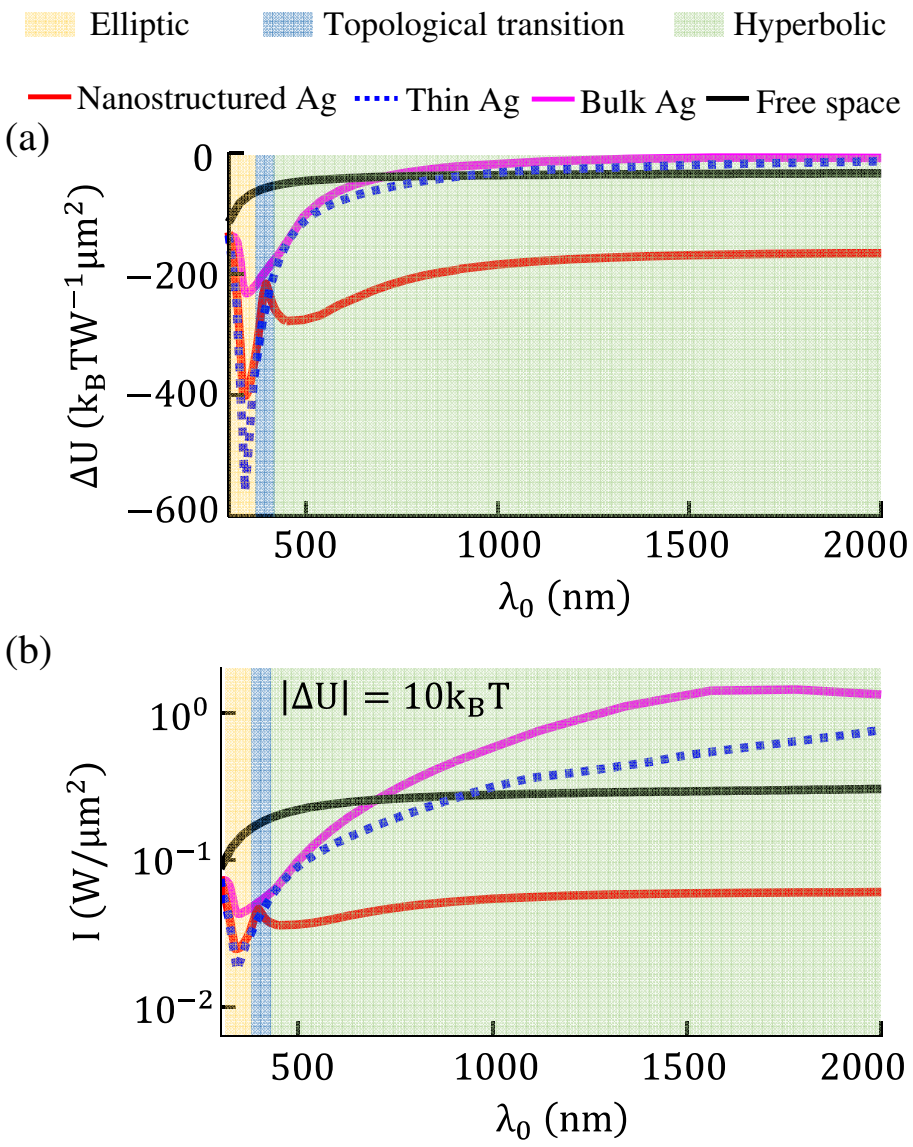

Figure 6.11: Performance of optical traps engineered over anisotropic metasurfaces versus frequency. (a) Trap depth normalized with respect to the power density available at the center of the incident Gaussian beam. (b) Minimum amount of power density required to achieve stable trapping. Results are computed for a nanoparticle that is illuminated by a Gaussian beam and is located above an array of silver nanorods (red), above bulk silver (magenta), above a thin silver layer (dotted blue), and in free space (black). The background shaded region corresponds to different metasurface topologies (yellow: elliptic, green: hyperbolic) going through the topological transition (blue) associated with the nanostructured silver layer. Other parameters are as in Figures 6.3 and 6.4.

correlates to the metasurface topology. Theoretically, the structure exhibits hyperbolic responses in the near-infrared and beyond. However, due to the difficulty to appropriately focus the beam at these

frequencies and the smaller amount of power scattered by the particle there, the analysis is restricted to the visible portion of the spectrum. It should be noted that different type of anisotropic and hyperbolic metasurfaces can be designed to operate in the infrared region [46-49]. Figure 6.11(a) also shows the trap depth obtained with a similar Gaussian beam focused over a thin silver layer (blue dotted line), bulk silver (magenta solid line) and in free space in the absence of any structure (black solid line). Results show that a thin layer of silver enables optical trapping with a performance comparable to the nanostructured one in the range of 325~425 nm wavelength and exhibits a slightly better trap depth (~1.4 times) at the intrinsic plasmon resonance frequency of silver (~340 nm). This response appears for two main reasons. First, the proposed nanostructured silver behaves as a hyperbolic metasurface only for wavelengths larger than 425nm. In the range of 340~425nm, it behaves as an anisotropic elliptical surface that exhibits moderate density of states. Therefore, in this frequency range the comparison is between two elliptical surfaces, one isotropic and another anisotropic. Note that nanostructured silver can be redesigned to exhibit hyperbolic response in this frequency range (340~425nm), but this might be challenging to fabricate in practice. Second, the electrical distance between the dipole and the surface is not negligible at 340nm. There is a clear trade-off [27,28] between the particle-surface distance and the surface modes that can be excited: when the particle is located in the very near field of the surface, it can couple to surface plasmons with large wavenumbers that boost the overall performance of the optical trap; when the particle is moved away from the surface, scattered fields are partially filtered out by free space and cannot efficiently excite surface plasmons. In the latter case, evanescent fields with low/moderate wavenumbers are not strongly attenuated and can still couple to structures that support them, as happens in the case of thin layer of silver. The combination of these two factors explains why a thin layer of silver exhibits a better response over nanostructured silver at 340 nm. In the case of bulk silver, maximum potential depth is obtained near 340nm and is approximately 2 times weaker than the one obtained above nanostructured silver. When the particle is illuminated in free space in the absence of any configurations, the trap depth increases as the laser wavelength decreases, a response associated to the higher amount of power scattered by an electrically larger particle. Results confirm that nanostructured silver exhibit very large trap depth over a very wide

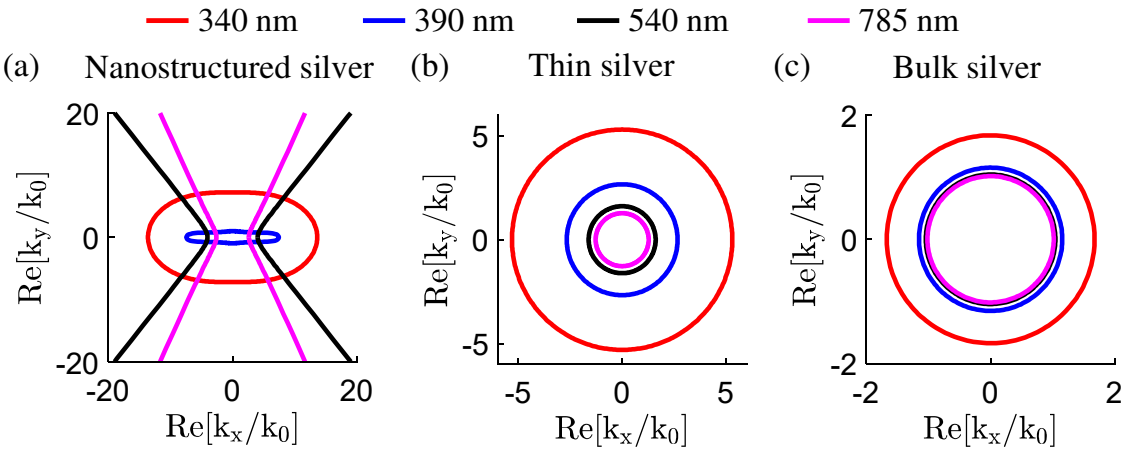

Figure 6.12: Isofrequency contour of (a) a nanostructured silver layer; (b) a thin silver layer; and (c) bulk silver at different wavelengths. The physical dimensions of the nanostructure are detailed in Figure 6.3.

bandwidth, which is not possible to achieve with uniform thin films. Figure 6.11(b) shows the minimum laser intensity required to achieve stable trapping (i.e., a trap depth $\sim 10\ k_B T$) in these configurations. This study reveals that the nanostructured metasurface permits to reduce the required beam intensity by an order of magnitude with respect to the other platforms. This has significant implications in practice as it allows to use low-intensity laser sources operating in the visible/infrared to trap and manipulate nanoparticles while avoiding delicate adjustment between the surface response and the laser wavelength.

To further investigate the performance of these platforms, Figure 6.12 shows their isofrequency contours – i.e., slices of the two-dimensional momentum space (k_x, k_y) at a constant wavelength. These contours describe the wavenumber of the supported SPPs versus their direction in space and are very useful to engineer plasmonic optical traps. From the figure, it is evident that hyperbolic metasurfaces support surface plasmons with larger momentum over a large wavelength range; whereas isotropic materials support surface plasmons with moderate momentum near the plasmon resonance frequency of the material. The potential distribution of the traps above these structures are shown in Figures 6.13 and 6.14. The potential energy is computed varying the particle position (x_0, y_0) over the surface with respect to the beam axis. At the silver plasmon resonance, found at $\lambda_0 \approx 340\text{nm}$ [18], both bulk and thin film configurations support

TM isotropic surface plasmons (Figure 6.12b) that lead to a rotationally symmetric potential distribution around the beam axis (Figure 6.13b-c). At this frequency, the nanostructured silver layer behaves as an elliptical anisotropic surface (Figure 6.12a) and supports rotationally nonsymmetric surface plasmons. Interestingly, the intrinsic metasurface anisotropy translates into a nonsymmetric potential distribution that is illustrated in a 3D fashion in Figure 6.13(a). Figure 6.14 further studies the 1D potential distribution above this configuration when the particle is moved along the main axes (i.e., $\hat{x}$ and $\hat{y}$) of the metasurface. At 340nm wavelength, along the silver nanorods (i.e., $\hat{x}$ axis with $y_0 = 0$), the potential is spatially smooth, and the trap depth ($\nabla U_x = \delta_d$) corresponds to the difference between the potential energies when the particle is located at the beam axis and infinity. Across the strips (i.e., $\hat{y}$ axis with $x_0 = 0$), the potential presents local maxima with energy larger than zero that leads to local barriers with potentials greater than the trap depth ($\nabla U_y > \delta_d$). Such local potential barriers appear above anisotropic surfaces because they support surface plasmons with different wavenumbers (momentum) along different polar directions within the surface. As a result, the lateral recoil force exerted on the particle strongly depends on its azimuthal position with respect to the beam axis. Remarkably, barriers with potential energies even larger than the trap depth can be obtained by leveraging extreme anisotropic responses, associated with SPPs possessing drastically dissimilar wavenumbers as they travel towards different directions within the plane. This case can be found at the metasurface topological transition, which appears at $\lambda_0 = 390$ nm (see Chapter 2) and exhibits a canalization-like response along the $\hat{y}$ direction [50]. There, plasmons propagating towards the $\hat{x}$ axis possess significantly larger momentum than those traveling toward the canalized direction, enabling local potential barriers along the strips (see Figure 6.14) with an energy $\nabla U_x > \nabla U_y$. In such configuration, a trapped particle that gains kinetic energy will probably escape in the direction perpendicular to the nanorods, which in addition to lower potential also exhibits a reduced trap stiffness. It should be noted that the trap depth at this wavelength slightly decreases (Figure 6.11a) due to the overall moderate local density of states exhibited by the metasurface (Figure 6.12a). However, the trap depth is still larger than the one found over uniform silver (Figure 6.13b) because this material provide reduced light-matter interactions

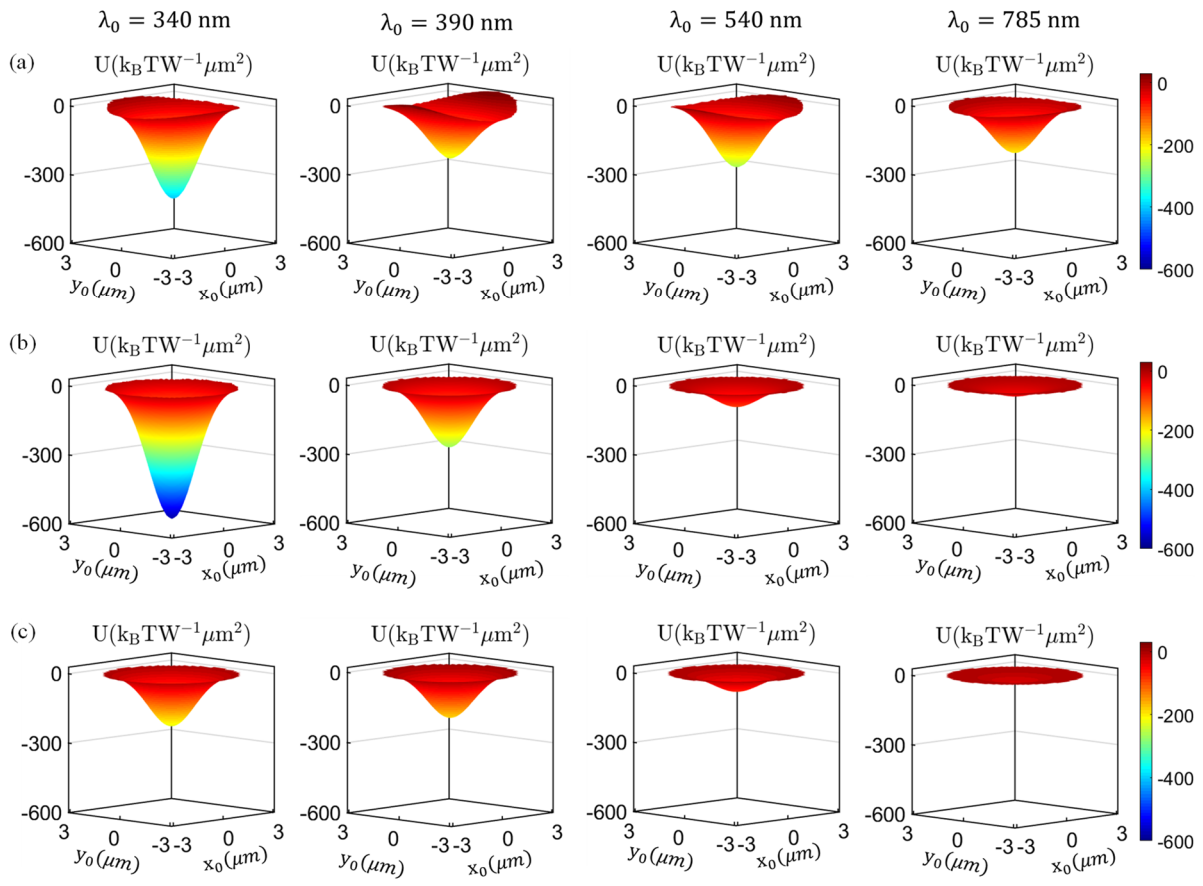

Figure 6.13: Trap potential versus the position (x_0, y_0) of the particle when it is illuminated by a Gaussian beam oscillating at 340 nm, 390 nm, 540 nm and 785 nm operation wavelength. Results are computed when the particle is located above (a) a nanostructured silver layer; (b) a thin silver layer; and (c) bulk silver. Other parameters are as in Figures 6.3 and 6.4.

when operated off-resonance. As the operation wavelength further increases, the nanostructured silver layer behaves as a hyperbolic metasurface and supports highly confined SPPs. Isofrequency contours of these SPPs and associated trapping potentials at $\lambda_0 = 540\text{nm}$ and $\lambda_0 = 785\text{nm}$ are shown in Figures 6.12-6.14. Hyperbolic surfaces lead to asymmetric potential distribution and very significant trap depths, greatly extending the functionality of the proposed anisotropic platform from the visible toward the infrared. Local potential barriers also arise in the hyperbolic case due to the different features of plasmons propagating towards x (see Figure 4.8a) and y semi-planes. SPPs properties evolve as the wavelength increases and the metasurface hyperbolic branches slowly close and tend to behave as in a canalization regime along the $\hat{x}$

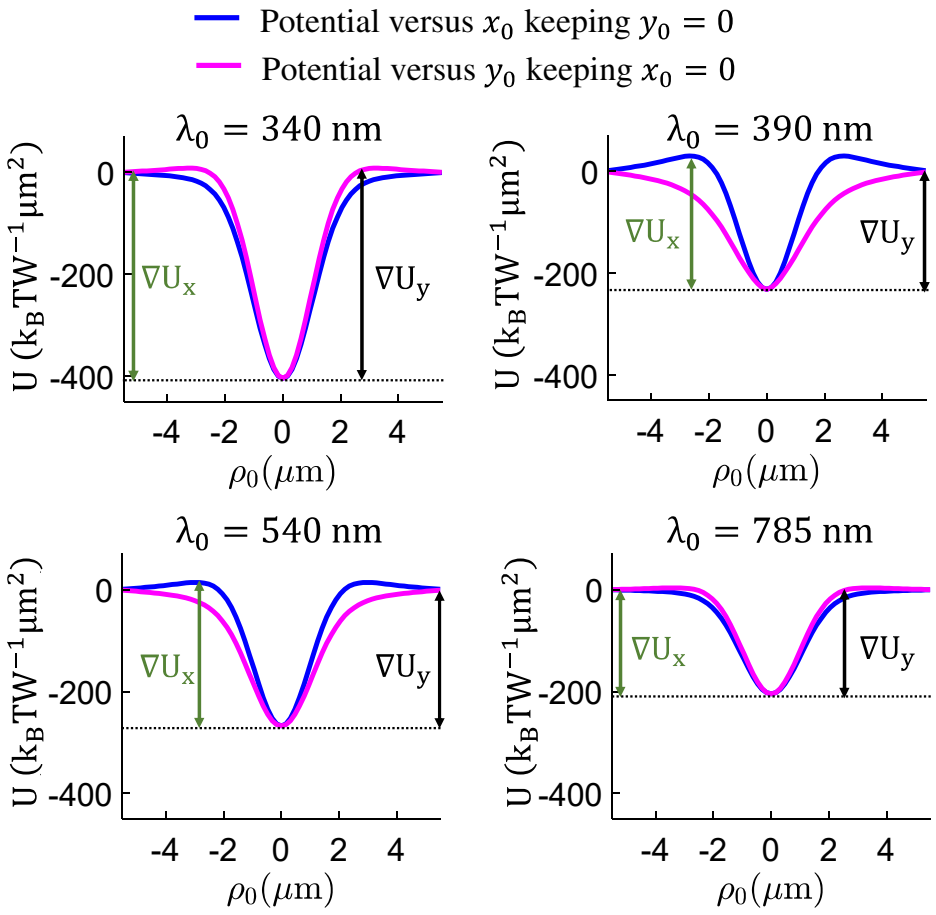

Figure 6.14: Trapping potential computed as a function of the particle position (x_0, y_0) along (x_0 with $y_0 = 0$; blue line) and across (y_0 with $x_0 = 0$; magenta line) the nanorods of a nanostructured silver layer for several operation wavelengths. Local potential barriers along and across the nanorods are denoted as ΔU_x and ΔU_y, respectively. Other parameters are as in Figures 6.3 and 6.4.

direction, which in turn leads to local potential barriers across the nanorods (i.e., $\hat{y}$-axis). For comparison, thin layer and bulk configuration mostly behave as a lossy dielectric reflector as the wavelength increases even further. At these frequencies, they do not effectively contribute to conform an optical trap rather than enhancing/decreasing the gradient force acting on the particle by modifying the standing wave field patterns.

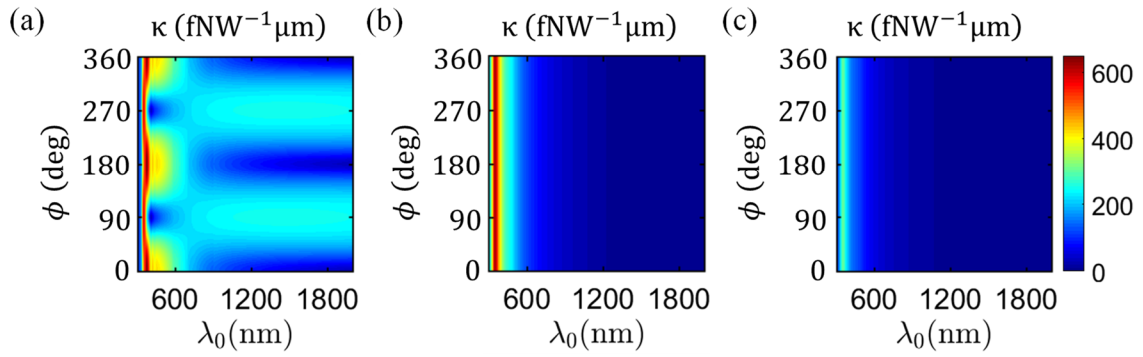

Figure 6.15: Trap stiffness induced on a nanoparticle as a function of the wavelength (λ_0) of the incident Gaussian beam and the polar angle (ϕ) defined with respect to the $\hat{x}$-axis in Fig. 1. Results are computed for a nanoparticle that is illuminated by a Gaussian beam and is located above (a) a nanostructured silver layer; (b) a thin silver layer; and (c) bulk silver. Other parameters are as in Figures 6.3 and 6.4.

6.4.2 TRAP STIFFNESS

To complete this performance analysis, Figure 6.15 shows the stiffness of the optical traps engineered over the considered platforms versus the beam wavelength and the azimuthal angle ϕ within the surface defined with respect to the positive $\hat{x}$-axis, i.e., along the strips. In the case of the nanostructured silver layer, the trap stiffness dramatically increases when the metasurface topology changes from elliptical TE to anisotropic elliptical TM, at around 340nm. As happens with the potential, the stiffness exhibits a rotationally nonsymmetric distribution and, starting from the topological transition at 390 nm to around 750nm, it presents local maxima in the directions along the metallic rods (i.e., $\phi = 0°$ and 180°) and minima in the orthogonal ones (i.e., $\phi = 90°$ and 270°). Such response is associated to the distribution of the nonconservative force that conforms the trap (as the one shown in Figure 6.9a-b) and is consistent with the local potential barriers found along the strips shown in Figure 6.14. Thus, it is probable that energetic particles will escape from these optical traps in the direction across the strips. As wavelength increases further, the metasurface changes its polarization profile and tends to canalize waves along the $\hat{x}$ axis. This mechanism swaps the direction of maximum (minimum) stiffness, which now appears across (along) the strips. In those optical traps, energetic particles will scape in the direction parallel to the strips. For

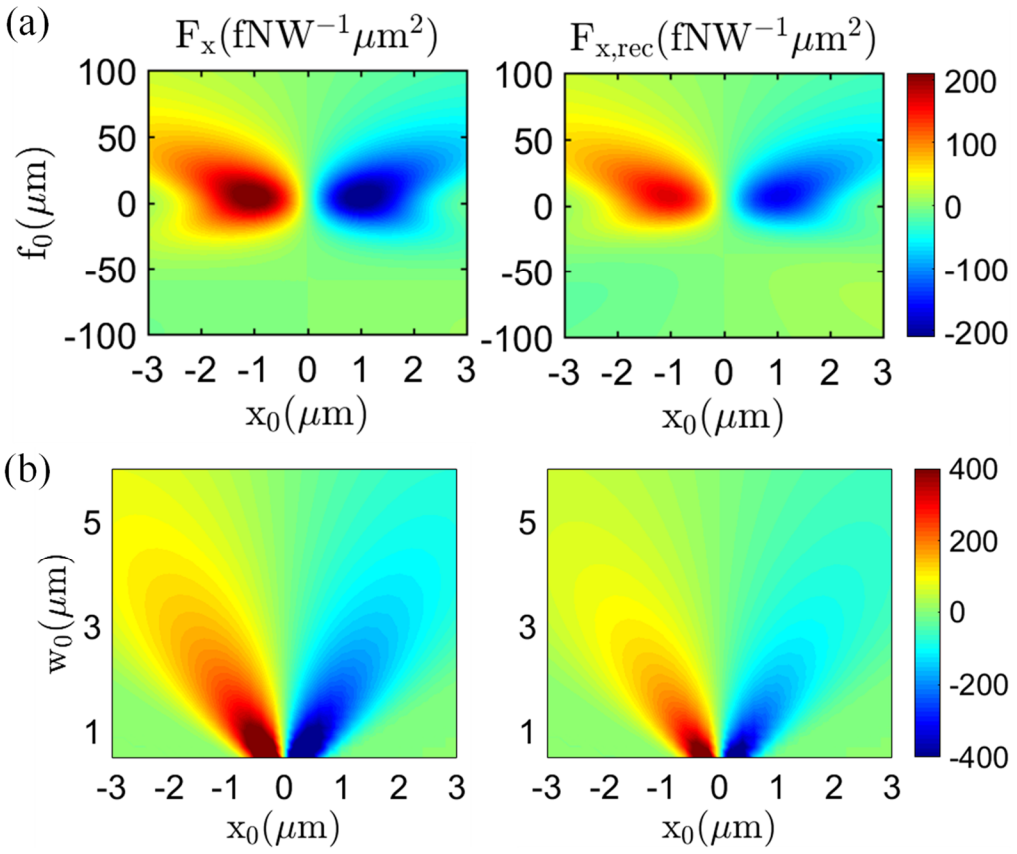

Figure 6.16: Influence of the Gaussian beam properties on the optical forces acting on a nanoparticle located above a hyperbolic metasurface. The first and second column correspond to the total lateral induced forces (F_x) and recoil forces ($F_{x,rec}$) exerted on the particle as a function of its position x_0 with respect to the beam axis. Results are plotted versus (a) the beam focus, keeping the beam waist to $w_0 = 2\mu m$; and (b) the beam waist, keeping the beam focused at $f_0 = 0$. Other parameters are as in Figures 6.3 and 6.4.

comparison, the trap stiffness obtained focusing the beam over a thin silver layer and over bulk silver is shown in Figure 6.15b-c. As expected, optical traps engineered over them only show better stiffness around the metal plasmon resonance and always exhibit a rotationally symmetrical profile around the trap. Overall, anisotropic metasurfaces significantly boost the stiffness of engineered optical traps over a large frequency band.

6.5 ADDITIONAL RESPONSE OF LATERAL AND VERTICAL FORCES

In this section, I investigate the influence of laser focus position and beam waist, substrate refractive index and particle size on the total optical forces exerted on the particle. The lateral trapping forces show a robust response against all these parameters. The only exception appears when the laser focus position is set well below the surface: anti-trapping forces appear in that case since the dipole $\bar{p}_2$ dominates the scattering process as discussed in section 6.3. The total vertical force is always attractive in nature that always confines the particle in the near field of the metasurface.

6.5.1 INFLUENCE OF THE LASER BEAM

The proposed optical traps and vertical force response are robust against the features of the incoming Gaussian beam. This is because the beam is mainly employed to adequately polarize the particle instead of generating additional trapping forces. To investigate the potential influence of the beam properties on the trap performance, Figure 6.16 displays the lateral forces acting on the nanoparticle as a function of the beam waist w_0 and focus position f_0. In particular, Figure 6.16(a) shows the total lateral forces and the contribution from the recoil forces as a function of particle location x_0 versus the focus position f_0, which is varied from positive (i.e., above the surface) to negative (i.e., below the surface) while keeping the beam waist constant to $w_0 = 2\mu m$. Results show that the particle experiences very large trapping forces when the beam is focused near the surface and that the force strength progressively lessens as the focus position is shifted away from the surface. Importantly, the recoil component of the force is very robust against the focus range and clearly dominate in all cases. It should be noted that when the beam is focused very close to the surface, the gradient force become noticeable and might contribute up to one fifth of the total induced force. In addition, the "trapping" forces might become "anti-trapping" when the beam is focused well below the metasurface [lower than -50μm in Figure 6.16(a)]. There, the particle acquires an effective out-of-plane polarization with a handedness pointing towards the beam (i.e., the effective dipole $\bar{p}_2$ dominates over the dipole $\bar{p}_1$ following the description in section 4.3). However, the strength of these anti-trapping forces is quite limited due to reduced amount of power that the particle scatters in this unfocused scenario – i.e., the

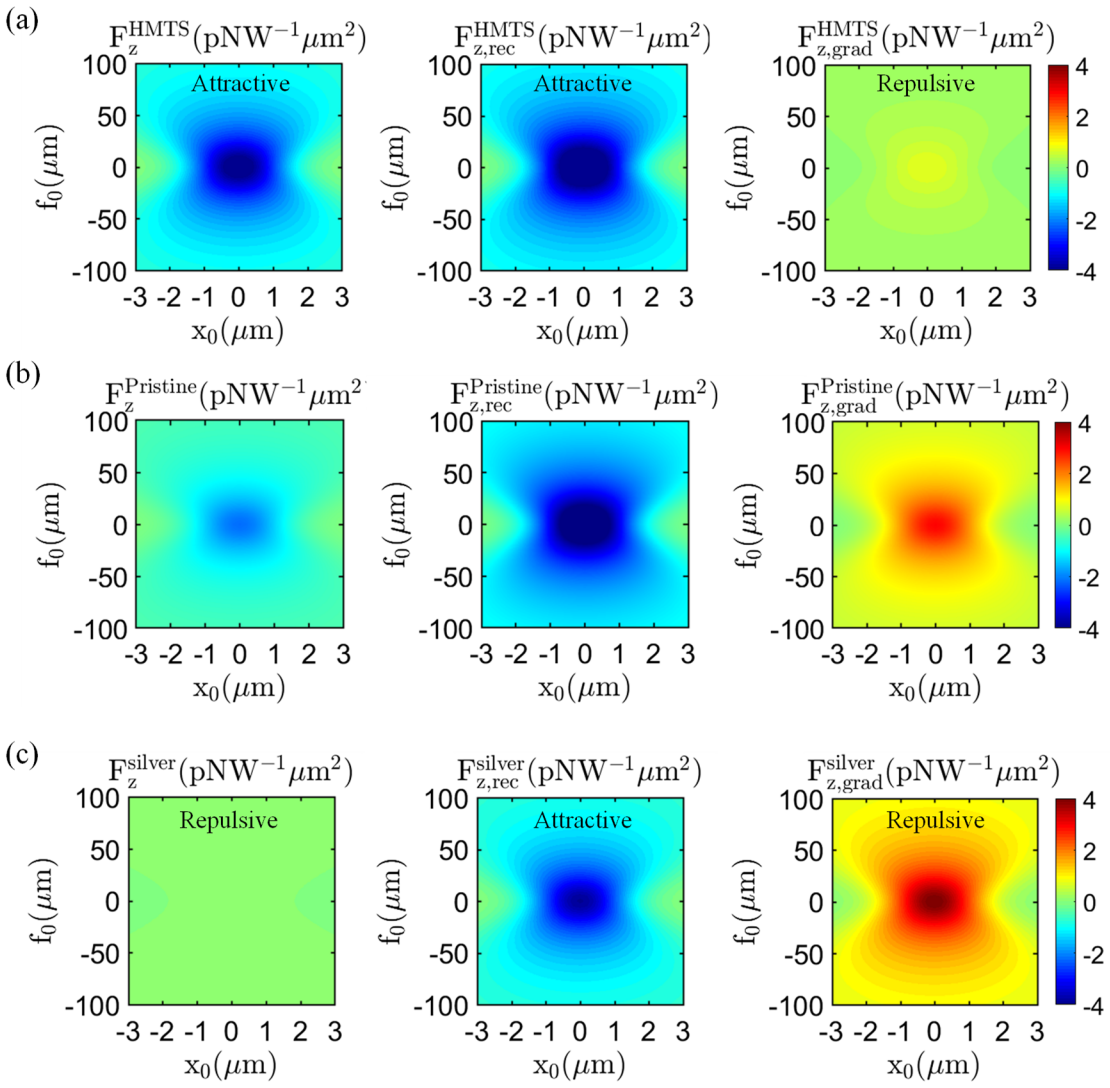

Figure 6.17: Influence of the Gaussian beam focus position on the vertical component of the total forces acting on a nanoparticle located above (a) a nanostructured silver layer; (b) a thin layer of silver; and (c) bulk silver. Results are computed as a function of particle position $x_0(\mu m)$ versus the beam focus position f_0 keeping the beam waist fixed to $w_0 = 2$ μm fixed. Left, middle and right columns show the response of the total, recoil, and gradient vertical forces, respectively. Results are in the same scale. Other parameters are as in Figures 6.3 and 6.4.

magnitude of the electric dipole $\bar{p}_2$ that characterizes this scattering process is very small. Figure 6.16(b) shows a similar study versus the beam waist w_0 considering that it has been focused exactly on the surface ($f_0 = 0$). It can be observed that trapping forces dramatically increases as the beam waist reduces. This is because the large confinement of the electric field near the focus spot boosts the power scattered by the

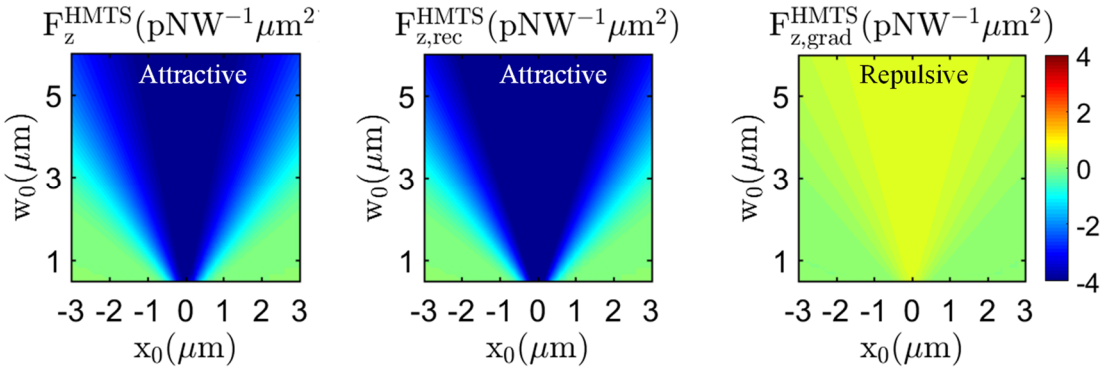

Figure 6.18: Influence of the Gaussian beam waist on the vertical component of the optical forces acting on a nanoparticle located above a hyperbolic metasurface. Results are computed as a function of particle position $x_0(\mu m)$ versus the beam waist w_0 with focus position set to $f_0 = 2$ μm. Left, middle and right columns show the response of total, recoil, and gradient vertical forces, respectively. Results are in the same scale. Other parameters are as in Figures 6.3 and 6.4.

particle in form of surface plasmons, which in turn enhances the strength of the recoil force. There, the gradient of the electric field intensity also increases thus enhancing the gradient force as well. In all cases, the particle always experiences attractive vertical forces that pushes it towards the surface as will be discussed now.

Figure 6.17 shows the vertical forces versus the particle position x_0 and beam focus f_0 when the particle is located above the nanostructured silver layer, uniform and thin silver layer, and bulk silver. Specifically, Figure 6.17(a)-(b) confirms that the vertical forces above the thin layers are negative and attract the particle towards the surfaces. Such response appears due to the dominant vertical recoil force where the evanescent tails of the surface plasmons introduce attractive response. However, the gradient component of the force is repulsive due to the superposition of the incident and reflected fields of the beam that aims to push the particle towards the nearest intensity hotspot above the surface (see Figure 6.3). Figure 6.17(c) shows that the net vertical forces induced above bulk silver is repulsive (positive). There, the repulsive gradient

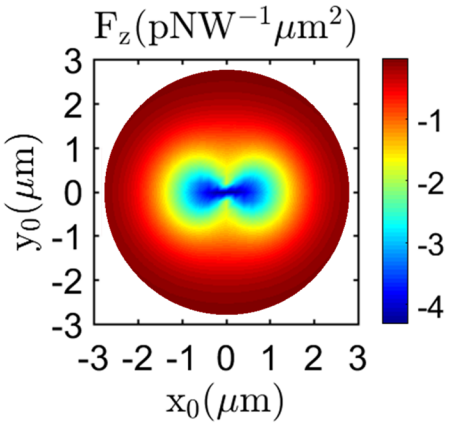

Figure 6.19: Vertical optical forces induced on a gold nanoparticle located above a hyperbolic metasurface when it is illuminated with a Gaussian beam. Result is computed as a function of particle position (x_0, y_0). Other parameters are as in Figures 6.3 and 6.4.

component is much stronger than the attractive recoil one and leads to positive vertical forces that tend to kick the particle away from the surface.

It is important to highlight that the attractive nature of the vertical forces above the nanostructured metasurface is preserved for Gaussian beams possessing different beam waist (w_0), as shown in Figure 6.18. This further confirms that the dominant behavior of the recoil component over the gradient one determines the vertical force response and pulls the particle near the surface. Finally, Figure 6.19 shows that such attractive response always appears above the metasurface independently of the particle position within the beam.

6.5.2 INFLUENCE OF SUBSTRATE REFRACTIVE INDEX

It is important to investigate the influence of the refractive index of the substrate that supports the hyperbolic metasurface on the optical force response. To this purpose, Figure 6.20 shows the response of lateral and vertical forces as a function of particle position. Three different substrates are considered here: (i) porous polymer ($n_2 = 1.05$), (ii) fused silica ($n_2 = 1.46$), and (iii) crystal silica ($n_2 = 1.52$). Results show that both the lateral and vertical force strengths decrease as the substrate refractive index increases. This can be attributed to the change on the particle helicity with respect to the substrate refractive index.

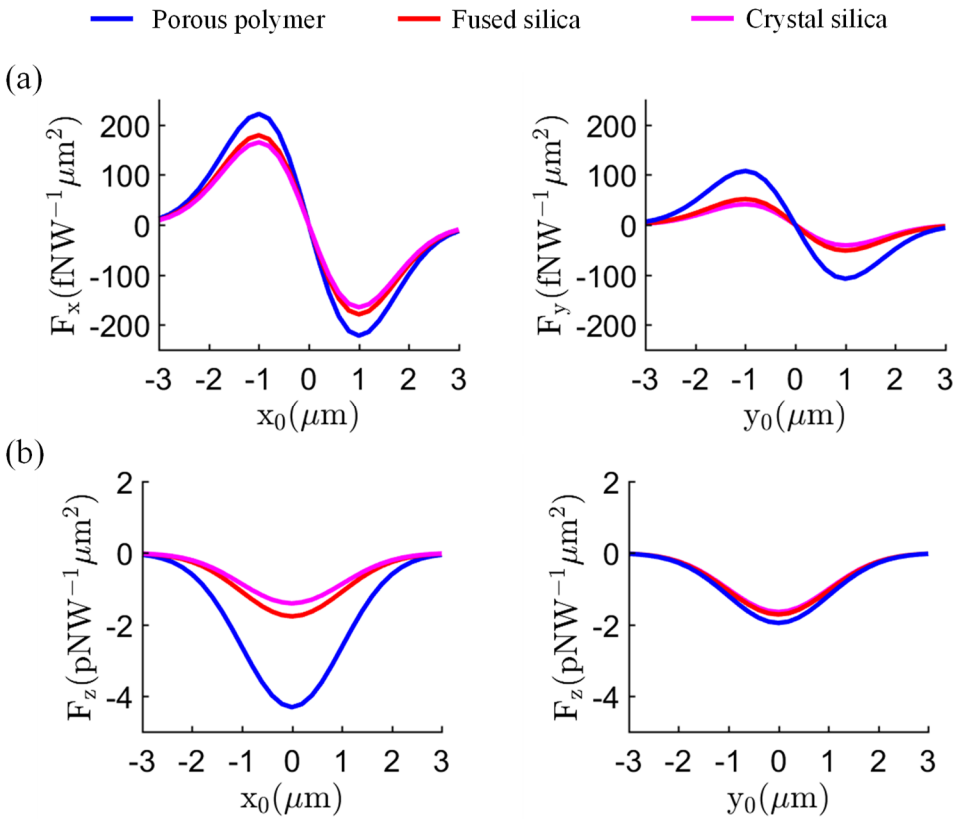

Figure 6.20: Optical forces induced on a nanoparticle located above a nanostructured silver layer versus the dipole position for different types of substrate. (a) Lateral trapping force. (b) Vertical force versus particle position x_0 (left column) and y_0 (right column) keeping $y_0 = 0$ and $x_0 = 0$ fixed, respectively. Blue, red, and magenta lines correspond to the case when the metasurface is supported by porous polymer ($n_2 = 1.05$), fused silica ($n_2 = 1.46$), and crystal silica ($n_2 = 1.52$), respectively. Other parameters are as in Figures 6.3 and 6.4.

6.5.3 INFLUENCE OF PARTICLE SIZE

The electrical distance between the dipole and the metasurface plays a key role on the performance of the induced trap. For instance, when the illuminating Gaussian beam oscillates near the silver resonance frequency (~340nm), the electrical distance between the particle (of radius 15nm) and the metasurface increases thus leading to a slightly better (~1.4 times) trap depth induced above thin silver in comparison to the nanostructured silver (see Figure 6.11). There is a clear trade-off [4,8] between the particle-surface distance and the state of modes that can be excited: when the particle is located in the very near field of the surface, it can couple to surface plasmons with large wavenumbers that boost the overall performance of

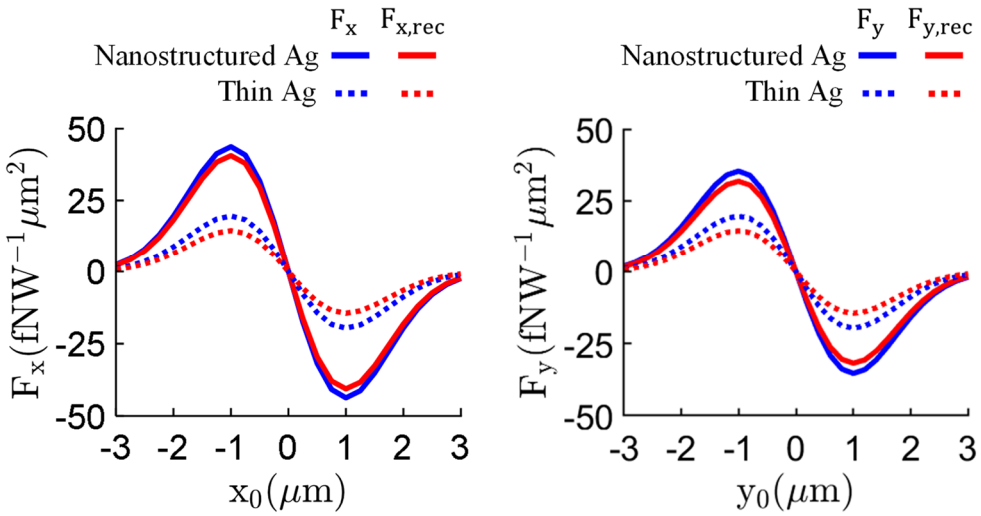

Figure 6.21: Trapping of gold nanoparticles over a nanostructured metasurface with a Gaussian beam. Total lateral forces (F_x, F_y: blue solid line) and recoil forces ($F_{x,rec}$, $F_{y,rec}$: red solid line) exerted on the nanoparticle versus x_0 (left panel) and y_0 (right panel) with $y_0 = 0$ and $x_0 = 0$ fixed. Dotted lines correspond to the forces acting on the particle when the metasurface is replaced with a thin layer of silver with identical thickness. The gold nanoparticle has a radius $a = 5$ nm and is located in free space at a distance $z_0 = a$ over the surface. Operating wavelength of the incident Gaussian beam is 340nm and other parameters are as in Figures 6.3 and 6.4.

the optical trap; when the particle is moved away from the surface, scattered fields are partially filtered out by free space and cannot efficiently excite surface plasmons. In the latter case, evanescent fields with low/moderate wavenumbers are not strongly attenuated and can still couple to the structures that support them, as happens with the thin layer of silver. The combination of these two factors explains why thin silver exhibits a better response over nanostructured silver at 340 nm for this specific configuration. Note that the electrical distance between the particle and the metasurface decreases in the case of particles with smaller radii. Figure 6.21 explores this scenario and shows the net lateral forces and the recoil force exerted over a nanoparticle with radius of 5nm located above nanostructured silver and thin layer of silver at 340nm. Results show that the strength of the lateral force is ~2 times stronger in the case of nanostructured silver.

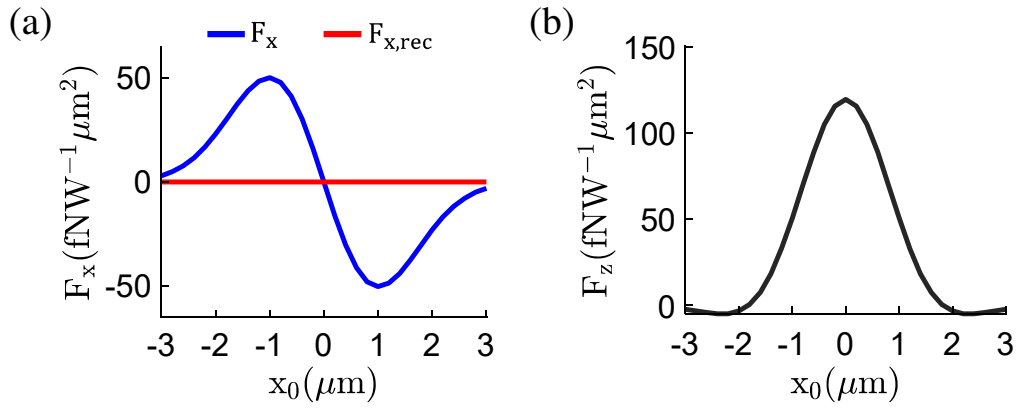

Figure 6.22: Optical trapping of a gold nanoparticle above a silver substrate illuminated with a p-polarized Gaussian beam operating at 540 nm wavelength. (a) Total lateral force F_x (blue solid line) and recoil force $F_{x,rec}$ (red solid line). (b) Total vertical force F_z exerted on the particle versus its position. Other parameters are as in Figures 6.3 and 6.4.

6.6 FORCE RESPONSE ABOVE BULK SILVER

The response of optical forces exerted on a gold nanoparticle located above a bulk silver when illuminated by a Gaussian beam oscillating at 540 nm wavelength is shown in Figure 6.22. Specifically, Figure 6.22(a) shows the lateral total and recoil forces versus the particle position. Results show that lateral recoil force strength is significantly weaker (but not strictly zero) and the trapping mechanism is primarily enabled by the gradient force arising from the beam – a response similar to the one obtained above thin silver (see Figure 6.8b). This analysis confirms that the trap performance above nonpatterned metals, operated away from the plasmon resonance frequency of metal, is mostly determined by the gradient force with minimal/negligible contribution from the recoil force. Moreover, Figure 6.22(b) shows the vertical force experienced by the nanoparticle above the silver substrate. There, one can see that the vertical force is positive – repels the nanoparticle away from the surface – thanks to the dominant contribution of repulsive vertical gradient force.

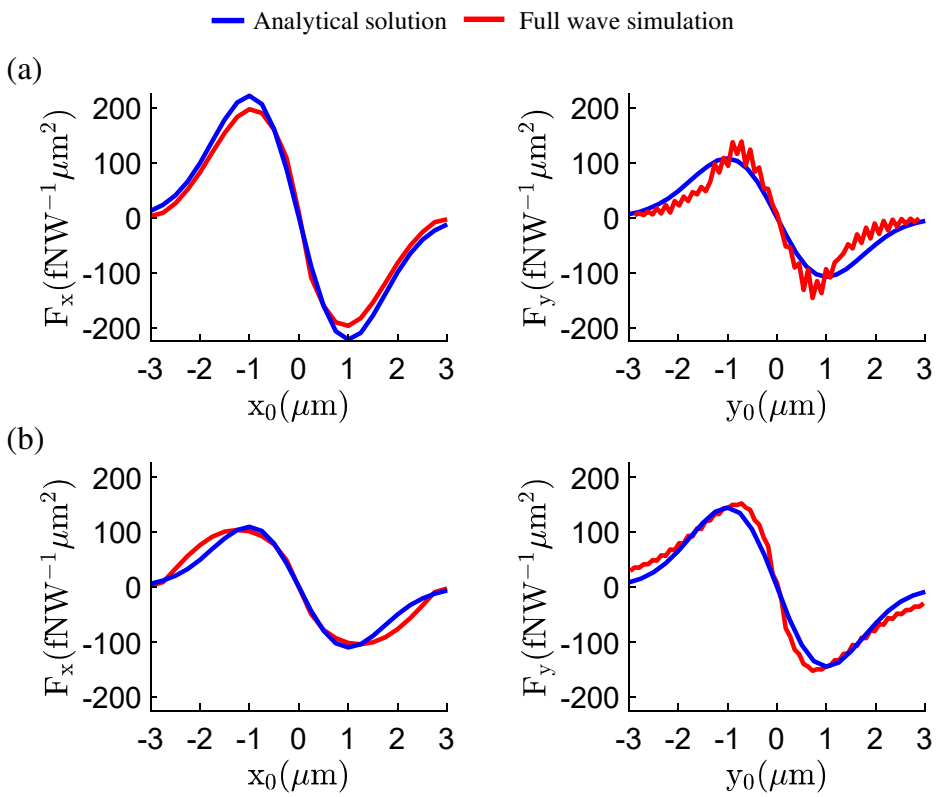

Figure 6.23: Optical trapping of a gold nanoparticle over a nanostructured silver illuminated by a normally incident p-polarized Gaussian beam. Lateral force components F_x and F_y exerted on a particle with radius $a = 15[nm]$ located at $(x_0, y_0, a + 0.5[nm])$. Results are computed versus x_0 (keeping $y_0 = 0$) and y_0 (keeping $x_0 = 0$), respectively, at (s) 540nm and (b) 785nm. Solid blue and red lines correspond to the results computed using our theoretical model and full wave simulations, respectively. Other parameters are as in Figures 6.3 and 6.4.

6.7 NUMERICAL SIMULATIONS

In this section, I detail the numerical simulations performed using COMSOL Multiphysics [20] and then compare the results with the ones obtained following the theoretical approach as detailed in Chapter 4.

6.7.1 SIMULATION SET UP

In numerical simulations, the nanostructured silver layer is characterized considering the frequency-dependent complex permittivity available in Ref. [51]. The gold nanoparticle is characterized using a Drude-Lorentz model [18]. The entire domain of the simulation is shown in Figure 4.11. Scattering

boundary conditions have been applied to the outer surfaces of the domain to avoid unwanted reflection of electromagnetic waves. A fine tetrahedral mesh has been applied to the entire domain. Note that the convergence of numerical simulation largely depends on the mesh applied to discretize the silver nanorods and gold nanoparticle. To better capture the electromagnetic interaction during the scattering process, I apply an extremely fine mesh with maximum element size of $\lambda_0/70$ and $\lambda_0/350$ to the silver layer and nanoparticle, respectively. Finally, I compute the total optical forces induced on the nanoparticle using Maxwell's stress tensor formalism [18].

6.7.2 COMPARISON OF FORCE RESPONSE: FULL WAVE SIMULATION VERSUS THEORY

To verify the accuracy of the theoretical model in the near field of the surface, I have performed full wave numerical simulations in COMSOL Multiphysics considering a spherical gold nanoparticle with radius $a = 15\text{nm}$ located at a position $\mathrm{r}_0 = (\mathrm{x}_0, \mathrm{y}_0, a + 0.5[\text{nm}])$. The setup is illuminated by a normally incident p-polarized Gaussian beam. Figure 6.23 shows the total lateral force components ($\mathrm{F_x}$ and $\mathrm{F_y}$) computed using my theory based on effective medium approach (blue solid line) and using full wave simulations (red solid line) considering actual nanostructured silver. Results show the force component as a function of the particle position when the incident Gaussian beams oscillates at (a) 540nm and (b) 785nm. Very good agreement between theory and simulations for the x-component of the force along the $\hat{x}$-axis is found in all cases. Such agreement appears because the effective medium approach captures very well the system response along the x-direction. However, it should be noted that the numerical response of y-component of the force ($\mathrm{F_y}$) is not completely smooth versus the particle position y_0 along the $\hat{y}$-axis. Numerical results show small ripples on the force as the particle moves along the $\hat{y}$-axis from one metallic rod to another through the airgap in between them. These ripples become stronger as the operation wavelength decreases and the particle is electrically closer to the surface. Even though theoretical results are not able to capture these small oscillations, as they arise due to the near-field interactions among the nanorods, the effective medium approach is able to predict well both the magnitude and the averaged spatial

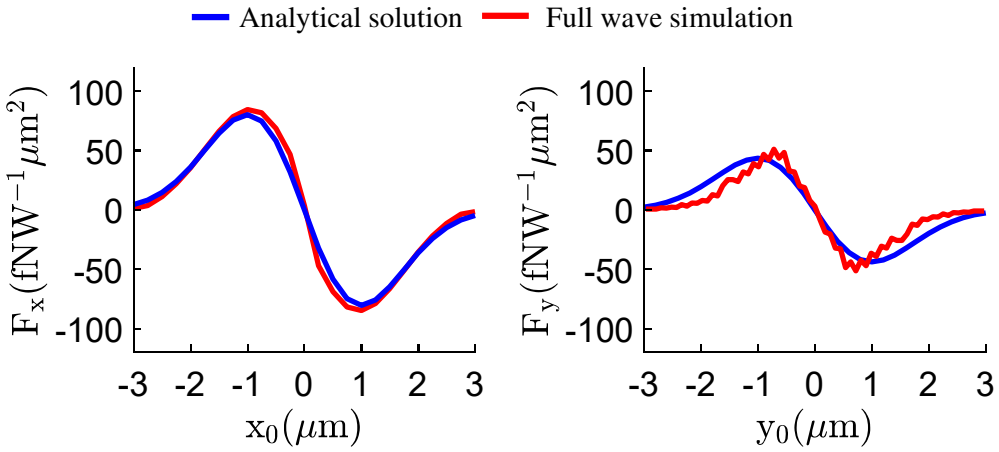

Figure 6.24: Optical trapping of a gold nanoparticle over a nanostructured silver layer illuminated by a normally incident p-polarized Gaussian beam. The figured show the lateral force components F_x and F_y exerted on a particle with radius $a = 15$nm located at $(x_0, y_0, 30[\mathrm{nm}])$. Results are computed versus x_0 (keeping $y_0 = 0$) and y_0 (keeping $x_0 = 0$), respectively, at 540nm. Solid blue and red lines correspond to the results computed using our theoretical model and full wave simulations, respectively. Other parameters are as in Figure 6.3 and 6.4.

profile of the force. It should be noted that these ripples (i) do not change the profile of F_y; and (ii) have a very limited impact on the force amplitude; therefore, they do not significantly modify the trap response.

To further investigate the accuracy of my model, I have performed a similar analysis at 540 nm considering that the particle is shifted away 15 nm from the surface and is now located at $r_0 = (x_0, y_0, 30[\mathrm{nm}])$. Results, shown in Figure 6.24, confirm again a very good agreement between the theory and simulations. Note that the strength of the ripples that appears due to near-field interactions among the nanorods is decreased, which is expected as the particle is electrically farther away from the surface.

6.8 CHAPTER CONCLUSIONS

I have put forward the concept of anisotropic and hyperbolic optical traps to manipulate nanoparticles. These optical traps are created by illuminating a nanoparticle over an anisotropic metasurface with a linearly polarized Gaussian beam and their properties strongly depend on the surface topology and light-matter interactions. To analyse this platform, I have developed a rigorous theoretical formalism able to compute the induced trapping forces based on the anisotropic scattered dyadic Green's function approach merged

with the Lorentz force within the Rayleigh approximation. This approach, validated with full-wave numerical simulations in COMSOL Multiphysics, reveals that giant, nonconservative recoil force pointing towards the beam axis dominates the overall trap response. This force appears due to the excitation of ultra-confined SPPs on the anisotropic metasurface. Then, I have applied the Helmholtz decomposition method to calculate the potential energy of the resulting nonconservative force-field. My formalism permits to compute fundamental metrics that characterize optical traps engineered over plasmonic materials through nonconservative fields, including spatial potential distribution, trap depth and stiffness, local potential barriers, as well as the minimum laser intensity that achieve stable optical trapping.

The performance of the proposed anisotropic optical traps is outstanding: they exhibit large trap depths over an extremely broadband frequency range that covers the entire visible spectrum extending well into the IR band. As a result, a wide variety of low-intensity laser sources can be employed to achieve stable trapping of nanoparticles avoiding precise alignments between the surface response and the operation wavelength, and significantly reducing the possibility of damaging trapped particles due to photoheating. As a specific example, I studied the performance of optical traps engineered over a nanostructured silver layer and analysed how the trap response evolves as the metasurface topology changes from anisotropic elliptical to hyperbolic going through the topological transition. In addition, I have found that the momentum imbalance of the SPPs excited by the particle on anisotropic surfaces gives rise to local potential barriers and larger trap stiffness along certain spatial directions, thus breaking the rotational symmetry that characterizes common optical traps. The engineered traps exhibit a much larger potential depth and stiffness than the one found focusing identical Gaussian beam over uniform thin silver, bulk silver or in free-space, and, more importantly, maintain such response over a large bandwidth. I note that my formalism is based on classical Maxwellian approach and omits additional forces that might originate from other mechanisms, such as Casimir forces [18]. Investigating the influence of such forces in the proposed platform is the scope of future research.

Moving forward, ultrathin metasurfaces enable unique possibilities to construct optical traps with excellent performance, including the possibility to engineer local potential barriers, at a desired wavelength, by tailoring the surface topology, local density of states, and the momentum of the supported plasmons. To this purpose, different plasmonic materials – including metals such as gold or silver and semimetals as graphene and WTe_2[52]– can be appropriately patterned in subwavelength arrangements. In addition, natural anisotropic and hyperbolic materials [53,54] can also be employed to trapping purposes, including hexagonal boron nitride [55], hybrid composites [56,57], van der Waals crystals [58-60] and an increasing family of 2D materials [46-49]. I envision that anisotropic and hyperbolic metasurfaces will lead to the next generation of low-power nano-optical tweezers.

6.9 CHAPTER REFERENCES

[1] Pang, Y. and Gordon, R., 2012. Optical trapping of a single protein. *Nano Letters*, *12*(1), pp.402-406.

[2] Ashkin, A. and Dziedzic, J.M., 1987. Optical trapping and manipulation of viruses and bacteria. *Science*, *235*(4795), pp.1517-1520.

[3] Yang, A.H., Moore, S.D., Schmidt, B.S., Klug, M., Lipson, M. and Erickson, D., 2009. Optical manipulation of nanoparticles and biomolecules in sub-wavelength slot waveguides. *Nature*, *457*(7225), pp.71-75.

[4] Roichman, Y., Sun, B., Stolarski, A. and Grier, D.G., 2008. Influence of nonconservative optical forces on the dynamics of optically trapped colloidal spheres: the fountain of probability. *Physical Review Letters*, *101*(12), p.128301.

[5] Eriksson, E., Enger, J., Nordlander, B., Erjavec, N., Ramser, K., Goksör, M., Hohmann, S., Nyström, T. and Hanstorp, D., 2007. A microfluidic system in combination with optical tweezers for analyzing rapid and reversible cytological alterations in single cells upon environmental changes. *Lab on a Chip*, *7*(1), pp.71-76.

[6] Neuman, K.C. and Block, S.M., 2004. Optical trapping. *Review Of Scientific Instruments*, *75*(9), pp.2787-2809.

[7] Favre-Bulle, I.A., Stilgoe, A.B., Scott, E.K. and Rubinsztein-Dunlop, H., 2019. Optical trapping in vivo: theory, practice, and applications. *Nanophotonics*, *8*(6), pp.1023-1040.

[8] Gao, D., Ding, W., Nieto-Vesperinas, M., Ding, X., Rahman, M., Zhang, T., Lim, C. and Qiu, C.W., 2017. Optical manipulation from the microscale to the nanoscale: fundamentals, advances and prospects. *Light: Science & Applications*, *6*(9), pp.e17039-e17039.

[9] Chaumet, P.C., Rahmani, A. and Nieto-Vesperinas, M., 2002. Optical trapping and manipulation of nano-objects with an apertureless probe. *Physical Review Letters*, *88*(12), p.123601.

[10] Furukawa, H. and Yamaguchi, I., 1998. Optical trapping of metallic particles by a fixed Gaussian beam. *Optics Letters*, *23*(3), pp.216-218.

[11] Ashkin, A., Dziedzic, J.M. and Yamane, T., 1987. Optical trapping and manipulation of single cells using infrared laser beams. *Nature*, *330*(6150), pp.769-771.

[12] Ashkin, A., Dziedzic, J.M., Bjorkholm, J.E. and Chu, S., 1986. Observation of a single-beam gradient force optical trap for dielectric particles. *Optics Letters*, *11*(5), pp.288-290.

[13] Ashkin, A., 1997. Optical trapping and manipulation of neutral particles using lasers. *Proceedings of the National Academy of Sciences*, *94*(10), pp.4853-4860.

[14] Chaumet, P.C. and Nieto-Vesperinas, M., 2000. Time-averaged total force on a dipolar sphere in an electromagnetic field. *Optics Letters*, *25*(15), pp.1065-1067.

[15] Volpe, G., Helden, L., Brettschneider, T., Wehr, J. and Bechinger, C., 2010. Influence of noise on force measurements. *Physical Review Letters*, *104*(17), p.170602.

[16] Silveirinha, M.G., Gangaraj, S.A.H., Hanson, G.W. and Antezza, M., 2018. Fluctuation-induced forces on an atom near a photonic topological material. *Physical Review A*, *97*(2), p.022509.

[17] Ivinskaya, A., Petrov, M.I., Bogdanov, A.A., Shishkin, I., Ginzburg, P. and Shalin, A.S., 2017. Plasmon-assisted optical trapping and anti-trapping. *Light: Science & Applications*, *6*(5), pp.e16258-e16258.

[18] Novotny, L. and Hecht, B., 2012. *Principles of nano-optics*. Cambridge university press.

[19] Bhatia, H., Norgard, G., Pascucci, V. and Bremer, P.T., 2012. The Helmholtz-Hodge decomposition—a survey. *IEEE Transactions on Visualization and Computer Graphics*, *19*(8), pp.1386-1404.

[20] www.comsol.com

[21] High, A.A., Devlin, R.C., Dibos, A., Polking, M., Wild, D.S., Perczel, J., De Leon, N.P., Lukin, M.D. and Park, H., 2015. Visible-frequency hyperbolic metasurface. *Nature*, *522*(7555), pp.192-196.

[22] Nemoto, S., 1990. Nonparaxial gaussian beams. *Applied Optics*, *29*(13), pp.1940-1946.

[23] Agrawal, G.P. and Pattanayak, D.N., 1979. Gaussian beam propagation beyond the paraxial approximation. *Journal of Optical Society of America A*, *69*(4), pp.575-578.

[24] Van Thourhout, D. and Roels, J., 2010. Optomechanical device actuation through the optical gradient force. *Nature Photonics*, *4*(4), pp.211-217.

[25] Kumar, J., Li, L., Jiang, X.L., Kim, D.Y., Lee, T.S. and Tripathy, S., 1998. Gradient force: The mechanism for surface relief grating formation in azobenzene functionalized polymers. *Applied Physics Letters*, *72*(17), pp.2096-2098.

[26] Paul, N.K. and Kemp, B.A., 2016. Optical manipulation of small particles on the surface of a material. *Journal of Optics*, *18*(8), p.085402.

[27] Rodríguez-Fortuño, F.J., Engheta, N., Martínez, A. and Zayats, A.V., 2015. Lateral forces on circularly polarizable particles near a surface. *Nature Communications*, *6*(1), pp.1-8.

[28] Petrov, M.I., Sukhov, S.V., Bogdanov, A.A., Shalin, A.S. and Dogariu, A., 2016. Surface plasmon polariton assisted optical pulling force. *Laser & Photonics Reviews*, *10*(1), pp.116-122.

[29] Kingsley-Smith, J.J., Picardi, M.F., Wei, L., Zayats, A.V. and Rodríguez-Fortuño, F.J., 2019. Optical forces from near-field directionalities in planar structures. *Physical Review B*, *99*(23), p.235410.

[30] Ivinskaya, A., Kostina, N., Proskurin, A., Petrov, M.I., Bogdanov, A.A., Sukhov, S., Krasavin, A.V., Karabchevsky, A., Shalin, A.S. and Ginzburg, P., 2018. Optomechanical manipulation with hyperbolic metasurfaces. *ACS Photonics*, *5*(11), pp.4371-4377.

[31] Rohrbach, A., 2005. Stiffness of optical traps: quantitative agreement between experiment and electromagnetic theory. *Physical Review Letters*, *95*(16), p.168102.

[32] Juan, M.L., Righini, M. and Quidant, R., 2011. Plasmon nano-optical tweezers. *Nature Photonics*, *5*(6), pp.349-356.

[33] Righini, M., Volpe, G., Girard, C., Petrov, D. and Quidant, R., 2008. Surface plasmon optical tweezers: tunable optical manipulation in the femtonewton range. *Physical Review Letters*, *100*(18), p.186804.

[34] Zaman, M.A., Padhy, P. and Hesselink, L., 2019. Near-field optical trapping in a non-conservative force field. *Scientific Reports*, *9*(1), pp.1-11.

[35] Sukhov, S. and Dogariu, A., 2017. Non-conservative optical forces. *Reports on Progress in Physics*, *80*(11), p.112001.

[36] M. A. Zaman, P. Padhy, and L. Hesselink, Solenoidal optical forces from a plasmonic Archimedean spiral, *Physical Review A*, 100, 013857 (2019).

[37] Zill, D.G., 2020. *Advanced engineering mathematics*. Jones & Bartlett Publishers.

[38] Hajizadeh, F. and Reihani, S.N.S., 2010. Optimized optical trapping of gold nanoparticles. *Optics Express*, *18*(2), pp.551-559.

[39] Šiler, M. and Zemánek, P., 2010. Particle jumps between optical traps in a one-dimensional (1D) optical lattice. *New Journal of Physics*, *12*(8), p.083001.

[40] Vakil, A. and Engheta, N., 2011. Transformation optics using graphene. *Science*, *332*(6035), pp.1291-1294.

[41] Yermakov, O.Y., Ovcharenko, A.I., Song, M., Bogdanov, A.A., Iorsh, I.V. and Kivshar, Y.S., 2015. Hybrid waves localized at hyperbolic metasurfaces. *Physical Review B*, *91*(23), p.235423.

[42] Trushkov, I. and Iorsh, I., 2015. Two-dimensional hyperbolic medium for electrons and photons based on the array of tunnel-coupled graphene nanoribbons. *Physical Review B*, *92*(4), p.045305.

[43] Nemilentsau, A., Low, T. and Hanson, G., 2016. Anisotropic 2D materials for tunable hyperbolic plasmonics. *Physical Review Letters*, *116*(6), p.066804.

[44] Bedeaux, D. and Vlieger, J., 2004. *Optical properties of surfaces*. Imperial College Press.

[45] Kildishev, A.V., Boltasseva, A. and Shalaev, V.M., 2013. Planar photonics with metasurfaces. *Science*, *339*(6125), p.1232009.

[46] Correas-Serrano, D., Gomez-Diaz, J.S., Melcon, A.A. and Alù, A., 2016. Black phosphorus plasmonics: anisotropic elliptical propagation and nonlocality-induced canalization. *Journal of Optics*, *18*(10), p.104006.

[47] Van Veen, E., Nemilentsau, A., Kumar, A., Roldán, R., Katsnelson, M.I., Low, T. and Yuan, S., 2019. Tuning two-dimensional hyperbolic plasmons in black phosphorus. *Physical Review Applied*, *12*(1), p.014011.

[48] Wang, C., Huang, S., Xing, Q., Xie, Y., Song, C., Wang, F. and Yan, H., 2020. Van der Waals thin films of WTe2 for natural hyperbolic plasmonic surfaces. *Nature Communications*, *11*(1), pp.1-9.

[49] Frenzel, A.J., Homes, C.C., Gibson, Q.D., Shao, Y.M., Post, K.W., Charnukha, A., Cava, R.J. and Basov, D.N., 2017. Anisotropic electrodynamics of type-II Weyl semimetal candidate WTe 2. *Physical Review B*, *95*(24), p.245140.

[50] Correas-Serrano, D., Alù, A. and Gomez-Diaz, J.S., 2017. Plasmon canalization and tunneling over anisotropic metasurfaces. *Physical Review B*, *96*(7), p.075436.

[51] Wu, Y., Zhang, C., Estakhri, N.M., Zhao, Y., Kim, J., Zhang, M., Liu, X.X., Pribil, G.K., Alù, A., Shih, C.K. and Li, X., 2014. Intrinsic optical properties and enhanced plasmonic response of epitaxial silver. *Advanced Materials*, *26*(35), pp.6106-6110.

[52] Homes, C.C., Ali, M.N. and Cava, R.J., 2015. Optical properties of the perfectly compensated semimetal WTe 2. *Physical Review B*, *92*(16), p.161109.

[53] Sun, J., Litchinitser, N.M. and Zhou, J., 2014. Indefinite by nature: from ultraviolet to terahertz. *ACS Photonics*, *1*(4), pp.293-303.

[54] Guan, S., Huang, S.Y., Yao, Y. and Yang, S.A., 2017. Tunable hyperbolic dispersion and negative refraction in natural electride materials. *Physical Review B*, *95*(16), p.165436.

[55] Caldwell, J.D., Kretinin, A.V., Chen, Y., Giannini, V., Fogler, M.M., Francescato, Y., Ellis, C.T., Tischler, J.G., Woods, C.R., Giles, A.J. and Hong, M., 2014. Sub-diffractional volume-confined polaritons in the natural hyperbolic material hexagonal boron nitride. *Nature Communications*, *5*(1), pp.1-9.

[56] Dai, S., Ma, Q., Liu, M.K., Andersen, T., Fei, Z., Goldflam, M.D., Wagner, M., Watanabe, K., Taniguchi, T., Thiemens, M. and Keilmann, F., 2015. Graphene on hexagonal boron nitride as a tunable hyperbolic metamaterial. *Nature Nanotechnology*, *10*(8), pp.682-686.

[57] Brar, V.W., Jang, M.S., Sherrott, M., Kim, S., Lopez, J.J., Kim, L.B., Choi, M. and Atwater, H., 2014. Hybrid surface-phonon-plasmon polariton modes in graphene/monolayer h-BN heterostructures. *Nano Letters*, *14*(7), pp.3876-3880.

[58] Ma, W., Alonso-González, P., Li, S., Nikitin, A.Y., Yuan, J., Martín-Sánchez, J., Taboada-Gutiérrez, J., Amenabar, I., Li, P., Vélez, S. and Tollan, C., 2018. In-plane anisotropic and ultra-low-loss polaritons in a natural van der Waals crystal. *Nature*, *562*(7728), pp.557-562.

[59] Zheng, Z., Xu, N., Oscurato, S.L., Tamagnone, M., Sun, F., Jiang, Y., Ke, Y., Chen, J., Huang, W., Wilson, W.L. and Ambrosio, A., 2019. A mid-infrared biaxial hyperbolic van der Waals crystal. *Science Advances*, *5*(5), p.eaav8690.

[60] Gjerding, M.N., Petersen, R., Pedersen, T.G., Mortensen, N.A. and Thygesen, K.S., 2017. Layered van der Waals crystals with hyperbolic light dispersion. *Nature Communications*, *8*(1), pp.1-8.

Chapter 7: Lateral Recoil Forces Above Nonreciprocal Metasurfaces

Lateral recoil forces on nanoparticles located near plasmonic surfaces have enabled trapping [1-6] and manipulation [7-13] if those objects with important applications in bioengineering and chemistry [14-21]. I recall that the origin of recoil forces relies on the spin-orbit interaction of light [22] that excites directionally propagating SPPs, as detailed in Chapters 5 and 6. Unfortunately, when the fields scattered by the particle are linearly polarized, the excited SPPs propagate symmetrically within the surface and the recoil forces completely vanish. This behavior restricts the practical use of those reciprocal plasmonic surfaces to manipulate linearly polarized dipolar objects. Potential approaches to achieve directional surface plasmon excitation with linearly polarized light rely on the use of magneto-dielectric particles, such as Janus and Huygens dipoles [23] and high-index particles [24-26], that exploit combined effects of electric and magnetic dipole moments [27-29]. Unfortunately, these complex particles are not commonly found in chemical and biological applications.

An alternative route to overcome these challenges is using nonreciprocal plasmonic surfaces, for instance using magneto-optic materials biased with a magnetic field [29-34]. When the applied external bias is perpendicular to the surface, the polarization symmetry of the supported plasmons is broken. There, a linearly polarized nanoparticle can experience lateral recoil forces [29] because the scattered light undergoes a polarization conversion that excites directional surface plasmons. The strength of this force is similar to the one found in reciprocal systems [7] whereas its direction depends on the incident angle of the laser beam. When the applied external magnetic bias is parallel to the surface, the supported modes exhibit a broken symmetry in both amplitude and polarization [35-46]. Such structures have been shown to exert fluctuation-induced recoil forces on polarized atoms located nearby [47-50], in which the main emission channel is associated to the excitation of unidirectional surface plasmons supported at the material interface. Even though this platform allows to control the strength and direction of the induced forces with the external

bias and the atom transition frequency, fluctuation-induced forces are uncapable of manipulating nanoparticles in practice.

In this Chapter, I investigate lateral optical recoil forces exerted on nanoparticles located near nonreciprocal interfaces illuminated with a plane wave. I focus on general plasmonic platforms with an in-plane nonreciprocity that appears by applying an external bias parallel to the surface, and manifests itself by a broken symmetry of the amplitude and polarization profile of the supported plasmons, as happens in the case of drift-bias graphene [35-40] and thin metals [41] or externally biased magneto-optic materials [42,44-46]. I have developed a theoretical formalism based on the scattered Green's functions of the system, and then derived *analytical* approximate expressions of lateral recoil forces as detailed in Chapter 4. This approach reveals that the dispersion relation of a plasmonic system suffices to determine these forces, shedding light into the underlying mechanisms that control recoil forces and facilitating the easy and accurate design of platforms capable of manipulating nanoparticles. Additionally, I show that momentum imbalance of nonreciprocal surface plasmons leads to a dominant lateral recoil force component that acts along/against the applied bias and is mostly independent of the properties of the incoming laser beam. I study these forces over drift-biased graphene [35-40], a plasmonic system that exhibits a nonreciprocal

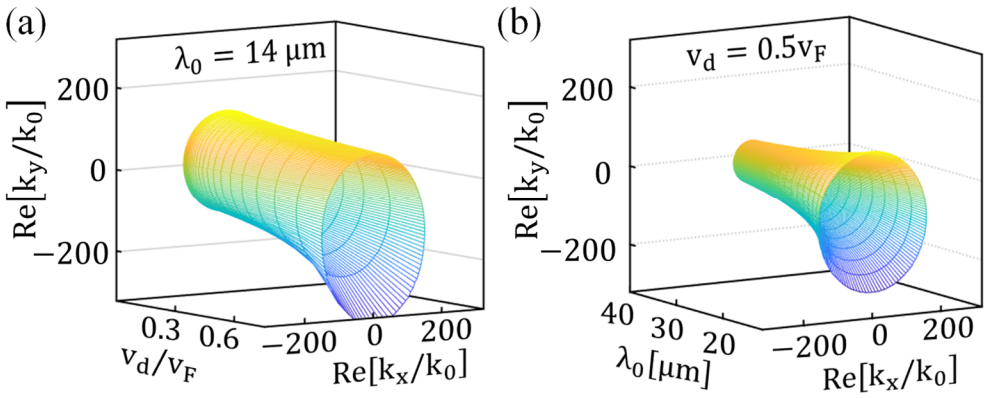

Figure 7.1: Dispersion relation of drift-biased nonreciprocal graphene. (a) Isofrequency contours of the states supported by the platform versus (a) the velocity of drifting electrons flowing along the graphene sheet and (b) wavelength. Graphene's chemical potential and relaxation time are set to $\mu_c = 0.1\mathrm{eV}$ and $\tau = 0.3\mathrm{ps}$, respectively.

response over a broad range in the infrared region and that is proposed here to sort nanoparticles as a function of their size. Taken together, these properties are very promising for trapping and manipulation of nanoparticles using nonreciprocal and plasmonic platforms.

7.1 ORIGIN OF RECOIL FORCES NEAR NONRECIPROCAL SURFACES

In this section, I provide a brief overview of the physical mechanisms enabling recoil optical forces on nanoparticles located near nonreciprocal metasurfaces based on the theoretical framework developed in section 4.3.

The overarching goal here is to capture the response of lateral recoil forces on a nanoparticle located near nonreciprocal plasmonic metasurface. To this purpose, I consider a platform subjected to an external in-plane bias along the $+y$ axis, as shown in Figure 4.3(a) for the case of drift-bias graphene. If the bias is applied along any other direction within the plane, such response can be captured by applying a coordinate rotation. An example of isofrequency contours of this structure is illustrated in Figure 4.3(b). Figures 7.1(a-b) complete the characterization of the platform by plotting its isofrequency contours versus drift velocity and wavelength, respectively. Following the procedure detailed in Chapter 4, the nonreciprocity-induced lateral recoil forces can be expressed in terms of the spatial derivatives of the scattered dyadic Green's function as

$$F_y^{nr-a} = \frac{6\pi}{c_0 k_0^2} \sum_{n=x,y,z} P_{rad}^n \mathrm{Re}\left\{\frac{d}{dq} G_{nn}^s(\bar{r}_0, \bar{r}_0)\right\}, \tag{7.1a}$$

$$F_x^{nr-p} = \frac{6\pi}{c_0 k_0^2} P_{rad}^{xy} \chi_{xy} \mathrm{Re}\left\{\frac{d}{dx} G_{xy}^s(\bar{r}_0, \bar{r}_0)\right\}, \tag{7.1b}$$

and the lateral spin-orbit forces read as

$$F_x^s = \frac{6\pi}{c_0 k_0^2} P_{rad}^{xz} \eta_y \mathrm{Im}\left\{\frac{d}{dx} G_{xz}^s(\bar{r}_0, \bar{r}_0)\right\}, \tag{7.2a}$$

$$F_y^s = \frac{6\pi}{c_0 k_0^2} P_{rad}^{yz} \eta_x \mathrm{Im}\left\{\frac{d}{dy} G_{yz}^s(\bar{r}_0, \bar{r}_0)\right\}. \tag{7.2b}$$

The definitions of the relevant parameters are available in Chapter 4. Note that F_y^{nr-a} strongly dominates over F_x^{nr-p} because it depends on the plasmon wavenumber with a power of six (see Eqs. 4.62-4.63 in Chapter 4), whereas F_x^{nr-p} shows a $\propto k_{plasmon}^4$ dependence (see Eq. 4.70 in Chapter 4). F_x^{nr-p} may still be relevant in case of magneto-optical substrates biased with a perpendicular magnetic field [29] in which F_y^{nr-a} vanishes. Therefore, I recall the analytical expressions of the dominant recoil forces from Chapter 4 that read as

$$F_y^{nr-a} \approx \frac{3\pi P_{rad}^{yz}}{8 c_0 \varepsilon_r}\left[\left(\frac{k_y^-}{k_0}\right)^4 e^{-2z_0\sqrt{(k_y^-)^2 - k_0^2}} - \left(\frac{k_y^+}{k_0}\right)^4 e^{-2z_0\sqrt{(k_y^+)^2 - k_0^2}}\right], \tag{7.3a}$$

$$F_x^s \approx \frac{6\pi P_{rad}^{xz} \eta_y}{8 c_0 \varepsilon_r}\left(\frac{k_x}{k_0}\right)^4 e^{-2z_0\sqrt{k_x{}^2 - k_0^2}}, \tag{7.3b}$$

$$F_y^s \approx \frac{3\pi P_{rad}^{yz} \eta_x}{8 c_0 \varepsilon_r}\left[\left(\frac{k_y^+}{k_0}\right)^4 e^{-2z_0\sqrt{(k_y^+)^2 - k_0^2}} + \left(\frac{k_y^-}{k_0}\right)^4 e^{-2z_0\sqrt{(k_y^-)^2 - k_0^2}}\right]. \tag{7.3c}$$

where k_y^- and k_y^+ are the wavenumber of the surface plasmons supported along and against the bias, respectively; and k_x is the plasmon wavenumber in the orthogonal lateral direction. Eq. (7.3a) shows that F_y^{nr-a} depends on the fourth power of $k_y^{\pm}$, gets attenuated as z_0 increases, and is independent of the polarization state acquired by the particle. The only dependence of this force component with the direction, polarization, and wavelength of the incoming laser is through the amount of scattered power, P_{rad}^{yz}. Eq. (7.3a) explicitly reveals that the force is significantly enhanced as the asymmetry in the $\bar{k}$-space along the

bias direction increases and that it is zero in case of reciprocal media (i.e., $k_y^+ = k_y^-$). This equation also shows that nonreciprocity leads to a two-state system governed by the interplay between the distance z_0 and the momentum of the supported modes. Specifically, the force acts along the bias direction when the particle is close to the surface and excites confined surface plasmons with wavenumber k_y^- that propagate against the bias. In this situation, the positive term of Eq. (7.3a) dominates because $z_0 \to 0$ and $k_y^- > k_y^+$ [see Figure 4.3(b)]. On contrary, the force acts against the bias direction when the particle is located relatively far away from the surface. There, the high-$\bar{k}$ components of the scattered waves are filtered out by the free-space –exponential terms in Eq. (7.3a)– and cannot efficiently excite confined k_y^- modes whereas they can still couple to the less confined k_y^+ state. The threshold distance z_t at which the direction of F_y^{nr-a} reverses can be approximated as

$$z_t \approx 2\frac{\ln(k_y^-)-\ln(k_y^+)}{k_y^- - k_y^+}, \tag{7.4}$$

which only depends on the plasmonic modes along/against the bias. Note that Eq. (7.3a) holds when the polarization of the particle dipole moment along the direction orthogonal to the bias is not dominant, and thus the scattered power fulfills $P_{rad}^x \leq P_{rad}^y$ and $P_{rad}^x \leq P_{rad}^z$. Such conditions are easily met in most practical scenarios (see Figure 4.5). An exception appears when the nanoparticle is illuminated from the normal direction of the platform with a beam polarized in the direction orthogonal to the bias. In such case, Eq. (7.3a) underestimates the strength of the induced forces, and Eq. (7.1) together with the complete dispersion relation of the platform should be employed.

In the following, I explore lateral recoil forces acting on a gold Rayleigh particle located near drift-bias graphene transferred on hexagonal boron nitride, a broadband nonreciprocal platform that has recently been demonstrated experimentally [39,40].

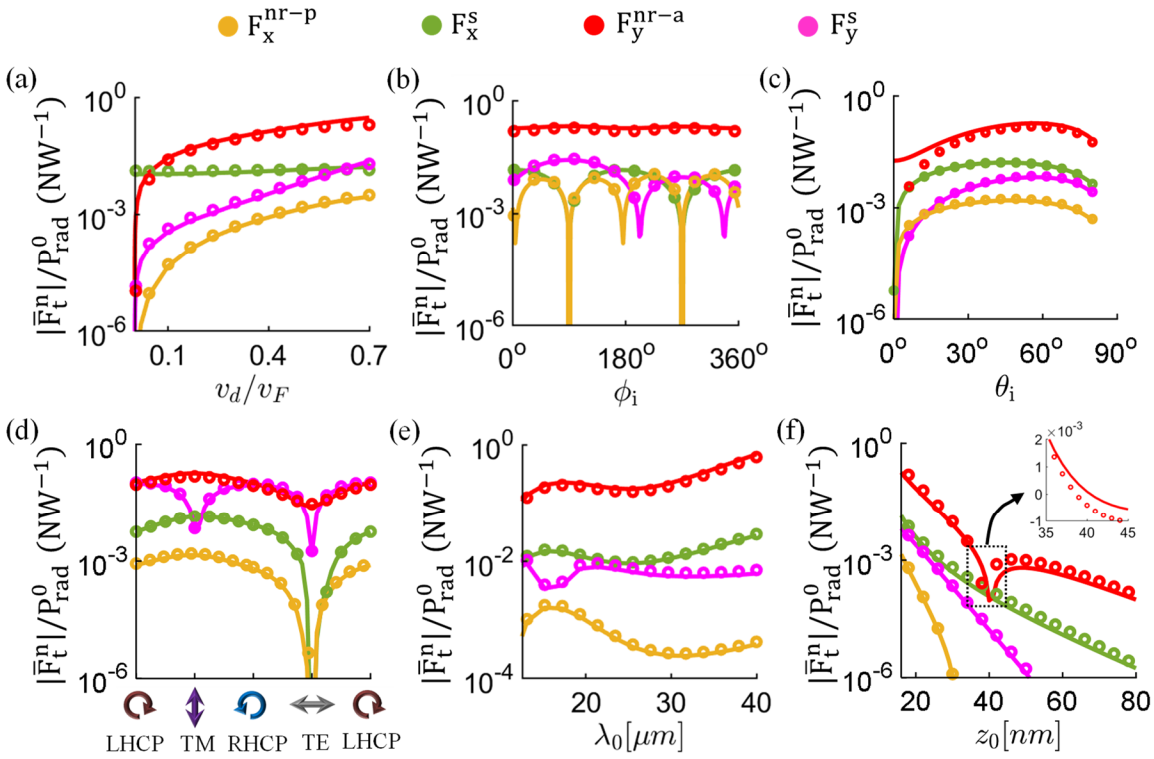

Figure 7.2: Normalized strength and direction of the lateral recoil force components acting on a gold nanoparticle with radius $a = 15$ nm located over the drift-bias graphene platform described in Figure 1. Results are calculated versus (a) the drift velocity of the flowing electrons, the properties of the incoming plane wave in terms of (b) azimuthal and (c) elevation angle of incidence, (d) polarization, and (e) wavelength; and (f) the separation distance z_0 between the particle and the surface. Solid lines are computed using the exact numerical solution [Eqs. (7.1)-(7.2)] and markers with the proposed formalism [Eqs. (7.3)]. Parameters that are not swept in a panel are kept to: $z_0 = a + 1$ [nm], $v_d = 0.5v_F$, $\phi_i = 0^0$, $\theta_i = 60^0$, and light with transverse magnetic polarization.

7.2 FORCE RESPONSE NEAR DRIFT-BIASED GRAPHENE

Figure 7.2 shows the strength of lateral recoil forces versus the drift velocity v_d, the properties of the incoming plane wave in terms of the azimuthal and elevation angles ϕ_i and θ_i, polarization, and wavelength, as well as the dipole position z_0 over the metasurface. The force is normalized with respect to the power radiated by the particle's acquired dipole moment when it is located in free space, $P_{rad}^0 = \frac{c_0 k_0^2}{12\pi}\left(|p_x|^2 + |p_y|^2 + |p_z|^2\right)$ [51]. Figure 7.2(a) shows the force components versus v_d assuming a transverse magnetic polarized incident light aligned with the $\hat{x}$-axis (see Figure 4.3a). As expected, F_y^{nr-a}

strength increases with the applied bias and outperforms all other force components by over an order of magnitude even with moderate drift velocities (i.e., $v_d \approx 0.2v_F$ [47-49]), whereas F_x^{nr-p} is negligible due to the weak polarization conversion in the system. Results reveal that the spin-orbit recoil force F_x^s does not depend on the external bias whereas the orthogonal component F_y^s increases with it. This is because larger bias enhances the confinement of the modes supported along the y direction whereas it does not affect the modes supported on the orthogonal x-axis. This analysis holds even when the linearly polarized light comes from different azimuthal directions ϕ_i, as shown in Figure 7.2(b). F_y^{nr-a} remains dominant in all cases and exhibits a unidirectional response that does not depend on the beam direction. However, both the strength and direction of all other force components strongly depend on the laser-particle alignment. Figure 7.2(c) explores the response of the recoil force components versus the elevation angle θ_i. Maximum force strength is found in a relatively large angular range, roughly from $15°$ to $80°$ measured from the normal direction. Polarization also plays a critical role in this process, as it determines the helicity acquired by the particle and the total power that it radiates. Figure 7.2(d) shows that F_y^{nr-a} dominates when the incoming light is quasi-linearly polarized and also reveals that, in case of quasi-circularly polarized light, spin orbit forces acquire a comparable strength due to the strong polarization spin acquired by the particle. There, the total recoil optical force is determined by the interplay between F_y^{nr-a} and F_y^s, and the net optical forces over the system are not unidirectional anymore but change with the laser angle of incidence. Figure 7.2(e) shows the recoil forces response versus operation wavelength. Again, F_y^{nr-a} dominates even for a laser beam oscillating over a wide frequency region in the infrared. Such response arises because drift-biased graphene exhibits a broadband nonreciprocal behavior (see Figure 7.1d), and it is in stark contrast with reciprocal [35,36] and even nonreciprocal plasmonic systems [29,51,52] that require lasers tuned to their plasma frequency to provide significant recoil forces. Finally, Figure 7.2(f) studies the system response versus the particle position z_0 over the surface and confirms that F_y^{nr-a} directs the nanoparticle along or against the applied bias with respect to the threshold position z_t described in Eq. (7.4). At exactly $z_0 = z_t$, the energy and momentum of plasmons flowing along and against the drift are equal thus yielding to $F_q^{nr-a} = 0$.

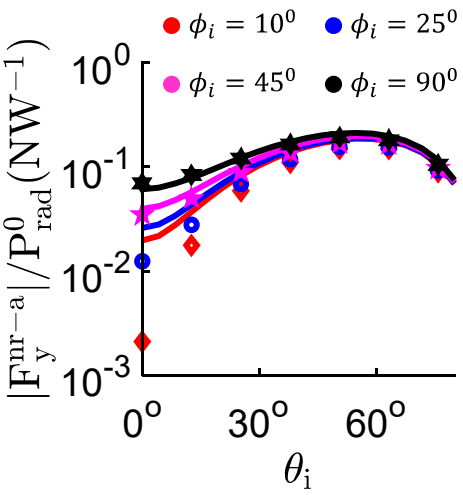

Figure 7.3: Strength of nonreciprocity-induced lateral recoil force due to the broken symmetry in amplitude of the surface plasmons excited on drift-biased graphene versus the elevation angle θi of the incoming light. Results are computed for different azimuthal angles $\phi_i = 10^0$ (red), $\phi_i = 25^0$ (blue), $\phi_i = 45^0$ (magenta) and $\phi_i = 90^0$ (black). Solid lines and markers correspond to the exact and analytical solutions calculated using Eq. 7.1 and Eq. 7.3(a), respectively. Other parameters are as in Figure 7.1.

When the particle is illuminated from the normal direction ($\theta_i \approx 0°$) with a transverse magnetic-polarized laser beam, it acquires a dominant x-directed dipole moment. In that specific scenario, Eq. (7.3a) underestimates the force F_y^{nr-a} because it does not account for the power scattered in the direction orthogonal to the bias, P_{rad}^x. Figure 7.3 shows such an example for different azimuthal directions of the incident light $\phi_i = \{10^0, 25^0, 45^0, 90^0\}$. As described before, Eq. (7.3a) may underestimate the recoil force response when the power radiated by the dipole along the direction orthogonal to the bias is dominant, a situation that appears when $\phi_i \approx< 25^0$ and $\theta_i \approx< 25^0$ (see Figure 4.5 in Chapter 4). Beyond these ranges of angles, P_{rad}^x becomes comparable/weaker than P_{rad}^y and P_{rad}^z and thus its influence on the lateral recoil force is negligible. Figure 7.3 shows two cases with $\phi_i = \{45^0, 90^0\}$ beyond the above-mentioned ranges with excellent agreement between the numerical and analytical solutions.

This nonreciprocal platform can readily be applied to sort nanoparticles as a function of their size. Figure 7.4(a) illustrates the normalized z-component of the electric field associated to the plasmons excited on the metasurface when it is biased with $\bar{v}_d = 0.5 v_F \hat{y}$ and a gold nanoparticle with radius a is located at

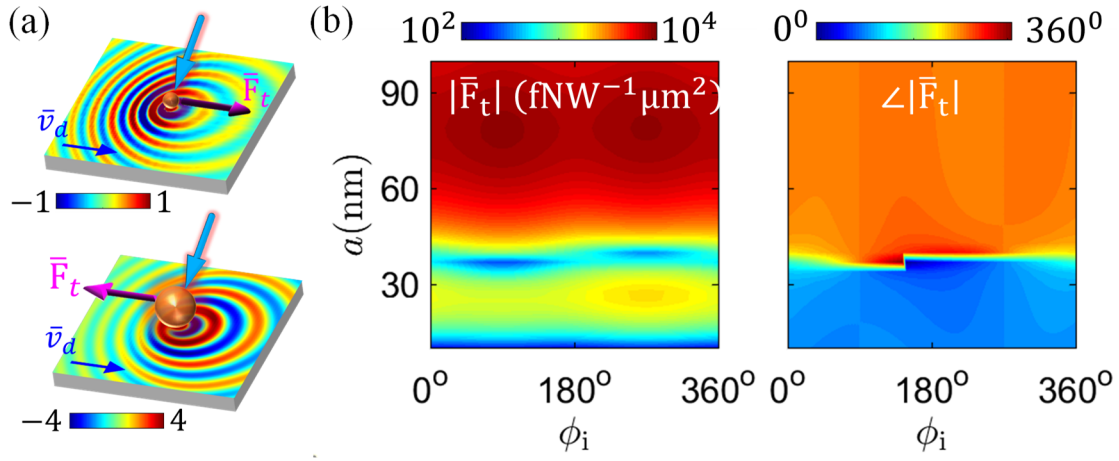

Figure 7.4: Lateral sorting of gold nanoparticles as a function of their radius a using the platform described in Figure 1 with drift velocity $v_d = 0.5v_F$. The particles are located at a distance $z_0 = a + 1[\text{nm}]$ over a drift-biased graphene and illuminated with a TM-polarized plane wave at $\lambda_0 = 14$ μm coming from the elevation angle $\theta_i = 60^0$. (a) Normalized z-component of the surface plasmons excited on the platform for particles with radii 20 nm (top) and 50 nm (bottom). (b) Normalized total lateral force strength $|\bar{F}_t| = \sqrt{F_x^2 + F_y^2}$ (left) and direction $\angle|\bar{F}_t| = \tan^{-1}(F_y/F_x)$ (right) versus the particles radii and azimuthal angle ϕ_i of the incident plane wave. Other parameters are as in Figure 7.1.

$z_0 = a + 1[\text{nm}]$ over the system and is illuminated with a transverse magnetic-plane wave. Top and bottom panels consider the case of a particle with radius $a = 20$ nm and $a = 50$ nm, respectively. In both cases, the particle scatters quasi-linearly polarized light (i.e., $\eta_m \to 0$) thus leading to almost negligible lateral spin-orbit forces F_q^s. In this scenario, the recoil force F_y^{nr-a} arising from the broken symmetry of the platform dominates the optical forces, leading to the two-state system described in Eq. (7.4). When the particle is small (top panel), the confined k_y^- plasmon propagating toward -y is efficiently excited and the recoil force is exerted along the bias direction; however, when the particle size increases, k_y^- states cannot be excited but the scattered light still couples to the less confined k_y^+ plasmons travelling toward the +y axis, which result in a recoil force acting against the bias direction. Figure 7.4(b) investigates the total forces acting on gold nanoparticles versus their size and the azimuthal direction of the incoming beam. As expected, the strength of the total optical force increases with the particle size as they scatter a larger amount

of power that couple to the system surface. Results show that particles with a radius larger than ~42 nm experience unidirectional forces against the drift, whereas those with a radius smaller than ~37 nm are dragged along the applied bias. Such response is preserved independently of the direction of the incoming laser beam. The numerically computed threshold between the two states of the system agrees well with the ~38 nm predicted by Eq. (7.4). The particles with radii close to the threshold experience lateral forces that smoothly change direction with respect to ϕ_i, a response that appears due to the interplay between spin-orbit and broken-symmetry recoil forces. Finally, it should be noted that this sorting platform is dynamic in the sense that the particles radii threshold to direct them along/against the bias (z_t) can be manipulated in real time by changing graphene's Fermi level through a gate bias. Figure 7.5 shows the normalized force strength versus the particle position above the surface for two different chemical potentials: $\mu_c = 0.1\text{eV}$ and $\mu_c = 0.15\text{eV}$. Results confirm that the nanoparticle size required to be sorted along/against the bias can

be tuned in real time by through graphene's gate-bias while barely affecting the force strength. Numerical and analytical (Eq. 7.4) are in good agreement.

7.3 CHAPTER CONCLUSIONS

In summary, I have explored lateral recoil forces acting on Rayleigh particles located over plasmonic platforms with in-plane nonreciprocal response. The study in Chapter 4 revealed that the Green's functions that describe such forces can be solved analytically using the integration along the imaginary axis technique combined with the residue theorem. The resulting approximate expressions establish a fundamental link between the dispersion relation of reciprocal and nonreciprocal platforms, and the lateral recoil forces acting on nanoparticles located nearby. Additionally, in-plane nonreciprocity leads to a lateral recoil force component that only depends on the broken symmetry of the supported plasmons and the total optical power scattered by the particle, while being almost-independent of any other property of the incoming light

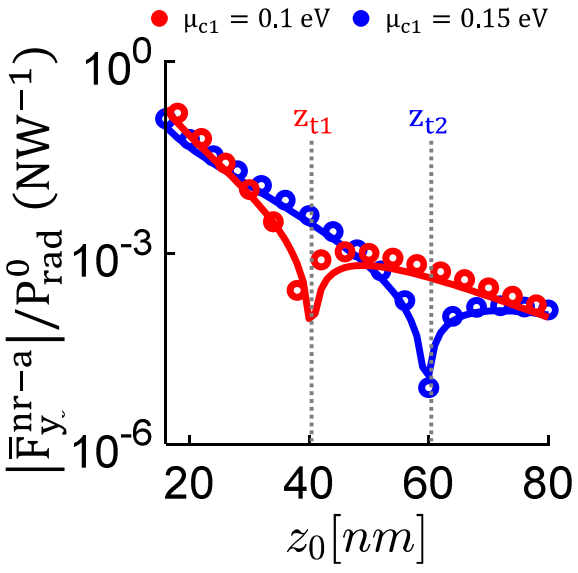

Figure 7.5: Normalized strength of nonreciprocity-induced lateral recoil force due to the broken symmetry in amplitude of the surface plasmons excited on drift-biased graphene versus the particle position z_0. Results are computed for graphene's chemical potential $\mu_c = 0.1$eV (red) and $\mu_c = 0.15$eV (blue). Solid lines and markers correspond to the exact and analytical solutions calculated using eq. 1a and eq. 4 of the main paper, respectively. z_t refers to the threshold distance where the force direction reverses. Other parameters are as in Figure 7.1.

(wavelength, angle of incidence, polarization). Such force can be significantly larger than other recoil force components and creates a two-state system in which the particles are dragged along/against the external bias depending on their size and distance to the platform surface. Moving beyond, I envision that lateral recoil forces based on nonreciprocal platforms, including those composed of magneto-optical materials such as cobalt-silver alloy [29], topological gyrotropic materials [52], photonic topological insulator [51], or drift-biased 2D materials [35-40] and thin-metallic layers [41], will find numerous applications in physics, chemistry and bioengineering, with emphasis on alleviating some of the challenges of conventional optical tweezers in terms of photoheating [53], alignment, operation wavelength, and resolution of the nanoparticles lateral position.

7.4 CHAPTER REFERENCES

[1] Juan, M.L., Righini, M. and Quidant, R., 2011. Plasmon nano-optical tweezers. *Nature Photonics*, *5*(6), pp.349-356.

[2] Zhang, Y., Min, C., Dou, X., Wang, X., Urbach, H.P., Somekh, M.G. and Yuan, X., 2021. Plasmonic tweezers: for nanoscale optical trapping and beyond. *Light: Science & Applications*, *10*(1), pp.1-41.

[3] Kotsifaki, D.G. and Chormaic, S.N., 2019. Plasmonic optical tweezers based on nanostructures: fundamentals, advances and prospects. *Nanophotonics*, *8*(7), pp.1227-1245.

[4] Wang, K., Schonbrun, E., Steinvurzel, P. and Crozier, K.B., 2011. Trapping and rotating nanoparticles using a plasmonic nano-tweezer with an integrated heat sink. *Nature Communications*, *2*(1), pp.1-6.

[5] Paul, N.K. and Gomez-Diaz, J.S., 2021. Low-power Optical Traps Using Anisotropic Metasurfaces: Asymmetric Potential Barriers and Broadband Response. *Physical Review Applied*, *15*(1), p.014018.

[6] Messina, E., Cavallaro, E., Cacciola, A., Iatì, M.A., Gucciardi, P.G., Borghese, F., Denti, P., Saija, R., Compagnini, G., Meneghetti, M. and Amendola, V., 2011. Plasmon-enhanced optical trapping of gold nanoaggregates with selected optical properties. *ACS Nano*, *5*(2), pp.905-913.

[7] Rodríguez-Fortuño, F.J., Engheta, N., Martínez, A. and Zayats, A.V., 2015. Lateral forces on circularly polarizable particles near a surface. *Nature Communications*, *6*(1), pp.1-8.

[8] Kingsley-Smith, J.J., Picardi, M.F., Wei, L., Zayats, A.V. and Rodríguez-Fortuño, F.J., 2019. Optical forces from near-field directionalities in planar structures. *Physical Review B*, *99*(23), p.235410.

[9] Girón-Sedas, J.A. and Rodríguez-Fortuño, F.J., 2020. Strong recoil optical forces on dipoles via high-k plasmons excitation in thin metallic films. *Applied Physics Letters*, *117*(18), p.181106.

[10] Paul, N.K., Correas-Serrano, D. and Gomez-Diaz, J.S., 2019. Giant lateral optical forces on Rayleigh particles near hyperbolic and extremely anisotropic metasurfaces. *Physical Review B*, *99*(12), p.121408.

[11] Petrov, M.I., Sukhov, S.V., Bogdanov, A.A., Shalin, A.S. and Dogariu, A., 2016. Surface plasmon polariton assisted optical pulling force. *Laser & Photonics Reviews*, *10*(1), pp.116-122.

[12] Quidant, R. and Girard, C., 2008. Surface-plasmon-based optical manipulation. *Laser & Photonics Reviews*, *2*(1-2), pp.47-57.

[13] Ren, Y., Chen, Q., He, M., Zhang, X., Qi, H. and Yan, Y., 2021. Plasmonic optical tweezers for particle manipulation: principles, methods, and applications. *ACS Nano*, *15*(4), pp.6105-6128.

[14] Koya, A.N., Cunha, J., Guo, T.L., Toma, A., Garoli, D., Wang, T., Juodkazis, S., Cojoc, D. and Proietti Zaccaria, R., 2020. Novel plasmonic nanocavities for optical trapping-assisted biosensing applications. *Advanced Optical Materials*, *8*(7), p.1901481.

[15] Tan, H., Hu, H., Huang, L. and Qian, K., 2020. Plasmonic tweezers for optical manipulation and biomedical applications. *Analyst*, *145*(17), pp.5699-5712.

[16] Ashkin, A., 1970. Acceleration and trapping of particles by radiation pressure. *Physical Review Letters*, *24*(4), p.156.

[17] Bagnato, V.S., Lafyatis, G.P., Martin, A.G., Raab, E.L., Ahmad-Bitar, R.N. and Pritchard, D.E., 1987. Continuous stopping and trapping of neutral atoms. *Physical Review Letters*, *58*(21), p.2194.

[18] Grier, D.G., 2003. A revolution in optical manipulation. *Nature*, *424*(6950), pp.810-816.

[19] Phillips, W.D., 1998. Nobel Lecture: Laser cooling and trapping of neutral atoms. *Reviews of Modern Physics*, *70*(3), p.721.

[20] Barry, J.F., McCarron, D.J., Norrgard, E.B., Steinecker, M.H. and DeMille, D., 2014. Magneto-optical trapping of a diatomic molecule. *Nature*, *512*(7514), pp.286-289.

[21] Schneider, C., Enderlein, M., Huber, T. and Schätz, T., 2010. Optical trapping of an ion. *Nature Photonics*, *4*(11), pp.772-775.

[22] Bliokh, K.Y., Rodríguez-Fortuño, F.J., Nori, F. and Zayats, A.V., 2015. Spin–orbit interactions of light. *Nature Photonics*, *9*(12), pp.796-808.

[23] Picardi, M.F., Zayats, A.V. and Rodríguez-Fortuño, F.J., 2018. Janus and Huygens dipoles: Near-field directionality beyond spin-momentum locking. *Physical Review Letters*, *120*(11), p.117402.

[24] Evlyukhin, A.B., Novikov, S.M., Zywietz, U., Eriksen, R.L., Reinhardt, C., Bozhevolnyi, S.I. and Chichkov, B.N., 2012. Demonstration of magnetic dipole resonances of dielectric nanospheres in the visible region. *Nano Letters*, *12*(7), pp.3749-3755.

[25] Fu, Y.H., Kuznetsov, A.I., Miroshnichenko, A.E., Yu, Y.F. and Luk'yanchuk, B., 2013. Directional visible light scattering by silicon nanoparticles. *Nature Communications*, *4*(1), pp.1-6.

[26] Kuznetsov, A.I., Miroshnichenko, A.E., Brongersma, M.L., Kivshar, Y.S. and Luk'yanchuk, B., 2016. Optically resonant dielectric nanostructures. *Science*, 354, aag2472.

[27] Neugebauer, M., Woźniak, P., Bag, A., Leuchs, G. and Banzer, P., 2016. Polarization-controlled directional scattering for nanoscopic position sensing. *Nature Communications*, *7*(1), pp.1-6.

[28] Rotenberg, N., Spasenović, M., Krijger, T.L., Le Feber, B., De Abajo, F.G. and Kuipers, L., 2012. Plasmon scattering from single subwavelength holes. *Physical Review Letters*, *108*(12), p.127402.

[29] Girón-Sedas, J.A., Kingsley-Smith, J.J. and Rodríguez-Fortuño, F.J., 2019. Lateral optical force on linearly polarized dipoles near a magneto-optical surface based on polarization conversion. *Physical Review B*, *100*(7), p.075419.

[30] Gangaraj, S.A.H., Hanson, G.W., Silveirinha, M.G., Shastri, K., Antezza, M. and Monticone, F., 2019. Unidirectional and diffractionless surface plasmon polaritons on three-dimensional nonreciprocal plasmonic platforms. *Physical Review B*, *99*(24), p.245414.

[31] Yu, Z., Veronis, G., Wang, Z. and Fan, S., 2008. One-way electromagnetic waveguide formed at the interface between a plasmonic metal under a static magnetic field and a photonic crystal. *Physical Review Letters*, *100*(2), p.023902.

[32] Davoyan, A.R. and Engheta, N., 2013. Theory of wave propagation in magnetized near-zero-epsilon metamaterials: evidence for one-way photonic states and magnetically switched transparency and opacity. *Physical Review Letters*, *111*(25), p.257401.

[33] Lin, X., Xu, Y., Zhang, B., Hao, R., Chen, H. and Li, E., 2013. Unidirectional surface plasmons in nonreciprocal graphene. *New Journal of Physics*, *15*(11), p.113003.

[34] Lu, L., Joannopoulos, J.D. and Soljačić, M., 2014. Topological photonics. *Nature Photonics*, *8*(11), pp.821-829.

[35] Correas-Serrano, D. and Gomez-Diaz, J.S., 2019. Nonreciprocal and collimated surface plasmons in drift-biased graphene metasurfaces. *Physical Review B*, *100*(8), p.081410.

[36] Paul, N.K. and Gomez-Diaz, J.S., 2021. Broadband and unidirectional plasmonic hyperlensing in drift-biased graphene. *Applied Physics Letters*, *118*(9), p.091107.

[37] Morgado, T.A. and Silveirinha, M.G., 2017. Negative Landau damping in bilayer graphene. *Physical Review Letters*, *119*(13), p.133901.

[38] Morgado, T.A. and Silveirinha, M.G., 2021. Active graphene plasmonics with a drift-current bias. *ACS Photonics*, *8*(4), pp.1129-1136.

[39] Dong, Y., Xiong, L., Phinney, I.Y., Sun, Z., Jing, R., McLeod, A.S., Zhang, S., Liu, S., Ruta, F.L., Gao, H. and Dong, Z., 2021. Fizeau drag in graphene plasmonics. *Nature*, *594*(7864), pp.513-516.

[40] Zhao, W., Zhao, S., Li, H., Wang, S., Wang, S., Utama, M., Kahn, S., Jiang, Y., Xiao, X., Yoo, S. and Watanabe, K., 2021. Efficient Fizeau drag from Dirac electrons in monolayer graphene. *Nature*, *594*(7864), pp.517-521.

[41] Bliokh, K.Y., Rodríguez-Fortuño, F.J., Bekshaev, A.Y., Kivshar, Y.S. and Nori, F., 2018. Electric-current-induced unidirectional propagation of surface plasmon-polaritons. *Optics letters*, *43*(5), pp.963-966.

[42] Gangaraj, S.A.H. and Monticone, F., 2019. Do truly unidirectional surface plasmon-polaritons exist?. *Optica*, *6*(9), pp.1158-1165.

[43] Sabbaghi, M., Lee, H.W., Stauber, T. and Kim, K.S., 2015. Drift-induced modifications to the dynamical polarization of graphene. *Physical Review B*, *92*(19), p.195429.

[44] Yu, Z., Veronis, G., Wang, Z. and Fan, S., 2008. One-way electromagnetic waveguide formed at the interface between a plasmonic metal under a static magnetic field and a photonic crystal. *Physical Review Letters*, *100*(2), p.023902.

[45] Hassani Gangaraj, S.A. and Monticone, F., 2022. Drifting Electrons: Nonreciprocal Plasmonics and Thermal Photonics. *ACS Photonics*, *9*(3), pp.806-819.

[46] Monticone, F., 2020. A truly one-way lane for surface plasmon polaritons. *Nature Photonics*, *14*(8), pp.461-465.

[47] Dorgan, V.E., Behnam, A., Conley, H.J., Bolotin, K.I. and Pop, E., 2013. High-field electrical and thermal transport in suspended graphene. *Nano Letters*, *13*(10), pp.4581-4586.

[48] Ramamoorthy, H., Somphonsane, R., Radice, J., He, G., Kwan, C.P. and Bird, J.P., 2016. "Freeing" graphene from its substrate: Observing intrinsic velocity saturation with rapid electrical pulsing. *Nano Letters*, *16*(1), pp.399-403.

[49] Yamoah, M.A., Yang, W., Pop, E. and Goldhaber-Gordon, D., 2017. High-velocity saturation in graphene encapsulated by hexagonal boron nitride. *ACS Nano*, *11*(10), pp.9914-9919.

[50] Grigorenko, A.N., Polini, M. and Novoselov, K.S., 2012. Graphene plasmonics. *Nature Photonics*, *6*(11), pp.749-758.

[51] Gangaraj, S.A.H., Hanson, G.W., Antezza, M. and Silveirinha, M.G., 2018. Spontaneous lateral atomic recoil force close to a photonic topological material. *Physical Review B*, *97*(20), p.201108.

[52] Silveirinha, M.G., Gangaraj, S.A.H., Hanson, G.W. and Antezza, M., 2018. Fluctuation-induced forces on an atom near a photonic topological material. *Physical Review A*, *97*(2), p.022509.

[53] Richardson, H.H., Carlson, M.T., Tandler, P.J., Hernandez, P. and Govorov, A.O., 2009. Experimental and theoretical studies of light-to-heat conversion and collective heating effects in metal nanoparticle solutions. *Nano Letters*, *9*(3), pp.1139-1146.

Chapter 8: Dynamic Manipulation of Stable Optical Traps Above Nonreciprocal Metasurfaces

Stable optical trapping of nanoparticles, in the range of 1∼50nm, and dynamic manipulation of those trap sites remain a challenge since the invention of optical tweezers in 1970 [1]. Over the years, the use of plasmonic nanostructures [2,3], such as metallic nanotips [4], nanoapertures [5,6] or nanocavities [7-9], have greatly resolved the issue of trapping nanoparticles by enhancing conservative gradient trapping force [10-13]. There, the trap sites strongly depend on the structure geometry and cannot be controlled in real time. As a partial solution, graphene nanostructures (i.e., couple strips [14], nanoribbons [15-18], nanoholes [19]) have been proposed to manipulate the traps. In these configurations, the position of the localized field intensity and the feature of gradient trapping force are controlled by changing the carrier density of graphene using a gate bias [18]. However, all these nanostructures exhibit a strong resonant behavior and require precise fabrication process thus limiting their applications in practice. Another common approach relies on the use of counter-propagating evanescent surface waves that creates a periodic potential well near planar waveguides [20-24]. There, the potential minima or trap sites are controlled by tuning the phase of one of these surface waves, as is commonly done using a microheater [22,23]. This technique is less efficient for nanoparticles, but sub-micrometer objects. This is because nanoparticles may jump out from one trap to the neighboring ones due to the weak gradient force in this scale thus resulting in unstable trapping [20].

To overcome the dependence of conservative gradient force, several studies have been performed to realize strong nonconservative spin-orbit recoil force on quasi-circularly polarized dipolar nanoparticles located near plasmonic surfaces [25-27]. The origin of this force is completely different than the conservative one [28] and it depends on the spin-orbit interaction of light [29,30] as discussed in Chapter 5 and 6. This phenomenon has been exploited to dramatically enhance the trapping forces on dipolar nanoparticles located near metallic surfaces when illuminated by a laser beam [31]. There, the particle exhibits dipole polarization spin rotating against the beam axis independently to its position, and the

resulting recoil force originates optical trap at the beam axis with superior performance (see Chapter 6). Unfortunately, these reciprocal systems are unable to manipulate the trap sites as they lack real-time tunability to dynamically control the optical forces.

In this context, nonreciprocal plasmonic systems with an external momentum bias, such as magnetic field [32-34] and drift-current bias [35-40], have been proposed to obtain tunable optical forces [41] as detailed in Chapter 7. These active structures exhibit a dispersion relation with broken symmetry in amplitude and polarization of the supported modes in the momentum space. Illumination of nanoparticles located above them, such as magneto-optical surface [41] or drift-biased graphene (see Chapter 7), introduces a novel nonreciprocity-induced recoil force thanks to the broken symmetry of the surface modes. Importantly, the strength of this force is directly linked to the dispersion relation of the system and can be dynamically controlled by tuning the applied bias strength.

In this Chapter, I propose dynamic manipulation of lateral optical traps on dipolar, spherical and Rayleigh nanoparticles [42] located near nonreciprocal plasmonic surfaces with in-plane momentum bias when illuminated by a normally incident laser beam. The trap mechanism is governed by the nonreciprocity-induced and spin-orbit recoil forces. On one hand, the spin-orbit recoil force depends on the dipole polarization spin and acts toward the laser beam axis. On the other hand, the nonreciprocity-induced force is independent of the dipole polarization, always acts along the bias axis and its strength can be controlled by tuning the bias strength. The interplay between these two recoil forces originates an optical trap that can be controlled in the physical space with ultra-subwavelength resolution. To investigate the importance of particle polarization, I derive an analytical expression of the required dipole polarization spin to trap it at any position above the metasurface with a given dispersion relation. As a practical example, I propose the use of drift-biased graphene, and explore the performance of stable optical trapping of nanoparticles located nearby and manipulate the trap site. Results show that drift-biased graphene provides stable trap response using a laser beam with power densities as little as $\sim 6\mathrm{mW}\mu\mathrm{m}^{-2}$ whereas the trap site can be finely manipulated with nanometric resolution by applying a voltage bias.

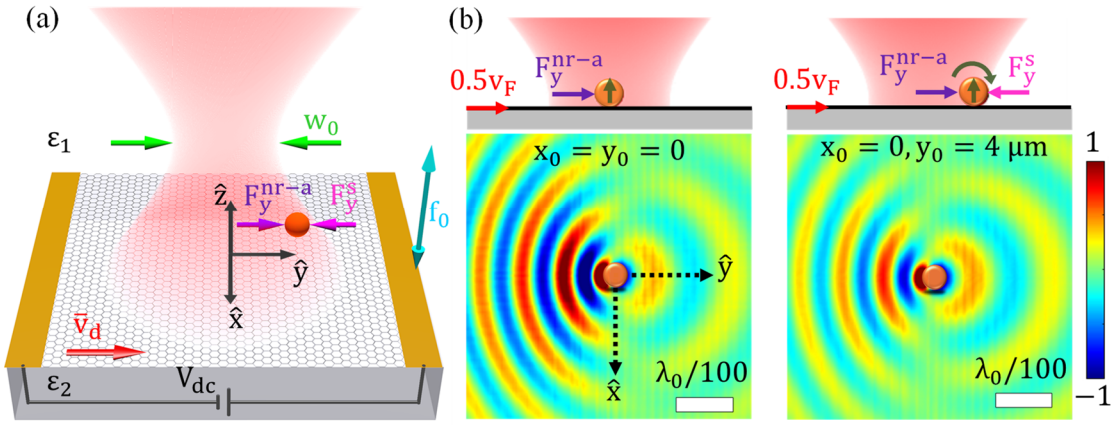

Figure 8.1: Nanoscale manipulation of optical traps induced on a nanoparticle near drift-biased graphene under illumination with a Gaussian laser beam. (a) Schematic of the configuration. (b) Normalized z-component of the excited SPP considering a gold nanoparticle located at the beam axis (left panel) and off the beam axis -exactly where the trap is created (right panel). The top inset indicates the dipole polarization state of the particle and the direction of the recoil forces. The particle's radius is $a = 15$ nm and its vertical position is $z_0 = a + 1$[nm]; the laser operation wavelength $\lambda_0 = 10$ μm, with a beam waist $w_0 = \lambda_0$ and focus position $f_0 = 0$; graphene's chemical potential and relaxation times are set to $\mu_c = 0.2$eV and $\tau = 0.3$ ps, respectively; and relative permittivity of the media above and below the metasurface are $\varepsilon_1 = 1$ and $\varepsilon_2 = 3.8$.

8.1 THEORETICAL FRAMEWORK

Consider In this section, I provide a brief overview of the lateral recoil optical forces on nanoparticles located near nonreciprocal metasurfaces that originates tunable optical traps based on the theoretical framework developed in section 4.3.

Let me consider a nonmagnetic, isotropic, spherical, and dipolar Rayleigh particle of radius a located at a position $\bar{r}_0 = \{x_0, y_0, z_0\}$ above a nonreciprocal plasmonic metasurface. The system nonreciprocity is obtained by applying an in-plane momentum bias, such as magnetic field [32] or drift-current bias [36,37]. Figure 8.1a shows the schematic considering a drift-biased graphene. The relative permittivity of the media above and below the surface are ε_1 and ε_2, respectively. The setup is illuminated by a normally incident TM-polarized Gaussian laser beam with waist w_0. The center axis of the beam is aligned with $\hat{z}$-axis of the reference coordinate system, and it is focused on a distance f_0 from the surface [31]. Here, the laser beam

is mainly employed to polarize the particle such that it exhibits a dipole polarization spin with rotation handedness against the beam axis [31]. As described in Chapter 6, this induces an optical trap exactly at the beam axis in the case of reciprocal systems. The electric field vector components of such a Gaussian beam can be modelled as detailed in section 6.1. Within the dipole approximation, total optical forces on the particle are calculated from the vector gradient of the local electric field at the particle position as derived in section 4.3. Following the framework described in Chapter 4, the total optical forces can be decomposed into two component: (i) conservative force $\bar{F}^{g} = \frac{1}{2}\mathrm{Re}\left[\bar{p}^{*} \cdot \nabla \bar{E}^{GW}(\bar{r}_0)\right]$; and (ii) nonconservative recoil Force $\bar{F}^{rec} = \frac{1}{2}\mathrm{Re}[\bar{p}^{*} \cdot \nabla \bar{E}^{s}(\bar{r}_0)]$. When the incident light is a Gaussian beam [31] or a plane wave, the conservative force is commonly referred as gradient force [31] or radiation pressure [25], respectively. This force is proportional to the third power of the particle size [42], is very weak (i.e., sub-femtonewton range) for nanoparticles whose radii lie below $\lambda_0/100$ [2,43], and its influence on the total force response is usually negligible. In nonreciprocal systems, the nonconservative forces are composed of two components: (i) spin-orbit force $\bar{F}^{s}$ that originates due to the dipole polarization spin [25]; and (ii) nonreciprocity-induced force $\bar{F}^{nr}$ that appears to compensate the momentum imbalance of the asymmetric surface plasmons excited on the platform (see Chapter 7 and Figure 8.1b).

Without loss of generality, I assume that the external bias is applied along $\hat{y}$-axis (see Figure 8.1a). Following the procedure detailed in Chapter 4, the dominant recoil forces are analytically expressed as

$$F_x^s \approx \frac{6\pi P_{rad}^{xz}\eta_y}{8c_0\varepsilon_r}\left(\frac{k_x}{k_0}\right)^4 e^{-2z_0 k_y^-}, \tag{8.1a}$$

$$F_y^s \approx \frac{3\pi P_{rad}^{yz}\eta_x}{8c_0\varepsilon_r}\left[\left(\frac{k_y^-}{k_0}\right)^4 e^{-2z_0 k_y^-} + \left(\frac{k_y^+}{k_0}\right)^4 e^{-2z_0 k_y^+}\right], \tag{8.1b}$$

$$F_y^{nr} \approx \frac{3\pi P_{rad}^{yz}}{8c_0\varepsilon_r}\left[\left(\frac{k_y^-}{k_0}\right)^4 e^{-2z_0 k_y^-} - \left(\frac{k_y^+}{k_0}\right)^4 e^{-2z_0 k_y^+}\right]. \tag{8.1c}$$

Here, k_y^+, k_y^- and k_x are the plasmon wavenumbers along, against and in the orthogonal lateral direction of the bias, respectively (see Figure 4.3); c_0 is speed of light in free space; and $\varepsilon_r = \frac{\varepsilon_1+\varepsilon_2}{2}$. Eq. (8.1) shows that the spin-orbit force direction is solely determined by the dipole rotation handedness (i.e., sign of helicity), whereas the direction of F_y^{nr} depends on the difference in plasmon momentum propagating along and against the bias. When the particle is located very close to the surface (i.e., $z_0 \to 0$), F_y^{nr} always acts along the bias direction since $k_y^- > k_y^+$ as shown in Figure 8.1b. When the forces F_y^s and F_y^{nr} are equal in magnitude and act in opposite directions, an optical trap is conformed. Importantly, the trap position can be manipulated along the bias axis since the strength of F_y^{nr} can be controlled by tuning the strength of the external bias.

Now, it is instructive to analyze the dipole properties to explore the importance of its polarization state in the trapping mechanism. To this purpose, let me consider that the trap appears at a position $(0, y_T, z_T)$ along the bias axis where $F_x^s = 0$ and $F_y^s + F_y^{nr-a} = 0$. From Eq. (8.1), the dipole helicity at the trap position can be computed as

$$\eta_y(x_T, y_T) = 0, \tag{8.2a}$$

$$\eta_x(x_T, y_T) = \frac{(k_y^+)^4 e^{-2z_T k_y^+} - (k_y^-)^4 e^{-2z_T k_y^-}}{(k_y^+)^4 e^{-2z_T k_y^+} + (k_y^-)^4 e^{-2z_T k_y^-}}. \tag{8.2b}$$

Eq. (8.2) shows that for a given dispersion relation of a system, one can easily calculate the required dipole helicity to trap it at a certain position. This situation is simpler in reciprocal systems since $k_y^+ = k_y^-$ and η_x is strictly zero [31].

In the following, I employ my formalism (see Chapter 4) to explore the lateral trapping forces on a dipolar gold nanoparticle located near drift-biased graphene supported by hexagonal boron nitride – a platform that has been demonstrated experimentally [36,37]. The overarching goal is to obtain stable optical

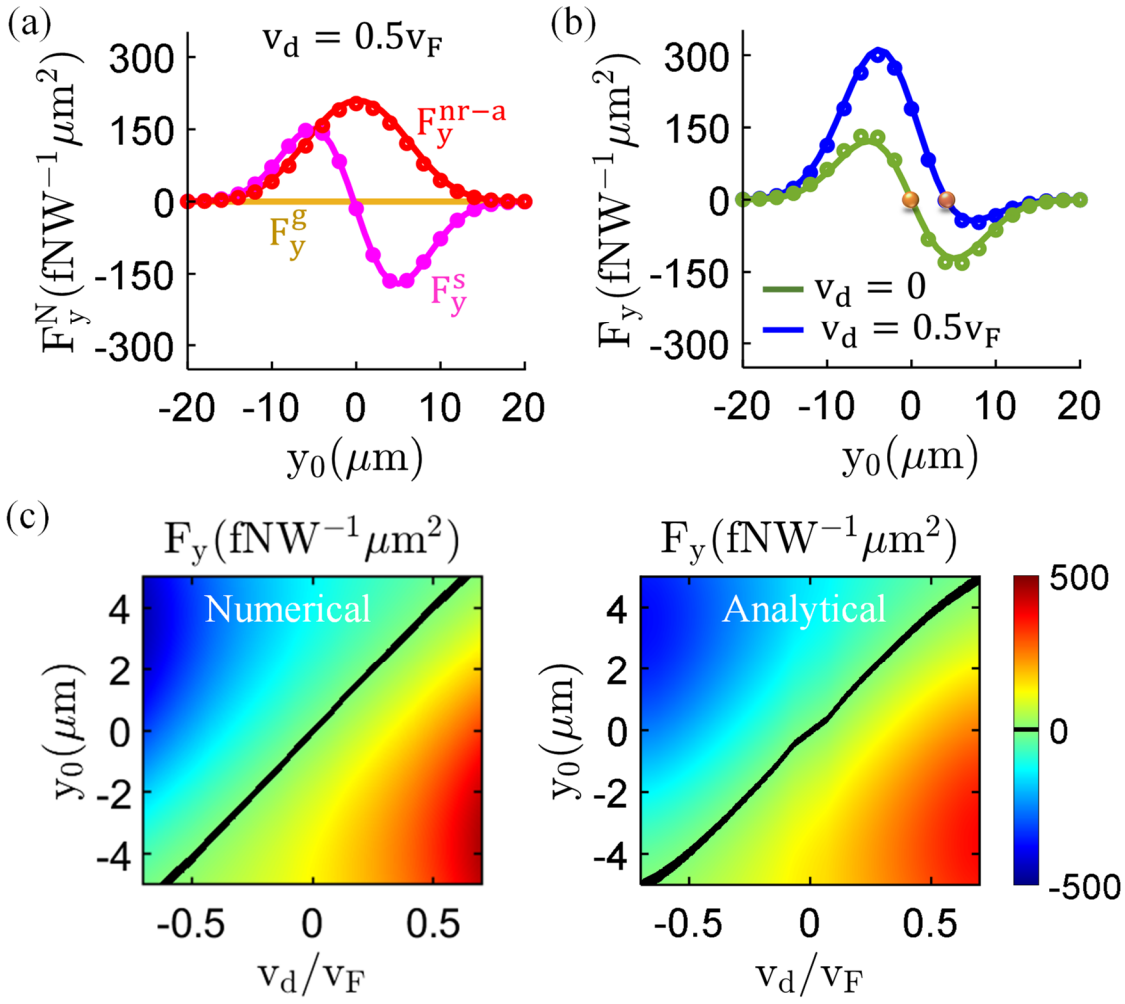

Figure 8.2: Response of lateral optical forces over the reconfigurable optical tweezer shown in Figure 8.1. (a) Nonreciprocity-induced (red) and spin-orbit (magenta) recoil forces, and gradient component (yellow) versus particle position y_0 keeping $x_0 = 0$. (b) Total lateral forces for biased (blue) and unbiased (green) graphene with gold spheres indicating the trap locations. Solid lines and markers correspond to the numerical and analytical solutions computed using Eqs. (7.1-7.2) and (7.3), respectively. (c) Total lateral forces versus drift velocity v_d and y_0 using numerical and analytical approaches with black line indicating the trap position. Results are normalized with respect to the laser power. Other parameters are as in Figure 8.1.

trap and dynamically manipulate the trap site with ultra-subwavelength resolution. I compute the potential energy and the required trap depth for stable trapping aiming to overcome the thermal fluctuations [44] and Brownian motion [2,45]. I also provide examples of realistic laser sources that can be readily applied to achieve such response in practice.

8.2 DYNAMIC MANIPULATION OF OPTICAL TRAPS

Let me assume that a gold nanoparticle of radius $a = 15\text{nm}$ is located at a position $(x_0, y_0, z_0) = (0, y_0, a + 1\text{nm})$ above a longitudinally dc-biased graphene that generates drifting electrons along the surface with velocity $\bar{v}_d = \hat{y}v_d$ (see Figure 8.1a). The platform is illuminated with a normally incident TM-polarized Gaussian beam (see Eq. 6.1) operated at wavelength $\lambda_0 = 10\mu\text{m}$, focused on the surface ($f_0 = 0$) with a waist $w_0 = \lambda_0$. Figure 8.1b shows the z-component of the electric field excited on the surface for two particle positions with $v_d = 0.5v_F$. When the nanoparticle is located at the beam axis (i.e., $y_0 = 0$), it behaves as a linearly polarized dipole and excites all possible modes supported by the surface. Particularly, the extremely confined modes with larger wavenumbers are strongly excited (i.e., in the $-\hat{y}$ half space), and the nonreciprocity-induced recoil force F_y^{nr-a} pushes the particle toward the drift to compensate the momentum imbalance. When the particle is located off the beam axis (i.e., $y_0 = 4\mu\text{m}$), the induced dipole polarization spin modifies the field distribution where the extremely confined modes are not strongly excited anymore. There, the spin-orbit force F_y^s cancels the counteracting nonreciprocity-induced one F_y^{nr},

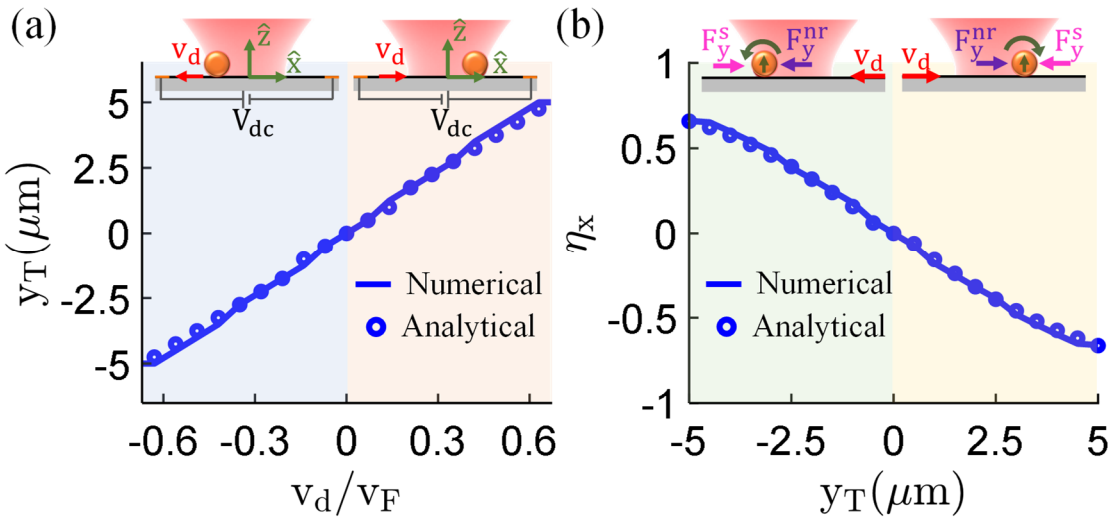

Figure 8.3: Tunable optical traps. (a) Position of the trap (y_T) versus drift velocity. Insets show the polarity of dc-bias for negative and positive v_d. (b) Particle helicity η_x at the trap position. Insets show the dipole polarization rotation handedness to trap it in the negative and positive y-half spaces. Other parameters are as in Figure 8.1.

and an optical trap is created. In these scenarios, the particle does not experience any force in the orthogonal lateral axis (i.e., $F_x \to 0$) since the platform response is symmetric along that direction.

Figure 8.2a shows all the lateral force components versus the particle position y_0. As expected, the gradient force F_y^g is very weak since the electrical size of the particle is very small (i.e., $a \approx \lambda_0/660$). The spin-orbit component F_y^s exhibits an odd symmetry versus y_0 and is strictly zero at the beam axis, i.e., $y_0 = 0$. The nonreciprocity-induced force F_y^{nr-a} always acts along the drift with maximum strength near the beam axis as the particle scatters optimum amount of power P_{rad}^{yz} , and progressively lessens away from it. The balance between F_y^{nr-a} and F_y^s creates an optical trap (indicated by a gold sphere) off the beam axis at $y_0 \approx 4\mu m$ as shown in Figure 8.2b. This is fully consistent with the analysis in Figure 8.1b. In the absence of drift, the trap is conformed at the beam axis as recently explored in the case of reciprocal systems [31] (Chapter 6). Figures 8.2c-d show the total force response versus y_0 and v_d to explore the real time tunability of the trap site (indicated by black line where $F_y \to 0$). Overall, the platform is capable to control the trap site up to a distance of $\sim 5\mu m$ with ultra-subwavelength resolution by adequately tuning the bias strength. Figure 8.3 explores the tunability of the platform to create optical traps. I highlight the excellent agreement between the numerical [Eq. (4.54)] and analytical results (i.e., $F_y \approx F_y^s + F_y^{nr-a}$) [Eqs. (4.65) and (4.72)] based on the theory developed in Chapter 4. Figure 8.3b shows the dipole helicity along x-direction at those trap sites and compare it with the one calculated analytically (markers) using Eq. (8.2). Insets show the required dipole rotation handedness to trap the particle in the positive or negative y-half spaces of the metasurface. This response is similar to the one obtained above reciprocal surfaces [31]: the dipole always exhibits a polarization spin with rotation handedness against the beam axis independent to its position. Exactly at the beam axis, the particle behaves as a linearly polarized dipole (i.e., $\eta_x \to 0$). Results confirm that Eq. (8.2) can be directly applied to calculate the required dipole polarization spin to trap it at a given position.

To investigate the platform performance, it is important to analyze the potential energy and trap depth that can be computed following the approach detailed in Chapter 6. Figure 8.4 shows the distribution of the trapping potential versus the particle position (x_0, y_0). As expected, the response is rotationally symmetric in the case of unbiased (isotropic) graphene and the trap appears at the beam axis, i.e., $(x_0, y_0) \approx (0,0)$ as shown in Figure 8.4a. In the presence of drift, Figure 8.4b shows that the potential minimum appears away from the beam axis at a position $(x_0, y_0) \approx (0,4\mu m)$ where the trap is conformed (see Figure 8.2b). Unlike the traps found near reciprocal surfaces [31], the nonreciprocal system introduces a rotationally asymmetric

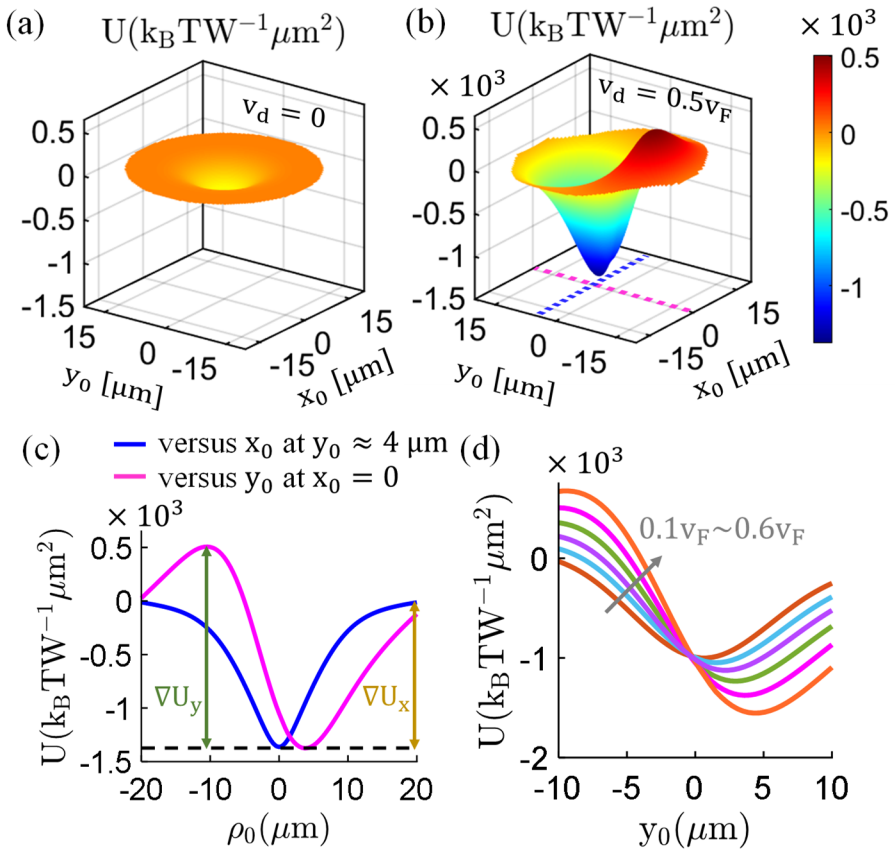

Figure 8.4: Normalized trap potential versus particle position (x_0, y_0). 3D-distribution of the trap potential versus x_0 and y_0 with (a) $v_d = 0$ and (b) $v_d = 0.5v_F$. (c) Response computed for particle position along the $\hat{x}$ and $\hat{y}$-axes going through the trap (versus x_0 keeping $y_0 \approx 4$ μm: blue line; versus y_0 keeping $x_0 = 0$: magenta line) as in panel-(b). (d) Potential versus y_0 keeping $x_0 = 0$ for different drift velocities v_d. Other parameters are as in Figure 8.1.

energy distribution within any in-plane directions. Figure 8.4c shows the potential energy in the direction along/orthogonal to the applied bias, going through the trap position (dashed lines in Figure 8.4b). Results shows that the nanoparticle experiences a local energy maximum in the $y < y_T$-half space. This response is consistent with the local enhancement in the force profile against the bias as shown in Figure 8.2b. Therefore, a local potential barrier and larger trap depth ∇U_y appears along the bias-axis, whereas the orthogonal direction (x) exhibits a symmetrical response with trap depth ΔU_x. In the case that the nanoparticle acquires sufficient energy to escape from the trap, it will avoid this local potential barrier and preferably follow a path in the $y_0 > y_T$ semi plane. Figure 8.4d shows a similar response versus y_0 with different drift velocities. It shows that the trap site progressively moves along the bias direction as the drift velocity increases following a similar trend as in Figure 8.3a. I stress that for stable trapping, the absolute value of potential minima should be larger than $10k_BT$ to overcome the thermal fluctuation and Brownian motion. To satisfy this condition, the required minimum amount of laser power is $6\sim10\text{mW}\mu\text{m}^{-2}$. This amount of power is readily available in practice using femtosecond pulses [46] and CO_2 laser beams [47,48] operating at $10\mu\text{m}$ wavelength.

8.3 CHAPTER CONCLUSIONS

In summary, I have investigated stable optical trapping of dipolar nanoparticles located near nonreciprocal metasurfaces when illuminated by a laser beam, and explored the possibility to manipulate the trap location in a dynamic fashion. The trap mechanism is governed by the spin-orbit and nonreciprocity-induced lateral recoil forces. In particular, the spin-orbit force is robust against the applied bias, whereas the nonreciprocity one strongly depends on the bias strength thus providing a tunable response of optical traps. To analyze the force response, I have developed rigorous analytical expressions solving the Green's function analytically using residue theorem [49]. These expressions directly link the forces with the dispersion relation of the nonreciprocal system, and allow to calculate the required dipole polarization spin to trap it at any position. Importantly, the theory can be applied to any nonreciprocal system with a given dispersion relation including topological gyrotropic materials [34], magneto-optical surface [32,33],

and drift-biased thin metals [35] or graphene [36-39], amongst many others. As a practical example, I have proposed the use of drift-biased graphene that has recently been experimental demonstrated [36,37]. I have assessed the stability of the platform for the ultra-subwavelength manipulation of optical traps by investigating the trapping potential and trap depth. Results show that stable trap performance can be obtained by using the conventional laser sources such as femtosecond pulses and CO_2 laser beams. I envisage that nonreciprocal platforms would significantly advance the field of nano-optical plasmonic tweezers in terms of dynamic and precise routing, trapping, and manipulation of nanoparticles.

8.4 CHAPTER REFERENCES

[1] Ashkin, A., 1970. Acceleration and trapping of particles by radiation pressure. *Physical Review Letters*, *24*(4), p.156.

[2] Juan, M.L., Righini, M. and Quidant, R., 2011. Plasmon nano-optical tweezers. *Nature Photonics*, *5*(6), pp.349-356.

[3] Righini, M., Volpe, G., Girard, C., Petrov, D. and Quidant, R., 2008. Surface plasmon optical tweezers: tunable optical manipulation in the femtonewton range. *Physical Review Letters*, *100*(18), p.186804.

[4] Novotny, L., Bian, R.X. and Xie, X.S., 1997. Theory of nanometric optical tweezers. *Physical Review Letters*, *79*(4), p.645.

[5] Yoo, D., Gurunatha, K.L., Choi, H.K., Mohr, D.A., Ertsgaard, C.T., Gordon, R. and Oh, S.H., 2018. Low-power optical trapping of nanoparticles and proteins with resonant coaxial nanoaperture using 10 nm gap. *Nano Letters*, *18*(6), pp.3637-3642.

[6] Jensen, R.A., Huang, I.C., Chen, O., Choy, J.T., Bischof, T.S., Loncar, M. and Bawendi, M.G., 2016. Optical trapping and two-photon excitation of colloidal quantum dots using bowtie apertures. *ACS Photonics*, *3*(3), pp.423-427.

[7] Juan, M.L., Gordon, R., Pang, Y., Eftekhari, F. and Quidant, R., 2009. Self-induced back-action optical trapping of dielectric nanoparticles. *Nature Physics*, *5*(12), pp.915-919.

[8] Pang, Y. and Gordon, R., 2011. Optical trapping of 12 nm dielectric spheres using double-nanoholes in a gold film. *Nano Letters*, *11*(9), pp.3763-3767.

[9] Zhang, W., Huang, L., Santschi, C. and Martin, O.J., 2010. Trapping and sensing 10 nm metal nanoparticles using plasmonic dipole antennas. *Nano Letters*, *10*(3), pp.1006-1011.

[10] Hansen, P., Zheng, Y., Ryan, J. and Hesselink, L., 2014. Nano-optical conveyor belt, part I: Theory. *Nano Letters*, *14*(6), pp.2965-2970.

[11] Svoboda, K. and Block, S.M., 1994. Biological applications of optical forces. *Annual Review of Biophysics And Biomolecular Structure*, *23*(1), pp.247-285.

[12] Pang, Y. and Gordon, R., 2012. Optical trapping of a single protein. *Nano Letters*, *12*(1), pp.402-406.

[13] Ashkin, A., 1997. Optical trapping and manipulation of neutral particles using lasers. *Proceedings of the National Academy of Sciences*, *94*(10), pp.4853-4860.

[14] Zhu, B., Ren, G., Gao, Y., Yang, Y., Cryan, M.J. and Jian, S., 2015. Giant gradient force for nanoparticle trapping in coupled graphene strips waveguides. *IEEE Photonics Technology Letters*, *27*(8), pp.891-894.

[15] Abbasi, M.M., Darbari, S. and Moravvej-Farshi, M.K., 2019. Tunable plasmonic force switch based on graphene nano-ring resonator for nanomanipulation. *Optics Express*, *27*(19), pp.26648-26660.

[16] Liu, P.Q. and Paul, P., 2020. Graphene Nanoribbon Plasmonic Conveyor Belt Network for Optical Trapping and Transportation of Nanoparticles. *ACS Photonics*, *7*(12), pp.3456-3466.

[17] Danesh, M., Zadeh, M.J., Zhang, T., Zhang, X., Gu, B., Lu, J.S., Cao, T., Liu, Z., Wee, A.T., Qiu, M. and Bao, Q., 2020. Monolayer Conveyor for Stably Trapping and Transporting Sub-1 nm Particles. *Laser & Photonics Reviews*, *14*(8), p.2000030.

[18] Paul, P. and Liu, P.Q., 2022. Dynamically Reconfigurable Bipolar Optical Gradient Force Induced by Mid-Infrared Graphene Plasmonic Tweezers for Sorting Dispersive Nanoscale Objects. *Advanced Optical Materials*, *10*(3), p.2101744.

[19] Zhang, J., Liu, W., Zhu, Z., Yuan, X. and Qin, S., 2016. Towards nano-optical tweezers with graphene plasmons: Numerical investigation of trapping 10-nm particles with mid-infrared light. *Scientific Reports*, *6*(1), pp.1-7.

[20] Šiler, M., Čižmár, T., Jonáš, A. and Zemanek, P., 2008. Surface delivery of a single nanoparticle under moving evanescent standing-wave illumination. *New Journal of Physics*, *10*(11), p.113010.

[21] Grujic, K. and Hellesø, O.G., 2007. Dielectric microsphere manipulation and chain assembly by counter-propagating waves in a channel waveguide. *Optics Express*, *15*(10), pp.6470-6477.

[22] Ye, F., Badman, R.P., Inman, J.T., Soltani, M., Killian, J.L. and Wang, M.D., 2016. Biocompatible and high stiffness nanophotonic trap array for precise and versatile manipulation. *Nano Letters*, *16*(10), pp.6661-6667.

[23] Ye, F., Soltani, M., Inman, J.T. and Wang, M.D., 2017. Tunable nanophotonic array traps with enhanced force and stability. *Optics Express*, *25*(7), pp.7907-7918.

[24] Paul, N.K. and Kemp, B.A., 2016. Optical manipulation of small particles on the surface of a material. *Journal of Optics*, *18*(8), p.085402.

[25] Rodríguez-Fortuño, F.J., Engheta, N., Martínez, A. and Zayats, A.V., 2015. Lateral forces on circularly polarizable particles near a surface. *Nature Communications*, *6*(1), pp.1-8.

[26] Petrov, M.I., Sukhov, S.V., Bogdanov, A.A., Shalin, A.S. and Dogariu, A., 2016. Surface plasmon polariton assisted optical pulling force. *Laser & Photonics Reviews*, *10*(1), pp.116-122.

[27] Kingsley-Smith, J.J., Picardi, M.F., Wei, L., Zayats, A.V. and Rodríguez-Fortuño, F.J., 2019. Optical forces from near-field directionalities in planar structures. *Physical Review B*, *99*(23), p.235410.

[28] Sukhov, S. and Dogariu, A., 2017. Non-conservative optical forces. *Reports on Progress in Physics*, *80*(11), p.112001.

[29] Bliokh, K.Y., Rodríguez-Fortuño, F.J., Nori, F. and Zayats, A.V., 2015. Spin–orbit interactions of light. *Nature Photonics*, *9*(12), pp.796-808.

[30] Bliokh, K.Y., Smirnova, D. and Nori, F., 2015. Quantum spin Hall effect of light. *Science*, *348*(6242), pp.1448-1451.

[31] Ivinskaya, A., Petrov, M.I., Bogdanov, A.A., Shishkin, I., Ginzburg, P. and Shalin, A.S., 2017. Plasmon-assisted optical trapping and anti-trapping. *Light: Science & Applications*, *6*(5), pp.e16258-e16258.

[32] Gangaraj, S.A.H., Hanson, G.W., Silveirinha, M.G., Shastri, K., Antezza, M. and Monticone, F., 2019. Unidirectional and diffractionless surface plasmon polaritons on three-dimensional nonreciprocal plasmonic platforms. *Physical Review B*, *99*(24), p.245414.

[33] Yu, Z., Veronis, G., Wang, Z. and Fan, S., 2008. One-way electromagnetic waveguide formed at the interface between a plasmonic metal under a static magnetic field and a photonic crystal. *Physical Review Letters*, *100*(2), p.023902.

[34] Lu, L., Joannopoulos, J.D. and Soljačić, M., 2014. Topological photonics. *Nature Photonics*, *8*(11), pp.821-829.

[35] Bliokh, K.Y., Rodríguez-Fortuño, F.J., Bekshaev, A.Y., Kivshar, Y.S. and Nori, F., 2018. Electric-current-induced unidirectional propagation of surface plasmon-polaritons. *Optics Letters*, *43*(5), pp.963-966.

[36] Zhao, W., Zhao, S., Li, H., Wang, S., Wang, S., Utama, M., Kahn, S., Jiang, Y., Xiao, X., Yoo, S. and Watanabe, K., 2021. Efficient Fizeau drag from Dirac electrons in monolayer graphene. *Nature*, *594*(7864), pp.517-521.

[37] Dong, Y., Xiong, L., Phinney, I.Y., Sun, Z., Jing, R., McLeod, A.S., Zhang, S., Liu, S., Ruta, F.L., Gao, H. and Dong, Z., 2021. Fizeau drag in graphene plasmonics. *Nature*, *594*(7864), pp.513-516.

[38] Morgado, T.A. and Silveirinha, M.G., 2021. Active graphene plasmonics with a drift-current bias. *ACS Photonics*, *8*(4), pp.1129-1136.

[39] Correas-Serrano, D. and Gomez-Diaz, J.S., 2019. Nonreciprocal and collimated surface plasmons in drift-biased graphene metasurfaces. *Physical Review B*, *100*(8), p.081410.

[40] Hassani Gangaraj, S.A. and Monticone, F., 2022. Drifting Electrons: Nonreciprocal Plasmonics and Thermal Photonics. *ACS Photonics*, *9*(3), pp.806-819.

[41] Girón-Sedas, J.A., Kingsley-Smith, J.J. and Rodríguez-Fortuño, F.J., 2019. Lateral optical force on linearly polarized dipoles near a magneto-optical surface based on polarization conversion. *Physical Review B*, *100*(7), p.075419.

[42] Novotny, L. and Hecht, B., 2012. *Principles of nano-optics*. Cambridge university press.

[43] Maragò, O.M., Jones, P.H., Gucciardi, P.G., Volpe, G. and Ferrari, A.C., 2013. Optical trapping and manipulation of nanostructures. *Nature Nanotechnology*, *8*(11), pp.807-819.

[44] Šiler, M. and Zemánek, P., 2010. Particle jumps between optical traps in a one-dimensional (1D) optical lattice. *New Journal of Physics*, *12*(8), p.083001.

[45] Ashkin, A., Dziedzic, J.M., Bjorkholm, J.E. and Chu, S., 1986. Observation of a single-beam gradient force optical trap for dielectric particles. *Optics Letters*, *11*(5), pp.288-290.

[46] Panagiotopoulos, P., Hastings, M.G., Kolesik, M., Tochitsky, S. and Moloney, J.V., 2020. Multi-terawatt femtosecond 10 μm laser pulses by self-compression in a CO 2 cell. *OSA Continuum*, *3*(11), pp.3040-3047.

[47] Haberberger, D., Tochitsky, S., Fiuza, F., Gong, C., Fonseca, R.A., Silva, L.O., Mori, W.B. and Joshi, C., 2012. Collisionless shocks in laser-produced plasma generate monoenergetic high-energy proton beams. *Nature Physics*, *8*(1), pp.95-99.

[48] Haberberger, D., Tochitsky, S. and Joshi, C., 2010. Fifteen terawatt picosecond CO 2 laser system. *Optics Express*, *18*(17), pp.17865-17875.

[49] Mitrinovic, D.S.; Keckic, J.D. The Cauchy method of residues: theory and applications. Springer Science & Business Media, 1984.

Chapter 9: Conclusions and Future Research

9.1 CONCLUSIONS

In this thesis, I have proposed a novel class of nano-optical plasmonic tweezers based on engineered hyperbolic and nonreciprocal plasmonic metasurfaces, and analyzed the performance of this type of devices with respect to the state of art in terms of operation frequency, beam alignment and focusing, power, and particle properties, among many others. I have exploited unusual near field properties provided by these metasurfaces to sort, route, trap and manipulate nanoparticles located above them in unprecedented ways while enhancing the strength of the induced force with respect to conventional systems. The key findings of each Chapter are briefly summarized below:

In Chapter 2, I have first presented a brief overview of anisotropic and hyperbolic metasurfaces, and studied their electromagnetic response using numerical and analytical methods. Then, I have analyzed the dispersion characteristics of the supported surface plasmons. Rooted on the exciting properties of such plasmons, I have exploited the photonic spin Hall effect of light to launch directionally propagating surface plasmons within the metasurface – a key mechanism to conform strong lateral recoil forces on nearby dipolar particles. This study constitutes the fundamental building block of the nano-optical plasmonic tweezers explored in this thesis.

In Chapter 3, I have shifted the focus from reciprocal to nonreciprocal responses. As a realistic platform, I have considered a drift-biased graphene-based nonreciprocal metasurface that supports surface plasmons with a broken symmetry in amplitude and polarization within the plane. First, I have studied the electromagnetic behavior of these metasurfaces analyzing their dispersion characteristic and the properties of the supported SPPs. Specifically, the applied drift-bias allows to manipulate the wavefront of the surface plasmons in unprecedented ways and to enforce energy canalization. Then, I have proposed a practical application of drift-biased graphene as a broadband and planar plasmonic hyperlens with extreme

subwavelength resolution. These exciting findings motivated the use of nonreciprocal plasmonic platforms to develop optical tweezers.

In Chapter 4, I have developed a rigorous theoretical framework to compute optical forces on Rayleigh particles located above plasmonic metasurfaces under illumination with a laser beam. To this purpose, I have applied the dispersions characteristics of the metasurface and the unusual properties of the supported surface plasmons discussed in Chapter 2 and 3. The proposed theory is general and can readily be applied to any class of metasurfaces including nonreciprocal ones. Moreover, I have developed a novel analytical formalism to calculate the lateral optical forces acting on nanoparticles. These expressions link the forces with the dispersion characteristics of the metasurfaces and unveil the underlying physical mechanisms that originate them. In addition, I have provided a brief overview on the numerical computation procedure of optical forces using full wave simulation in COMSOL Multiphysics.

In Chapter 5, I have applied the theory developed in Chapter 4 to investigate the response of lateral optical forces on nanoparticles located near anisotropic, reciprocal, metasurfaces. First, I have analyzed all possible plasmonic metasurface topologies and compare the strength and direction of the recoil forces acting on particles located over them. Results have shown that the use of hyperbolic metasurfaces permits to enhance the force dramatically in comparison to the other topologies. Then, I have proposed a realistic visible frequency hyperbolic metasurface based on nanostructured silver that provides force enhancement up to 3 orders magnitude in comparison to the state of art plasmonic surfaces. Importantly, such enhancement appears over a broadband frequency in the sense that can be obtained using laser operating at from visible to infrared frequencies.

In Chapter 6, I have extended this study aiming to stably trap nanoparticles located near nanostructured silver using low power laser beam. Results have shown that this hyperbolic metasurface enhances the trap depth and stiffness induced on the particle by at least an order of magnitude over a broadband frequency. Importantly, such response is robust against the beam focus that significantly relaxes the beam alignment issue in modern optical tweezers systems.

In Chapter 7, I have investigated lateral optical forces on nanoparticles located near nonreciprocal metasurfaces. The primary purpose of using nonreciprocal metasurfaces is to overcome the laser alignment issue in practice to manipulate the particle toward a desired direction. Here, I have considered drift-biased graphene based nonreciprocal metasurface and applied my theoretical framework developed in Chapter 4. Lateral recoil forces in this system exhibit interesting features, including (i) their direction barely changes with respect to the incident laser beam angle of incidence; (ii) the particle can be driven laterally along or against the applied bias as a function of its position, leading into a two-state system; and (iii) the force strength is significantly enhanced thanks to the confined nature of the supported modes.

In Chapter 8, I have applied the concept of optical trapping to the case of nonreciprocal metasurfaces aiming to dynamically manipulate the trap position with subwavelength, precise, resolution. Results have shown that the use of drift-biased graphene enables to manipulate the trap site in-plane up to few microns by tuning the applied bias strength. These findings may significantly push the boundaries of optical tweezers as such tunable response cannot be obtained by common state of art devices.

9.2 ONGOING EXPERIMENTS

The proposed experimental set up to measure the lateral recoil force in the near field of hyperbolic metamaterial is based on lateral atomic force microscopy (see Figure 9.1a). The metamaterial is constructed by periodically organized gold and silicon dioxide layers with subwavelength scale. For the design purposes, I have performed theoretical and numerical studies to identify the required dimension that provides hyperbolic dispersion in the visible frequency band. With that given data, another member in our group fabricated it in the clean room and the scanning electron microscopic image is shown in Figure 9.1 b. Rather than using a nanoparticle, a cantilever with a given torsional spring constant γ_c is used. The set up is illuminated by a green laser beam operating at 532nm. The tip head of the cantilever scatters light with similar properties as the ones of an electric point dipole, and excites directional hyperbolic modes in the structure following the physics as detailed in Chapter 5. To compensate the momentum surge, the cantilever experiences a lateral deflection Δ_L in the opposite direction (see inset in Figure 9.1a). The

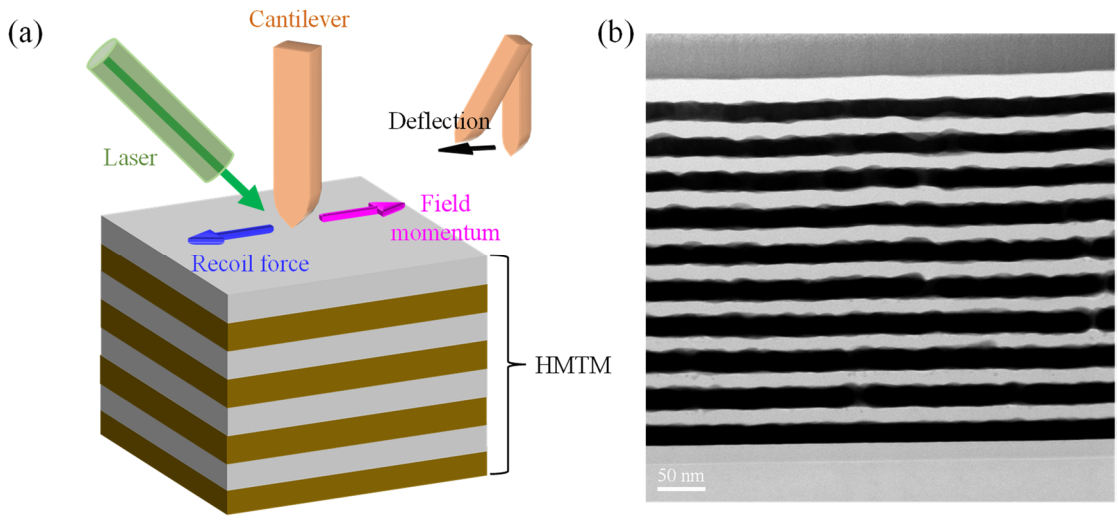

Figure 9.1: Proposed experimental set-up to measure lateral recoil forces near hyperbolic metamaterial (HMTM) using lateral atomic force microscopy. (a) Schematic of the set up. A cantilever is suspended above a HMTM and illuminated by a green laser beam (green arrow). To compensate the momentum of directional hyperbolic modes (magenta arrow), the cantilever deflects in the opposite direction (see inset) thanks to the lateral recoil force (blue arrow). (b) Scanning electronic microscopic image of a HMTM constructed by periodically organized gold and silicon dioxide layer fabricated in our group.

deflection is measured through the lateral atomic force microscopy system, and the resulting recoil force can be computed as $F_{rec} = \gamma_c \Delta_L$. Note that this experiment is still in progress and expected to be finalized in the upcoming months. I stress that measurement of optical forces using cantilever is well known in the community and similar experiment has been carried out in ref-[1]. However, recoil forces using laser beams have not been measured to date. If successful, this experiment would constitute the first experimental report of recoil forces.

To compare the force response with the state of art nano-optical tweezer systems, similar experiment will be carried out by replacing the hyperbolic media with pristine metal and bulk silicon dioxide structures. Following my theoretical and numerical analysis in Chapter 5, I anticipate at least an order of magnitude force enhancement near hyperbolic metamaterial in comparison to others. In addition, I would like to stress that hyperbolic metasurfaces (see Chapter 2) constructed by ultrathin nanostructured metal is being fabricated by one of our group members, and it is in advanced stage. The future goal is to use those

metasurface aiming to further enhance the force strength. Moving beyond, I envision the development of optical tweezer by combining Gaussian laser beam operated in the visible or near infrared with these plasmonic metasurfaces.

9.3 FUTURE RESEARCH LINES

Most of the concepts developed in this thesis can be further refined and expanded in future research. For instance, past few years have gathered enormous interests in manipulating biological cells and atoms that exhibits chirality in nature [2,3]. Rigorous electromagnetic modeling of such chiral molecules, in terms of electric and magnetic dipole, can be combined with my theoretical framework to accurately measure the optical forces exerted on them. Another class of artificially engineered structures namely Moire metasurfaces [4-6], constructed by stacking periodically organized metals on top of each other, and the light-matter interactions provided by them have become a hot topic in photonic research community during the past years. These structures can also be integrated with nano-optical plasmonic tweezer systems to realize unusual recoil force response.

Importantly, the experience gathered in the design and modeling of hyperbolic and nonreciprocal metasurface goes well beyond the field of optical tweezers and can be exploited in many other nanophotonic applications. In this context, I am currently involved in some collaborating research projects. A brief summary of such multidisciplinary *current and future research lines* is documented below:

(i) *X-ray detection using hyperbolic media*: Recently, it has been reported that hyperbolic metamaterials enable Cerenkov radiation in the presence of a bunch of electrons flying above them thanks to the large plasmon wavenumber thus reducing the phase velocity of electromagnetic waves [7]. In this context, visible frequency hyperbolic metamaterials designed in our group (see Figure 9.1a) can readily be applied to generate Cerenkov radiation at visible frequencies upon illumination of X-ray waves. I have performed theoretical and numerical analysis to confirm the appearance of such Cherenkov radiation. Experimental

validation of this work is currently being pursued my other group members in the Lawrence Berkeley National Laboratory.

(ii) *Terahertz electromagnetic waves generation using drift-biased graphene*: Recently, it has been shown that multilayer graphene structures support hyperbolic surface modes inside it [8,9]. In this work, the goal is to design a similar hyperbolic metamaterial and apply a drift-bias to the graphene sheets. The drifting electrons will couple to hyperbolic photonic modes inside the structure without requiring any external laser beams, effectively generating THz electromagnetic waves. Note that one of these structured is being fabricated in our group following my theoretical analysis, and it will be tested very soon.

In summary, my theoretical and numerical analysis, and the ongoing experimental breakthroughs as detailed in this thesis may significantly push the boundaries of nano-optical plasmonic tweezers, and enable many other novel nanophotonic applications in bioengineering, physics, and chemistry.

9.4 CHAPTER REFERENCES

[1] Antognozzi, M., Bermingham, C.R., Harniman, R.L., Simpson, S., Senior, J., Hayward, R., Hoerber, H., Dennis, M.R., Bekshaev, A.Y., Bliokh, K.Y. and Nori, F., 2016. Direct measurements of the extraordinary optical momentum and transverse spin-dependent force using a nano-cantilever. *Nature Physics*, *12*(8), pp.731-735.

[2] Ben-Moshe, A., Wolf, S.G., Sadan, M.B., Houben, L., Fan, Z., Govorov, A.O. and Markovich, G., 2014. Enantioselective control of lattice and shape chirality in inorganic nanostructures using chiral biomolecules. *Nature Communications*, *5*(1), pp.1-9.

[3] Wang, S.B. and Chan, C.T., 2014. Lateral optical force on chiral particles near a surface. *Nature Communications*, *5*(1), pp.1-8.

[4] Wu, Z. and Zheng, Y., 2018. Moiré metamaterials and metasurfaces. *Advanced Optical Materials*, *6*(3), p.1701057.

[5] Hu, G., Krasnok, A., Mazor, Y., Qiu, C.W. and Alù, A., 2020. Moiré hyperbolic metasurfaces. *Nano Letters*, *20*(5), pp.3217-3224.

[6] Hu, G., Wang, M., Mazor, Y., Qiu, C.W. and Alù, A., 2021. Tailoring light with layered and moiré metasurfaces. *Trends in Chemistry*, *3*(5), pp.342-358.

[7] Liu, F., Xiao, L., Ye, Y., Wang, M., Cui, K., Feng, X., Zhang, W. and Huang, Y., 2017. Integrated Cherenkov radiation emitter eliminating the electron velocity threshold. *Nature Photonics*, *11*(5), pp.289-292.

[8] Xiang, Y., Dai, X., Guo, J., Zhang, H., Wen, S. and Tang, D., 2014. Critical coupling with graphene-based hyperbolic metamaterials. *Scientific reports*, *4*(1), pp.1-7.

[9] Sreekanth, K.V., De Luca, A. and Strangi, G., 2013. Negative refraction in graphene-based hyperbolic metamaterials. *Applied Physics Letters*, *103*(2), p.023107.

Vita

Nayan Kumar Paul was born in Rajshahi, Bangladesh. He received the Bachelor of Science in Electrical & Electronic Engineering from Rajshahi University of Engineering & Technology, Bangladesh, and the Master of Science in Electrical Engineering from Arkansas State University, USA, in 2012 and 2016, respectively. He is currently a PhD candidate under the supervision of Prof. Juan Sebastian Gomez Diaz in the Department of Electrical and Computer Engineering at the University of California, Davis, USA. His doctoral research focuses on investigating light-matter interactions in artificially engineered structures, namely metamaterials and metasurfaces, and apply them in existing as well as to develop novel nanophotonic devices with superior performance. Prior to joining University of California Davis, he held a graduate research assistant position at the Arkansas State University under the supervision of Prof. Brandon Kemp, where he worked on the design of optical tractor beams using guided waves. In 2014, he acted as a lecturer in the department of Electrical & Electronic Engineering at Uttara University, Dhaka, Bangladesh. He serves as an active reviewer for IEEE Transactions on Antennas and Propagation, Scientific Reports Optics Express, and Optical Engineering.

AWARDS AND RECOGNITIONS

- 2022: UC Davis Dissertation Quarter Fellowship.
- 2020: UC Davis Advancement-to-candidacy Fellowship.
- 2019: UC Davis Summer Graduate Student Research Fellowship.
- 2018: NSF Travel Grant, 2D Materials Sumer School.
- 2016: 1st winner for oral presentation in Create@State-2016 Research Symposium.
- 2015: 2nd winner for poster presentation in Create@State-2016 Research Symposium.
- 2009: Undergraduate Scholarship from Rajshahi University of Engineering & Technology, Bangladesh.

PEER-REVIEWED JOURNAL PUBLICATIONS

- **Paul, N.K.** and Gomez-Diaz, J.S., 2022. Dynamic manipulation of optical traps near nonreciprocal surface", under review in *Optics Letters.*
- **Paul, N.K.** and Gomez-Diaz, J.S., 2022. Lateral recoil optical forces on nanoparticles near nonreciprocal surfaces. *arXiv preprint arXiv:2203.08955*, under review in *Physical Review B*.
- Domulevicz, L., Jeong, H., **Paul, N.K.**, Gomez-Diaz, J.S. and Hihath, J., 2021. Multidimensional Characterization of Single-Molecule Dynamics in a Plasmonic Nanocavity. *Angewandte Chemie International Edition*, *60*(30), pp.16436-16441. (Selected as **Very Important Paper**)
- **Paul, N.K.** and Gomez-Diaz, J.S., 2021. Broadband and unidirectional plasmonic hyperlensing in drift-biased graphene. *Applied Physics Letters*, *118*(9), p.091107. (**Editor's Pick**)
- **Paul, N.K.** and Gomez-Diaz, J.S., 2021. Low-power Optical Traps Using Anisotropic Metasurfaces: Asymmetric Potential Barriers and Broadband Response. *Physical Review Applied*, *15*(1), p.014018.
- Correas-Serrano, D., **Paul, N.K.** and Gomez-Diaz, J.S., 2019. Plasmonic and photonic isolators based on the spatiotemporal modulation of graphene. In *Micro-and Nanotechnology Sensors, Systems, and Applications XI* (Vol. 10982, p. 109821I). International Society for Optics and Photonics.
- **Paul, N.K.**, Correas-Serrano, D. and Gomez-Diaz, J.S., 2019. Giant lateral optical forces on Rayleigh particles near hyperbolic and extremely anisotropic metasurfaces. *Physical Review B*, *99*(12), p.121408.
- **Paul, N.K.** and Kemp, B.A., 2016. Optical manipulation of small particles on the surface of a material. *Journal of Optics*, *18*(8), p.085402.
- **Paul, N.K.** and Kemp, B.A., 2016. Optical pulling force on a particle near the surface of a dielectric slab waveguide. *Optical Engineering*, *55*(1), p.015106.
- **Paul, N.K.** and Kemp, B.A., 2015. Push-pull phenomenon of a dielectric particle in a rectangular waveguide. *Progress In Electromagnetics Research*, *151*, pp.73-81.

MANUSCRIPTS UNDER PREPARATION

- L. Wang, **N. K. Paul**, and J. S. Gomez-Diaz, "Broadband and efficient surface plasmon generation using drift-biased nanostructured graphene based hyperbolic metasurfaces", Journal manuscript under preparation.
- **N. K. Paul** and J. S. Gomez-Diaz, "Reconfigurable lateral optical forces on nanoparticles near nanostructured graphene", Journal manuscript under preparation.

INTERNATIONAL CONFERENCE PROCEEDINGS

- L. Wang, **N. K. Paul**, and J. S. Gomez-Diaz, "THz and IR Plasmonic Sources based on Drift-biased Nanostructures," IEEE International Symposium on Antennas & Propagation & USNC-URSI Radio Science Meeting, June 2022.
- **N. K. Paul** and J. S. Gomez-Diaz, "Drift-biased Graphene Nanoplasmonics", *URSI National Symposium XXXVI*, September 2021 (invited, accepted and in press).
- L. Wang, **N. K. Paul**, and J. S. Gomez-Diaz, "Broadband and efficient surface plasmon generation on drift-biased graphene-based hyperbolic metasurfaces", *National Radio Science Meeting Virtual Conference*, January 2021 (Invited).
- **N. K. Paul** and J. S. Gomez-Diaz, "On the dynamic tailoring of one-way surface plasmons over drift-biased graphene metasurfaces", *14th International Congress on Artificial Materials for Novel Wave Phenomena – Metamaterials*, New York, October 2020.
- **N. K. Paul** and J. S. Gomez-Diaz, "Unidirectional lateral optical forces on polarizable nanoparticles near drift-biased graphene metasurfaces", *Active Photonic Platforms XII 11461*, 1146106 (2020).
- **N. K. Paul** and J. S. Gomez-Diaz, "Manipulation of Nanoparticles using Hyperbolic Metasurfaces", *Meta19-the 10th International Conference of Metamaterials, Photonic Crystals and Plasmonics*, Lisbon (Portugal), July 2019 (Invited).

- **N. K. Paul**, D. Correas-Serrano and J. S. Gomez-Diaz, “Giant Optical Forces Exerted on Nanoparticles Near Hyperbolic Metasurface”, *2nd URSI Atlantic Radio Science Meeting*, Gran Canaria, Spain, May 2018 (Invited).